MHD modeling and numerical simulation with finite volume-type methods. Application to fusion plasma

Élise Estibals

École doctorale de Sciences Fondamentales et Appliquées
Unité de recherche : Sciences

Thèse de doctorat

Présentée en vue de l'obtention du
grade de docteur en Mathématiques
de
UNIVERSITÉ CÔTE D'AZUR

par
Élise Estibals

Modélisation MHD et Simulation Numérique par des Méthodes Volumes Finis. Application aux Plasmas de Fusion

MHD Modeling and Numerical Simulation with Finite Volume-type Methods.
Application to Fusion Plasmas

Dirigée par Hervé Guillard, Directeur de recherche, INRIA Sophia Antipolis
et co-dirigée par Afeintou Sangam, Maître de conférence, LJAD Nice

Soutenue le 2 mai 2017
Devant le jury composé de :

Rémi	Abgrall	Prof., Université de Zürich	Examinateur
Christophe	Berthon	Prof., Lab. de Math. J. Leray, Nantes	Rapporteur
Hervé	Guillard	DR INRIA, LJAD, Université de Nice	Directeur de thèse
Boniface	Nkonga	Prof., LJAD, Université de Nice	Examinateur
Afeintou	Sangam	MCF, LJAD, Université de Nice	Co-directeur de thèse
Éric	Serre	DR CNRS, Lab. M2P2, Centrale Marseille	Rapporteur

Remerciements

Contents

List of Figures v

List of Tables xi

Introduction 1
- I Nuclear fusion . . . 1
- II Inertial Confinement Fusion . . . 2
- III Magnetic Confinement Fusion . . . 4
- IV Fusion modeling . . . 6
- V Organization of the manuscript . . . 7

Introduction 9
- I La fusion thermonucléaire contrôlée . . . 9
- II Fusion par Confinement Inertiel . . . 11
- III La Fusion par Confinement Magnétique . . . 12
- IV Modélisation de la fusion . . . 15
- V Organisation du manuscrit . . . 16

Résumé 19

1 Fluid models 25
- I Plasma modeling . . . 25
  - I.1 Kinetic model . . . 25
  - I.2 Macroscopic quantities . . . 26
  - I.3 Collision operators . . . 26
  - I.4 Moment equations . . . 28
    - i Mass conservation equation . . . 28
    - ii Momentum equation . . . 28
    - iii Energy equation . . . 30
  - I.5 Maxwell equations . . . 30
  - I.6 Bi-fluid MHD equations . . . 31
- II Bi-fluid MHD equations in quasi-neutral regime . . . 34
- III Bi-temperature Euler model . . . 36
  - III.1 Derivation of the bi-temperature model . . . 37
  - III.2 The bi-temperature model for large β parameter . . . 41
  - III.3 Properties of the bi-temperature Euler model . . . 43
- IV Mono-fluid MHD models . . . 45
  - IV.1 Non-dimensional bi-fluid MHD model . . . 45
  - IV.2 Resistive MHD model for small $\delta^*_{e,i}$ and bounded R_m . . . 49
  - IV.3 Ideal MHD model from small $\delta^*_{e,i}$ and large R_m . . . 50

i Conservative system . . . 50
ii Properties of the ideal MHD model . . . 51
IV.4 Discussion on the assumptions leading to MHD models . . . 53
V Conclusions . . . 53

2 Finite volume method **55**
I Generalities on finite volume method . . . 55
I.1 Principles of finite volume method . . . 55
I.2 2-D cell-centered finite volume on rectangular mesh . . . 56
I.3 2-D vertex-centered finite volume on a triangular mesh . . . 59
II Cell-centered approach for cylindrical coordinates . . . 61
II.1 Ideal MHD equations in cylindrical coordinates . . . 61
II.2 Cell-centered approach in a circular mesh . . . 63
III Vertex-centered approach for the toroidal geometry . . . 67
III.1 Cylindrical coordinates for toroidal problem and divergence form . . . 67
III.2 Mesh design and adaptation to the finite volume method . . . 69
IV Conclusions . . . 74

3 Relaxation scheme for the bi-temperature Euler model **75**
I Presentation of the scheme . . . 75
II Transport step . . . 76
II.1 Properties of the relaxed system . . . 76
II.2 Relaxation flux . . . 78
III Projection step . . . 80
IV Numerical tests . . . 81
IV.1 Shock tube . . . 81
IV.2 Implosion . . . 85
IV.3 Sedov injection in 2-D Cartesian geometry . . . 92
IV.4 Sedov injection in a poloidal plane of a torus with axisymmetry initialization . . . 94
IV.5 Triple point problem in a rectangular computational domain . . . 97
IV.6 Triple point problem in a disc in 2-D Cartesian geometry . . . 103
IV.7 Triple point problem in the plane of a torus with axisymmetry initialization . . . 106
IV.8 Triple point problem in 3-D toroidal geometry . . . 108
V Conclusions . . . 111

4 On Euler potential for MHD models **113**
I Issues on the divergence-free constraint . . . 113
I.1 Vector potential **A** method . . . 113
I.2 Powell's source term . . . 114
I.3 Generalized Lagrange Multiplier . . . 114
I.4 Contrained transport method . . . 115
II An alternate method for divergence-free problem . . . 116
III Numerical resolution of ideal MHD equations with Euler potential . . . 117
III.1 Presentation of the scheme . . . 117
III.2 Transport step . . . 117
i Rusanov flux . . . 118
ii HLL flux . . . 118
iii HLLD flux . . . 119

III.3 Projection step . . . 122
i Cartesian coordinates . . . 122
ii Issue for cylindrical coordinates . . . 123
IV Numerical resolution of resistive MHD equations . . . 123
IV.1 Presentation of the proposed scheme . . . 124
IV.2 Presentation of the resistive step . . . 124
IV.3 Resistive step in Cartesian coordinates . . . 125
i Order 2 . . . 125
ii Order 4 . . . 126
IV.4 Resistive step in cylindrical coordinates . . . 129
i Order 2 . . . 129
ii Order 4 . . . 131
V Numerical results . . . 133
V.1 Brio-Wu problem for ideal MHD . . . 133
V.2 Orszag-Tang problem for ideal MHD . . . 141
V.3 Kelvin-Helmholtz instabilities for ideal MHD . . . 145
V.4 Kelvin-Helmholtz instabilities for resistive MHD . . . 147
V.5 Screw pinch equilibrium with uniform density in cylindrical coordinates for ideal MHD . . . 150
V.6 Screw pinch equilibrium with uniform density in Cartesian coordinates for ideal MHD . . . 155
V.7 Screw pinch equilibrium with uniform density in Cartesian coordinates for resistive MHD . . . 157
VI Conclusions . . . 160

Conclusions **161**

Conclusions **163**

Bibliography **165**

List of Figures

1 Fusion reaction [1]. 1
2 Direct drive of the laser beam to heat and compress the target [2]. 3
3 Indirect drive of the laser beam to heat and compress the target [3]. 3
4 Fast ignition for the direct drive method [4]. 4
5 Representation of a tokamak [5]. 5
6 Representation of the future ITER tokamak [6]. 6
1 La réaction de fusion [1]. 9
2 Attaque directe d'un laser pour chauffer et comprimer la cible [2]. 11
3 Attaque indirecte d'un laser pour chauffer et comprimer la cible [3]. 12
4 Allumage rapide pour l'attaque directe [4]. 12
5 Représentation d'un tokamak [5]. 13
6 Représentation du futur tokamak ITER [6]. 15

1.1 The four cases of Riemann problem for the bi-temperature Euler equation: (a) 1-Rarefaction and 3-Shock, (b) 1-Shock and 3-Rarefaction, (c) 1-Rarefaction and 3-Rarefaction, (d) 1-Shock and 3-Shock. 45
1.2 Riemann fan of the ideal MHD system. 52

2.1 Representation of a control cell $\Omega_{i,j}$ in the cell-centered approach. 56
2.2 Piecewise linear reconstruction for the 1-D case. 59
2.3 Representation of a control cell Ω_i in the vertex-centered approach. 60
2.4 Cartesian and cylindrical basis representation. 63
2.5 Representation of a cell $\Omega_{i,j}$ in the cylindrical coordinates for the cell-centered approach. 67
2.6 Projection on $\mathbf{e}_\varphi$ of the Ω_i cell control. 70

3.1 Riemann fan for the relaxed system (3.1). 80
3.2 Shock tube problem at $t = 8.6289 \times 10^{-8}s$ with $\nu_{ei} = \nu_{ie} = 0$. Solution at $y = 0.5$. Left-Top: Density, Right-Top: x-velocity in red, and y-velocity in blue, Left-Center: Electronic (red) and ionic (blue) temperatures, Right-Center: Electronic (red) and ionic(blue) pressures, Left-Bottom: Electronic entropy, Right-Bottom: Ionic entropy. 83
3.3 Shock tube problem at $t = 8.6289 \times 10^{-8}s$ with $\nu_{ei} \neq 0$, $\nu_{ie} \neq 0$. Solution at $y = 0.5$. Left-Top: Density, Right-Top: x-velocity in red, and y-velocity in blue, Left-Center: Electronic (red) and ionic (blue) temperatures, Right-Center: Electronic (red) and ionic(blue) pressures, Left-Bottom: Electronic entropy, Right-Bottom: Ionic entropy. 84

3.4 Implosion problem, Similar mesh with 2145 points as the one used in numerical simulation. The mesh used in Section IV.2 has been obtained by a refinement of a factor 4 from the present one and contains 33153 ($\approx 4 \times 4 \times 2145$). 86
3.5 Implosion problem at $t_1 = 4.0901 \times 10^{-7}s$. 2-D fields of Left-Top: Density, Right-Top: Velocity, Left-Center: Electronic pressure, Right-Center: Ionic pressure, Left-Bottom: Electronic temperature, Right-Bottom: Ionic temperature. 87
3.6 Implosion problem at $t_1 = 4.0901 \times 10^{-7}s$. 1-D fields at $y = x$ of Left-Top: Density, Right-Top: Radial (red) and tangential (blue) velocities, Left-Center: Electronic (red) and ionic (blue) temperatures, Right-Center: Electronic (red) and ionic (blue) pressures, Left-Bottom: Electronic entropy, Right-Bottom: Ionic entropy. 88
3.7 Implosion problem at $t_2 = 6.22 \times 10^{-7}s$. 2-D fields of Left-Top: Density, Right-Top: Velocity, Left-Center: Electronic pressure, Right-Center: Ionic pressure, Left-Bottom: Electronic temperature, Right-Bottom: Ionic temperature. 89
3.8 Implosion problem at $t_2 = 6.22 \times 10^{-7}s$. 1-D fields at $y = x$ of Left-Top: Density, Right-Top: Radial (red) and tangential (blue) velocities, Left-Center: Electronic (red) and ionic (blue) temperatures, Right-Center: Electronic (red) and ionic (blue) pressures, Left-Bottom: Electronic entropy, Right-Bottom: Ionic entropy. 90
3.9 Implosion problem, Density, Left: 1-D fields at $y = x$, Right: 2-D isolines at $\rho = 1$ (black), $\rho = 1.585$ (violet), $\rho = 2.369$ (blue), $\rho = 4.259$ (green), and $\rho = 6.047$ (red). Top: $t_1 = 4.0901 \times 10^{-7}s$, Middle: $t_2 = 6.22 \times 10^{-7}s$, Bottom: $t_3 = 8.4973 \times 10^{-7}s$. 91
3.10 Sedov injection in 2-D Cartesian geometry at $t = 9.7634 \times 10^{-6}s$. Left: Density, Center: Electronic pressure, Right: Ionic pressure. 93
3.11 Sedov injection in 2-D Cartesian geometry. 1-D profiles at Left: $t = 6.73 \times 10^{-10}s$, Middle: $t = 6.73 \times 10^{-9}s$, Right: $t = 9.7634 \times 10^{-6}s$, Top: Density. Bottom: Electronic (red) and Ionic (blue) temperatures. 93
3.12 Sedov injection in axisymmetric toroidal geometry at $t = 9.7634 \times 10^{-6}s$. Comparison of the 2-D axisymmetric and 3D computations. Left: 2-D run, Right: 3-D run, Top: Density, Center: Electronic pressure, Bottom: Ionic pressure. 95
3.13 Sedov injection in 3-D toroidal geometry, toroidal velocity u_φ at $t = 9.7634 \times 10^{-6}s$ along $Z = 0$. 96
3.14 Initialization of the triple point problem in a rectangle. 98
3.15 Triple point problem total internal energy at $t = 3.5$ (left) and at $t = 5.0$ (right), Top: Results from [40] for mono-temperature Euler equations where the top of the domain is obtained with the Volume of Fluid method and the bottom of the domain with the concentration equations, Bottom: Relaxation scheme for bi-temperature Euler equations with $\nu_{ei} = \nu_{ie} = 0$. . 99
3.16 Triple point problem without thermal exchange, $\nu_{ei} = \nu_{ie} = 0$, $\dfrac{T_i - T_e}{T_e}$ 2-D field at $t = 3.5$ (Left), and $t = 5.0$ (Right). 99
3.17 Triple point problem with $\nu_{ei} = \nu_{ie} = 0$ at $t = 3.5$ (Left), and $t = 5$ (Right). 2-D fields of Top: Density, Middle: Electronic temperature, Bottom: Ionic temperature. 100

3.18 Triple point in a rectangular domain at $t = 3.5$ (left) and $t = 5.0$ (right). Comparison between the temperature of the case $\nu_{ei} \neq 0$ and $\nu_{ie} \neq 0$ (Top) and the electronic (middle) and ionic (bottom) temperatures of the case $\nu_{ei} = \nu_{ie} = 0$. 101
3.19 Triple point in a rectangular domain at $t = 3.5$ (left) and $t = 5.0$ (right). Comparison between the density of the case $\nu_{ei} \neq 0$ and $\nu_{ie} \neq 0$ (Top) and the one of the case $\nu_{ei} = \nu_{ie} = 0$ (Bottom). 102
3.20 The three domain of the triple point problem in the (R, Z) plane. 103
3.21 Triple point problem in Cartesian geometry. $\frac{T_i - T_e}{T_e}$ 2-D fields at $t = 2.1 \times 10^{-9}s$ (left), $t = 4.7 \times 10^{-9}s$ (middle), and $t = 1.35 \times 10^{-8}s$ (right). . 104
3.22 Triple point problem in Cartesian geometry. Initial data (Left) and solution at $t = 1.1574 \times 10^{-5}s$ (Right). Top: Density, Center: Electronic temperature, Bottom: Total pressure. 105
3.23 Triple point problem at $t = 1.1574 \times 10^{-5}s$. Comparison of the results obtained in Cartesian geometry and in a torus. Left: 2-D axisymmetric run, Right: 2-D Cartesian run. Top: Density, Center: Electronic temperature, Bottom: Total pressure. 107
3.24 Triple point problem at $t = 1.1574 \times 10^{-5}s$. Comparison of the results obtained in Cartesian geometry and in a torus. Velocity vectors with density contours. Left: 2-D axisymmetric run, Right: 2-D Cartesian run. 108
3.25 Triple point problem initial domain in 3-D toroidal geometry. Left: for the poloidal planes 1 to 3. Right: for the rest of the poloidal planes (4 to 20). 109
3.26 Triple point problem initialization. Top: Poloidal planes 1 to 3, Bottom: Poloidal planes 4 to 20. Left: Density, Center: Electronic temperature, Right: Total pressure. 109
3.27 Triple point problem in 3-D toroidal geometry. Density at $t = 1.1574 \times 10^{-5}s$. Top-Left: Plane 1, Top-Center: Plane 2, Top-Right: Plane 3, Bottom-Left: Plane 4, Bottom-Center: Plane 20, Bottom-Right: Plane 10. 110
3.28 Triple point problem in 3-D toroidal geometry. Electronic temperature at $t = 1.1574 \times 10^{-5}s$. Top-Left: Plane 1, Top-Center: Plane 2, Top-Right: Plane 3, Bottom-Left: Plane 4, Bottom-Center: Plane 20, Bottom-Right: Plane 10. 110
3.29 Triple point problem in 3-D toroidal geometry. Total pressure at $t = 1.1574 \times 10^{-5}s$. Top-Left: Plane 1, Top-Center: Plane 2, Top-Right: Plane 3, Bottom-Left: Plane 4, Bottom-Center: Plane 20, Bottom-Right: Plane 10. 111

4.1 Localization of the magnetic and electric fields for the contrained transport method. Source: [11]. 115
4.2 Riemann fan with one intermediate state. 118
4.3 Riemann fan with four intermediate states. 122
4.4 Representation of the ghost cells for a Cartesian mesh. 127
4.5 1-D Brio-Wu problem, Solution at $t = 0.1$, O(1) Rusanov flux with and without projection, Top-Left: Density, Top-Right: Pressure, Middle-Left: x-velocity, Middle-Right: y-velocity, Bottom-Left: y-magnetic field, Bottom-Right: Euler potential. 135

4.6 1-D Brio-Wu problem, Solution at $t = 0.1$, O(1) HLL flux with and without projection, Top-Left: Density, Top-Right: Pressure, Middle-Left: x-velocity, Middle-Right: y-velocity, Bottom-Left: y-magnetic field, Bottom-Right: Euler potential. 136

4.7 1-D Brio-Wu problem, Solution at $t = 0.1$, O(1) HLLD flux with and without projection, Top-Left: Density, Top-Right: Pressure, Middle-Left: x-velocity, Middle-Right: y-velocity, Bottom-Left: y-magnetic field, Bottom-Right: Euler potential. 137

4.8 1-D Brio-Wu problem, Solution at $t = 0.1$, O(2) Rusanov flux with and without projection, Top-Left: Density, Top-Right: Pressure, Middle-Left: x-velocity, Middle-Right: y-velocity, Bottom-Left: y-magnetic field, Bottom-Right: Euler potential. 138

4.9 1-D Brio-Wu problem, Solution at $t = 0.1$, O(2) HLL flux with and without projection, Top-Left: Density, Top-Right: Pressure, Middle-Left: x-velocity, Middle-Right: y-velocity, Bottom-Left: y-magnetic field, Bottom-Right: Euler potential. 139

4.10 1-D Brio-Wu problem, Solution at $t = 0.1$, O(2) HLLD flux with and without projection, Top-Left: Density, Top-Right: Pressure, Middle-Left: x-velocity, Middle-Right: y-velocity, Bottom-Left: y-magnetic field, Bottom-Right: Euler potential. 140

4.11 2-D Brio-Wu problem, Euler potential ψ at $t = 0.1$. HLLD flux with projection, Left: Order 1 in time and space, Right: Order 2 in time and space. 141

4.12 Orszag-Tang problem, HLLD O(2), $t = 0.5$, Top: Density field, Bottom: Pressure field, Left: Scheme without projection, Right: Scheme with projection. 143

4.13 Orszag-Tang problem, HLLD O(2), $t = 0.5$, Pressure along $y = 0.3125$, Red: Scheme without projection, Blue: Scheme with projection. 143

4.14 Orszag-Tang problem, HLLD O(2), Top-Left: $\nabla \cdot \mathbf{B}$ field at $t = 0.5$ scheme without projection, Top-Right: $\nabla \cdot \mathbf{B}$ field at $t = 0.5$ scheme with projection, Bottom-Left: $\|\nabla \cdot \mathbf{B}\|_{L^2}(t)$, Bottom-Right: $\|\nabla \cdot \mathbf{B}\|_{\infty}(t)$, ... 144

4.15 Orszag-Tang problem, HLLD O(2) with projection, $t = 1.0$, Left: Density field, Right: Pressure field. 144

4.16 Kelvin-Helmholtz instabilities for ideal MHD, Ratio $\frac{B_{pol}}{B_{tor}}$, 256×512 mesh, O(2) HLLD flux. Column 1: $t = 5.0$, Column 2: $t = 8.0$, Column 3: $t = 12.0$, Column 4: $t = 20.0$. 146

4.17 Kelvin-Helmholtz instabilities for ideal MHD, 256×512 mesh, O(2) HLLD flux. Left: $||\nabla \cdot \mathbf{B}||_{L^2}||(t)$, Right: $||\nabla \cdot \mathbf{B}||_{\infty}(t)$. 146

4.18 Kelvin-Helmholtz instabilities for ideal MHD, Ratio $\frac{B_{pol}}{B_{tor}}$, O(2) HLLD flux with projection. Column 1: $t = 5.0$, Column 2: $t = 8.0$, Column 3: $t = 12.0$, Column 4: $t = 20.0$. 147

4.19 Kelvin-Helmholtz instabilities for resistive MHD, $\eta = 5 \times 10^{-4}$, Ratio $\frac{B_{pol}}{B_{tor}}$, HLLD O(2), Top: Order 2 for the resistive step, Bottom: Order 4 for the resistive step, Column 1: $t = 5.0$, Column 2: $t = 8.0$, Column 3: $t = 12.0$, Column 4: $t = 20.0$. 148

4.20 Kelvin-Helmholtz instabilities for resistive MHD, $\eta = 10^{-3}$, Ratio $\frac{B_{pol}}{B_{tor}}$, HLLD O(2), Top: Order 2 for the resistive step, Bottom: Order 4 for the resistive step, Column 1: $t = 5.0$, Column 2: $t = 8.0$, Column 3: $t = 12.0$, Column 4: $t = 20.0$. 149
4.21 Screw pinch equilibrium: Exact solution. Left: Pressure, Right: φ-magnetic field. 151
4.22 Screw pinch equilibrium in cylindrical coordinates, All R. Rusanov O(1). Left: Pressure, Right: B_φ. 151
4.23 Screw pinch equilibrium in cylindrical coordinates, All R. HLL O(1). Left: Pressure, Right: B_φ. 152
4.24 Screw pinch equilibrium in cylindrical coordinates, All R. HLLD O(1). Left: Pressure, Right: B_φ. 152
4.25 Screw pinch equilibrium in cylindrical coordinates. First order in time and space. Comparison of the scheme with projection and of the one without projection. Left: Rusanov flux, Right: HLL flux. 152
4.26 Screw pinch equilibrium in cylindrical coordinates. O(1) HLLD flux. Evolution of Left: the Residu in function time iteration. Right: Relative error of B_φ in function of time. 153
4.27 Screw pinch equilibrium in cylindrical coordinates, All R. Rusanov O(2). Left: Pressure, Right: B_φ. 153
4.28 Screw pinch equilibrium in cylindrical coordinates, All R. HLL O(2). Left: Pressure, Right: B_φ. 153
4.29 Screw pinch equilibrium in cylindrical coordinates, All R. HLLD O(2). Left: Pressure, Right: B_φ. 154
4.30 Screw pinch equilibrium in cylindrical coordinates. Second order in time and space. Comparison of the scheme with projection and of the one without projection. Left: Rusanov flux, Right: HLL flux. 154
4.31 Screw pinch equilibrium in cylindrical coordinates. O(2) HLLD flux. Evolution of Left: the Residu in function time iteration. Right: Relative error of B_φ in function of time. 154
4.32 Screw pinch in Cartesian geometry. Comparison of the HLLD scheme with and without projection at the second order in time and space. Relative error of the pressure in function of Alfvén time. 156
4.33 Screw pinch equilibrium in Cartesian geometry for ideal MHD. Comparison of the HLLD schemes with and without projection. Final pressure field, Left: Scheme with projection, Right: Scheme without projection. 156
4.34 Screw pinch in Cartesian geometry for resistive MHD with $\eta = 1.0 \times 10^{-6}$. Comparison of the HLLD scheme with and without projection at the second order in time and space. Relative error of the pressure in function of Alfvén time. Left: Resistive step at the second order, Right: Resistive step at the fourth order. 158
4.35 Screw pinch equilibrium in Cartesian geometry for resistive MHD. $\eta = 1.0 \times 10^{-6}$. Comparison of the HLLD schemes with and without projection. Final pressure field, Left: Scheme with projection, Right: Scheme without projection. Top: Resistive step at the second order, Bottom: Resistive step at the fourth order. 159

List of Tables

1 Confinement parameters in ICF and MCF. 2
2 Paramètres de confinement de la FCI et de la FCM. 10

1.1 Value of the inertial lengths and resistivity for the tokamak *Iter* at the center, and at the edge of the plasma. 53

3.1 Initial data for the shock tube problem. 81
3.2 Initial data for the implosion problem. 86
3.3 Initial data of the three states of the triple points problem. 103

4.1 Initial data of Brio-Wu problem. 134
4.2 Initial data of Orszag-Tang 2-D problem. 142
4.3 Initial data of Kelvin-Helmholtz instabilities. 145
4.4 Initial data of screw pinch equilibrium. 151

Introduction

The question of energy remains important and central for human being. Energy enters greatly in all domains of human activities: food production, home heat and light, industrial facility operations, public and private transportation demands, communication needs, state safety requirement. The standard of living and energy consumption are intimately linked so that the quality of life is correlated with a reasonable price of consumed energy.

The increasing demand of energy, the very limited energy resource accessibility by the world will probably become worse in the next future. This situation is intensified by environment requirements imposed to the portfolio energy resources available. Energy sources having reduced greenhouse gases, limited waste disposal, cheap cost production are then investigated to alleviate the world energy situation. Among world existing energy source options [37]: coal, oil, natural gas, wind energy, solar power, hydroelectricity, and nuclear fission energy, nuclear fusion power potentially fulfills the above standards.

I Nuclear fusion

Fusion is the thermonuclear reaction that consists of merging two light atoms to produce a heavy one, and fast neutrons carrying a lot of energy as shown in Figure 1.

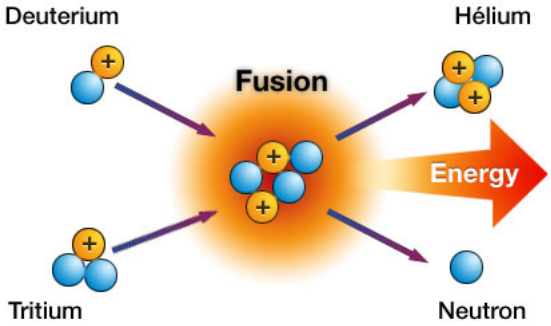

Figure 1: Fusion reaction [1].

Fusion is the process which powers the sun and the stars. In future fusion reactors envisaged on Earth, energy will be released by gathering together hydrogen isotopes, namely deuterium and tritium. These fuels are virtually unlimited. Deuterium is abundant in ocean water. There is 1 atom of deuterium for every 6700 atoms of hydrogen [37]. It will take 2 billions years to exhaust all the deuterium to operate fusion if we keep the present rate of world energy consumption. Deuterium can be easily extracted from ocean water at very low coast. Conversely, there is no natural tritium, it can be generated by lithium reacting with neutrons directly in fusion reactor. Lithium is relatively abundant

on Earth and resources are estimated to be sufficient for 20000 years at the current world energy consumption. Nevertheless, this fusion reaction has two inconveniences: tritium is a radioactive element and lithium is a harmful substance. However, according to fission reactors, these situations are relatively minor, given that the half-life of tritium is 12.5 years compared with 2.4×10^7 years for uranium 236, 7.13×10^8 years for uranium 235, 4.5×10^9 years for uranium 236, 24000 years for plutonium 238, and still 6600 years for plutonium 240 [65].

Moreover, no greenhouse emissions, no other poisonous chemical materials are emitted into atmosphere by fusion reactions. Only the harmless inert gas helium is a product of the fusion reaction. Therefore, fusion reaction is attractive with respect to environment.

Fusion energy is thus a sustainable power source with favorable economic, environmental and safety attributes. Fusion occurs naturally at the extremely high pressures and temperatures which exist at the center of the sun, 15 millions of degrees Celsius. At the high temperatures experienced in the sun, any gas becomes a plasma, a mixture of negatively charged electrons and either positively charged atomic nuclei or ions. In order to reproduce fusion on earth, gases need to be heated to extremely high temperatures whereby atoms become completely ionized yielding a hot plasma. In fact, the amount of energy released and the number of thermonuclear fusion reactions in the volume of plasma depend on the density of particles and their temperature. The reaction gain becomes higher than one when the energy released by fusion reactions is larger than the one invested in the plasma heating and confinement. This is formulated in the *Lawson criterion* relating the density n, temperature of the plasma and its confinement time τ [52]. For deuterium-tritium plasma heated to the temperature of 10 keV or 10^8 K, this criterion reads:

$$n\tau > 10^{20}\ \mathrm{m}^{-3}\mathrm{s}.$$

This condition can be fulfilled in different ways. A tremendous mass insures through gravitation forces a very large confinement time in stars. The confinement time is the leading factor of fusion achievement. On earth two methods are currently actively studied, both experimentally, theoretically and numerically, to attain a large gain in fusion reactions: Inertial Fusion Confinement, abbreviated ICF, and Magnetic Fusion Confinement, known briefly as MCF. ICF leads to confine the plasma at extremely high density for a short time whereas MCF yields to achieve low densities for the relatively long times of several seconds. Comparison of the confinement times and densities in the two approaches is given in Table 1. The two ways are the matter of the next two sections.

	ICF	MCF
Particle density n in cm^{-3}	10^{26}	10^{14}
Confinement time τ in s	10^{-11}	10
Lawson criterion $n\,\tau$ in $s\ cm^{-3}$	10^{15}	10^{15}

Table 1: Confinement parameters in ICF and MCF.

II Inertial Confinement Fusion

Inertial Confinement Fusion relies exclusively on mass inertia to hold a fusion plasma in a small spherical volume for a short time corresponding to the time a sound wave needs to propagate from the surface to the center [8, 65]. Put simply, during this short time, the small volume of fuel is bringing to very high density, roughly about thousand times its solid

density or liquid density, and high temperature by short energetic laser or ion beam pulses. Two principal schemes of interest are nowadays investigated to achieve ICF. The former, known as *ablative* implosive scheme, based on the action-reaction principle, consists in the irradiation of deuterium-tritium spherical shell by the use of powerful laser beam neatly set to obtain a symmetric illumination. Under the effect of the laser irradiation, the outer part of the spherical shell is vaporized, yielding a coronal plasma, which in turn expands towards the exterior: this is the so-called ablative process. By action-reaction principle, the coronal plasma expansion pushes the internal part of the shell toward the center in form of compressible waves. As the imploding material stagnates in the center, its kinetic energy is converted into internal energy. At this instant, the fuel consists of a highly compressed shell enclosing a hot spot of igniting fuel in the target center. A thermonuclear burn starts from the hot spot, travels radially from the target center to the periphery in the form of a wave, igniting then the whole fuel, which afterwards explodes. This process constitutes the **direct-drive** ICF illustrated in Figure 2.

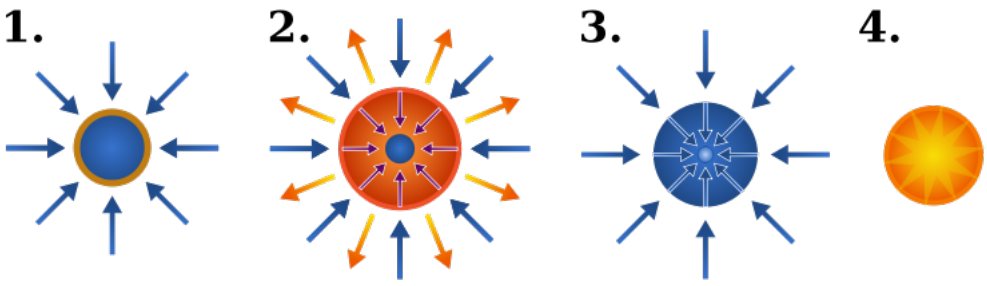

Figure 2: Direct drive of the laser beam to heat and compress the target [2].

An important problem in the implementation of direct-drive approach is the attainment of a high irradiation symmetry and accordingly the symmetry of dynamic plasma compression. In fact, a dissymetric irradiation of the target could be a seed of Rayleigh-Taylor-type instabilities that would hinder the efficiency of the fusion operation. To overcome this situation, another ablative implosive-type approach, known as **indirect-drive**, process has been developed and shown in Figure 3. It consists in irradiation of cylindrical metallic cavity, made of gold or high-Z materials, of few millimeters in diameter and one centimeter long, the so-called **hohlraum**, from inside by using many intense laser beams. The deposited energy in the hohlraum is transformed in X-rays and generates then a isotropic and uniform illumination of the target inside the cavity [8, 56, 65].

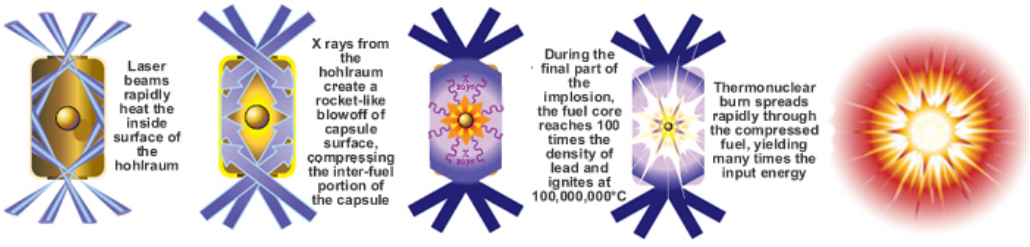

Figure 3: Indirect drive of the laser beam to heat and compress the target [3].

Two largest facilities have been constructed to access conditions for ICF: **National Ignition Facility** (NIF) at Livermore in California in USA [47], and **Laser Mégajoule** (LMJ) at Barp near Bordeaux in France [16]. The NIF is operational since 2009.

In ablative scheme, the compression and ignition of the fuel are both dependent phases, and own contradictory conditions to fulfill at the same time. In order to cope this situation, the **fast ignition** concept has been developed [8, 56, 65]. The idea is to separate the two phases. In particular, one starts by compressing the target by using either direct-drive or indirect-drive, then launches a ultrahigh-power short-pulse laser [62] to burn the compressed fuel [72]. Figure 4 shows this process for the direct-drive.

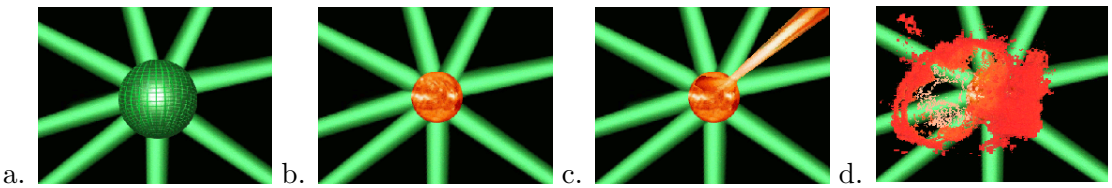

Figure 4: Fast ignition for the direct drive method [4].

III Magnetic Confinement Fusion

Since plasma particles have high temperature, a contact with a material vessel intended to contain them will cool the plasma, leading to a possible fail of fusion reactions. Because plasma particles are charged, their dynamics across magnetic field lines is bounded whereas they move freely along magnetic field lines. The contact of plasma particles with the vessel walls due to a transversal movement could be thus avoided while their escape from the vessel by their helical trajectories along the magnetic field lines would still be plausible. The idea of MCF approach is to confine the plasma particles in devices with appropriate magnetic field configuration. There is plentiful magnetic configurations to maintain a hot plasma in a bounded domain, depending on the magnetic coils arrangement. They can split into two classes. The first one, known as **open-ended confinement**, is based on straight disposition of the magnetic coils. Such as a scheme is unable itself to confine a plasma since magnetic field lines are not closed, the device is then equipped with a driver allowing to bring back inside in the machine possible charged particles arriving at its ends. Open-ended confinement machines are thus MCF trap devices. Magnetic trap mirror [64], field reversed configuration [37] are for instance open-ended confinement devices.
The second class aim at using closed magnetic field lines to hold the plasma in bounded domain, thus it is termed **toroidal confinement**. In this way, magnetic coils are arranged such that they produce a toroidal field. However, in such a configuration, the magnetic field strength decreases with radius, which yields a radial velocity component and a drift of the particles towards the outside. To confine the plasma for a relatively long time, the field lines have to be twisted in such a manner as to lead to an absence of any radial field component. Stellarator, spheromak, reversed field pinch, levitated dipole, are examples of toroidal confinement devices [37].

Tokamak, a toroidal confinement machine, is the major device for MCF approach [19, 38, 50, 79]. The main principal magnetic field is the toroidal field, which is produced by current external coils as illustrated in Figure 5. Tokamak approach also exploits largely the fact that the plasma is held inside the device by a balance of the magnetic field force and the gradient of the plasma pressure. As a consequence of this equilibrium, a poloidal component of magnetic field is immediately required for the magnetic force. In a tokamak, the poloidal field is principally generated by the plasma current, this current flowing in the toroidal direction. These currents and fields are shown in Figure 5.

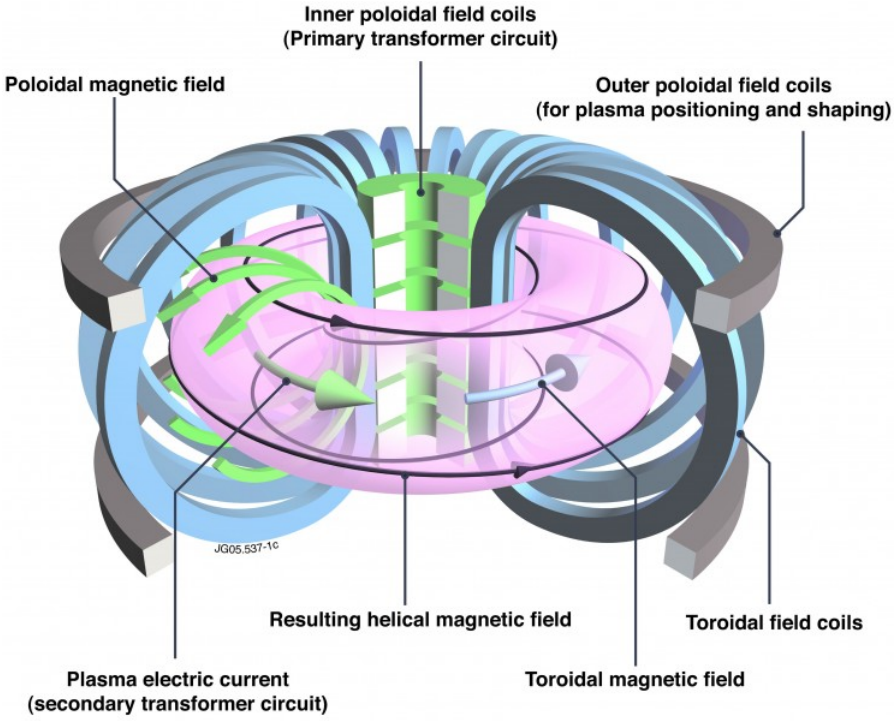

Figure 5: Representation of a tokamak [5].

Moreover, the above equilibrium implies that the plasma pressure p is constrained to be not larger than a certain amount $\beta_{\max}$ of the magnetic energy $\mathbf{B}^2/2\mu_0$, where the plasma β-parameter is given by:

$$\beta = \frac{p}{\frac{\mathbf{B}^2}{2\mu_0}}.$$

Creating strong magnetic field is technically challenging and cost-intensive, leading to the β-parameter to be not too small. As matter of fact, finding confinement configurations with β of a few percent constitutes current active research in MCF.

Controlled nuclear fusion reaction is expected to operate in a tokamak as follows. A mixture of deuterium and tritium is injected into the vacuum vessel contained in the tokamak. The mixture is heated externally until ignition is reached. There is three heating mechanisms: ohmic heating through the plasma resistivity, heating by high-frequency waves, heating by injection of beams of neutral particles. The two latter mechanisms could be used at any time of the heating phase whereas the former one is only used in the initial heating phase of the plasma, and then one of the two latter must take the relay. At the same time of heating phase, the magnetic field is generated by passing an electric current through coils wound around the torus. The plasma current produces a poloidal magnetic field and the two fields combine to produce a magnetic field as displayed in Figure 5. As soon as the plasma is heated to sufficiently high temperatures, it will be ignite yielding α-particles and neutrons. The α-particles are stopped in the plasma, provide additional plasma heating while the fusion mechanism continues running, whereas the neutrons penetrate the blanket of absorbing material surrounding the torus. If the confinement were ideal, the fusion operation could go until all fuel is used up.

However, the fusion process in a tokamak faces complex questions at each phase such

as the stability requirement of the device [19, 38, 79], plasma heating, transport including turbulence and various types of instabilities [37, 38, 79], and technological issues as the design of coils supplying adequate magnetic fields.

Nevertheless, the quest of fusion energy with tokamak approach receives a great credit to go forward in this way. The **International Thermonuclear Experimental Reactor**, known as **ITER**, currently being built in Cadarache, France, is the largest tokamak dedicated to fusion energy, as shown in Figure 6. The roles of the ITER facility are to investigate burning plasma physics in long pulse, high-temperature, deuterium-tritium experiment, and address and solve a number of fusion technology issues that will arrive in a fusion reactor. The beginning of its operational phase is scheduled for 2025-2030 and the construction of the demonstration fusion reactor **DEMO** [80] will follow if ITER is successful. Finally, the commercial fusion reactor **PROTO** will be constructed upon DEMO results.

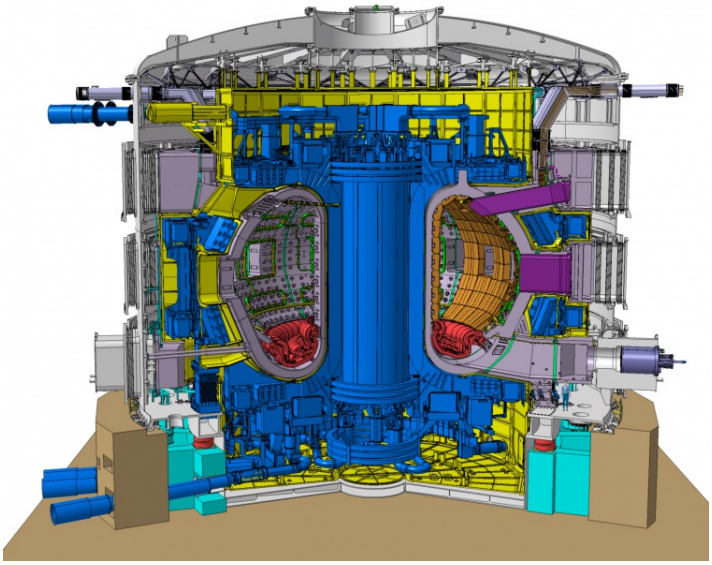

Figure 6: Representation of the future ITER tokamak [6].

IV Fusion modeling

Issues on controlled thermonuclear fusion can be basically split into plasma physics and technological requirements.
Technological issues are dependent of the approach chosen to achieve fusion. ICF technological demands roughly turned around high powerful laser, high-ion accelerators, targets. These issues are described in [8, 27, 65] and references there in. MCF technological requirements concern mainly the design of supraconductor coils magnets intended to generate high-toroidal magnetic fields, of efficient heating sources. However, ICF and MCF schemes share the problem regarding material would be used to design the wall receiving energetic neutrons that escape from ICF target or that MCF device vessel vacuum.

Fusion plasma physics is concerned with the description of charged particle dynamics inside the considered device. There are three basics approaches to plasma physics: **particle theory**, **kinetic theory**, and **hydrodynamic theory**.
The particle theory is using equations of motion for individual plasma particles, and with the help simulation codes and appropriate averages the plasma physics is analyzed. This

approach is also called N-body model, where N is assumed to represent the number of plasma particles. As the fusion plasma owns very large number of particles, as quoted in previous Sections, the accuracy of the model will require a large N in order simulate the plasma. Despite the existence of codes dealing with N-body model, kinetic theory is favored with respect to the particle approach, N-body model becoming thus the base model of hierarchy ones to derive from it.
Kinetic theory is based on a set equations for distribution functions of the plasma particles that encodes their dynamics in time, physical and velocities space, together with Maxwell equations. Kinetic theories can accurately model such a system owning large number of particles. However, numerical computations of kinetic theories are, in general, resource consuming both in time and storage space, and are limited in a small computational domain of physical/velocities space [44]. Large information yielded by kinetic models are not often accessible by experiment. Conversely fluid models constructed on velocity moments provide pertinent plasma parameters on a large time and a large domain [54, 55], which fit with experimental data.

In the either hydrodynamic or fluid models the conservation laws of mass, momentum and energy are coupled to Maxwell equations. One-fluid equations, two-fluid system, MHD equations [24, 9, 10, 37, 38, 43, 42], two-temperature Euler system [26, 29, 51, 69, 7, 32] are for instance fluid models.
Plasma modeling enables to study the plasma behavior which translates to three important types of transport theory: heat conduction, particles diffusion, and magnetic field diffusion. It infers that plasma modeling tackles the understanding and controlling of energy confinement. Analyzing waves contained in systems brought by the modeling gives ways on choosing frequency waves that will heat the plasma.

V Organization of the manuscript

This work is a combination of plasma physics modeling and numerical analysis. It is structured in four chapters and a conclusion. The first two deals with modeling whereas the last two concern numerical analysis. The content is the following.

Chapter 1. In this chapter we recall the kinetic equation of a magnetized plasma and its corresponding bi-fluid MHD equations. Then, using the non-dimensional scaling of the bi-fluid MHD equations, we give the assumptions leading to the bi-temperature Euler model and the ideal and resistive MHD ones. The proposed derivation of the bi-temperature Euler model is more general than the ones suggested in [26, 37, 43, 51, 7].

Chapter 2. General principles of finite volume method are reviewed in this chapter, both for structured and non-structured tessellations aimed at approximating the three models derived previously. Having in the mind future applications to MCF in tokamak approach, we study the modification of finite volume type method to approximate the solutions of these models in a toroidal geometry. The scheme we proposed is based on recent works reported in [21, 18]. However, such as application is not straightforward due to both the complexity of the models and the unstructured tessellation used to adequately mesh the toroidal geometry of the torus.

Chapter 3. The numerical strategy set up in Chapter 2 uses a relaxation scheme to approximate the bi-temperature Euler model. In this chapter we give all steps leading to

the construction of this relaxation scheme. Numerical tests are also proposed to assess the performance of this scheme. This scheme has been accepted for publication [7].

Chapters 1–3 are gathered in [32] and published as internal report.

Chapter 4. The MHD equations coupled to the Maxwell's equation which contains the divergence-free constraint of the magnetic field, has to be maintained by the numerical approximation. A strategy is designed ensuring that the magnetic field computed by standard Finite volume approximation will be solenoidal, both for Cartesian and cylindrical coordinates. Various numerical tests on well-known standard problems in MHD in 2D-geometry are performed in different geometries in order to validate the proposed numerical method.

Conclusion. Finally, our conclusions are given in the last chapter. Forthcoming works are also proposed.

Introduction

La question de l'énergie reste importante et centrale pour l'humanité. L'énergie entre largement dans tous les grands domaines des activités humaines : la production de nourriture, le chauffage et l'éclairage des habitations, les transports privés et publics, les usines industrielles de production, les communications, la sécurité de l'État. Le niveau de vie et la consommation d'énergie sont intimement liées si bien que la qualité de vie est corrélée à un prix raisonnable de l'énergie consommée.

L'augmentation des besoins en énergie ainsi la quantité très limitée des ressources énergétiques accessibles sur Terre s'empireront probablement dans les années à venir. Cette situation est amplifiée par les normes environnementales exigées à l'ensemble des énergies disponibles. Les sources d'énergie à moindre effet de serre et quantité de déchets, et à un coût de production relativement faible sont alors explorées. Parmi les différentes sources d'énergie envisageables [37], le charbon, le pétrole, le gaz naturel, l'énergie éolienne, l'énergie solaire, l'énergie hydroélectrique, ainsi que la fission nucléaire, la fusion thermonucléaire contrôlée satisferait les critères précédents.

I La fusion thermonucléaire contrôlée

La fusion est une réaction thermonucléaire qui consiste à mettre ensemble deux atomes légers pour obtenir un atome plus lourd et des neutrons rapides transportant une grande quantité d'énergie, comme le montre la figure 1.

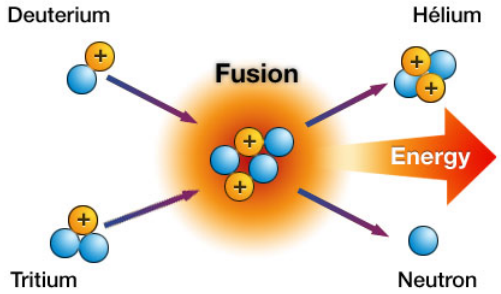

Figure 1: La réaction de fusion [1].

C'est de la réaction de fusion de leurs composants chimiques que le soleil et les étoiles s'auto-entretiennent. Dans les futurs réacteurs de fusion envisagés sur Terre, l'énergie sera obtenue par la fusion de deux isotopes de l'hydrogène, le deuterium et le tritium. Les réserves de ces combustibles sont relativement illimitées. Le deuterium est très abondant dans les océans. Il y a un atome de deuterium pour 6700 atomes d'hydrogène [**?**]. Il faudrait plus de 2 millions d'années pour épuiser tout le deuterium nécessaire à la fusion

si on garde le niveau actuel de consommation d'énergie. Le deuterium peut être extrait aisément de l'eau des océans à un coût minimum. Au contraire, le tritium n'existe pas naturellement sur Terre, il peut être obtenu directement à partir de la réaction du lithium et des neutrons du réacteur de fusion. Le lithium est relativement abondant sur Terre et ses ressources sont estimées suffisantes pour les 20000 prochaines années. Néanmoins, la fusion a deux inconvénients : le tritium est radioactif et le lithium est une substance dangereuse. Cependant, ces deux situations sont relativement mineures en comparaison aux données des réacteurs de fission, étant donné que la demi-vie du tritium est de $12,5$ ans alors qu'elle est de $2,4 \times 10^7$ pour l'uranium 234, $7,13 \times 10^8$ ans pour l'uranium 235, $4,5 \times 10^9$ pour l'uranium 236, 24000 pour le plutonium 238, et de 6600 ans pour le plutonium 240 [65].

De plus, il n'y a pas d'émission de gaz à effet de serre ainsi que d'autres substances chimiques nocives dans l'atmosphère par la fusion thermonucléaire. Seul l'hélium, gaz non nocif, est rejeté par la fusion. Ainsi, la fusion est une source d'énergie attrayante respectant l'environnement.

La fusion est donc une source d'énergie viable ayant d'avantageuses qualités économiques, environnementales et sécuritaires. La fusion se produit naturellement à des pressions et températures extrêmement élevées qui existent au centre du soleil : 15 millions de degrés Celsius. À ces hautes températures présentes dans le soleil, tout gaz devient un plasma, un mélange d'électrons chargés négativement et de nucléons ou encore d'ions chargés positivement. Afin de reproduire la fusion sur Terre, les gaz doivent être chauffés à des températures extrêmes auxquelles les atomes deviennent complètement ionisés engendrant ainsi un plasma chaud. En fait, la quantité d'énergie libérée et le nombre de réactions de fusion thermonucléaire dépendent de la densité de particules ainsi que de leurs températures. Le rendement de la réaction dépasse 1 lorsque l'énergie produite par la fusion est supérieure à celle fournie pour confiner le plasma. Ceci est formulé par le *critère de Lawson* reliant la densité n, la température T au temps de confinement τ [52]. Pour un plasma composé de deuterium et de tritium chauffé à 10 keV soit 10^8 K, ce critère donne :

$$n\tau > 10^{20}\ \mathrm{m}^{-3}\mathrm{s}.$$

Cette condition peut être satisfaite de différentes manières. Une masse énorme assure sous l'action de forces gravitationnelles un long temps de confinement. Ce temps est un facteur majeur pour obtenir des réactions de fusion. Actuellement, il existe deux méthodes faisant l'objet de recherche active à la fois expérimentale, théorique, et numérique pour atteindre des rendements suffisamment grands pour la fusion : la Fusion par Confinement Inertiel, abrégée FCI, et la Fusion par Confinement Magnétique appelée dénommée FCM. La FCI confine des plasmas extrêmement denses sur des temps très court alors que la FCM se propose d'obtenir la fusion avec des densités faibles sur des longs temps de confinement. La comparaison des temps de confinement et des densités de ces deux approches est donnée par le tableau 2.

	FCI	FCM
Densité de particules n in cm^{-3}	10^{26}	10^{14}
Temps de confinement τ in s	10^{-11}	10
Critère de Lawson $n\,\tau$ in $s\ cm^{-3}$	10^{15}	10^{15}

Table 2: Paramètres de confinement de la FCI et de la FCM.

Ces deux méthodes sont discutées dans les deux parties suivantes.

II Fusion par Confinement Inertiel

La fusion par confinement inertiel se base exclusivement sur l'inertie des masses pour maintenir les plasmas de fusion dans un petit volume sphérique pour un temps court correspondant au temps nécessaire pour qu'une onde sonore se propage de la surface au centre [8, 65]. Pour être plus précis, pendant ce petit laps de temps, le volume de combustible est amené à une très grande densité environ mille fois supérieure à sa densité solide ou liquide et à de hautes températures par des rayons lasers énergétiques à implusions courtes ou de puissants faisceaux d'ions. Actuellement, deux méthodes sont étudiées pour réaliser la FCI. La première connue sous le nom de schéma d'implosion *ablatif* est basé sur le principe d'action-réaction et consiste à irradier un cible sphérique composé de deuterium et de tritium par des rayons lasers de manière à éclairer la cible de façon symétrique. Sous l'effet de l'irradiation, la coquille extérieure de la cible se vaporise créant ainsi un plasma de couronne, qui se détend vers l'extérieur : ce processus est dit ablatif. Grâce au principe d'action-réaction, la détente du plasma de couronne pousse la partie interne de la cible vers le centre sous la forme d'une onde de compression. Comme l'implosion stagne au centre, son énergie cinétique est se transforme en énergie interne. À cet instant, le combustible est constitué d'une coquille fortement comprimée enfermant un point chaud de combustible allumé au centre de la cible. Un réaction thermonucléaire se déclenche au centre du point chaud, se déplace radialement du centre vers la périphérie de la cible, allume le reste du combustible qui ensuite explose. Ce processus est la **FCI par l'attaque directe**, et illustré par la figure 2.

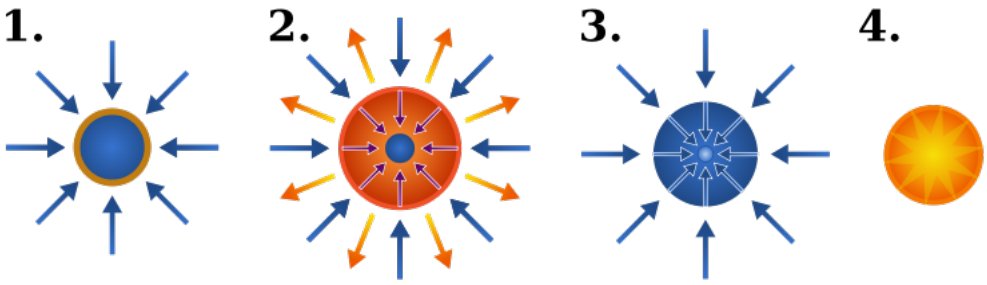

Figure 2: Attaque directe d'un laser pour chauffer et comprimer la cible [2].

Un problème important dans l'implémentation de l'attaque directe est d'atteindre une haute irradiation symétrique et donc une compression symétrique du plasma. En fait, une dissymétrie de l'irradiation de la cible serait la source d'instabilités du type Rayleigh-Taylor, qui diminueraient l'efficacité de la fusion. Afin de surmonter cette situation, une méthode du type ablation-implosion, appelée **attaque indirecte** a été développée, elle est montrée sur la figure 3. Il s'agit de l'irradiation par l'intérieur via de nombreux faisceaux laser intenses d'une cavité métallique et cylindrique, faite d'or ou de matériaux à grand numéro atomique Z, de diamètre de quelques millimètres et long d'un centimètre appelé **hohlraum**. L'énergie déposée dans l'hohlraum est convertie en rayons X et génère alors une irradiation isentropique et uniforme de la cible à l'intérieur de la cavité [8, 56, 65].

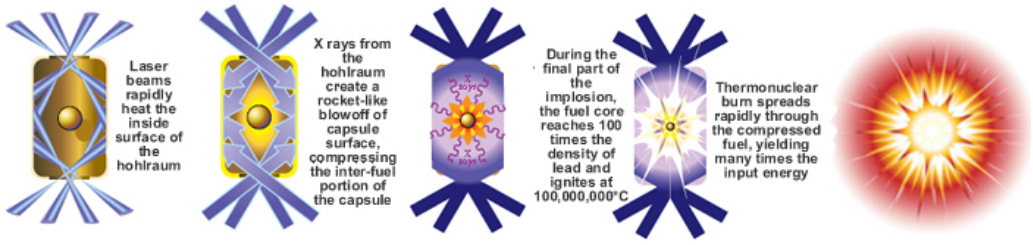

Figure 3: Attaque indirecte d'un laser pour chauffer et comprimer la cible [3].

Deux grandes installations ont été construites pour accéder aux conditions de la FCI : le **National Ignition Facility** (NIF) à Livermore en Californie aux USA [47], et le **Laser MégaJoule** (LMJ) au Barp près de Bordeaux en France [16]. Le NIF est opérationnel depuis 2009.

Dans les schémas ablatifs, la compression et l'allumage du combustible sont deux phases se déroulant simultanément et possédant pourtant des conditions contradictoires à satisfaire en même temps. Afin de faire face à cette situation, le concept d'**allumage rapide** a été développé [8, 56, 65]. L'idée est de séparer les deux phases. En particulier, la première phase commence par la compression de la cible par l'utilisation de l'attaque directe ou indirecte puis de tirer de très courtes impulsions lasers très intenses [62] pour allumer le combustible comprimé [72]. La figure 4 illustre l'allumage rapide par l'attaque directe.

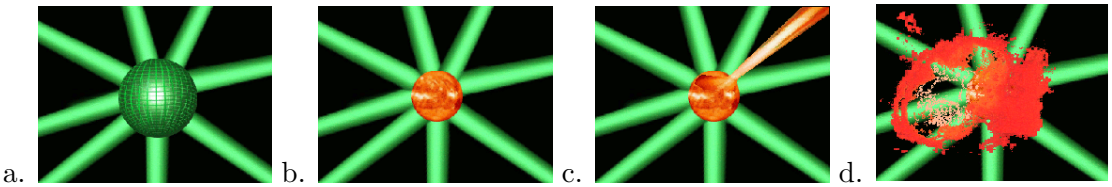

Figure 4: Allumage rapide pour l'attaque directe [4].

III La Fusion par Confinement Magnétique

Puisque les particules du plasma ont des hautes températures, un contact avec d'autres matériaux refroidirait le plasma, conduisant à un possible arrêt de la réaction de fusion. Comme les particules du plasma sont chargées, leur dynamique le long des lignes d'un champ magnétique est bornée, cependant elles déplacent librement le long de ces lignes de champ. Le contact entre les particules du plasma avec les parois dû aux mouvements transverses pourrait être donc évité tandis que leurs trajectoires hélicoïdales le long des lignes de champ serait toujours possible. L'idée de l'approche FCM est de confiner les particules du plasma dans des machines équipées de configurations de champs magnétiques appropriées. Il existe une multitude de configurations de champs magnétiques pour maintenir le plasma chaud dans un domaine borné, dépendant de la position des bobines magnétiques. Elles peuvent se diviser en deux catégories. La première, appelée en anglais **open-ended confinement**, est basée sur une disposition droite des bobines magnétiques. De tels schémas ne sont pas capable de confiner la plasma puisque les lignes de champ sont ouvertes, la machine est alors équipée d'un mécanisme permettant d'y ramener les particules chargées lorsqu'elles arrivent aux extrémités de la machine. Les machines open-ended confinement sont donc des machines-pièges de la FCM. Les miroirs à pièges magnétiques [64], les configurations à renversement du champ [37] sont des exemples de machines **open-ended**

confinement.

La seconde catégorie de configuration se propose d'utiliser des lignes de champ fermées pour maintenir le plasma dans un domaine borné, d'où la dénomination de **confinement toroïdal**. Dans ce schéma, les bobines magnétiques sont disposées de telle façon qu'elles produisent un champ toroïdal. Cependant, pour une telle configuration, l'intensité du champ magnétique décroît avec le rayon, entraînant ainsi une génération de la composante radiale de la vitesse et de la dérive des particules vers l'extérieur. Pour confiner le plasma sur un temps relativement long, les lignes de champ s'incurveraient de manière à maintenir une abscence de champ radial. Parmi les machines à confinement toroïdal, on peut citer le stellarator, le spheromak, le pinch à champ renversé, le *levitated dipole* [37].

Le tokamak, un autre système à confinement toroïdal, est la principale machine pour le schéma de la FCM [19, 38, 50, 79]. Le champ magnétique principal est toroïdal, produit par des bobines extérieures comme le montre la figure 5. L'approche des tokamaks exploitent largement le fait que le plasma est maintenu à l'intérieur de la machine par l'équilibre entre la force du champ magnétique et le gradient de pression du plasma. Dans un tokamak, le champ poloïdal est principalement généré par le courant du plasma, ce courant se déplaçant dans la direction toroïdale. Ces courants et champs sont également illustrés sur la figure 5.

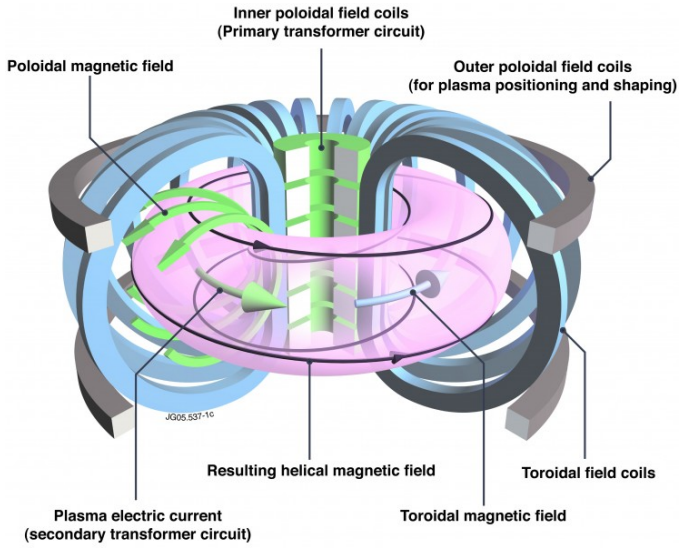

Figure 5: Représentation d'un tokamak [5].

De plus, l'équilibre cité précédemment implique que la pression du plasma p est contrainte à ne pas dépasser une certaine fraction $\beta_{\max}$ de l'énergie magnétique $\dfrac{\mathbf{B}^2}{2\mu_0}$ où le paramètre β du plasma est donné par :

$$\beta = \frac{p}{\dfrac{\mathbf{B}^2}{2\mu_0}}.$$

Créer un champ magnétique intense est un défi technique et très couteux, menant à un paramètre β pas trop petit. En réalité, trouver une configuration du confinement avec un β de l'ordre d'un relativement faible pourcentage constitue un sujet de recherche actif pour la FCM.

La réaction du fusion nucléaire contrôlée se réaliserait dans un tokamak suivant la procédure suivante. Un mélange de deuterium-tritium est injecté dans la chambre vide contenu dans le tokamak. Le mélange est chauffé par l'extérieur jusqu'à ce que l'allumage soit atteint. Il existe trois mécanismes pour le chauffage : le chauffage ohmique grâce à la résistivité du plasma, le chauffage par des ondes hautes fréquences, et le chauffage par l'injection de faisceaux de particules neutres. Les deux derniers mécanismes pourraient être utilisés à tout stade de la phase de chauffage alors que le premier s'utiliserait uniquement pour l'initialisation de cette phase et ensuite un des deux autres mécanismes prendrait le relais. Au même moment de la phase de chauffage, le champ magnétique est généré par le passage d'un courant électrique par les bobines placées le long du tore. Le courant du plasma produit un champ magnétique poloïdal et les deux champs se combinent pour donner naissance à un champ magnétique comme celui illustré sur la figure 5. Dès que le plasma est chauffé à des températures suffisamment élevées, la réaction de fusion se déclenche, libérant ainsi des particules α et des neutrons. Les particules α sont piègées dans le plasma, fournissant alors un chauffage supplémentaire pendant que la réaction de fusion continue de se dérouler, tandis que les neutrons pénètrent dans la couche de matériau entourant le tore. Si le confinement est idéal alors la fusion continuera aussi longtemps qu'il y aura du combustible.

Cependant, chaque phase du processus de fusion dans un tokamak est sujette à des situations complexes, comme par exemple la stabilité nécessaire à la machine [19, 38, 79], le chauffage du plasma, le transport incluant la turbulence et une variété d'instabilités du plasma [37, 38, 79], ainsi qu'aux problèmes techniques comme la forme des bobines magnétiques fournissant un champ magnétique adéquat.

Néanmoins, la quête de l'énergie de fusion par l'approche des tokamaks connaît d'importants engouements. L'**International Thermonuclear Experimental Reactor**, connue sous le nom d'**ITER**, en cours de construction à Cadarache en France est le plus grand tokamak dédié à la fusion et schématisé sur la figure 6. Les rôles d'ITER sont d'explorer tous les champs de connaissances de la physique des plasmas chauds pour de longues impulsions, à de hautes températures, sur les expériences de deuterium-tritium, et de recenser et de résoudre les problèmes techniques qui arriveraient dans les réacteurs de fusion. Le début de la phase opérationnelle est programmé pour 2025-2030 et la construction du réacteur de démonstration **DEMO** [80] suivra si le projet ITER obtient des résultats satisfaisants. Finalement, le réacteur commercial **PROTO** sera construit à partir des résultats de DEMO.

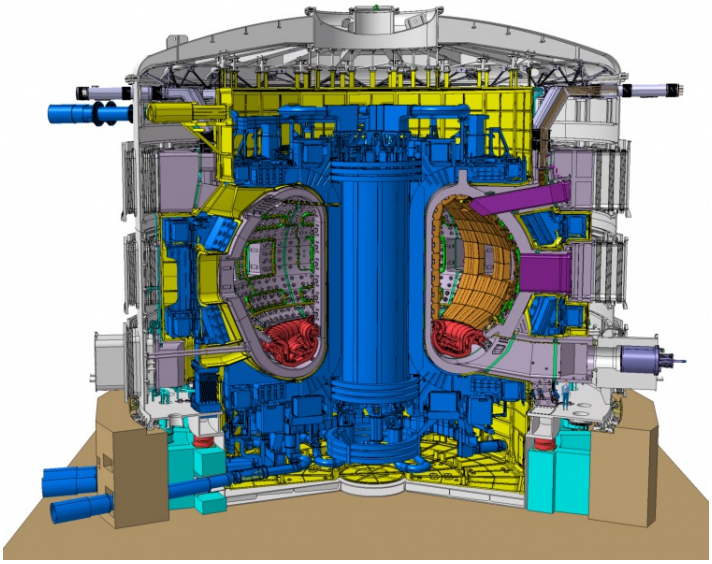

Figure 6: Représentation du futur tokamak ITER [6].

IV Modélisation de la fusion

Les problèmes liés à la fusion thermonucléaire contrôlée peuvent être classées en deux catégories : la physique des plasmas et les besoins technologiques.

Les enjeux technologiques dépendent de l'approche choisie pour atteindre la fusion. Les besoins technologiques de la FCI sont essentiellement liés à la puissance du laser, aux grands accélérateurs d'ions, et des cibles. Ces problèmes sont décrits et référencés dans [8, 27, 65]. Les technologies nécessaires à la FCM concernent principalement la production de bobines magnétiques super-conductrices dédiés génération de champs toroïdaux intenses, et à la conception de sources efficaces de chauffage. Cependant, la FCI et la FCM partagent les mêmes problématiques sur les matériaux à utiliser pour concevoir les parois des murs supportant des neutrons énergétiques qui s'échapperaient de la cible de la FCI et de la chambre à vide de la machine FCM.

La Physique des Plasmas de fusion se consacre à la description de la dynamique des particules chargées à l'intérieur de la machine considérée. Il y a trois approches classiques pour décrire la comportement des particules des plasmas : **la théorie particulaire**, **la théorie cinétique**, et **la théorie hydrodynamique**.

La théorie particulaire s'intéresse aux équations de mouvement de chaque particule individuelle du plasma, et avec l'aide de codes de simulation et des moyennes appropriés, la physique des plasmas est analysée. Cette théorie est également appelée modèle à N corps où N est supposé représenter le nombre de particules dans le plasma. Comme un plasma de fusion possède un très grand nombre de particules, la précision de ce modèle demande un N suffisamment grand pour simuler le plasma. Malgré l'existence de codes traitant le modèle à N corps, la théorie cinétique est largement préféré à celle du modèle à N corps. Le modèle à N corps devient alors dans ce cadre le modèle de base à partir duquel sera dérivée une hierarchie de modèles.

La théorie cinétique repose sur un ensemble d'équations sur les fonctions de distributions des particules du plasma, qui encodent leur dynamique au cours du temps, dans l'espace physique et celui de vitesses, et couplé aux équations de Maxwell. Les théories cinétiques modélisent avec une notable précision un système possédant un grand nombre de particules. Cependant, les codes cinétiques requièrent en général de grandes ressources à la fois pour l'espace stockage et le temps de calcul, et ils sont limités aux petits domaines de calcul de l'espace des phases. Les modèles cinétiques donnent un grand nombre d'informations qui ne sont pas toujours accessibles au cours des expériences. Inversement, les modèles fluides, obtenus comme moments en vitesses des fonctions de distribution des particules, fournissent des paramètres pertinents du plasma sur de grandes échelles de temps et grands domaines de calculs [54, 55] qui correspondent aux résultats des expériences.

Dans les modèles hydrodynamiques ou fluides, les lois de conservation de la masse, de la quantité de mouvement, et d'énergie sont couplés aux équations de Maxwell. Les équations mono-fluides, les systèmes bi-fluides, les équations de la MHD [24, 9, 10, 37, 38, 43, 42], les équations d'Euler bi-températures [26, 29, 51, 69, 7, 32] sont des exemples de modèles fluides.

La modélisation des plasmas permet d'étudier le comportement du plasma qui traduit les trois grandes théories de transport : la chaleur par conduction, la diffusion de particules, et la diffusion du champ magnétique. Il en résulte que la modélisation des plasmas s'intéresse à la compréhension et au contrôle de l'énergie confinée. L'analyse des ondes des systèmes obtenus grâce à la modélisation permet également un choix raisonné des fréquences auxquelles le plasma serait chauffé.

V Organisation du manuscrit

Ce travail est une combinaison de la modélisation de la Physique des Plasmas, et de l'Analyse Numérique. Il est composé de quatre chapitres et d'une conclusion. Les deux premiers traitent de la modélisation alors que les deux derniers concernent l'Analyse Numérique. Le contenu est le suivant.
Chapitre 1. Dans ce chapitre, on rappelle la théorie cinétique d'un plasma magnétisé et des équations de la MHD bi-fluides correspondants. Ensuite, en adimensionnant les équations de la MHD bi-fluide, nous donnons des hypothèses conduisant aux équations d'Euler bi-températures, et aux équations de la MHD idéale et résistive. La dérivation proposée pour les équations d'Euler bi-températures est plus générale que celle suggérées dans [26, 37, 43, 51, 7].

Chapitre 2. Les principes de la méthode volumes finis sont revus dans ce chapitre à la fois pour des maillages structurés et non-structurés. En gardant à l'esprit de futures applications à la FCM pour l'approche des tokamaks, nous avons étudié les modifications de la méthode volumes finis pour approcher les solutions de ces modèles en géométrie toroïdale. Les schémas que nous avons proposés se basent sur le travail récent rapporté dans [21, 18]. Cependant, de telles applications ne sont pas directes tant par la complexité des modèles que par l'utilisation de maillages non-structurés afin de décrire correctement la géométrie toroïdale du tore.

Chapitre 3. La stratégie numérique mise en place dans le chapitre 2 utilise un schéma

de relaxation pour approcher numériquement le modèle d'Euler bi-températures. Dans ce chapitre, nous donnons toutes les étapes permettant de construire ce schéma de relaxation. Des tests numériques sont alors proposés pour éprouver la précision de ce schéma. Ce chapitre a été accepté pour publication [7].

Les chapitres 1-3 sont rassemblés dans [32] sous la forme d'un rapport interne.

Chapitre 4. Les équations de la MHD qui sont couplés aux équations de Maxwell contiennent la contrainte de divergence nulle du champ magnétique qui doit être maintenue tout au long de la simulation numérique. Une stratégie est construite permettant de calculer le champ magnétique avec des méthodes volumes finis à la fois pour les coordonnées cartésiennes et cylindriques. Différents cas-tests standards de la MHD sont proposés pour des géométries 2D afin de valider la méthode proposée.
Conclusion. Enfin, nos conclusions sont données dans ce dernier chapitre. Des perspectives à nos travaux sont également proposés.

Résumé

La simulation numérique est de plus en plus présente dans la plupart des domaines scientifiques. Cette technique consiste à résoudre des modèles mathématiques décrivant différents phénomènes physiques. Dans cette thèse, on s'intéressera à la mise en place de schémas numériques pour résoudre trois systèmes d'équations différents : les équations d'Euler bi-températures, et les équations de la MHD résistive et idéale.

Le chapitre 1 se concentre sur l'établissement de ces trois modèles fluides. Pour cela, on repart des équations de Boltzmann qui décrit le comportement des ions et des électrons à l'échelle microscopique :

$$\partial_t f_\alpha + \mathbf{v}\cdot\nabla f_\alpha + \frac{q_\alpha}{m_\alpha}\left(\mathbf{E}+\mathbf{v}\times\mathbf{B}\right)\cdot\nabla_{\mathbf{v}} f_\alpha = C_{\alpha,\alpha} + C_{\alpha,\beta}.$$

La fonction f_α est appelée fonction de distribution, et elle décrit le comportement de l'espèce $\alpha = e, i$ en fonction du temps, de la physique, et de l'espace des vitesses. Cette équation prend aussi en compte les interactions au sein d'une même espèce avec l'opérateur de collision $C_{\alpha,\alpha}$ ainsi que celles entre les deux espèces avec l'opérateur de collision $C_{\alpha,\beta}$. Dans les modèles cinétiques, les vitesses sont notées $\mathbf{v}$ alors que pour les modèles fluides elles seront appelées $\mathbf{u}$.
En prenant les différents moments de vitesse de cette équation, on obtient des lois de conservation pour les densités, les vitesses, et les énergies de chacune des deux espèces que l'on couple aux quatre équations de Maxwell. On a alors le modèle de la MHD bi-fluide.

Après avoir reformulé le système d'équation dans le régime quasi-neutre, on l'adimensionne faisant ainsi apparaître certains paramètres tels que le paramètre plasma β, les longueurs inertielles des ions et des électrons $\delta^*_{e,i}$, et le nombre de Reynolds magnétique R_m. Suivant les phénomènes physiques que l'on cherche à observer, différentes limites du modèle bi-fluide peuvent être données. Dans cette thèse, nous nous intéresserons à trois limites de ce modèle.
La première limite donnée correspond à des plasmas dans lesquels les effets hydrodynamiques sont bien plus important que les effets magnétiques ce qui correspond à supposer que le paramètre plasma β est très grand. Le domaine d'application de cette limite est celui de la FCI. Le modèle obtenu est alors celui d'Euler bi-températures :

$$\begin{cases} \partial_t \rho + \nabla\cdot(\rho\mathbf{u}) &= 0, \\ \partial_t(\rho\mathbf{u}) + \nabla\cdot(\rho\mathbf{u}\otimes\mathbf{u}) + \nabla(p_e+p_i) &= 0, \\ \partial_t\mathcal{E} + \nabla\cdot\left[(\mathcal{E}+p_e+p_i)\,\mathbf{u}\right] &= 0, \\ \partial_t(\rho_e S_e) + \nabla\cdot(\rho_e S_e\mathbf{u}) &= \rho_e^{\gamma-1}(\gamma-1)\nu_{ei}^{\mathcal{E}}(T_i-T_e). \end{cases}$$

Il s'agit d'un modèle mono-fluide où celui est considéré comme un mélange d'ions et d'électrons que l'on distingue uniquement par leur température. En effet, l'équation sur l'entropie électronique fait apparaitre des termes d'échange thermique entre les deux espèces.
Les deux autres modèles étudiés sont deux modèles MHD mono-fluide où on ne différencie

plus les ions des électrons. On se place maintenant dans le domaine de la FCM en supposant que les longueurs inertielles des ions et des électrons sont très petites. Pour le premier de ces deux modèles MHD, on ajoute l'hypothèse que le nombre de Reynolds magnétique est borné et on obtient ainsi les équations de la MHD résistive :

$$\begin{cases} \partial_t \rho + \nabla \cdot (\rho \mathbf{u}) & = & 0, \\ \partial_t (\rho \mathbf{u}) + \nabla \cdot [\rho \mathbf{u} \otimes \mathbf{u} - \mathbf{B} \otimes \mathbf{B}] + \nabla p_T & = & 0, \\ \partial_t \mathcal{E}_T + \nabla \cdot [(\mathcal{E}_T + p_T)\,\mathbf{u} - (\mathbf{u} \cdot \mathbf{B})\mathbf{B}] & = & \eta \nabla \cdot (\mathbf{B} \times (\nabla \times \mathbf{B}))\,, \\ \partial_t \mathbf{B} + \nabla \cdot [\mathbf{B} \otimes \mathbf{u} - \mathbf{u} \otimes \mathbf{B}] & = & \eta \nabla^2 \mathbf{B}. \end{cases}$$

Pour le second modèle, le plasma est vu comme un conducteur parfait ce qui se traduit par l'hypothèse que le nombre de Reynolds magnétique est très grand. Ce modèle est alors appelé le modèle de la MHD idéale :

$$\begin{cases} \partial_t \rho + \nabla \cdot (\rho \mathbf{u}) & = & 0, \\ \partial_t (\rho \mathbf{u}) + \nabla \cdot [\rho \mathbf{u} \otimes \mathbf{u} - \mathbf{B} \otimes \mathbf{B}] + \nabla p_T & = & 0, \\ \partial_t \mathcal{E}_T + \nabla \cdot [(\mathcal{E}_T + p_T)\,\mathbf{u} - (\mathbf{u} \cdot \mathbf{B})\mathbf{B}] & = & 0, \\ \partial_t \mathbf{B} + \nabla \cdot [\mathbf{B} \otimes \mathbf{u} - \mathbf{u} \otimes \mathbf{B}] & = & 0. \end{cases}$$

Afin de résoudre numériquement les trois systèmes d'équations précédents, on s'intéresse, dans le chapitre 2, à la modélisation géométrique des domaines de calculs afin de pouvoir écrire des méthodes type volumes finis.
Pour cela, on considère un système de lois de conservation écrit sous la forme

$$\partial_t U + \nabla \cdot F(U) = 0.$$

On maille ensuite le domaine de calculs. Afin d'approcher la solution de la loi de conservation, on peut soit l'approximer au centre de chaque élément du maillage, c'est l'approche *cell-centered*, soit l'approcher en chaque point du maillage avec l'approche *vertex-centered*. Ici, les calculs seront faits pour ces deux approches avec différents types de maillages pour des géométries cartésiennes.
Dans cette thèse, on garde à l'esprit l'application aux tokamaks. Sa géométrie est basée sur celle d'un tore que l'on voit comme une section 2D en rotation autour de l'axe Z. Ainsi, les coordonnées cylindriques semblent bien plus adaptées que les coordonnées cartésiennes. Il nous faut donc écrire des méthodes volumes finis pour ce type de géométrie pour les deux approches citées précédemment. Or, cela n'est pas si simple. En effet, pour des variables vectorielles lorsque que l'on projette leur équation de conservation sur la base cylindrique, des termes sources, dus à la dérivation de la base cylindrique, apparaissent. Ces termes peuvent être pris en compte de différentes manières.
L'une d'elles serait de manipuler les équations afin de supprimer autant que possible les termes sources dans les équations. Ce choix sera appliqué aux équations de la MHD idéale pour l'approche *cell-centered*.
La seconde serait de reprendre la définition originale de la divergence pour cette base :

$$\nabla \cdot F(U) = \frac{1}{R} \partial_k (R F(U) \cdot \mathbf{e}^k),$$

en utilisant la convention d'Einstein pour la somme. Ainsi, la formulation forte des équations conservatives peut être gardée. On présentera ce choix pour l'approche *vertex-centered* pour la géométrie toroïdale 3D. Pour cette modélisation 3D, on se basera sur le maillage 2D d'une section de tore que l'on mettra en rotation autour de l'axe Z définissant

alors des éléments 3D.
De manière générale, pour les deux approches décrites, la solution approchée au temps t^{n+1} en une cellule de contrôle Ω_i peut s'écrire sous la forme suivante :

$$U_i^{n+1} = U_i^n - \frac{\Delta t}{|\Omega_i|} \sum_{j \in \mathcal{V}(i)} F(U_i^n, U_j^n, \mathbf{n}_{ij}) |\partial\Omega_{ij}|,$$

où $\mathcal{V}(i)$ est l'ensemble des voisins de i et $F(U_i^n, U_j^n, \mathbf{n}_{ij})$ est le flux numérique. Ces derniers seront calculés avec des flux utilisant des solveurs de Riemann dans les chapitres 3 et 4.

Intéressons-nous tout d'abord à la construction d'un schéma numérique pour résoudre les équations d'Euler bi-températures. Pour ce faire, on se basera sur les méthodes des schémas de relaxation pour l'équation d'Euler. Cela consiste à remplacer les pressions électroniques et ioniques par des variables dite de relaxation. Il en résulte le système relaxé suivant

$$\begin{cases} \partial_t \rho + \nabla \cdot (\rho \mathbf{u}) & = & 0, \\ \partial_t (\rho \mathbf{u}) + \nabla \cdot (\rho \mathbf{u} \otimes \mathbf{u}) + \nabla(\pi_e + \pi_i) & = & 0, \\ \partial_t \mathcal{E} + \nabla \cdot [(\mathcal{E} + \pi_e + \pi_i)\mathbf{u}] & = & 0, \\ \partial_t (\rho_e S_e) + \nabla \cdot (\rho_e S_e \mathbf{u}) & = & (\gamma - 1)\rho_e^{\gamma-1} \nu_{ei}^{\mathcal{E}} (T_i - T_e), \\ \partial_t (\rho \pi_e) + \nabla \cdot \left[\left(\rho \pi_e + a^2 c_e \right) \mathbf{u} \right] & = & \nu(p_e - \pi_e), \\ \partial_t (\rho \pi_i) + \nabla \cdot \left[\left(\rho \pi_i + a^2 c_i \right) \mathbf{u} \right] & = & \nu(p_i - \pi_i), \\ \partial_t (\rho a) + \nabla \cdot (\rho a \mathbf{u}) & = & 0. \end{cases}$$

Ce système est mis sous la forme

$$\partial_t U + \nabla \cdot F(U) = S_\nu(U),$$

que l'on résout en deux étapes. Tout d'abord, avec une méthode volumes finis *vertex-centered* où les flux numériques sont obtenus par la résolution exacte du problème de Riemann aux interfaces, on calcule la solution approchée du système

$$\partial_t U + \nabla \cdot F(U) = 0.$$

Ensuite, on prend la limite $\nu \to 0$ et on résout le système

$$\partial_t U = S_\nu(U).$$

Ce qui revient à résoudre pour les variables de relaxation et les températures

$$\begin{cases} \partial_t T_e & = & \nu_{ei}(T_i - T_e), \\ \partial_t T_i & = & -\nu_{ie}(T_i - T_e), \\ \pi_e & = & p_e, \\ \pi_i & = & p_i. \end{cases}$$

En pratique, à chaque fin de pas de temps, on calcule la solution exacte des équations différentielles couplées des températures électroniques et ioniques. Puis, les variables de relaxation sont recalculées avec les nouvelles pressions du système à l'aide des lois d'états. Ce schéma sera testé en géométrie cartésienne et toroïdale. Les résultats seront alors discutés.

Ré-intéressons-nous maintenant aux équations de la MHD idéale et résistive. Rappelons aussi que ces équations sont couplées aux équations de Maxwell parmi lesquelles on

trouve la contrainte de divergence nulle du champs magnétique qu'il faut maintenir tout au long de la simulation. Il a été montré qu'en général dans les simulations numériques dans les cas 2D et 3D, on a

$$\partial_t(\nabla \cdot \mathbf{B}) \neq 0.$$

C'est pour cela que dans le chapitre 4, on s'intéresse à la construction d'un schéma numérique pour résoudre les équations de la MHD idéale et résistive tout en conservant $\nabla \cdot \mathbf{B} = 0$ au cours du temps.
Afin de maintenir la contrainte de divergence nulle, le champs magnétique peut s'écrire sous la forme

$$\mathbf{B} = \nabla\alpha \times \nabla\beta,$$

où les grandeurs α et β sont appelées potentiels d'Euler. Ici, ces schémas seront présentés uniquement pour des géométries 2D cartésiennes et cylindriques en supposant l'invariance par translation $\partial_Z \cdot = 0$. Le champs magnétique peut alors se réécrire sous la forme :

$$\mathbf{B} = B_z\mathbf{e}_z + \nabla\psi \times \mathbf{e}_z,$$

où ψ est un potentiel d'Euler. Ainsi avec cette expression, on assure que le champs magnétique est à divergence nulle. La méthode proposée dans un premier temps pour les équations de la MHD idéale est elle aussi basé sur celle des schémas de relaxation. En effet, cette fois-ci le champs magnétique jouera le rôle de variable de relaxation, et on ajoutera au système initiale l'équation du potentiel ψ. Le nouveau système considéré est alors

$$\begin{cases} \partial_t\rho + \nabla\cdot(\rho\mathbf{u}) & = & 0, \\ \partial_t(\rho\mathbf{u}) + \nabla\cdot(\rho\mathbf{u}\otimes\mathbf{u} - \mathbf{B}\otimes\mathbf{B}) + \nabla p_T & = & 0, \\ \partial_t\mathcal{E}_T + \nabla\cdot\left[(\mathcal{E}_T + p_T)\,\mathbf{u} - (\mathbf{u}\cdot\mathbf{B})\mathbf{B}\right] & = & 0, \\ \partial_t\mathbf{B} + \nabla\cdot\left[\mathbf{B}\otimes\mathbf{u} - \mathbf{u}\otimes\mathbf{B}\right] & = & 0, \\ \partial_t(\rho\psi) + \nabla\cdot(\rho\psi\mathbf{u}) & = & 0. \end{cases}$$

Durant une étape de transport, on appliquera les méthodes volumes finis en approche *cell-centered* pour résoudre ce système, les flux numériques seront calculés avec soit un flux de Rusanov, soit un flux type HLL, soit un flux HLLD. Enfin, on projettera le gradient de ψ sur le champs magnétique afin de le ré-évaluer correctement et de maintenir la contrainte $\nabla\cdot\mathbf{B} = 0$. Les dérivés du potentiel seront approchées avec des différences finies centrées d'ordre 2.
Pour les équations de la MHD résistive, des termes sources viennent s'ajouter dans les équations de l'énergie totale, de Faraday, et du potentiel ψ. Ainsi, le nouveau système à résoudre est

$$\begin{cases} \partial_t\rho + \nabla\cdot(\rho\mathbf{u}) & = & 0, \\ \partial_t(\rho\mathbf{u}) + \nabla\cdot(\rho\mathbf{u}\otimes\mathbf{u} - \mathbf{B}\otimes\mathbf{B}) + \nabla p_T & = & 0, \\ \partial_t\mathcal{E}_T + \nabla\cdot\left[(\mathcal{E}_T + p_T)\,\mathbf{u} - (\mathbf{u}\cdot\mathbf{B})\mathbf{B}\right] & = & \eta\nabla\cdot\left[\mathbf{B}\times(\nabla\times\mathbf{B})\right], \\ \partial_t\mathbf{B} + \nabla\cdot\left[\mathbf{B}\otimes\mathbf{u} - \mathbf{u}\otimes\mathbf{B}\right] & = & \eta\nabla^2\mathbf{B}, \\ \partial_t(\rho\psi) + \nabla\cdot(\rho\psi\mathbf{u}) & = & \rho\eta\nabla^2\psi. \end{cases}$$

La méthode numérique présentée est adaptée de celle pour la MHD idéale. En effet, une étape intermédiaire est ajoutée pour traiter les termes résistifs. Pour ce faire, à la place de traiter les variables conservatives, on réécrira le système à résoudre pour les variables physiques :

$$\begin{cases} \partial_t\rho & = & 0, \\ \partial_t\mathbf{u} & = & 0, \\ \partial_t p & = & (\gamma-1)\eta\left[(\nabla B_z)^2 + (\nabla^2\psi)^2\right], \\ \partial_t B_z & = & \nabla^2 B_z, \\ \partial_t\psi & = & \nabla^2\psi. \end{cases}$$

On remarque que seule la composante B_z du champs magnétique apparait dans ce système. En effet, comme le potentiel ψ sera projeté sur le champs magnétique, il est donc inutile de résoudre les termes résistifs des deux autres composantes du champs magnétiques. Le système précédent sera résolue de manière implicite à l'aide des méthodes de type différences finies à l'ordre 2 ainsi qu'à l'ordre 4.
Les deux schémas précédents seront appelés schéma avec projection en opposition au schéma sans projection dans lesquels la projection du potentiels ψ ne sera pas appliquée et cette dernière variable sera considérée comme indépendante du champs magnétique.
Ces deux schémas seront ensuite testés ainsi que comparés avec les résultats de la littérature.

Chapter 1

Fluid models

In this chapter, we consider a charged plasma composed of electrons and one species of ions. The physics linked to such a plasma can be described at different scales: microscopic, macroscopic, or mezoscopic. First, we present the kinetic model describing the evolution of particles of each species in the phase space. Then, this model is derived to obtain a bi-fluid MHD model. Finally, in the two last Sections, we obtain all the different models studied in this thesis in Chapters 3 and 4 under some assumptions and give some mathematical properties of those resulting systems.

I Plasma modeling

In this Section, we present the kinetic model leading to the bi-fluid MHD equations. First, we present the kinetic model for two species: the electrons denoted e, and the ions denoted i. Then, we give the definitions of some macroscopic quantities. Those definitions are then used to derive the kinetic equations leading to the bi-fluid macroscopic equations. Finally, the Maxwell equations are added to the bi-fluid ones in order to obtain the bi-fluid MHD equations.

I.1 Kinetic model

The plasma is composed of electrons and ions submitted to an electric field $\mathbf{E} \in \mathbb{R}^3$ and to a magnetic field $\mathbf{B} \in \mathbb{R}^3$. The kinetic model describes at the microscopic scale the behavior of the particles in the plasma [24]. To each species $\alpha = e, i$, is associated a distribution function f_α. This function depends on the time $t \in \mathbb{R}_+$, on the position $\mathbf{x} \in \mathbb{R}^3$, and on the velocity $\mathbf{v} \in \mathbb{R}^3$. The distribution function is solution of the Boltzmann equation

$$\partial_t f_\alpha + \mathbf{v} \cdot \nabla f_\alpha + \frac{q_\alpha}{m_\alpha}(\mathbf{E} + \mathbf{v} \times \mathbf{B}) \cdot \nabla_{\mathbf{v}} f_\alpha = C_{\alpha,\alpha} + C_{\alpha,\beta}, \ (\alpha, \beta) = (e, i), (i, e), \tag{1.1}$$

where $C_{\alpha,\alpha}$ represents the collisions between α particles, and $C_{\alpha,\beta}$ represents the collisions between α particles and β particles. The operator $\nabla_{\mathbf{v}}$ is the gradient operator in the velocity space. The Lorentz force applied to the plasma is defined by

$$\mathbf{a}_\alpha = \frac{q_\alpha}{m_\alpha}(\mathbf{E} + \mathbf{v} \times \mathbf{B}),$$

where q_α is the charge associated to the species α, and m_α is its mass.

The minimal required properties that collision operators must fulfill are to conserve the mass per species, the total momentum, and the total energy. Hence, we have

$$\int_{\mathbb{R}^3} m_\alpha C_{\alpha,\beta} d\mathbf{v} = 0, \ \alpha = e, i, \ \beta = e, i, \tag{1.2}$$

$$\int_{\mathbb{R}^3} m_\alpha \mathbf{v} C_{\alpha,\beta} d\mathbf{v} + \int_{\mathbb{R}^3} m_\beta \mathbf{v} C_{\beta,\alpha} d\mathbf{v} = 0,\ \alpha = e,i,\ \beta = e,i, \tag{1.3}$$

$$\int_{\mathbb{R}^3} \frac{1}{2} m_\alpha \mathbf{v}^2 C_{\alpha,\beta} d\mathbf{v} + \int_{\mathbb{R}^3} \frac{1}{2} m_\beta \mathbf{v}^2 C_{\beta,\alpha} d\mathbf{v} = 0,\ \alpha = e,i,\ \beta = e,i. \tag{1.4}$$

The relations (1.3) and (1.4) show that the collision operator $C_{\alpha,\alpha}$ also conserves the momentum and the energy of each species

$$\int_{\mathbb{R}^3} m_\alpha \mathbf{v} C_{\alpha,\alpha} d\mathbf{v} = 0,\ \alpha = e,i,$$

$$\int_{\mathbb{R}^3} \frac{1}{2} m_\alpha \mathbf{v}^2 C_{\alpha,\alpha} d\mathbf{v} = 0,\ \alpha = e,i.$$

I.2 Macroscopic quantities

The macroscopic quantities are obtained with the extraction of the different moments of the distribution function. For example, the density n_α, the velocity $\mathbf{u}_\alpha$, and the total energy $\mathcal{E}_\alpha$ of the species $\alpha = e,i$ are respectively given by the zeroth, the first, and the second moments of f_α:

$$n_\alpha = \int_{\mathbb{R}^3} f_\alpha d\mathbf{v}, \tag{1.5}$$

$$\mathbf{u}_\alpha = \frac{1}{n_\alpha} \int_{\mathbb{R}^3} \mathbf{v} f_\alpha d\mathbf{v}, \tag{1.6}$$

$$\mathcal{E}_\alpha = \int_{\mathbb{R}^3} \frac{1}{2} m_\alpha \mathbf{v}^2 f_\alpha d\mathbf{v} = \frac{3}{2} n_\alpha k_B T_\alpha + \frac{1}{2} \rho_\alpha \mathbf{u}_\alpha^2, \tag{1.7}$$

where $\rho_\alpha = n_\alpha m_\alpha$, T_α is defined as the temperature of the species, and $k_B = 1.3806 \times 10^{-23} J.K^{-1}$ is the Boltzmann constant.

We also introduce the velocity of the mixture and the temperature of the mixture with

$$\mathbf{u} = \frac{\rho_e \mathbf{u}_e + \rho_i \mathbf{u}_i}{\rho}, \tag{1.8}$$

$$\frac{3}{2} n k_B T = \sum_{\alpha=e,i} \left[\frac{1}{2} \rho_\alpha (\mathbf{u}_\alpha^2 - \mathbf{u}^2) + \frac{3}{2} n_\alpha k_B T_\alpha \right],$$

where $n = n_e + n_i$ and $\rho = \rho_e + \rho_i$.

The total charge and the current are defined by

$$\overline{\rho} = \int_{\mathbb{R}^3} q_e f_e d\mathbf{v} + \int_{\mathbb{R}^3} q_i f_i d\mathbf{v} = n_e q_e + n_i q_i,$$

$$\mathbf{J} = \int_{\mathbb{R}^3} q_e \mathbf{v} f_e d\mathbf{v} + \int_{\mathbb{R}^3} q_i \mathbf{v} f_i d\mathbf{v} = q_e n_e \mathbf{u}_e + q_i n_i \mathbf{u}_i. \tag{1.9}$$

I.3 Collision operators

There are a great number of collision operators. In this model, we limit ourselves to BGK type operators [17]. Then, the two collision operators are written in the form

$$\begin{cases} C_{\alpha,\alpha} &= \dfrac{1}{\tau_\alpha} \left(\mathcal{M}_\alpha - f_\alpha \right), \\ C_{\alpha,\beta} &= \dfrac{1}{\tau_{\alpha\beta}} \left(\overline{\mathcal{M}_\alpha} - f_\alpha \right), \end{cases}$$

where $\frac{1}{\tau_\alpha}$ is the frequency of collision between particles of the same species α. The frequency of electron/ion collisions $\frac{1}{\tau_{ei}}$, the frequency of ion/electron collisions is $\frac{1}{\tau_{ie}}$. The functions $\mathcal{M}_\alpha$ and $\overline{\mathcal{M}_\alpha}$ are two Maxwellian distributions defined in [7] by

$$\mathcal{M}_\alpha(f_\alpha) = \frac{n_\alpha}{(2\pi k_B T_\alpha/m_\alpha)^{3/2}} \exp\left(-\frac{(\mathbf{v}-\mathbf{u}_\alpha)^2}{2k_B T_\alpha/m_\alpha}\right),$$

$$\overline{\mathcal{M}_\alpha}(f_e, f_i) = \frac{n_\alpha}{(2\pi k_B \overline{T}/m_\alpha)^{3/2}} \exp\left(-\frac{(\mathbf{v}-\overline{\mathbf{u}})^2}{2k_B \overline{T}/m_\alpha}\right),$$

where

$$\overline{\mathbf{u}} = \frac{\tau_{ie}\rho_e \mathbf{u}_e + \tau_{ei}\rho_i \mathbf{u}_i}{\tau_{ie}\rho_e + \tau_{ei}\rho_i}, \tag{1.10}$$

$$\overline{T} = \frac{\frac{3}{2}k_B(\tau_{ie} n_e T_e + \tau_{ei} n_i T_i) + \frac{1}{2}\tau_{ie}\rho_e(\mathbf{u_e}^2 - \overline{\mathbf{u}}^2) + \frac{1}{2}\tau_{ei}\rho_i(\mathbf{u_i}^2 - \overline{\mathbf{u}}^2)}{\frac{3}{2}k_B(\tau_{ie} n_e + \tau_{ei} n_i)}. \tag{1.11}$$

The variables $\overline{\mathbf{u}}$ and $\overline{T}$ are chosen such as the three following moments are

$$\int_{\mathbb{R}^3} m_\alpha \mathcal{M}_\alpha d\mathbf{v} = \int_{\mathbb{R}^3} m_\alpha \overline{\mathcal{M}_\alpha} d\mathbf{v} = \rho_\alpha, \tag{1.12}$$

$$\int_{\mathbb{R}^3} m_\alpha \mathbf{v} \mathcal{M}_\alpha d\mathbf{v} = \rho_\alpha \mathbf{u}_\alpha, \ \int_{\mathbb{R}^3} m_\alpha \mathbf{v} \overline{\mathcal{M}_\alpha} d\mathbf{v} = \rho_\alpha \overline{\mathbf{u}}, \tag{1.13}$$

$$\int_{\mathbb{R}^3} \frac{1}{2} m_\alpha \mathbf{v}^2 \mathcal{M}_\alpha d\mathbf{v} = \frac{3}{2} n_\alpha k_B T_\alpha + \frac{1}{2}\rho_\alpha \mathbf{u}_\alpha^2, \ \int_{\mathbb{R}^3} \frac{1}{2} m_\alpha \mathbf{v}^2 \overline{\mathcal{M}_\alpha} d\mathbf{v} = \frac{3}{2} n_\alpha k_B \overline{T} + \frac{1}{2}\rho_\alpha \overline{\mathbf{u}}^2. \tag{1.14}$$

We define $\mathbf{F}_{\alpha,\beta}$ and $\mathcal{W}_{\alpha,\beta}$ the first and the second moments of the collision operator $C_{\alpha,\beta}$ with

$$\mathbf{F}_{\alpha,\beta} = \int_{\mathbb{R}^3} m_\alpha \mathbf{v} C_{\alpha,\beta} d\mathbf{v}, \tag{1.15}$$

$$\mathcal{W}_{\alpha,\beta} = \int_{\mathbb{R}^3} \frac{1}{2} m_\alpha \mathbf{v}^2 C_{\alpha,\beta} d\mathbf{v}. \tag{1.16}$$

According to the properties (1.3) and (1.4) we have

$$\mathbf{F}_{ie} = -\mathbf{F}_{ei}, \ \mathcal{W}_{ie} = -\mathcal{W}_{ei}.$$

Using the results (1.10)-(1.13) we have

$$\mathbf{F}_{ei} = \frac{1}{\tau_{ei}}(\overline{\mathbf{u}} - \mathbf{u}_e) = \frac{\rho_e \rho_i}{\tau_{ie}\rho_e + \tau_{ei}\rho_i}(\mathbf{u}_i - \mathbf{u}_e), \tag{1.17}$$

$$\begin{aligned} \mathcal{W}_{ei} &= \frac{1}{\tau_{ei}}\left[\frac{3}{2} n_e k_B(\overline{T} - T_e) + \frac{1}{2}\rho(\overline{\mathbf{u}}^2 - \mathbf{u}_e^2)\right]^2, \\ &= \nu_{ei}^{\mathcal{E}}(T_i - T_e) + \mathbf{F}_{ei} \cdot \left[\frac{1}{2}\left(\overline{\mathbf{u}} + \frac{\tau_{ie} n_e \mathbf{u}_i + \tau_{ei} n_i \mathbf{u}_e}{\tau_{ie} n_e + \tau_{ei} n_i}\right)\right], \end{aligned} \tag{1.18}$$

where

$$\nu_{ei}^{\mathcal{E}} = \frac{3}{2} k_B \frac{n_e n_i}{\tau_{ie} n_e + \tau_{ei} n_i}. \tag{1.19}$$

In order to simplify the expression (1.18), we define

$$\widetilde{\mathcal{W}}_{\alpha,\beta} = \int_{\mathbb{R}^3} \frac{1}{2} m_\alpha (\mathbf{v} - \mathbf{u}_\alpha)^2 C_{\alpha,\beta} d\mathbf{v},$$

Then, we have

$$\mathcal{W}_{\alpha,\beta} = \widetilde{\mathcal{W}}_{\alpha,\beta} + \mathbf{F}_{\alpha,\beta} \cdot \mathbf{u}_\alpha, \tag{1.20}$$

where

$$\begin{cases} \widetilde{\mathcal{W}}_{ei} &= \nu_{ei}^{\mathcal{E}}(T_i - T_e) + \dfrac{1}{2}\left[\dfrac{\tau_{ei}\rho_i}{\tau_{ie}\rho_e + \tau_{ei}\rho_i} + \dfrac{\tau_{ie}n_e}{\tau_{ie}n_e + \tau_{ei}n_i}\right] \mathbf{F}_{ei} \cdot (\mathbf{u}_i - \mathbf{u}_e), \\ \widetilde{\mathcal{W}}_{ie} &= -\nu_{ei}^{\mathcal{E}}(T_i - T_e) + \dfrac{1}{2}\left[\dfrac{\tau_{ie}\rho_e}{\tau_{ie}\rho_e + \tau_{ei}\rho_i} + \dfrac{\tau_{ei}n_i}{\tau_{ie}n_e + \tau_{ei}n_i}\right] \mathbf{F}_{ei} \cdot (\mathbf{u}_i - \mathbf{u}_e). \end{cases} \tag{1.21}$$

I.4 Moment equations

In this subsection, we extract the zeroth, first, and the second moments of (1.1) to obtain the macroscopic equations. Since we have

$$\frac{q_\alpha}{m_\alpha}(\mathbf{E} + \mathbf{v} \times \mathbf{B}) \cdot \nabla_{\mathbf{v}} f_\alpha = \nabla_{\mathbf{v}} \cdot \left[\frac{q_\alpha}{m_\alpha}(\mathbf{E} + \mathbf{v} \times \mathbf{B}) f_\alpha\right],$$

then the equation (1.1) can be rewritten as

$$\partial_t f_\alpha + \nabla \cdot (\mathbf{v} f_\alpha) + \nabla_{\mathbf{v}} \cdot \left[\frac{q_\alpha}{m_\alpha}(\mathbf{E} + \mathbf{v} \times \mathbf{B}) f_\alpha\right] = C_{\alpha,\alpha} + C_{\alpha,\beta}. \tag{1.22}$$

i Mass conservation equation

The mass equation per species $\alpha = e, i$ is obtained by taking the zeroth moment of (1.22) meaning that we multiply it by the mass m_α, and integrate the results over the velocity space

$$\int_{\mathbb{R}^3} m_\alpha \Big[\partial_t f_\alpha + \nabla \cdot (\mathbf{v} f_\alpha) + \nabla_{\mathbf{v}} \cdot (\mathbf{a}_\alpha f_\alpha)\Big] d\mathbf{v} = \int_{\mathbb{R}^3} m_\alpha \Big(C_{\alpha,\alpha} + C_{\alpha,\beta}\Big) d\mathbf{v}. \tag{1.23}$$

According to (1.2), the two collision operators conserve the mass per species. Hence, the right side of (1.23) is zero. For the left side, as the distribution function is supposed to be zero at the infinity, the integral of the velocity divergence is also zero. For the two last terms, we use the definitions (1.5) and (1.6). Hence, the mass conservation equation per species is

$$\partial_t \rho_\alpha + \nabla \cdot (\rho_\alpha \mathbf{u}_\alpha) = 0, \ \ \alpha = e, i.$$

ii Momentum equation

To obtain the momentum equation for each species $\alpha = e, i$, the equation (1.22) is multiplied by $m_\alpha \mathbf{v}$ and integrated over the velocity space

$$\int_{\mathbb{R}^3} m_\alpha \mathbf{v} \Big(\partial_t f_\alpha + \nabla \cdot (\mathbf{v} f_\alpha) + \nabla_{\mathbf{v}} \cdot [\mathbf{a}_\alpha f_\alpha]\Big) d\mathbf{v} = \int_{\mathbb{R}^3} m_\alpha \mathbf{v} \Big(C_{\alpha,\alpha} + C_{\alpha,\beta}\Big) d\mathbf{v}.$$

According to the relation (1.3) and (1.15), we have

$$\int_{\mathbb{R}^3} m_\alpha \mathbf{v} \Big(C_{\alpha,\alpha} + C_{\alpha,\beta}\Big) d\mathbf{v} = \mathbf{F}_{\alpha,\beta}. \tag{1.24}$$

Writing that

$$m_\alpha \mathbf{v} \nabla_{\mathbf{v}} \cdot (\mathbf{a}_\alpha f_\alpha) = \nabla_{\mathbf{v}} \cdot (m_\alpha \mathbf{v} \otimes \mathbf{a}_\alpha f_\alpha) - m_\alpha \mathbf{a}_\alpha f_\alpha,$$

we deduce that the integral with the velocity divergence is

$$\int_{\mathbb{R}^3} m_\alpha \mathbf{v} \nabla_{\mathbf{v}} \cdot (\mathbf{a}_\alpha f_\alpha)\, d\mathbf{v} = -q_\alpha n_\alpha (\mathbf{E} + \mathbf{u}_\alpha \times \mathbf{B}). \tag{1.25}$$

Concerning the spatial divergence term, we remark that

$$\mathbf{v} \otimes \mathbf{v} = (\mathbf{v} - \mathbf{u}_\alpha) \otimes (\mathbf{v} - \mathbf{u}_\alpha) + \mathbf{v} \otimes \mathbf{u}_\alpha + \mathbf{u}_\alpha \otimes \mathbf{v} - \mathbf{u}_\alpha \otimes \mathbf{u}_\alpha.$$

Then, we obtain

$$\int_{\mathbb{R}^3} m_\alpha \mathbf{v} \otimes \mathbf{v} f_\alpha d\mathbf{v} = \rho_\alpha \mathbf{u}_\alpha \otimes \mathbf{u}_\alpha + \overline{\overline{P_\alpha}}, \tag{1.26}$$

where $\overline{\overline{P_\alpha}}$ is the pressure tensor defined by

$$\overline{\overline{P_\alpha}} = \int_{\mathbb{R}^3} m_\alpha (\mathbf{v} - \mathbf{u}_\alpha) \otimes (\mathbf{v} - \mathbf{u}_\alpha) f_\alpha d\mathbf{v}.$$

The scalar pressure is then defined by

$$p_\alpha = \frac{1}{3} trace \left(\overline{\overline{P_\alpha}} \right).$$

Therefore, the total energy of the species α (1.7) writes

$$\mathcal{E}_\alpha = \frac{3}{2} p_\alpha + \frac{1}{2} \rho_\alpha \mathbf{u}_\alpha^2,$$

and the ideal gas law that links the temperature and the pressure of the species α is

$$n_\alpha k_B T_\alpha = p_\alpha. \tag{1.27}$$

Finally, the pressure tensor rewrites

$$\overline{\overline{P_\alpha}} = p_\alpha \overline{\overline{I}} + \overline{\overline{\Pi_\alpha}},$$

where $\overline{\overline{I}}$ is the identity tensor and $\overline{\overline{\Pi_\alpha}}$ is known as the stress tensor. Hence the relation (1.26) becomes

$$\int_{\mathbb{R}^3} m_\alpha \mathbf{v} \otimes \mathbf{v} f_\alpha d\mathbf{v} = \rho_\alpha \mathbf{u}_\alpha \otimes \mathbf{u}_\alpha + p_\alpha \overline{\overline{I}} + \overline{\overline{\Pi_\alpha}}. \tag{1.28}$$

Using the results (1.6), (1.24), (1.25), and (1.28), we get the momentum equation of the species $\alpha = e, i$

$$\partial_t (\rho_\alpha \mathbf{u}_\alpha) + \nabla \cdot (\rho_\alpha \mathbf{u}_\alpha \otimes \mathbf{u}_\alpha) + \nabla p_\alpha = q_\alpha n_\alpha (\mathbf{E} + \mathbf{u}_\alpha \times \mathbf{B}) - \nabla \cdot \overline{\overline{\Pi_\alpha}} + \mathbf{F}_{\alpha,\beta}.$$

iii Energy equation

In this part, we extract the second moment of (1.22) in order to obtain the equation on the total energy per species $\alpha = e, i$. Hence, we multiply by $\frac{1}{2}m_\alpha \mathbf{v}^2$ the kinetic equation and integrate the result over the velocity space

$$\int_{\mathbb{R}^3} \frac{1}{2}m_\alpha \mathbf{v}^2 \Big[\partial_t f_\alpha + \nabla \cdot (\mathbf{v} f_\alpha) + \nabla_{\mathbf{v}} \cdot (\mathbf{a}_\alpha f_\alpha)\Big] d\mathbf{v} = \int_{\mathbb{R}^3} \frac{1}{2}m_\alpha \mathbf{v}^2 \Big(C_{\alpha,\alpha} + C_{\alpha,\beta}\Big) d\mathbf{v}. \quad (1.29)$$

Let us first concentrate on the right side of (1.29). According to (1.20), we have

$$\int_{\mathbb{R}^3} \frac{1}{2}m_\alpha \mathbf{v}^2 \Big(C_{\alpha,\alpha} + C_{\alpha,\beta}\Big) d\mathbf{v} = \widetilde{\mathcal{W}}_{\alpha,\beta} + \mathbf{F}_{\alpha,\beta} \cdot \mathbf{u}_\alpha. \quad (1.30)$$

Concerning the last left term of (1.29) we remark that

$$\frac{1}{2}m_\alpha \mathbf{v}^2 \nabla_{\mathbf{v}} \cdot [\mathbf{a}_\alpha f_\alpha] = \nabla_{\mathbf{v}} \cdot \left[\frac{1}{2}m_\alpha \mathbf{v}^2 \mathbf{a}_\alpha f_\alpha\right] - m_\alpha \mathbf{v} \cdot \mathbf{a}_\alpha f_\alpha,$$

hence we have

$$\int_{\mathbb{R}^3} \frac{1}{2}m_\alpha \mathbf{v}^2 \nabla_{\mathbf{v}} \cdot [\mathbf{a}_\alpha f_\alpha]\, d\mathbf{v} = -q_\alpha n_\alpha \mathbf{E} \cdot \mathbf{u}_\alpha. \quad (1.31)$$

Indeed, as the force $\frac{q_\alpha}{m_\alpha}\mathbf{v} \times \mathbf{B}$ and the velocity $\mathbf{v}$ are perpendicular, then this force does not produce work. Using the same method as the one for the momentum equation, the spatial divergence term is

$$\nabla \cdot \left(\int_{\mathbb{R}^3} \frac{1}{2}m_\alpha \mathbf{v}^2 \mathbf{v} f_\alpha d\mathbf{v}\right) = \nabla \cdot [(\mathcal{E}_\alpha + p_\alpha)\, \mathbf{u}_\alpha] + \nabla \cdot \mathbf{Q}_\alpha + \nabla \cdot \left(\overline{\overline{\Pi_\alpha}}\mathbf{u}_\alpha\right), \quad (1.32)$$

where $\mathbf{Q}_\alpha$ is the heat flux of the species α given by

$$\mathbf{Q}_\alpha = \int_{\mathbb{R}^3} \frac{1}{2}m_\alpha (\mathbf{v} - \mathbf{u}_\alpha)^2 (\mathbf{v} - \mathbf{u}_\alpha) f_\alpha d\mathbf{v}.$$

Finally, with the definition (1.7) and the results (1.30)-(1.32), the total energy equation of the species $\alpha = e, i$ is

$$\partial_t \mathcal{E}_\alpha + \nabla \cdot [(\mathcal{E}_\alpha + p_\alpha)\, \mathbf{u}_\alpha] + \nabla \cdot \mathbf{Q}_\alpha = q_\alpha n_\alpha \mathbf{E} \cdot \mathbf{u}_\alpha - \nabla \cdot \left(\overline{\overline{\Pi_\alpha}}\mathbf{u}_\alpha\right) + \widetilde{\mathcal{W}}_{\alpha,\beta} + \mathbf{F}_{\alpha,\beta} \cdot \mathbf{u}_\alpha.$$

I.5 Maxwell equations

To complete the kinetic model, we add the four Maxwell equations to (1.1)

$$\begin{cases} \partial_t \mathbf{B} & = & -\nabla \times \mathbf{E}, & (1.33.a) \\ \frac{1}{c^2}\partial_t \mathbf{E} + \mu_0 \mathbf{J} & = & \nabla \times \mathbf{B}, & (1.33.b) \\ \varepsilon_0 \nabla \cdot \mathbf{E} & = & \overline{\rho}, & (1.33.c) \\ \nabla \cdot \mathbf{B} & = & 0, & (1.33.d) \end{cases}$$

where ε_0 is the permittivity of free space, μ_0 is the permeability of free space, and the speed of light in the vacuum is denoted $c = \frac{1}{\sqrt{\varepsilon_0 \mu_0}}$. To the Maxwell system is associated an

electromagnetic energy conservation equation: take the scalar product of (1.33.a) with $\frac{\mathbf{B}}{\mu_0}$, take the scalar product of (1.33.b) with $\frac{\mathbf{E}}{\mu_0}$, add the resulting equations to obtain

$$\partial_t \mathcal{E}_{EM} + \nabla \cdot \mathbf{E} \times \frac{\mathbf{B}}{\mu_0} = -\mathbf{E} \cdot \mathbf{J}, \tag{1.34}$$

where the electromagnetic energy is defined by:

$$\mathcal{E}_{EM} = \frac{1}{2}\varepsilon_0 \mathbf{E}^2 + \frac{1}{2\mu_0}\mathbf{B}^2.$$

Since plasma particles move with velocities much smaller than the light celerity $c = 3 \times 10^8 m.s^{-1}$, it is usual to neglect in (1.33.b) the displacement current $\frac{1}{c^2}\partial_t \mathbf{E}$. Hence, the Maxwell equations become

$$\left\{ \begin{array}{lcl} \partial_t \mathbf{B} & = & -\nabla \times \mathbf{E}, \\ \mu_0 \mathbf{J} & = & \nabla \times \mathbf{B}, \\ \varepsilon_0 \nabla \cdot \mathbf{E} & = & \overline{\rho}, \\ \nabla \cdot \mathbf{B} & = & 0. \end{array} \right. \tag{1.35}$$

One can check that (1.34) remains valid except that the electromagnetic energy is now defined by

$$\mathcal{E}_{EM} = \frac{1}{2\mu_0}\mathbf{B}^2,$$

that is the electric energy is considered negligible in front of the magnetic one.

I.6 Bi-fluid MHD equations

The bi-fluid MHD equations are composed of the hydrodynamic equations and the low frequency Maxwell equations (1.35). Then, the bi-fluid MHD equations are given by the following system

$$\left\{ \begin{array}{lcll} \partial_t \rho_e + \nabla \cdot (\rho_e \mathbf{u}_e) & = & 0, & (1.36.a) \\ \partial_t \rho_i + \nabla \cdot (\rho_i \mathbf{u}_i) & = & 0, & (1.36.b) \\ \partial_t (\rho_e \mathbf{u}_e) + \nabla \cdot (\rho_e \mathbf{u}_e \otimes \mathbf{u}_e) + \nabla p_e + \nabla \cdot \overline{\overline{\Pi_e}} & = & q_e n_e (\mathbf{E} + \mathbf{u}_e \times \mathbf{B}) + \mathbf{F}_{ei}, & (1.36.c) \\ \partial_t (\rho_i \mathbf{u}_i) + \nabla \cdot (\rho_i \mathbf{u}_i \otimes \mathbf{u}_i) + \nabla p_i + \nabla \cdot \overline{\overline{\Pi_i}} & = & q_i n_i (\mathbf{E} + \mathbf{u}_i \times \mathbf{B}) - \mathbf{F}_{ei}, & (1.36.d) \\ \partial_t \mathcal{E}_e + \nabla \cdot [(\mathcal{E}_e + p_e)\mathbf{u}_e] + \nabla \cdot \left(\overline{\overline{\Pi_e}} \mathbf{u}_e\right) + \nabla \cdot \mathbf{Q}_e & = & q_e n_e \mathbf{E} \cdot \mathbf{u}_e + \widetilde{\mathcal{W}}_{ei} + \mathbf{F}_{ei} \cdot \mathbf{u}_e, & (1.36.e) \\ \partial_t \mathcal{E}_i + \nabla \cdot [(\mathcal{E}_i + p_i)\mathbf{u}_i] + \nabla \cdot \left(\overline{\overline{\Pi_i}} \mathbf{u}_i\right) + \nabla \cdot \mathbf{Q}_i & = & q_i n_i \mathbf{E} \cdot \mathbf{u}_i + \widetilde{\mathcal{W}}_{ie} - \mathbf{F}_{ei} \cdot \mathbf{u}_i, & (1.36.f) \\ \partial_t \mathbf{B} & = & -\nabla \times \mathbf{E}, & (1.36.g) \\ \mu_0 \mathbf{J} & = & \nabla \times \mathbf{B}, & (1.36.h) \\ \varepsilon_0 \nabla \cdot \mathbf{E} & = & \overline{\rho}, & (1.36.i) \\ \nabla \cdot \mathbf{B} & = & 0, & (1.36.j) \end{array} \right.$$

Using the definition of the velocity of the mixture $\mathbf{u}$ in (1.8) and the one of the current $\mathbf{J}$ in (1.9), the two momentum equations can be replaced by one equation for the total momentum and one equation for the current $\mathbf{J}$. First, we write the electronic and ionic velocities as a function of $\mathbf{u}$ and $\mathbf{J}$

$$\left\{ \begin{array}{lcl} \mathbf{u}_e & = & \dfrac{1}{n_e(m_e q_i - m_i q_e)} \left(\rho q_i \mathbf{u} - m_i \mathbf{J}\right), \\ \\ \mathbf{u}_i & = & \dfrac{1}{n_i(m_i q_e - m_e q_i)} \left(\rho q_e \mathbf{u} - m_e \mathbf{J}\right). \end{array} \right. \tag{1.37}$$

Then, the total momentum equation writes

$$\partial_t(\rho\mathbf{u}) + \nabla\cdot(\rho\mathbf{u}\otimes\mathbf{u}) + \nabla\cdot[\rho_i\mathbf{u}_e\otimes(\mathbf{u}-\mathbf{u}_i) + \rho_e\mathbf{u}_i\otimes(\mathbf{u}-\mathbf{u}_e)] + \nabla p + \nabla\cdot\overline{\overline{\Pi}} = \overline{\rho}\,\mathbf{E} + \mathbf{J}\times\mathbf{B}, \quad (1.38)$$

where $p = p_e + p_i$ is the total pressure and $\overline{\overline{\Pi}} = \overline{\overline{\Pi}}_e + \overline{\overline{\Pi}}_i$ is the total stress tensor.

For the current equation, the momentum equations per species are rewritten in the following form

$$\partial_t(n_e\mathbf{u}_e) + \nabla\cdot(n_e\mathbf{u}_e\otimes\mathbf{u}_e) + \frac{1}{m_e}\left(\nabla p_e + \nabla\cdot\overline{\overline{\Pi}}_e\right) = \frac{q_e n_e}{m_e}\left(\mathbf{E} + \mathbf{u}_e\times\mathbf{B}\right) + \frac{1}{m_e}\mathbf{F}_{ei}, \quad (1.39)$$

$$\partial_t(n_i\mathbf{u}_i) + \nabla\cdot(n_i\mathbf{u}_i\otimes\mathbf{u}_i) + \frac{1}{m_i}\left(\nabla p_i + \nabla\cdot\overline{\overline{\Pi}}_i\right) = \frac{q_i n_i}{m_i}\left(\mathbf{E} + \mathbf{u}_i\times\mathbf{B}\right) - \frac{1}{m_i}\mathbf{F}_{ei}, \quad (1.40)$$

By multiplying the equation (1.39) by q_e and the equation (1.40) by q_i and finally summing both of them, the result leads to the generalized Ohm's law

$$\begin{aligned}&\partial_t\mathbf{J} + \nabla\cdot[n_e q_e\mathbf{u}_e\otimes\mathbf{u}_e + n_i q_i\mathbf{u}_i\otimes\mathbf{u}_i] + \frac{n_e q_e}{\rho_e}\left(\nabla p_e + \nabla\cdot\overline{\overline{\Pi}}_e\right) + \frac{n_i q_i}{\rho_i}\left(\nabla p_i + \nabla\cdot\overline{\overline{\Pi}}_i\right)\\ &= \left(\frac{(n_e q_e)^2}{\rho_e} + \frac{(n_i q_i)^2}{\rho_i}\right)\mathbf{E} + \left(\frac{(n_e q_e)^2}{\rho_e}\mathbf{u}_e + \frac{(n_i q_i)^2}{\rho_i}\mathbf{u}_i\right)\times\mathbf{B} + \left(\frac{n_e q_e}{\rho_e} - \frac{n_i q_i}{\rho_i}\right)\mathbf{F}_{ei},\end{aligned} \quad (1.41)$$

The total energy of each species $\alpha = e, i$ are defined by $\mathcal{E}_\alpha$

$$\mathcal{E}_\alpha = \frac{p_\alpha}{\gamma_\alpha - 1} + \frac{1}{2}\rho_\alpha\mathbf{u}_\alpha^2, \quad (1.42)$$

where γ_α is the adiabatic index of the species α. This definition is consistent with the one of the kinetic definition (1.7) if these indexes correspond to the mono-atomic case

$$\gamma_e = \gamma_i = \frac{5}{3} = \gamma. \quad (1.43)$$

The total energy is defined as the sum of the total energy of the species:

$$\mathcal{E} = \mathcal{E}_i + \mathcal{E}_e = \frac{p_i + p_e}{\gamma - 1} + \frac{1}{2}\rho_i\mathbf{u}_i^2 + \frac{1}{2}\rho_e\mathbf{u}_e^2, \quad (1.44)$$

and the total mechanical energy is obtained by summing the energy equation of the ions and electrons:

$$\partial_t\mathcal{E} + \nabla\cdot[(\mathcal{E}_e + p_e)\mathbf{u}_e + (\mathcal{E}_i + p_i)\mathbf{u}_i] + \nabla\cdot\left(\overline{\overline{\Pi}}_e\mathbf{u}_e + \overline{\overline{\Pi}}_i\mathbf{u}_i\right) + \nabla\cdot(\mathbf{Q}_e + \mathbf{Q}_i) \quad = \quad \mathbf{E}\cdot\mathbf{J}. \quad (1.45)$$

Comparing this equation with (1.34), we see that the source term $\mathbf{E}\cdot\mathbf{J}$ represents a transfer of energy between mechanical energy and electromagnetic one. An equivalent relation to (1.45) in term of total energy, mechanical + electromagnetic, can therefore be

$$\partial_t\mathcal{E}_T + \nabla\cdot\left[(\mathcal{E}_e + p_e)\mathbf{u}_e + (\mathcal{E}_i + p_i)\mathbf{u}_i + \mathbf{E}\times\frac{\mathbf{B}}{\mu_0}\right] + \nabla\cdot\left(\overline{\overline{\Pi}}_e\mathbf{u}_e + \overline{\overline{\Pi}}_i\mathbf{u}_i\right) + \nabla\cdot(\mathbf{Q}_e + \mathbf{Q}_i) = 0, \quad (1.46)$$

where the total energy is now defined as the sum of the mechanical and electromagnetic energies

$$\mathcal{E}_T = \mathcal{E}_i + \mathcal{E}_e + \frac{1}{2\mu_0}\mathbf{B}^2 = \frac{p_i + p_e}{\gamma - 1} + \frac{1}{2}\rho_i\mathbf{u}_i^2 + \frac{1}{2}\rho_e\mathbf{u}_e^2 + \frac{1}{2\mu_0}\mathbf{B}^2. \quad (1.47)$$

Observe that this equation is under conservative form as it should be: the total energy is a conserved quantity that can only change due to fluxes through the boundary of the domain.

Instead of the equations (1.36.e)-(1.36.f) we can also use the definition (1.42) to get an equation for each pressure

$$\partial_t p_\alpha + \mathbf{u}_\alpha \cdot \nabla p_\alpha + \gamma p_\alpha \nabla \cdot \mathbf{u}_\alpha + (\gamma - 1)\left[\overline{\overline{\Pi}}_\alpha : \nabla \mathbf{u}_\alpha + \nabla \cdot \mathbf{Q}_\alpha\right] = (\gamma - 1)\widetilde{\mathcal{W}}_{\alpha,\beta}. \tag{1.48}$$

In the same way, by summing the equation of the electronic pressure and the ionic pressure and the relation (1.21), an equation for the total pressure can be obtained:

$$\begin{aligned}
&\partial_t(p_e + p_i) + \mathbf{u} \cdot \nabla(p_e + p_i) + \gamma(p_e + p_i)\nabla \cdot \mathbf{u} + (\gamma - 1)\left[\overline{\overline{\Pi}} : \nabla \mathbf{u} + \nabla \cdot \mathbf{Q}\right] \\
&\frac{\rho_i}{\rho_e}(\mathbf{u} - \mathbf{u}_i)\nabla p_e + \frac{\rho_e}{\rho_i}(\mathbf{u} - \mathbf{u}_e)\nabla p_i + \gamma\left[p_e \nabla \cdot \left(\frac{\rho_i}{\rho_e}(\mathbf{u} - \mathbf{u}_i)\right) + p_i \nabla \cdot \left(\frac{\rho_e}{\rho_i}(\mathbf{u} - \mathbf{u}_e)\right)\right] \\
&+(\gamma - 1)\left[\overline{\overline{\Pi}}_e : \nabla\left(\frac{\rho_i}{\rho_e}(\mathbf{u} - \mathbf{u}_i)\right) + \overline{\overline{\Pi}}_i : \nabla\left(\frac{\rho_e}{\rho_i}(\mathbf{u} - \mathbf{u}_e)\right)\right] = (\gamma - 1)\mathbf{F}_{ei} \cdot (\mathbf{u}_i - \mathbf{u}_e).
\end{aligned}$$

For smooth ($\mathcal{C}^2$) solutions, it is mathematically equivalent to use in (1.36) instead of the two equations for the mechanical energies of the species, the two pressure equations (1.48) or the total energy equation and one pressure equation or any two independent equations derived from any combination of these equations. However, for discontinuous solutions, these combinations are not equivalent. In the sequel, we will choose for one of these two equations, the total energy equation (1.46) since this one has a clear physical meaning. We must then supplement it by another equation. A rigorous procedure [13] would be to choose this equation based on the analysis of traveling wave solutions of the system (1.36). However, this analysis presents formidable mathematical difficulties that are far beyond the scope of this work. Instead we will complement equation (1.46) by an equation for the electronic entropy. For discontinuous solutions, this implies (see the next Section III) that we assume that the electronic entropy remains constant through a shock. Although this assumption has no physical justification, it is reasonable since the mass of the electrons is considerably smaller than the one of the ions. Thus one can expect that the changes in the electronic entropy will have a minimal impact on the behavior of the other macroscopic quantities. This assumption has also been used in different context than plasma physics for instance in the modeling of multiphase flows where the hypothesis that the entropy of the lighter species is constant has shown to give results in reasonable agreement with the experiments [39]. Thus, we define the electronic entropy by

$$S_e = p_e \rho_e^{-\gamma}. \tag{1.49}$$

By using the equation of the electronic pressure (1.48), we get

$$\partial_t(\rho_e S_e) + \nabla \cdot (\rho_e S_e \mathbf{u}_e) + \rho_e^{1-\gamma}(\gamma - 1)\left[\overline{\overline{\Pi}}_e : \nabla \mathbf{u}_e + \nabla \cdot \mathbf{Q}_e\right] = \rho_e^{1-\gamma}(\gamma - 1)\widetilde{\mathcal{W}}_{ei}. \tag{1.50}$$

With the results (1.38), (1.41), (1.46), and (1.50), an equivalent system for smooth

solution to the bi-fluid MHD equations (1.36) can therefore be

$$\left\{\begin{array}{ll}
\partial_t \rho_e & +\nabla\cdot(\rho_e \mathbf{u}_e) = 0,\\
\partial_t \rho_i & +\nabla\cdot(\rho_i \mathbf{u}_i) = 0,\\
\partial_t(\rho\mathbf{u}) & +\nabla\cdot(\rho\mathbf{u}\otimes\mathbf{u}) + \nabla\cdot[\rho_i\mathbf{u}_e\otimes(\mathbf{u}-\mathbf{u}_i) + \rho_e\mathbf{u}_i\otimes(\mathbf{u}-\mathbf{u}_e)] + \nabla p + \nabla\cdot\overline{\overline{\Pi}}\\
& = \overline{\rho}\,\mathbf{E} + \mathbf{J}\times\mathbf{B},\\
\partial_t\mathbf{J} & +\nabla\cdot[n_e q_e \mathbf{u}_e\otimes\mathbf{u}_e + n_i q_i \mathbf{u}_i\otimes\mathbf{u}_i] + \dfrac{n_e q_e}{\rho_e}\left(\nabla p_e + \nabla\cdot\overline{\overline{\Pi}}_e\right) + \dfrac{n_i q_i}{\rho_i}\left(\nabla p_i + \nabla\cdot\overline{\overline{\Pi}}_i\right)\\
& = \left(\dfrac{(n_e q_e)^2}{\rho_e} + \dfrac{(n_i q_i)^2}{\rho_i}\right)\mathbf{E} + \left(\dfrac{(n_e q_e)^2}{\rho_e}\mathbf{u}_e + \dfrac{(n_i q_i)^2}{\rho_i}\mathbf{u}_i\right)\times\mathbf{B} + \left(\dfrac{n_e q_e}{\rho_e} - \dfrac{n_i q_i}{\rho_i}\right)\mathbf{F}_{ei},\\
\partial_t\mathcal{E}_T & +\nabla\cdot\left[(\mathcal{E}_e + p_e)\mathbf{u}_e + (\mathcal{E}_i + p_i)\mathbf{u}_i + \mathbf{E}\times\dfrac{\mathbf{B}}{\mu_0}\right] + \nabla\cdot\left(\overline{\overline{\Pi}}_e\mathbf{u}_e + \overline{\overline{\Pi}}_i\mathbf{u}_i\right)\\
& +\nabla\cdot(\mathbf{Q}_e + \mathbf{Q}_i) = 0,\\
\partial_t(\rho_e S_e) & +\nabla\cdot(\rho_e S_e\mathbf{u}_e) + \rho_e^{1-\gamma}(\gamma-1)\left[\overline{\overline{\Pi}}_e : \nabla\mathbf{u}_e + \nabla\cdot\mathbf{Q}_e\right] = \rho_e^{1-\gamma}(\gamma-1)\widetilde{\mathcal{W}}_{ei},\\
\partial_t\mathbf{B} & = -\nabla\times\mathbf{E},\\
\mu_0\mathbf{J} & = \nabla\times\mathbf{B},\\
\varepsilon_0\nabla\cdot\mathbf{E} & = \overline{\rho},\\
\nabla\cdot\mathbf{B} & = 0.
\end{array}\right. \tag{1.51}$$

II Bi-fluid MHD equations in quasi-neutral regime

In this Section, we consider the quasi-neutral regime in the bi-fluid MHD system. Assuming that the constant ε_0 is very small, we suppose that the net charge is near zero

$$\varepsilon_0\nabla\cdot\mathbf{E} \approx 0,$$

hence we have

$$\overline{\rho} = n_e q_e + n_i q_i = 0. \tag{1.52}$$

This hypothesis corresponds to quasi-neutral plasma. Then, we only need one equation on density. The charges q_e and q_i are given by

$$q_e = -e,\ \ q_i = Ze,$$

where $e = 1.6022\times10^{-19}C$ is the elementary charge, and Z is the ion charge state. Here, we consider the case $Z = 1$ corresponding to hydrogen isotopes as Deuterium and Tritium. Then, we deduce from (1.52)

$$\left\{\begin{array}{lcl}
n_e & = & n_i = n,\\
\mathbf{u} & = & \dfrac{m_e}{m_e+m_i}\mathbf{u}_e + \dfrac{m_i}{m_e+m_i}\mathbf{u}_i,\\
\mathbf{J} & = & ne(\mathbf{u}_i - \mathbf{u}_e).
\end{array}\right.$$

Then, the system (1.37) becomes

$$\left\{\begin{array}{lcl}
\mathbf{u}_e & = & \mathbf{u} - \dfrac{c_i}{ne}\mathbf{J},\\
\mathbf{u}_i & = & \mathbf{u} + \dfrac{c_e}{ne}\mathbf{J},
\end{array}\right. \tag{1.53}$$

where c_α is the mass fraction of the species $\alpha = e, i$ given by

$$c_\alpha = \frac{\rho_\alpha}{\rho} = \frac{m_\alpha}{m_e + m_i}.$$

With these results, the momentum equation of system (1.51) becomes

$$\partial_t(\rho\mathbf{u}) + \nabla\cdot(\rho\mathbf{u}\otimes\mathbf{u}) + \frac{m_e m_i}{m_e+m_i}\nabla\cdot\left(\frac{1}{ne^2}\mathbf{J}\otimes\mathbf{J}\right) + \nabla p + \nabla\cdot\overline{\overline{\Pi}} = \mathbf{J}\times\mathbf{B}. \tag{1.54}$$

The vector $\mathbf{F}_{ei}$ given in (1.17) is rewritten in function of the current $\mathbf{J}$

$$\mathbf{F}_{ei} = \frac{m_e m_i}{(\tau_{ie}m_e + \tau_{ei}m_i)e}\mathbf{J}, \tag{1.55}$$

therefore the Ohm's law becomes with quasi-neutrality simplifications

$$\begin{aligned}&\frac{m_i m_e}{m_e+m_i}\left[\frac{1}{e}\Big(\partial_t\mathbf{J} + \nabla\cdot(\mathbf{u}\otimes\mathbf{J} + \mathbf{J}\otimes\mathbf{u})\Big)\right] - \frac{m_e m_i(m_i-m_e)}{(m_e+m_i)^2}\nabla\cdot\left(\frac{1}{ne^2}\mathbf{J}\otimes\mathbf{J}\right)\\ &+c_e\left[\nabla p_i + \nabla\cdot\overline{\overline{\Pi}}_i\right] - c_i\left[\nabla p_e + \nabla\cdot\overline{\overline{\Pi}}_e\right] = ne\Big[\mathbf{E} + \mathbf{u}\times\mathbf{B} - \eta\mathbf{J}\Big] - \frac{m_i-m_e}{m_i+m_e}\mathbf{J}\times\mathbf{B},\end{aligned} \tag{1.56}$$

where η is the isotropic resistivity of the plasma and is defined by

$$\eta = \frac{m_i m_e}{ne^2(\tau_{ie}m_e + \tau_{ei}m_i)}. \tag{1.57}$$

Concerning the total energy, by using the system (1.53), the definition of the resistivity (1.57), and the result (1.55), we get

$$\begin{aligned}\partial_t\mathcal{E}_T \quad &+\nabla\cdot\left[(\mathcal{E}+p_e+p_i)\mathbf{u} + \mathbf{E}\times\frac{\mathbf{B}}{\mu_0}\right] + \nabla\cdot\left[\Big(c_e(\mathcal{E}_i+p_i) - c_i(\mathcal{E}_e+p_e)\Big)\frac{1}{ne}\mathbf{J}\right]\\ &+\nabla\cdot\Big(\overline{\overline{\Pi}}_e\mathbf{u}_e + \overline{\overline{\Pi}}_i\mathbf{u}_i\Big) + \nabla\cdot(\mathbf{Q}_e+\mathbf{Q}_i) = 0.\end{aligned}$$

For the electronic entropy, we simplify the results (1.21) with the quasi-neutrality hypothesis

$$\widetilde{\mathcal{W}}_{ei} = \nu^{\mathcal{E}}_{ei}(T_i - T_e) + \zeta_{ei}\eta\mathbf{J}^2,$$

where

$$\zeta_{ei} = \frac{1}{2}\left[\frac{\tau_{ei}m_i}{\tau_{ie}m_e + \tau_{ei}m_i} + \frac{\tau_{ie}}{\tau_{ie}+\tau_{ei}}\right], \tag{1.58}$$

and finally, the electronic entropy equation of system (1.51) becomes

$$\begin{aligned}&\partial_t(\rho_e S_e) + \nabla\cdot(\rho_e S_e\mathbf{u}) - c_i\nabla\cdot\left(\frac{1}{ne}\rho_e S_e\mathbf{J}\right) + \rho_e^{1-\gamma}(\gamma-1)\left[\overline{\overline{\Pi}}_e : \nabla\mathbf{u} + \nabla\cdot\mathbf{Q}_e\right]\\ &-c_i\rho_e^{1-\gamma}(\gamma-1)\overline{\overline{\Pi}}_e : \nabla\left(\frac{1}{ne}\mathbf{J}\right) = \rho_e^{1-\gamma}(\gamma-1)\left[\nu^{\mathcal{E}}_{ei}(T_i-T_e) + \zeta_{ei}\eta\mathbf{J}^2\right].\end{aligned}$$

Then, the bi-fluid MHD system (1.51) writes with the quasi-neutrality assumption

$$\begin{cases}
\partial_t \rho + \nabla\cdot(\rho\mathbf{u}) = 0,\\
\partial_t(\rho\mathbf{u}) + \nabla\cdot(\rho\mathbf{u}\otimes\mathbf{u}) + \dfrac{m_e m_i}{m_e+m_i}\nabla\cdot\left(\dfrac{1}{ne^2}\mathbf{J}\otimes\mathbf{J}\right) + \nabla p + \nabla\cdot\overline{\overline{\Pi}} = \mathbf{J}\times\mathbf{B},\\
\dfrac{m_i m_e}{m_e+m_i}\left[\dfrac{1}{e}\Big(\partial_t\mathbf{J} + \nabla\cdot(\mathbf{u}\otimes\mathbf{J}+\mathbf{J}\otimes\mathbf{u})\Big)\right] - \dfrac{m_e m_i(m_i-m_e)}{(m_e+m_i)^2}\nabla\cdot\left(\dfrac{1}{ne^2}\mathbf{J}\otimes\mathbf{J}\right)\\
+c_e\left[\nabla p_i + \nabla\cdot\overline{\overline{\Pi}}_i\right] - c_i\left[\nabla p_e + \nabla\cdot\overline{\overline{\Pi}}_e\right] = ne\Big[\mathbf{E}+\mathbf{u}\times\mathbf{B}-\eta\mathbf{J}\Big] - \dfrac{m_i-m_e}{m_i+m_e}\mathbf{J}\times\mathbf{B},\\
\partial_t\mathcal{E}_T + \nabla\cdot\left[(\mathcal{E}+p_e+p_i)\mathbf{u} + \mathbf{E}\times\dfrac{\mathbf{B}}{\mu_0}\right] + \nabla\cdot\left[\Big(c_e(\mathcal{E}_i+p_i) - c_i(\mathcal{E}_e+p_e)\Big)\dfrac{1}{ne}\mathbf{J}\right]\\
+\nabla\cdot\Big(\overline{\overline{\Pi}}_e\mathbf{u}_e + \overline{\overline{\Pi}}_i\mathbf{u}_i\Big) + \nabla\cdot(\mathbf{Q}_e+\mathbf{Q}_i) = 0,\\
\partial_t(\rho_e S_e) + \nabla\cdot(\rho_e S_e\mathbf{u}) - c_i\nabla\cdot\left(\dfrac{1}{ne}\rho_e S_e\mathbf{J}\right) + \rho_e^{1-\gamma}(\gamma-1)\left[\overline{\overline{\Pi}}_e : \nabla\mathbf{u} + \nabla\cdot\mathbf{Q}_e\right]\\
-c_i\rho_e^{1-\gamma}(\gamma-1)\overline{\overline{\Pi}}_e : \nabla\left(\dfrac{1}{ne}\mathbf{J}\right) = \rho_e^{1-\gamma}(\gamma-1)\left[\nu_{ei}^{\mathcal{E}}(T_i-T_e) + \zeta_{ei}\eta\mathbf{J}^2\right],\\
\partial_t\mathbf{B} = -\nabla\times\mathbf{E},\\
\mu_0\mathbf{J} = \nabla\times\mathbf{B},\\
\nabla\cdot\mathbf{B} = 0.
\end{cases}$$

In the sequel, we will neglect the dissipative effects in the previous system in order to concentrate on the first-order part of the system. Neglecting dissipative terms usually means that we are mainly interested in the short term behavior of the system since dissipative phenomena are generally associated to large time scales. Therefore, the system that we will consider from now on is

$$\begin{cases}
\partial_t \rho + \nabla\cdot(\rho\mathbf{u}) = 0,\\
\partial_t(\rho\mathbf{u}) + \nabla\cdot(\rho\mathbf{u}\otimes\mathbf{u}) + \dfrac{m_e m_i}{m_e+m_i}\nabla\cdot\left(\dfrac{1}{ne^2}\mathbf{J}\otimes\mathbf{J}\right) + \nabla(p_e+p_i) = \mathbf{J}\times\mathbf{B},\\
\dfrac{m_i m_e}{m_e+m_i}\left[\dfrac{1}{e}\Big(\partial_t\mathbf{J} + \nabla\cdot(\mathbf{u}\otimes\mathbf{J}+\mathbf{J}\otimes\mathbf{u})\Big)\right] - \dfrac{m_e m_i(m_i-m_e)}{(m_e+m_i)^2}\nabla\cdot\left(\dfrac{1}{ne^2}\mathbf{J}\otimes\mathbf{J}\right)\\
+c_e\nabla p_i - c_i\nabla p_e = ne\Big[\mathbf{E}+\mathbf{u}\times\mathbf{B}-\eta\mathbf{J}\Big] - \dfrac{m_i-m_e}{m_i+m_e}\mathbf{J}\times\mathbf{B},\\
\partial_t\mathcal{E}_T + \nabla\cdot\left[(\mathcal{E}+p_e+p_i)\mathbf{u} + \mathbf{E}\times\dfrac{\mathbf{B}}{\mu_0}\right] + \nabla\cdot\left[\Big(c_e(\mathcal{E}_i+p_i) - c_i(\mathcal{E}_e+p_e)\Big)\dfrac{1}{ne}\mathbf{J}\right] = 0,\\
\partial_t(\rho_e S_e) + \nabla\cdot(\rho_e S_e\mathbf{u}) - c_i\nabla\cdot\left(\dfrac{1}{ne}\rho_e S_e\mathbf{J}\right) = \rho_e^{1-\gamma}(\gamma-1)\left[\nu_{ei}^{\mathcal{E}}(T_i-T_e) + \zeta_{ei}\eta\mathbf{J}^2\right],\\
\partial_t\mathbf{B} = -\nabla\times\mathbf{E},\\
\mu_0\mathbf{J} = \nabla\times\mathbf{B},\\
\nabla\cdot\mathbf{B} = 0.
\end{cases} \tag{1.59}$$

III Bi-temperature Euler model

In this Section, we present the derivation of bi-temperature Euler equations from the bi-fluid MHD equations in quasi-neutral regime. In this model, only one density and

one velocity are used but the two species can have different temperatures. In addition to the quasi-neutrality assumption, the fundamental hypothesis leading from the bi-fluid MHD system to the two temperature Euler model is that the dynamical pressure largely dominates the electromagnetic effects (large β). Hence, all the terms involving the current can be neglected. We conclude this Section by a mathematical study of the resulting equations.

III.1 Derivation of the bi-temperature model

The system (1.59) contains two momentum equations: one for the total momentum (ions + electrons) and one for the current density $\mathbf{J}$. Our goal now is to eliminate the fast part of the dynamics related to the movement of the electrons while keeping the possibility for the ions and electrons to have different temperatures. To establish the range of validity of this simplification, we introduce non-dimensional parameters and to this end, we first begin to introduce reference quantities in order to express (1.59) in non-dimensional form. First, we denote respectively, L_0, n_0, $T_{e,0}$, $T_{i,0}$, and B_0 the reference length, density, electronic temperature, ionic temperature, and magnetic field. Then, since we are interested in phenomena where the velocities can be large, we introduce a reference velocity u_0 defined as:

$$u_0 = \sqrt{\frac{k_B(T_{e,0} + T_{i,0})}{m_e + m_i}}. \tag{1.60}$$

Later on, we will see that this velocity corresponds to the speed of sound of the ion-electron mixture. Thus, this choice of velocity scale means that we are interested in phenomena where the material velocity is comparable to the speed of sound. The time scale is chosen such that

$$t_0 = \frac{L_0}{u_0},$$

and this implies as usual that this choice of scales leaves unchanged the continuity equation and the material derivatives. Then from the state laws (1.27), the pressure scales are defined by

$$p_{\alpha,0} = n_0 k_B T_{\alpha,0}. \tag{1.61}$$

From the Maxwell-Ampère equation, we will also use the following scaling to define the reference current:

$$J_0 = \frac{B_0}{L_0 \mu_0}.$$

Then each variable is re-defined in term of reference quantities and non-dimensional variables as:

$$\widetilde{t} = \frac{t}{t_0},\ \widetilde{\mathbf{x}} = \frac{1}{L_0}\mathbf{x},\ \widetilde{\mathbf{u}} = \frac{1}{u_0}\mathbf{u},\ \widetilde{\rho} = \frac{\rho}{(m_e+m_i)n_0},\ \widetilde{T_\alpha} = \frac{T_\alpha}{T_{\alpha,0}},\ \alpha = e,i,\ \widetilde{\mathbf{B}} = \frac{1}{B_0}\mathbf{B},$$

where a super tilde $\widetilde{\cdot}$ denotes a non-dimensional variable.

The momentum equation can be re-written in the following form

$$\begin{aligned}&\widetilde{\partial}_t(\widetilde{\rho}\widetilde{\mathbf{u}}) + \widetilde{\nabla}\cdot(\widetilde{\rho}\widetilde{\mathbf{u}}\otimes\widetilde{\mathbf{u}}) + \frac{m_e m_i}{(m_e+m_i)^2}\frac{B_0^2}{n_0^2 e^2 \mu_0^2 L_0^2 u_0^2}\widetilde{\nabla}\cdot\left[\frac{1}{\widetilde{n}}\widetilde{\mathbf{J}}\otimes\widetilde{\mathbf{J}}\right]\\ &+\frac{k_B T_{e,0}}{(m_e+m_i)u_0^2}\widetilde{\nabla}\widetilde{p}_e + \frac{k_B T_{i,0}}{(m_e+m_i)u_0^2}\widetilde{\nabla}\widetilde{p}_i = \frac{B_0^2}{\mu_0 n_0 (m_e+m_i)u_0^2}\widetilde{\mathbf{J}}\times\widetilde{\mathbf{B}}.\end{aligned} \tag{1.62}$$

Let us define the (total) plasma β parameter by:

$$\beta = \frac{(m_e + m_i) n_0 u_0^2}{B_0^2/\mu_0} = \frac{n_0 k_B (T_{e,0} + T_{i,0})}{B_0^2/\mu_0} \tag{1.63}$$

The plasma β is a well known non-dimensional parameter used in plasma physics, it measures the ratio between the dynamic pressure and the magnetic pressure[1].
We also introduce the (electron) plasma frequency by:

$$\omega_{pe}^2 = \frac{n_0 e^2}{\varepsilon_0 m_e} = \frac{n_0 e^2 c^2 \mu_0}{m_e}. \tag{1.64}$$

as well as the length scale:

$$\delta_e^2 = \frac{c^2}{\omega_{pe}^2} = \frac{m_e}{n_0 e^2 \mu_0}. \tag{1.65}$$

This ratio is called the electron skin depth[2] in [37] while it is denoted electron inertial length [48] p.28 and in other references. According to [36] the value of the plasma frequency ω_{pe} varies between 6.10^{11} in tokamaks and 6.10^{15} in inertial confinement experiments while [48] gives the value of 6.10^{14} for laser plasma. Therefore the electron skin depth is always small in fusion plasma. Similar definitions exist to define the ion plasma frequency and inertial length:

$$\omega_{pi}^2 = \frac{n_0 e^2}{\varepsilon_0 m_i} = \frac{n_0 e^2 c^2 \mu_0}{m_i}, \qquad \delta_i^2 = \frac{c^2}{\omega_{pi}^2} = \frac{m_i}{n_0 e^2 \mu_0}. \tag{1.66}$$

The ratio between the ion and electron inertial lengths $\sqrt{m_i/m_e} \sim 40$ and thus the electron inertial length is significantly smaller than its ion counterpart.

Remark: Another commonly used parameters in magnetized plasma are the Larmor radii defined by:

$$\rho_{e,i} = \frac{m_{e,i} \nu_{e,i}}{e B_0}, \tag{1.67}$$

where $\nu_{e,i} = \sqrt{\dfrac{k_B T_{e,i}}{m_{e,i}}}$ are the thermal velocities of respectively the electrons and ions. We note the following relation between inertial lengths, plasma β and Larmor radii:

$$\rho_{e,i}^2 = \beta \delta_{e,i}^2,$$

and thus the non-dimensional form of the governing equations can also be done in term of Larmor radii instead of inertial lengths. Here we choose to use the inertial lengths in order to separate the magnetic effects from the electric ones.

Now let us introduce the non-dimensional version of the inertial lengths by:

$$\delta_{e,i}^* = \frac{\delta_{e,i}}{L_0}. \tag{1.68}$$

[1] this parameter is usually defined as $\beta = \dfrac{(m_e + m_i) n_0 u_0^2}{B_0^2/2\mu_0}$, the difference by a factor 2 with the definition given in this section is of no importance since in the sequel we are considering the asymptotic form of the equation obtained when $\beta \to +\infty$

[2] not to be confused with the resistive skin depth

With these definitions and the choice (1.60) of the velocity scale, we can re-write (1.62) as

$$\begin{aligned}\widetilde{\partial}_t(\widetilde{\rho}\widetilde{\mathbf{u}}) + \widetilde{\nabla}\cdot(\widetilde{\rho}\widetilde{\mathbf{u}}\otimes\widetilde{\mathbf{u}}) + c_i\frac{(\delta_e^*)^2}{\beta}\widetilde{\nabla}\cdot\left[\frac{1}{\widetilde{n}}\widetilde{\mathbf{J}}\otimes\widetilde{\mathbf{J}}\right]\\ +\frac{T_{e,0}}{T_{e,0}+T_{i,0}}\widetilde{\nabla}\widetilde{p}_e + \frac{T_{i,0}}{T_{e,0}+T_{i,0}}\widetilde{\nabla}\widetilde{p}_i = \frac{1}{\beta}\widetilde{\mathbf{J}}\times\widetilde{\mathbf{B}}.\end{aligned} \tag{1.69}$$

This expression establishes that except for small β the factor in front of the quadratic term in the current in the equation (1.69) is small and therefore the current term can be neglected in this equation. Note that this result is valid independently of the mass ratio between electrons and ions. In particular, this result does not rely on the usual assumption that the electrons can be considered as mass-less. Actually, in the sequel, as we will consider large plasma β parameter, we do not need any assumption on the inertial length except that it is bounded.

We have now to consider the entropy equation. Nevertheless, since this is equivalent, we will work here with the electronic pressure equation

$$\partial_t p_e+\mathbf{u}\cdot\nabla p_e+\gamma p_e\nabla\cdot\mathbf{u}-c_i\left[\frac{1}{ne}\mathbf{J}\cdot\nabla p_e+\gamma p_e\nabla\cdot\left(\frac{1}{ne}\mathbf{J}\right)\right]=(\gamma-1)\left[\nu_{ei}^{\mathcal{E}}(T_i-T_e)+\zeta_{ei}\eta\mathbf{J}^2\right].$$

We recall definition (1.19) giving the expression of the temperature relaxation coefficient (note that $(\gamma-1)^{-1}=3/2$ in the mono-atomic case)

$$\nu_{ei}^{\mathcal{E}} = \frac{k_B}{\gamma-1}\frac{n}{\tau_{ei}+\tau_{ie}},$$

and that the resistivity (1.57) is given by

$$\eta = \frac{m_i m_e}{ne^2(\tau_{ie}m_e+\tau_{ei}m_i)}.$$

Hence, we deduce that the non-dimensional electronic pressure equation can be written

$$\begin{aligned}&\widetilde{\partial}_t\widetilde{p_e} + \widetilde{\mathbf{u}}\cdot\widetilde{\nabla}\widetilde{p_e} + \gamma\widetilde{p_e}\widetilde{\nabla}\cdot\widetilde{\mathbf{u}} - \sqrt{c_i}\frac{\delta_i^*}{\sqrt{\beta}}\left[\frac{1}{\widetilde{n}}\widetilde{\mathbf{J}}\cdot\widetilde{\nabla}\widetilde{p_e}+\gamma\widetilde{p_e}\widetilde{\nabla}\cdot\left(\frac{1}{\widetilde{n}}\widetilde{\mathbf{J}}\right)\right]\\ &=\left(\frac{T_{i,0}}{T_{e,0}}\widetilde{T}_i-\widetilde{T}_e\right)\widetilde{\nu}_{ei}^{\mathcal{E}}+(\gamma-1)\zeta_{ei}\left(1+\frac{T_{i,0}}{T_{e,0}}\right)\frac{(\delta_e^*)^2}{\beta}\widetilde{\eta}\widetilde{\mathbf{J}}^2.\end{aligned} \tag{1.70}$$

where the non dimensional temperature relaxation coefficient is defined as

$$\widetilde{\nu}_{ei}^{\mathcal{E}} = \frac{\widetilde{n}}{\widetilde{\tau}_{ei}+\widetilde{\tau}_{ie}},$$

where $\widetilde{\tau}_{ei}=\tau_{ei}u_0/L_0$, and $\widetilde{\tau}_{ie}=\tau_{ie}u_0/L_0$ denote the non-dimensional temperature relaxation times while the non-dimensional resistivity is

$$\widetilde{\eta} = \frac{m_i}{\widetilde{n}(\widetilde{\tau}_{ie}m_e+\widetilde{\tau}_{ei}m_i)}. \tag{1.71}$$

We notice that in this equation, ζ_{ei} does not change. Indeed, according to its definition (1.58), ζ_{ei} is already a non-dimension variable.

Note that in this equation the advective terms involving the current are multiplied by the *ion* inertial length. Symmetrically the corresponding term in the ion pressure equation

will involve the *electron* inertial length.
The last term in equation (1.70) corresponds to Ohmic heating and is representative of the transfer between electromagnetic and internal energy.

According to the definition of the electronic entropy (1.49), the non-dimensional corresponding variable is

$$\widetilde{S}_e = \widetilde{\rho_e}^{-\gamma}\widetilde{p}_e,$$

then, the equation (1.70) re-writes

$$\begin{aligned}&\widetilde{\partial}_t(\widetilde{\rho}_e\widetilde{S}_e) + \widetilde{\nabla}\cdot(\widetilde{\rho}_e\widetilde{S}_e\widetilde{\mathbf{u}}) - \sqrt{c_i}\frac{\delta_i^*}{\sqrt{\beta}}\widetilde{\nabla}\cdot\left[\frac{\widetilde{\rho}_e\widetilde{S}_e}{\widetilde{n}}\widetilde{\mathbf{J}}\right]\\ &= \widetilde{\rho}_e^{1-\gamma}\left[\left(\frac{T_{i,0}}{T_{e,0}}\widetilde{T}_i - \widetilde{T}_e\right)\widetilde{\nu}_{ei}^{\mathcal{E}} + (\gamma-1)\zeta_{ei}\left(1+\frac{T_{i,0}}{T_{e,0}}\right)\frac{(\delta_e^*)^2}{\beta}\widetilde{\eta}\widetilde{\mathbf{J}}^2\right].\end{aligned} \tag{1.72}$$

We now consider the total energy equation (1.59). With the choice of the velocity scaling (1.60), the kinetic energy is of the same order as the thermal energy and therefore we choose to define the non-dimensional total energy and the non-dimensional total energy by species by:

$$\mathcal{E} = n_0(m_e+m_i)u_0^2\widetilde{\mathcal{E}}, \quad \mathcal{E}_\alpha = n_0 k_B T_{\alpha,0}\widetilde{\mathcal{E}}_\alpha,\ \alpha = e,i.$$

The choice of a scale for the electric field is delicate. Faraday's law favors the use of the scaling

$$\mathbf{E} = B_0u_0\widetilde{\mathbf{E}}. \tag{1.73}$$

and this is the choice that is usually done in MHD. However, since Faraday's law involve the curl of $\mathbf{E}$, we see that the gradient part of $\mathbf{E}$ (if it exists) has no reason to scale with B_0u_0. To take this possibility into account, we will set

$$\mathbf{E} = \kappa B_0u_0\widetilde{\mathbf{E}},$$

leaving for the present time the parameter κ unspecified[3]. With these choices, we obtain:

$$\begin{aligned}&\widetilde{\partial}_t\left(\widetilde{\mathcal{E}} + \frac{\widetilde{\mathbf{B}}^2}{2\beta}\right) + \widetilde{\nabla}\cdot\left[(\widetilde{\mathcal{E}} + \frac{T_{e,0}}{T_{e,0}+T_{i,0}}\widetilde{p}_e + \frac{T_{i,0}}{T_{e,0}+T_{i,0}}\widetilde{p}_i)\widetilde{\mathbf{u}} + \frac{\kappa\widetilde{\mathbf{E}}\times\widetilde{\mathbf{B}}}{\beta}\right] +\\ &\frac{1}{\sqrt{\beta}}\widetilde{\nabla}\cdot\left[\left(\sqrt{c_e}\delta_e^*\frac{T_{i,0}}{T_{e,0}+T_{i,0}}(\widetilde{p}_i+\widetilde{\mathcal{E}}_i) - \sqrt{c_i}\delta_i^*\frac{T_{e,0}}{T_{e,0}+T_{i,0}}(\widetilde{p}_e+\widetilde{\mathcal{E}}_e)\right)\frac{\widetilde{\mathbf{J}}}{\widetilde{n}}\right] = 0.\end{aligned} \tag{1.74}$$

Again, the terms containing the current are multiplied by expressions involving the inertial lengths.

It remains to consider the electron momentum equations or alternatively the equation governing the evolution of the current. For the Ohm's law, the same scaling procedure

[3]To be more specific, we note that $\mathbf{E}$ being a 3-D vector field, the 3 components of this vector have no reason to have the same scales. In particular, Ohm's law shows that the parallel component (defined as $\mathbf{E}\cdot\mathbf{B}/|\mathbf{B}|$) of the electric field has no reason to scale with B_0u_0. A detailed analysis would therefore imply to use different scalings according to the different spatial directions. Here we simplify this analysis by introducing an additional parameter

gives:

$$\begin{aligned}\kappa\widetilde{\mathbf{E}}+\widetilde{\mathbf{u}}\times\widetilde{\mathbf{B}} &= (\delta_e^*)^2\widetilde{\eta}\widetilde{\mathbf{J}}+\frac{\sqrt{c_i}\delta_i^*-\sqrt{c_e}\delta_e^*}{\sqrt{\beta}}\frac{\widetilde{\mathbf{J}}\times\widetilde{\mathbf{B}}}{\widetilde{n}}\\ &-\sqrt{c_i}\delta_i^*\sqrt{\beta}\frac{T_{e,0}}{T_{e,0}+T_{i,0}}\frac{1}{\widetilde{n}}\widetilde{\nabla}\widetilde{p}_e+\sqrt{c_e}\delta_e^*\sqrt{\beta}\frac{T_{i,0}}{T_{e,0}+T_{i,0}}\frac{1}{\widetilde{n}}\widetilde{\nabla}\widetilde{p}_i\\ &+c_i(\delta_e^*)^2\frac{1}{\widetilde{n}}\left[\widetilde{\partial}_t\widetilde{\mathbf{J}}+\widetilde{\nabla}\cdot\left(\widetilde{\mathbf{u}}\otimes\widetilde{\mathbf{J}}+\widetilde{\mathbf{J}}\otimes\widetilde{\mathbf{u}}\right)\right]\\ &+\sqrt{c_i}(c_i-c_e)\frac{(\delta_e^*)^2\delta_i^*}{\sqrt{\beta}}\frac{1}{\widetilde{n}}\widetilde{\nabla}\cdot\left[\frac{1}{\widetilde{n}}\widetilde{\mathbf{J}}\otimes\widetilde{\mathbf{J}}\right].\end{aligned}\tag{1.75}$$

III.2 The bi-temperature model for large β parameter

In equations (1.69), (1.70), (1.74), and (1.75), the non-dimensional parameters $c_{e,i}, \delta^*_{e,i}, \beta$, and κ appear. According to the different values of these parameters, the equations can take many different limiting forms describing a huge range of phenomena. Ideal MHD for instance, corresponds to situations where $\delta^*_{e,i}\to 0$ while β stays bounded. In this Section, with applications to laser plasma in mind, we will consider phenomena characterized by very large plasma β parameter where the dynamical pressure is far larger than the magnetic one. Although the model considers two different temperatures, we will also assume that these temperatures remain comparable and that the ratio $T_{i,0}/T_{e,0}$ remains bounded. We then formally consider the limit $\beta\to+\infty$ in equations (1.69), (1.74) and (1.72) and we obtain the system:

$$\begin{cases}\partial_t\rho+\nabla\cdot(\rho\mathbf{u}) &= 0,\\ \partial_t(\rho\mathbf{u})+\nabla\cdot(\rho\mathbf{u}\otimes\mathbf{u})+\nabla(p_e+p_i) &= 0,\\ \partial_t\mathcal{E}+\nabla\cdot\left[(\mathcal{E}+p_e+p_i)\,\mathbf{u}\right] &= 0,\\ \partial_t(\rho_e S_e)+\nabla\cdot(\rho_e S_e\mathbf{u}) &= \rho_e^{\gamma-1}(\gamma-1)\nu_{ei}^{\mathcal{E}}(T_i-T_e).\end{cases}\tag{1.76}$$

The system (1.76) has been obtained with the assumption that $\kappa/\beta\to 0$. In this case, we emphasize that (1.76) is a *closed* system: corresponding to the hypothesis of large β the electromagnetic energy becomes negligible with respect to the mechanical one. Moreover in the definition of the mechanical energy (1.44)

$$\mathcal{E}=\frac{p_i+p_e}{\gamma-1}+\frac{1}{2}\rho_i\mathbf{u}_i^2+\frac{1}{2}\rho_e\mathbf{u}_e^2=\frac{p_i+p_e}{\gamma-1}+\frac{1}{2}\rho\mathbf{u}^2+\frac{m_em_i}{m_e+m_i}\frac{\mathbf{J}^2}{ne^2},\tag{1.77}$$

the last term is of order $\mathcal{O}(c_i(\delta_e^*)^2/\beta)$ and thus must be neglected.

Let us remark that to obtain (1.76), we do not need to consider Ohm's law (1.75). In this sense, (1.76) is independent of the precise form of Ohm's that is used. However if we check for consistency the behavior of Ohm's law in the limit $\beta\to+\infty$, we will get at the higher order in β:

$$\kappa\widetilde{\mathbf{E}}=-\sqrt{c_i}\delta_i^*\sqrt{\beta}\frac{T_{e,0}}{T_{e,0}+T_{i,0}}\frac{1}{\widetilde{n}}\widetilde{\nabla}\widetilde{p}_e+\sqrt{c_e}\delta_e^*\sqrt{\beta}\frac{T_{i,0}}{T_{e,0}+T_{i,0}}\frac{1}{\widetilde{n}}\widetilde{\nabla}\widetilde{p}_i,\tag{1.78}$$

and this relation establishes that the parameter κ (ratio between the electric field and the product u_0B_0) has to scale with $\delta_i^*\sqrt{\beta}$ in the $\beta\to+\infty$ limit. Therefore the ratio $\kappa/\beta\to 0$

when $\beta \to +\infty$ and the scaling is self-consistent.

Note also that in this derivation of (1.76), we have never used any assumption on the electron mass. This system is therefore also relevant in the case where instead of electrons, a mixture of positive and negative ions is considered. However, in this case, there is no definite reason to choose the electronic entropy equation to close the system and another choice can be more physically relevant.

The system (1.76) can be also established using different assumptions. In [7], a bi-fluid model in the absence of any magnetic field is considered with the assumption that the two species have the same velocity. Then the comparison of the momentum equations from (1.36) (with $\mathbf{u}_e = \mathbf{u}_i = \mathbf{u}$) implies Ohm's law (1.78) from which a non-conservative system equivalent for smooth solutions to (1.76) is derived. The same assumption (with in addition $m_e = 0$) is also used in [26].

System (1.76) is also considered in [69], with the assumption that the electron mass is small. The derivation we have presented here seems more general and do not rely on the strong assumptions of the absence of current and magnetic field and that the two species have the same velocities. It only requires quasi-neutrality and that the magnetic effects are weak.

Let us now check that the characteristic value of laser plasma agree with our assumptions on the values of the non-dimensional parameter. According to the NRL [48], the order of value of density, temperature are of the order of

$$\left\{ \begin{array}{lcl} n_0 & = & 10^{26} m^{-3}, \\ T_{e/i,0} & = & 100eV = 1.1605 \times 10^6 K. \end{array} \right.$$

Therefore, the electron and ion inertial lengths are

$$\left\{ \begin{array}{lcl} \delta_e^* & = & 5.31 \times 10^{-4}, \\ \delta_i^* & = & 2.28 \times 10^{-2}. \end{array} \right.$$

The reference velocity and the size of a target are then given by

$$\left\{ \begin{array}{lcl} u_0 & = & 1.38 \times 10^5 m.s^{-1}, \\ L_0 & = & 2 \times 10^{-3} m. \end{array} \right.$$

Then, the characteristic time is given by

$$t_0 = 1,72 \times 10^{-9} s.$$

The NRL [48] gives also in page 40, the collision frequency electron/ion:

$$\frac{1}{\tau_{ei}} = 2 \times 10^{12} s^{-1}, \ \tau_{ei} = 5 \times 10^{-11} s.$$

Then for short time simulation it is interesting to study the thermal equilibrium.

The next subsection is devoted to a study of the mathematical properties of this system.

III.3 Properties of the bi-temperature Euler model

This subsection presents a mathematical study of (1.76) for the mono-atomic case (1.43). In [26], a mathematical study of the multi-fluid system with the equation on the electronic entropy is also presented. Since the bi-temperature Euler system is invariant by rotation, then it is sufficient to study the 1-D system in the x-direction

$$\left\{\begin{array}{lcl} \partial_t\rho + \partial_x(\rho u) & = & 0, \\ \partial_t(\rho u) + \partial_x(\rho u^2 + p_e + p_i) & = & 0, \\ \partial_t(\rho v) + \partial_x(\rho uv) & = & 0, \\ \partial_t(\rho w) + \partial_x(\rho uw) & = & 0, \\ \partial_t\mathcal{E} + \partial_x\left[(\mathcal{E} + p_e + p_i)u\right] & = & 0, \\ \partial_t(\rho_e S_e) + \partial_x(\rho_e S_e u) & = & (\gamma-1)\nu_{ei}^{\mathcal{E}}\rho_e^{1-\gamma}(T_i - T_e). \end{array}\right. \tag{1.79}$$

The system (1.79) is written in the form

$$\partial_t U + \partial_x F(U) = S(U),$$

where

$$U = \begin{bmatrix} \rho \\ \rho u \\ \rho v \\ \rho w \\ \mathcal{E} \\ \rho_e S_e \end{bmatrix}, \; F(U) = \begin{bmatrix} \rho u \\ \rho u^2 + p_e + p_i \\ \rho uv \\ \rho uw \\ (\mathcal{E} + p_e + p_i)u \\ \rho_e S_e u \end{bmatrix}, \; S(U) = \begin{bmatrix} 0 \\ 0 \\ 0 \\ 0 \\ 0 \\ (\gamma-1)\nu_{ei}^{\mathcal{E}}\rho_e^{1-\gamma}(T_i - T_e) \end{bmatrix}.$$

In order to determine the eigensystem of the problem, we compute $A(U) = \partial_U F(U)$ known as the Jacobian and get

$$\begin{bmatrix} 0 & 1 & 0 & 0 & 0 & 0 \\ \frac{\gamma-3}{2}u^2 + \frac{\gamma-1}{2}(v^2+w^2) & (3-\gamma)u & (1-\gamma)v & (1-\gamma)w & \gamma-1 & 0 \\ -uv & v & u & 0 & 0 & 0 \\ -uw & w & 0 & u & 0 & 0 \\ u\left[-\frac{c_s^2}{\gamma-1} + \frac{\gamma-2}{2}(u^2+v^2+w^2)\right] & \frac{c_s^2}{\gamma-1} + \frac{3-2\gamma}{2}u^2 + \frac{v^2+w^2}{2} & (1-\gamma)uv & (1-\gamma)uw & \gamma u & 0 \\ -c_e S_e u & c_e S_e & 0 & 0 & 0 & u \end{bmatrix}.$$

This matrix has three different eigenvalues given by

$$\left\{\begin{array}{lcl} \lambda_1 & = & u - c_s, \\ \lambda_2 & = & u, \\ \lambda_3 & = & u + c_s, \end{array}\right. \tag{1.80}$$

where c_s is the sound speed of the mixture

$$c_s = \sqrt{\gamma\,\frac{p_e + p_i}{\rho}}.$$

Those eigenvalues and the definition of the sound speed of the mixture correspond to the one given in [26]. The eigenvalue λ_2 has an order of multiplicity of 4, and the eigenvectors

R_1, R_2, and R_3, respectively associated to λ_1, λ_2, and λ_3, are given by

$$\begin{cases} R_1 = \begin{bmatrix} 1 \\ u - c_s \\ v \\ w \\ \dfrac{c_s^2}{\gamma - 1} + \dfrac{u^2 + v^2 + w^2}{2} - uc_s \\ c_e S_e \end{bmatrix}, \quad R_2 = \begin{bmatrix} 1 \\ u \\ v \\ w \\ \dfrac{u^2 + v^2 + w^2}{2} \\ 1 \end{bmatrix}, \\ R_3 = \begin{bmatrix} 1 \\ u + c_s \\ v \\ w \\ \dfrac{c_s^2}{\gamma - 1} + \dfrac{u^2 + v^2 + w^2}{2} + uc_s \\ c_e S_e \end{bmatrix}. \end{cases} \tag{1.81}$$

With the results (1.80) and (1.81), we find that the waves λ_1 and λ_3 are genuinely non linear and consequently those two waves can be shock or rarefaction waves. Concerning the wave λ_2, the computations lead to determine that this wave is linearly degenerate meaning that it is a contact discontinuity.

We now consider the Riemann problem with the initial data U_L, and U_R associated to the homogeneous conservative system

$$\partial_t U + \partial_x F(U) = 0.$$

The intermediate states are denoted U_L^* and U_R^* (see Figure 1.1). The Riemann invariants associated to each waves are

$$\begin{aligned} (u - c_s) - \text{wave} \quad &: \quad v,\ w,\ \rho_e p_e^{-\gamma},\ \rho_i p_i^{-\gamma},\ \text{and } u + \frac{2}{\gamma - 1} c_s, \\ u - \text{wave} \quad &: \quad u,\ \text{and } p_e + p_i, \\ (u + c_s) - \text{wave} \quad &: \quad v,\ w,\ \rho_e p_e^{-\gamma},\ \rho_i p_i^{-\gamma},\ \text{and } u - \frac{2}{\gamma - 1} c_s. \end{aligned}$$

For the 1-wave, associated to the $u - c_s$ eigenvalue, the shock and the rarefaction conditions are given by

$$\begin{cases} \lambda_1(U_L) \leq S_1 \leq \lambda_1(U_L^*) & \text{Rarefaction condition,} \\ \lambda_1(U_L) \geq S_1 \geq \lambda_1(U_L^*) & \text{Shock condition,} \end{cases}$$

where S_1 is the speed of the 1-wave. To compute, the intermediate state U_L^* in the case of a 1-shock the Rankine-Hugoniot relation has to be used

$$F(U_L^*) - F(U_L) = S_1 \left(U_L^* - U_L\right).$$

The Rankine-Hugoniot condition is not any more valuable for the 1-rarefaction and then the Riemann invariant of λ_1 are used to compute U_L^*.

Likewise, the shock and the rarefaction conditions for the 3-wave, associated to the $u + c_s$ eigenvalue, are given by

$$\begin{cases} \lambda_3(U_R^*) & \leq S_3 \leq & \lambda_3(U_R) & \text{Rarefaction condition,} \\ \lambda_3(U_R^*) & \geq S_3 \geq & \lambda_3(U_R) & \text{Shock condition,} \end{cases}$$

where S_3 is the speed of the 3-wave. The Rankine-Hugoniot relation for the 3-shock is given by

$$F(U_R^*) - F(U_R) = S_3 \left(U_R^* - U_R\right).$$

For the 3-rarefaction, we use the Riemann invariants of λ_3 to get U_R^*. The four different cases are shown in Figure 1.1.

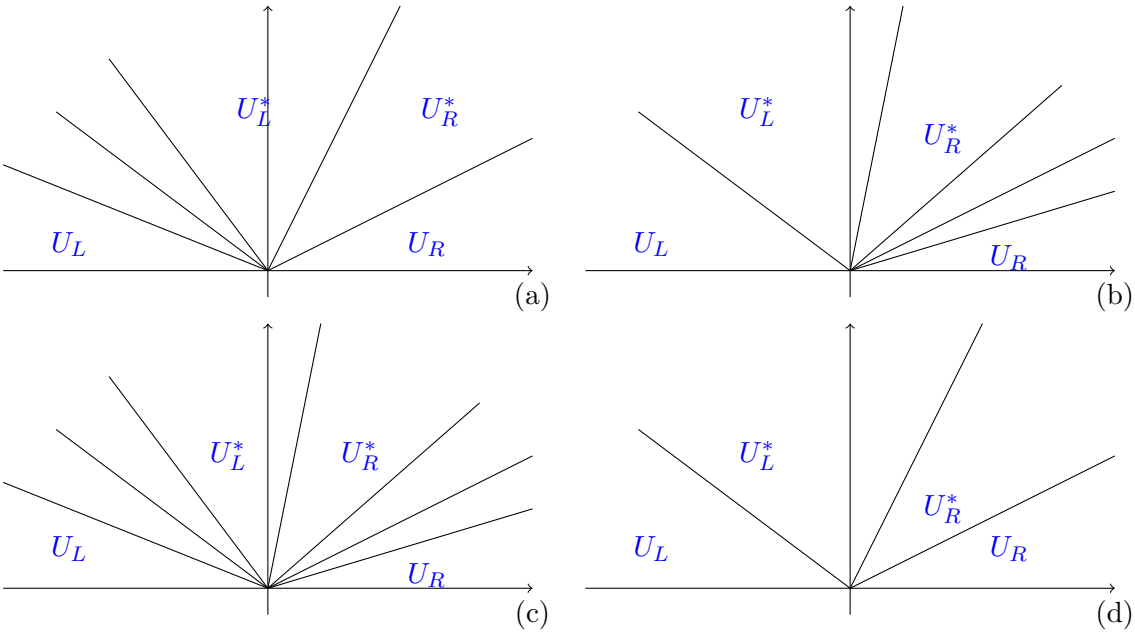

Figure 1.1: The four cases of Riemann problem for the bi-temperature Euler equation: (a) 1-Rarefaction and 3-Shock, (b) 1-Shock and 3-Rarefaction, (c) 1-Rarefaction and 3-Rarefaction, (d) 1-Shock and 3-Shock.

IV Mono-fluid MHD models

In this Section, we go back to the bi-fluid MHD equations in quasi-neutral regime (1.59), and consider a different assymptotic regime leading to some mono-fluid MHD models. These mono-fluid MHD models assume that the *ion* and *electron* depth skin are small leading to the ideal and the resistive MHD models in contrast to section III, we will now consider that the plasma β parameter is finite. Finally, a mathematical study of the ideal MHD model properties is performed at this end of this section.

IV.1 Non-dimensional bi-fluid MHD model

In this subsection, we use the same notations and definitions as the ones of subsection III.1.

We are now interested by phenomena where the hydrodynamics effects are comparable to the magnetic ones, meaning that we suppose that the β parameter is bounded. In fact,

here we assume that

$$\beta \approx 1.$$

We deduce from this hypothesis that the reference velocity u_0 in (1.60) can also be defined as

$$u_0 = \frac{B_0/\sqrt{\mu_0}}{\sqrt{n_0(m_e+m_i)}}. \tag{1.82}$$

We will see later that this velocity corresponds to the Alfvén speed.

First, starting from the total energy and the electronic entropy equations of system (1.59), we write the two non-dimensional equations on each pressure:

$$\left\{\begin{array}{rcl} \widetilde{\partial}_t\widetilde{p}_e + \widetilde{\mathbf{u}}\cdot\widetilde{\nabla}\widetilde{p}_e - \sqrt{c_i}\delta_i^*\left[\dfrac{1}{\widetilde{n}}\widetilde{\mathbf{J}}\cdot\widetilde{\nabla}\widetilde{p}_e + \gamma\widetilde{p}_e\widetilde{\nabla}\cdot\left(\dfrac{1}{\widetilde{n}}\widetilde{\mathbf{J}}\right)\right] \\ \qquad = \left[\dfrac{T_{i,0}}{T_{e,0}}\widetilde{T}_i - \widetilde{T}_e\right]\widetilde{\nu}_{ei}^{\mathcal{E}} + (\gamma-1)\zeta_{ei}(\delta_e^*)^2\widetilde{\eta}\widetilde{\mathbf{J}}^2, \\ \widetilde{\partial}_t\widetilde{p}_i + \widetilde{\mathbf{u}}\cdot\widetilde{\nabla}\widetilde{p}_i - \sqrt{c_e}\delta_e^*\left[\dfrac{1}{\widetilde{n}}\widetilde{\mathbf{J}}\cdot\widetilde{\nabla}\widetilde{p}_i + \gamma\widetilde{p}_i\widetilde{\nabla}\cdot\left(\dfrac{1}{\widetilde{n}}\widetilde{\mathbf{J}}\right)\right] \\ \qquad = \left[\dfrac{T_{e,0}}{T_{i,0}}\widetilde{T}_e - \widetilde{T}_i\right]\widetilde{\nu}_{ei}^{\mathcal{E}} + (\gamma-1)\zeta_{ie}(\delta_e^*)^2\widetilde{\eta}\widetilde{\mathbf{J}}^2. \end{array}\right.$$

where

$$\left\{\begin{array}{rcl} \zeta_{ei} &=& \dfrac{1}{2}\left[\dfrac{\tau_{ei}m_i}{\tau_{ie}m_e+\tau_{ei}m_i} + \dfrac{\tau_{ie}}{\tau_{ie}+\tau_{ei}}\right], \\ \zeta_{ie} &=& \dfrac{1}{2}\left[\dfrac{\tau_{ie}m_e}{\tau_{ie}m_e+\tau_{ei}m_i} + \dfrac{\tau_{ei}}{\tau_{ie}+\tau_{ei}}\right]. \end{array}\right.$$

Then, the non-dimensional equations on the difference and the sum of the two pressure ones are

$$\left\{\begin{array}{rcl} \widetilde{\partial}_t(\widetilde{p}_e+\widetilde{p}_i) + \widetilde{\mathbf{u}}\cdot\widetilde{\nabla}(\widetilde{p}_e+\widetilde{p}_i) + \gamma(\widetilde{p}_e+\widetilde{p}_i)\widetilde{\nabla}\cdot\widetilde{\mathbf{u}} - \dfrac{1}{\widetilde{n}}\widetilde{\mathbf{J}}\cdot\widetilde{\nabla}\left(\sqrt{c_i}\delta_i^*\widetilde{p}_e + \sqrt{c_e}\delta_e^*\widetilde{p}_i\right) \\ \qquad - \left(\sqrt{c_i}\delta_i^*\widetilde{p}_e + \sqrt{c_e}\delta_e^*\widetilde{p}_i\right)\widetilde{\nabla}\cdot\left(\dfrac{1}{\widetilde{n}}\widetilde{\mathbf{J}}\right) \\ \qquad = \dfrac{T_{e,0}-T_{i,0}}{T_{e,0}T_{i,0}}\left(T_{i,0}\widetilde{T}_i - T_{e,0}\widetilde{T}_e\right)\widetilde{\nu}_{ei}^{\mathcal{E}} + (\gamma-1)(\delta_e^*)^2\widetilde{\eta}\widetilde{\mathbf{J}}^2, \\ \widetilde{\partial}_t(\widetilde{p}_i-\widetilde{p}_e) + \widetilde{\mathbf{u}}\cdot\widetilde{\nabla}(\widetilde{p}_i-\widetilde{p}_e) + \gamma(\widetilde{p}_i-\widetilde{p}_e)\widetilde{\nabla}\cdot\widetilde{\mathbf{u}} - \dfrac{1}{\widetilde{n}}\widetilde{\mathbf{J}}\cdot\widetilde{\nabla}\left(\sqrt{c_e}\delta_e^*\widetilde{p}_i - \sqrt{c_i}\delta_i^*\widetilde{p}_e\right) \\ \qquad - \left(\sqrt{c_e}\delta_e^*\widetilde{p}_i - \sqrt{c_i}\delta_i^*\widetilde{p}_e\right)\widetilde{\nabla}\cdot\left(\dfrac{1}{\widetilde{n}}\widetilde{\mathbf{J}}\right) \\ \qquad = -\dfrac{T_{e,0}+T_{i,0}}{T_{e,0}T_{i,0}}\left(T_{i,0}\widetilde{T}_i - T_{e,0}\widetilde{T}_e\right)\widetilde{\nu}_{ei}^{\mathcal{E}} + (\gamma-1)(\zeta_{ie}-\zeta_{ie})(\delta_e^*)^2\widetilde{\eta}\widetilde{\mathbf{J}}^2. \end{array}\right.$$

According to [68], experiments show that in a tokamak the temperatures and the density are

$$\left\{\begin{array}{rcl} Te,0 &=& T_{i,0} = 10-12keV = 1.30\times10^8K, \\ n_0 &=& 10^{20}m^{-3}. \end{array}\right.$$

Then, the relaxation time is

$$\frac{1}{\tau_{ei}+\tau_{ie}} \approx 4\times10^4 s^{-1}.$$

Then, this term can be considerate large. By using the previous equation with the limit of small electron inertial length, we deduce that

$$T_e \approx T_i.$$

Therefore, instead of considering a bi-fluid MHD model, we suppose that we have a single-fluid as a mixture of electrons and ions with a single temperature and pressure defined as follow

$$\left\{ \begin{array}{rcccl} T & = & T_e & = & T_i, \\ p & = & p_e & = & p_i, \end{array} \right. \tag{1.83}$$

linked by the relation

$$p = nk_BT.$$

Then, the non-dimensional temperature and pressure write

$$\left\{ \begin{array}{rcl} T & = & T_0\widetilde{T}, \\ p & = & n_0k_BT_0\widetilde{p}, \end{array} \right.$$

where $T_0 = T_{0,e} = T_{0,i}$. Therefore, the non-dimensional momentum equation (1.69) becomes

$$\widetilde{\partial}_t(\widetilde{\rho}\widetilde{\mathbf{u}}) + \widetilde{\nabla}\cdot(\widetilde{\rho}\widetilde{\mathbf{u}}\otimes\widetilde{\mathbf{u}}) + c_i(\delta_e^*)^2\widetilde{\nabla}\cdot\left[\frac{1}{\widetilde{n}}\widetilde{\mathbf{J}}\otimes\widetilde{\mathbf{J}}\right] + \widetilde{\nabla}\widetilde{p} = \widetilde{\mathbf{J}}\times\widetilde{\mathbf{B}}. \tag{1.84}$$

Concerning the scaling of the electric field $\mathbf{E}$, we will use the usual MHD scaling (1.73) in this part. Thus, the total energy equation (1.74) is now

$$\begin{aligned} \widetilde{\partial}_t\widetilde{\mathcal{E}}_T \quad & +\widetilde{\nabla}\cdot\left[\left(\widetilde{\mathcal{E}}+\widetilde{p}\right)\widetilde{\mathbf{u}}+\widetilde{\mathbf{E}}\times\widetilde{\mathbf{B}}\right] \\ & +\frac{1}{2}\widetilde{\nabla}\cdot\left[\left(\sqrt{c_e}\delta_e^*(\widetilde{\mathcal{E}}_i+\widetilde{p}) - \sqrt{c_i}\delta_i^*(\widetilde{\mathcal{E}}_e+\widetilde{p})\right)\frac{\widetilde{\mathbf{J}}}{\widetilde{n}}\right] = 0, \end{aligned} \tag{1.85}$$

where $\widetilde{\mathcal{E}}_T = \widetilde{\mathcal{E}} + \frac{1}{2}\widetilde{\mathbf{B}}^2$.

We are now interested in the Ohm's law (1.75). First, we rewrite the non-dimensional resistivity (1.71) in the following form

$$\eta = \frac{1}{\eta_0}\widetilde{\eta},$$

where η_0 is defined in [37] p240

$$\eta_0 = \frac{\sqrt{2}}{12\pi^{3/2}}\frac{e^2\sqrt{m_e}}{\varepsilon_0 T_e^{3/2}}\lambda_{ei},$$

and $\widetilde{\eta}$ is still given by (1.71). We remark that in the above definition of η_0, the electron inertial length is contained. This definition is also simplify with the relation

$$\eta_0 = 6.5\times10^{-8}\frac{1}{T_e^{3/2}}\Omega m,$$

where T_e is express in keV. We now introduce the magnetic Reynolds number

$$R_m = \frac{\mu_0 L_o u_0}{\eta_0}.$$

According to the NRL formulary [48], this number represents the ratio between the flow velocity and the magnetic diffusion one. Using the same process as before, we obtain that the non-dimensional Ohm's law (1.75) becomes

$$\begin{aligned}\widetilde{\mathbf{E}}+\widetilde{\mathbf{u}}\times\widetilde{\mathbf{B}} &= \frac{1}{R_m}\widetilde{\eta}\widetilde{\mathbf{J}}+(\sqrt{c_i}\delta_i^*-\sqrt{c_e}\delta_e^*)\frac{\widetilde{\mathbf{J}}\times\widetilde{\mathbf{B}}}{\widetilde{n}}\\ &\quad -\frac{1}{2}(\sqrt{c_i}\delta_i^*-\sqrt{c_e}\delta_e^*)\frac{1}{\widetilde{n}}\widetilde{\nabla}\widetilde{p}\\ &\quad +c_i(\delta_e^*)^2\frac{1}{\widetilde{n}}\left[\widetilde{\partial}_t\widetilde{\mathbf{J}}+\widetilde{\nabla}\cdot\left(\widetilde{\mathbf{J}}\otimes\widetilde{\mathbf{u}}+\widetilde{\mathbf{u}}\otimes\widetilde{\mathbf{J}}\right)\right]\\ &\quad +\sqrt{c_i}(c_i-c_e)(\delta_e^*)^2\delta_i^*\frac{1}{\widetilde{n}}\widetilde{\nabla}\cdot\left[\frac{1}{\widetilde{n}}\widetilde{\mathbf{J}}\otimes\widetilde{\mathbf{J}}\right].\end{aligned} \tag{1.86}$$

In Chapter 4, we will work only with the non-dimensional MHD models. Then, from now we do not use anymore the super tilde $\widetilde{\cdot}$ for the non-dimensional variables in order to simplify the notation.

Using the results (1.84)-(1.86), we write that the non-dimensional single-fluid MHD equations are

$$\begin{cases}\partial_t\rho + \nabla\cdot(\rho\mathbf{u})=0,\\ \partial_t(\rho\mathbf{u}) + \nabla\cdot(\rho\mathbf{u}\otimes\mathbf{u})+c_i(\delta_e^*)^2\nabla\cdot\left[\frac{1}{n}\mathbf{J}\otimes\mathbf{J}\right]+\nabla p=\mathbf{J}\times\mathbf{B},\\ \partial_t\mathcal{E}_T + \nabla\cdot[(\mathcal{E}+p)\,\mathbf{u}+\mathbf{E}\times\mathbf{B}]\\ \qquad + \frac{1}{2}\nabla\cdot\left[(\sqrt{c_e}\delta_e^*(\mathcal{E}_i+p)-\sqrt{c_i}\delta_i^*(\mathcal{E}_e+p))\frac{\mathbf{J}}{n}\right]=0,\\ \partial_t\mathbf{B} + \nabla\times\mathbf{E}=0.\end{cases} \tag{1.87}$$

To this system, the non-dimensional Maxwell-Ampère, the divergence-free constraint, and the Ohm's law (1.86) are added:

$$\begin{cases}\nabla\times\mathbf{B} &= \mathbf{J},\\ \nabla\cdot\mathbf{B} &= 0,\\ \mathbf{E}+\mathbf{u}\times\mathbf{B} &= \frac{1}{R_m}\eta\mathbf{J}+(\sqrt{c_i}\delta_i^*-\sqrt{c_e}\delta_e^*)\frac{\mathbf{J}\times\mathbf{B}}{n}\\ &\quad -\frac{1}{2}(\sqrt{c_i}\delta_i^*-\sqrt{c_e}\delta_e^*)\frac{1}{n}\nabla p\\ &\quad +c_i(\delta_e^*)^2\frac{1}{n}\left[\partial_t\mathbf{J}+\nabla\cdot(\mathbf{J}\otimes\mathbf{u}+\mathbf{u}\otimes\mathbf{J})\right]\\ &\quad +\sqrt{c_i}(c_i-c_e)(\delta_e^*)^2\delta_i^*\frac{1}{n}\nabla\cdot\left[\frac{1}{n}\mathbf{J}\otimes\mathbf{J}\right].\end{cases} \tag{1.88}$$

In systems (1.87) and (1.88), the parameters $\delta_{e,i}^*$, $c_{e,i}$, and R_m appear. Then, as we have noticed in III.2, the different values of these parameters correspond to different

limiting models. For example, from the Ohm's law of (1.88), considering that $\delta_e^* \to 0$ we can obtain the three different models:

$$\begin{cases} \text{Hall MHD:} & \mathbf{E}+\mathbf{u}\times\mathbf{B} &=& \dfrac{1}{R_m}\eta\mathbf{J} + \sqrt{c_i}\delta_i^*\dfrac{\mathbf{J}\times\mathbf{B}}{n} - \sqrt{c_i}\delta_i^*\nabla p_i, \\ \text{Resistive MHD:} & \mathbf{E}+\mathbf{u}\times\mathbf{B} &=& \eta\mathbf{J}, \\ \text{Ideal MHD:} & \mathbf{E}+\mathbf{u}\times\mathbf{B} &=& 0. \end{cases}$$

The two next subsections are devoted to the limit of the resistive and ideal MHD models.

IV.2 Resistive MHD model for small $\delta_{e,i}^*$ and bounded R_m

To obtain the single-fluid MHD system, assuming in addition that $\delta_i^* \to 0$, we get

$$\begin{cases} \partial_t\rho + \nabla\cdot(\rho\mathbf{u}) &=& 0, \\ \partial_t(\rho\mathbf{u}) + \nabla\cdot(\rho\mathbf{u}\otimes\mathbf{u}) + \nabla p &=& \mathbf{J}\times\mathbf{B}, \\ \partial_t\mathcal{E}_T + \nabla\cdot[(\mathcal{E}+p)\,\mathbf{u} + \mathbf{E}\times\mathbf{B}] &=& 0, \\ \partial_t\mathbf{B} + \nabla\times\mathbf{E} &=& 0. \end{cases} \tag{1.89}$$

The Ohm's law from the closure system (1.88) is now

$$\mathbf{E}+\mathbf{u}\times\mathbf{B} = \frac{1}{R_m}\eta\mathbf{J}.$$

The resistive term $\dfrac{1}{R_m}\eta\mathbf{J}$ is of the same order or smaller that the Hall term $c_i\delta_i^*\dfrac{\mathbf{J}\times\mathbf{B}}{n}$. One can therefore ask why this term is kept while the Hall term is neglected. The reason is that in the direction if the magnetic field , the Ohm's law becomes

$$\mathbf{E}\cdot\frac{\mathbf{B}}{|\mathbf{B}|} = \frac{1}{R_m}\eta\mathbf{J}\cdot\frac{\mathbf{B}}{|\mathbf{B}|},$$

and the Hall term, as well as the $\mathbf{u}\times\mathbf{B}$ term, disappears. Thus, the only term that correct the electric field in the parallel direction is the resistivity term. Although small, this term is responsable of some important physical phenomena like for instance magnetic reconnection [79]. To take this into account, R_m is assumed bounded and therefore the Ohm's law writes

$$\mathbf{E}+\mathbf{u}\times\mathbf{B} = \eta\mathbf{J}. \tag{1.90}$$

In order to use finite volume method to solve the resistive MHD equations in Chapter 4, we derive the system (1.89) to get a system as conservative as possible. Then, in the momentum equation, we replace the current $\mathbf{J}$ by the Ampère's law of system (1.88), then the right side of this equation is given by

$$\mathbf{J}\times\mathbf{B} = (\nabla\times\mathbf{B})\times\mathbf{B} = \nabla\cdot(\mathbf{B}\otimes\mathbf{B}) - \nabla\left(\frac{1}{2}\mathbf{B}^2\right).$$

We now introduce the total pressure that is the sum of the hydrodynamical pressure and of the magnetic one with

$$p_T = p + \frac{1}{2}\mathbf{B}^2.$$

We deduce from these results that the momentum equation can be rewritten in the following conservative form

$$\partial_t(\rho\mathbf{u}) + \nabla\cdot[\rho\mathbf{u}\otimes\mathbf{u} - \mathbf{B}\otimes\mathbf{B}] + \nabla p_T = 0. \tag{1.91}$$

In the energy equation, we replace both the electric field $\mathbf{E}$ and the current $\mathbf{J}$ by respectively the Ohm's law (1.90) and the Maxwell-Ampère equation. Thus, the cross product $\mathbf{E} \times \mathbf{B}$ is

$$\mathbf{E} \times \mathbf{B} = \mathbf{B}^2\mathbf{u} - (\mathbf{u} \cdot \mathbf{B})\mathbf{B} + \eta(\nabla \times \mathbf{B}) \times \mathbf{B}.$$

Then we have

$$\partial_t \mathcal{E}_T + \nabla \cdot \left[(\mathcal{E}_T + p_T)\,\mathbf{u} - (\mathbf{u} \cdot \mathbf{B})\mathbf{B} \right] = \nabla \cdot \left(\eta \mathbf{B} \times (\nabla \times \mathbf{B}) \right). \tag{1.92}$$

By using the same process, we first write that

$$\nabla \times \mathbf{E} = \nabla \times (\mathbf{B} \times \mathbf{u} + \eta \mathbf{J}) = \nabla \cdot [\mathbf{B} \otimes \mathbf{u} - \mathbf{u} \otimes \mathbf{B}] - \eta \nabla^2 \mathbf{B} + \nabla \eta \times (\nabla \times \mathbf{B}).$$

Therefore, the Maxwell-Faraday equation is also

$$\partial_t \mathbf{B} + \nabla \cdot [\mathbf{B} \otimes \mathbf{u} - \mathbf{u} \otimes \mathbf{B}] = \eta \nabla^2 \mathbf{B} - \nabla \eta \times (\nabla \times \mathbf{B}). \tag{1.93}$$

With the results (1.91)-(1.93), the system (1.89) becomes

$$\begin{cases} \partial_t \rho + \nabla \cdot (\rho \mathbf{u}) & = & 0, \\ \partial_t (\rho \mathbf{u}) + \nabla \cdot [\rho \mathbf{u} \otimes \mathbf{u} - \mathbf{B} \otimes \mathbf{B}] + \nabla p_T & = & 0, \\ \partial_t \mathcal{E}_T + \nabla \cdot \left[(\mathcal{E}_T + p_T)\,\mathbf{u} - (\mathbf{u} \cdot \mathbf{B})\mathbf{B} \right] & = & \nabla \cdot \left(\eta \mathbf{B} \times (\nabla \times \mathbf{B}) \right), \\ \partial_t \mathbf{B} + \nabla \cdot [\mathbf{B} \otimes \mathbf{u} - \mathbf{u} \otimes \mathbf{B}] & = & \eta \nabla^2 \mathbf{B} - \nabla \eta \times (\nabla \times \mathbf{B}). \end{cases}$$

The numerical test of Chapter 4 will consider an uniform resistivity η. Then the previous system becomes

$$\begin{cases} \partial_t \rho + \nabla \cdot (\rho \mathbf{u}) & = & 0, \\ \partial_t (\rho \mathbf{u}) + \nabla \cdot [\rho \mathbf{u} \otimes \mathbf{u} - \mathbf{B} \otimes \mathbf{B}] + \nabla p_T & = & 0, \\ \partial_t \mathcal{E}_T + \nabla \cdot \left[(\mathcal{E}_T + p_T)\,\mathbf{u} - (\mathbf{u} \cdot \mathbf{B})\mathbf{B} \right] & = & \eta \nabla \cdot \left(\mathbf{B} \times (\nabla \times \mathbf{B}) \right), \\ \partial_t \mathbf{B} + \nabla \cdot [\mathbf{B} \otimes \mathbf{u} - \mathbf{u} \otimes \mathbf{B}] & = & \eta \nabla^2 \mathbf{B}. \end{cases} \tag{1.94}$$

We note that the previous system have been obtained without assuming $m_e \to 0$. The derivation is more general than the ones of [37, 43, 51].

IV.3 Ideal MHD model from small $\delta^*_{e,i}$ and large R_m

The ideal MHD model is the most basic mono-fluid MHD model. This model is usually use to determine equilibrium and properties about the stability of the plasma [42].

i Conservative system

Likewise the resistive MHD model, we still formally consider the limit $\delta^*_{e,i} \to 0$. The difference between the two models comes from the magnetic Reynolds number which is now supposed to be large. The plasma in this model is then considered to be a perfect electric conductor. Ohm's law changes which is now

$$\mathbf{E} + \mathbf{u} \times \mathbf{B} = 0. \tag{1.95}$$

By using the same method as the one for the resistive MHD equations. The conservative form of the ideal MHD equations is given by

$$\begin{cases} \partial_t \rho + \nabla \cdot (\rho \mathbf{u}) & = & 0, \\ \partial_t (\rho \mathbf{u}) + \nabla \cdot [\rho \mathbf{u} \otimes \mathbf{u} - \mathbf{B} \otimes \mathbf{B}] + \nabla p_T & = & 0, \\ \partial_t \mathcal{E}_T + \nabla \cdot \left[(\mathcal{E}_T + p_T)\,\mathbf{u} - (\mathbf{u} \cdot \mathbf{B})\mathbf{B} \right] & = & 0, \\ \partial_t \mathbf{B} + \nabla \cdot [\mathbf{B} \otimes \mathbf{u} - \mathbf{u} \otimes \mathbf{B}] & = & 0. \end{cases} \tag{1.96}$$

We now perform a mathematical study of this system as we have done for the bi-temperature Euler model.

We notice that in system (1.94) and (1.96), the divergence-free constraint on the magnetic field does not appear explicitely. Indeed, this subject will be discuss in Chapter 4.

ii Properties of the ideal MHD model

The mathematical study of the ideal MHD equations is for instance presented in [25, 42]. Here, we will present some properties about the different waves of the system. Likewise the bi-temperature Euler model, the system (1.96) is invariant by rotation. Then, we rewrite the system in the form

$$\begin{cases} \partial_t \rho + \partial_x(\rho u) &= 0, \\ \partial_t(\rho u) + \partial_x(\rho u^2 + p_T - B_1^2) &= 0, \\ \partial_t(\rho v) + \partial_x(\rho uv - B_1 B_2) &= 0, \\ \partial_t(\rho w) + \partial_x(\rho uw - B_1 B_3) &= 0, \\ \partial_t \mathcal{E}_T + \partial_x\left[(\mathcal{E}_T + p_T)u - (\mathbf{u}\cdot\mathbf{B})B_1\right] &= 0, \\ \partial_t B_1 &= 0, \\ \partial_t B_2 + \partial_x\left(uB_2 - vB_1\right) &= 0, \\ \partial_t B_3 + \partial_x\left(uB_3 - wB_1\right) &= 0, \end{cases}$$

where $(u, v, w)^T$ are the component of $\mathbf{u}$, and $(B_1, B_2, B_3)^T$ are the ones of the magnetic field $\mathbf{B}$. According to this system B_1 is constant then we consider the system

$$\partial_t U + \partial_x F(U) = 0,$$

where

$$U = \begin{bmatrix} \rho \\ \rho u \\ \rho v \\ \rho w \\ \mathcal{E}_T \\ B_2 \\ B_3 \end{bmatrix}, \quad F(U) = \begin{bmatrix} \rho u \\ \rho u^2 + p_T - B_1^2 \\ \rho uv - B_1 B_2 \\ \rho uw - B_1 B_3 \\ (\mathcal{E}_T + p_T)u - (\mathbf{u}\cdot\mathbf{B})B_1 \\ uB_2 - vB_1 \\ uB_3 - wB_1 \end{bmatrix}.$$

The Jacobian $A(U) = \partial_U F(U)$ is given by

$$\begin{bmatrix} 0 & 1 & 0 & 0 & 0 & 0 & 0 \\ \frac{\gamma-3}{2}u^2 + \frac{\gamma-1}{2}(v^2+w^2) & (3-\gamma)u & (1-\gamma)v & (1-\gamma)w & \gamma - 1 & (2-\gamma)B_2 & (2-\gamma)B_3 \\ -uv & v & u & 0 & 0 & -B_1 & 0 \\ -uw & w & 0 & u & 0 & 0 & -B_1 \\ a_{51} & a_{52} & a_{53} & a_{54} & \gamma u & a_{56} & a_{57} \\ \frac{vB_1 - uB_2}{\rho} & \frac{B_2}{\rho} & -\frac{B_1}{\rho} & 0 & 0 & u & 0 \\ \frac{wB_1 - uB_3}{\rho} & \frac{B_3}{\rho} & 0 & -\frac{B_1}{\rho} & 0 & u & 0 \end{bmatrix}$$

where

$$\begin{cases} a_{51} &= \left[\dfrac{\gamma-2}{2}\mathbf{u}^2 - \dfrac{c^2}{\gamma-1} - v_a^2 + c_a^2\right]u + \dfrac{B_1B_2}{\rho}v + \dfrac{B_1B_3}{\rho}w, \\ a_{52} &= \dfrac{3-2\gamma}{2}u^2 + \dfrac{v^2+w^2}{2} + v_a^2 - c_a^2, \\ a_{53} &= (1-\gamma)uv - \dfrac{B_1B_2}{\rho}, \\ a_{54} &= (1-\gamma)uw - \dfrac{B_1B_3}{\rho}, \\ a_{56} &= (2-\gamma)uB_2 - vB_1, \\ a_{57} &= (2-\gamma)uB_3 - wB_1, \end{cases}$$

where

$$c^2 = \gamma\frac{p}{\rho},\ c_a^2 = \frac{B_1^2}{\rho},\ v_a^2 = \frac{\mathbf{B}^2}{\rho}.$$

With those results, we have that the Jacobian $A(U)$ is diagonalizable and the eigenvalues are given by

$$\lambda_1 \le \lambda_2 \le \lambda_3 \le \lambda_4 \le \lambda_5 \le \lambda_6 \le \lambda_7,$$

$$\begin{cases} \lambda_{1,7} &= u \mp c_f, \\ \lambda_{2,6} &= u \mp c_a, \\ \lambda_{3,5} &= u \mp c_s, \\ \lambda_4 &= u, \end{cases}$$

where

$$c_{f/s}^2 = \frac{c^2+v_a^2}{2} \pm \frac{1}{2}\sqrt{(c^2+v_a^2)^2 - 4c_s^2c_a^2}. \tag{1.97}$$

The waves of the MHD equations are composed of two fast waves at the speeds λ_1 and λ_7, two Alfvén waves at the speeds λ_2 and λ_6, two slow waves at the speeds λ_3 and λ_5 and an entropy wave at the speed λ_4. All this data are summarized in Figure 1.2. In [25], Brio and Wu explain that as the MHD system is not convex, then the waves can not genuinely non linear or linearly degenerate. Moreover, the Riemann problem solution may contain compound waves or over compressive shocks.

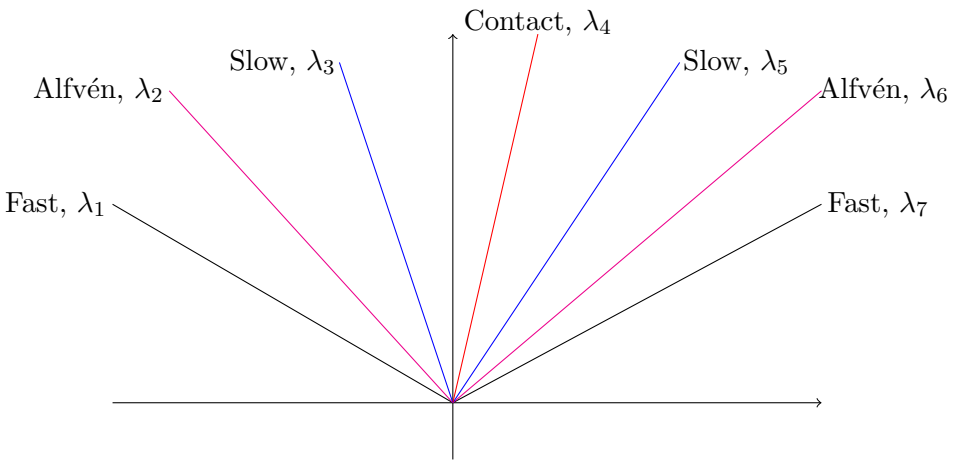

Figure 1.2: Riemann fan of the ideal MHD system.

IV.4 Discussion on the assumptions leading to MHD models

For the ideal and resistive MHD models, we have supposed that the inertial lengths are small. Let us take the example of the *Iter* tokamak. In [37], Friedberg summarizes all the different parameters of this future device for the center of the plasma at page 641. For the edge of the plasma, we use the parameters given in [20] at page 160. With those data, we compute the electronic and ionic inertial lengths values at the center, at the edge of the tokamak and the results are presented in Table 1.1. We also report the ratio $\dfrac{1}{\tau_{ei}+\tau_{ie}}$ given in [68].

At the center and the edge of the plasma, we remark that the inertial length of the ions is not that small, around 10^{-2}. Then, only the transport terms in the Ohm's should be neglected

$$\mathbf{E}+\mathbf{u}\times\mathbf{B}=\frac{1}{R_m}\eta\mathbf{J}+\sqrt{c_i}\delta_i^*\frac{\mathbf{J}\times\mathbf{B}}{n}-\frac{1}{2}\sqrt{c_i}\delta_i^*\frac{1}{n}\nabla p.$$

According to Table 1.1, the magnetic Reynolds number is very large, and the Hall MHD should be a model more appropriate for tokamaks that the ideal or resistive one. However, as many important physical phenomena are occuring in toakamak are well represented by resistive and ideal MHD models, these models are of wide use in this domain and will be considered in this work.

	Center	Edge
$n_0(m^{-3})$	0.91×10^{20}	10^{19}
$T_e(keV)$	11.2	0.04998
$B_0(T)$	5.3	5.3
$\eta_0(\Omega m)$	1.73×10^{-9}	5.82×10^{-6}
$u_0(m.s^{-1})$	1.2115×10^{7}	3.4479×10^{7}
δ_e^*	2.7853×10^{-4}	8.4022×10^{-4}
δ_i^*	1.19×10^{-2}	3.6003×10^{-2}
R_m	1.7559×10^{10}	1.4896×10^{7}
$\dfrac{1}{\tau_{ei}+\tau_{ie}}(s^{-1})$	4×10^{4}	4×10^{4}

Table 1.1: Value of the inertial lengths and resistivity for the tokamak *Iter* at the center, and at the edge of the plasma.

V Conclusions

In this Chapter, starting from a kinetic description of the plasma, we have derived three different fluid models: bi-temperature Euler, ideal MHD, and resistive MHD models. The first one consider the ion-electron mixture as a single fluid but retains two temperature or energy equations to describe the thermodynamics of the mixture. The two others are also mono-fluid models but this time we keep only one energy equation. The derivation of those models corresponds to different asymptotic regimes depending of the values of the parameters β, $\delta_{e,i}^*$, and R_m.

After presenting the finite volume method in Chapter 2, we will present numerical schemes to approximate solutions of these three models in Chapter 3 and 4.

Chapter 2

Finite volume method

This chapter is devoted to finite volume-type methods. First, we give the general form of the method for two different approaches: cell-centered made of rectangles, and vertex-centered with triangular elements. Finally, these two approaches are adapted to the cylindrical coordinates. In fact, in the case of the cell-centered approach, the goal is to write a finite volume method for the toroidal geometry.

I Generalities on finite volume method

After re-calling the principle of finite volume methods, we give two examples in Cartesian coordinates: the cell-centered approach, and the vertex-centered one.

I.1 Principles of finite volume method

Here, we consider a general hyperbolic conservative system written in the form

$$\partial_t U + \nabla \cdot F(U) = 0. \tag{2.1}$$

A tessellation is used to mesh the computational domain. Then, the control cells Ω are constructed. Let Ω be a typical control cell. We suppose that the solution U_Ω^n is known on the control cell Ω at the time t^n. In order to have the solution U_Ω^{n+1} at the time $t^{n+1} = t^n + \Delta t$ where Δt is obtained with a CFL-type condition [41, 53, 73, 45], the equation (2.1) is integrated over $\Omega \times \left[t^n, t^{n+1}\right]$

$$\int_\Omega \int_{t^n}^{t^{n+1}} \partial_t U(\mathbf{x}, t) dt d\Omega + \int_{t^n}^{t^{n+1}} \int_\Omega \nabla \cdot F(U(\mathbf{x}, t)) d\Omega dt = 0,$$

which is equivalent to

$$\int_\Omega U(\mathbf{x}, t^{n+1}) d\Omega - \int_\Omega U(\mathbf{x}, t^n) d\Omega + \int_{t^n}^{t^{n+1}} \int_\Omega \nabla \cdot F(U(\mathbf{x}, t)) d\Omega dt = 0. \tag{2.2}$$

The solution U_Ω^n is defined as the average of U on the control cell Ω

$$U_\Omega^n = \frac{1}{|\Omega|} \int_\Omega U(\mathbf{x}, t^n) dt d\Omega, \ |\Omega| = \int_\Omega d\Omega. \tag{2.3}$$

Hence, the equation (2.2) is equivalent to

$$U_\Omega^{n+1} = U_\Omega^n - \frac{1}{|\Omega|} \int_{t^n}^{t^{n+1}} \int_\Omega \nabla \cdot F(U(\mathbf{x}, t)) d\Omega dt.$$

In our numerical tests, we only use explicit numerical fluxes then we have

$$U_{\Omega}^{n+1} = U_{\Omega}^{n} - \frac{\Delta t}{|\Omega|}\int_{\Omega} \nabla \cdot F(U(\mathbf{x}, t^n))d\Omega. \tag{2.4}$$

The computation of the numerical flux term $\int_{\Omega} \nabla \cdot F(U(\mathbf{x}, t^n))d\Omega$ depends on the approach and of the control cell form. The two next subsections are devoted to the computation of the numerical flux for both cell-centered and vertex-centered approaches.

I.2 2-D cell-centered finite volume on rectangular mesh

The computational domain is a rectangle meshed with quadrangle elements aligned with the x and y-direction. Let N_x, respectively N_y be the number of control cells in the x, respectively y-directions. For $i = 1..N_x$, and $j = 1..N_y$, a typical control cell is now denoted $\Omega_{i,j}$ [41] and shown in Figure 2.1:

$$\Omega_{i,j} = [x_{i-1/2}, x_{i+1/2}] \times [y_{j-1/2}, y_{j+1/2}],\ i = 1..N_x,\ j = 1..N_y.$$

The center point (x_i, y_j) of the cell is given by

$$\begin{cases} x_i &= \dfrac{x_{i-1/2} + x_{i+1/2}}{2}, \quad i = 1..N_x, \\ y_j &= \dfrac{y_{j-1/2} + y_{j+1/2}}{2}, \quad j = 1..N_y. \end{cases} \tag{2.5}$$

We also define the space increments in x and y-directions

$$\begin{cases} \Delta x_i &= x_{i+1/2} - x_{i-1/2}, \quad i = 1..N_x, \\ \Delta y_j &= y_{j+1/2} - y_{j-1/2}, \quad j = 1..N_y. \end{cases}$$

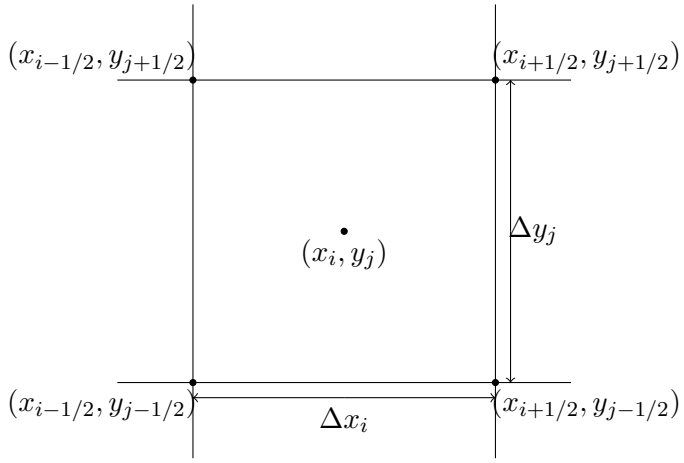

Figure 2.1: Representation of a control cell $\Omega_{i,j}$ in the cell-centered approach.

According to the Cartesian coordinates, we rewrite the divergence as

$$\nabla \cdot F(U) = \partial_x F_x(U) + \partial_y F_y(U).$$

With all this description, we have

$$|\Omega_{i,j}| = \Delta x_i \Delta y_j,$$

and the equation (2.4) becomes

$$\begin{aligned} U_{i,j}^{n+1} = U_{i,j}^{n} &- \frac{\Delta t}{\Delta x_i \Delta y_j} \int_{x_{i-1/2}}^{x_{i+1/2}} \int_{y_{j-1/2}}^{y_{j+1/2}} \partial_x F_x(U) dxdy \\ &- \frac{\Delta t}{\Delta x_i \Delta y_j} \int_{x_{i-1/2}}^{x_{i+1/2}} \int_{y_{j-1/2}}^{y_{j+1/2}} \partial_y F_y(U) dxdy, \end{aligned} \tag{2.6}$$

where $U_{i,j}^n$ is computed with the definition (2.3)

$$U_{i,j}^{n} = \frac{1}{\Delta x_i \Delta y_j} \int_{x_{i-1/2}}^{x_{i+1/2}} \int_{y_{j-1/2}}^{y_{j+1/2}} U(x, y, t^n) dxdy.$$

The equation (2.6) rewrites

$$\begin{aligned} U_{i,j}^{n+1} = U_{i,j}^{n} &- \frac{\Delta t}{\Delta x_i \Delta y_j} \int_{y_{j-1/2}}^{y_{j+1/2}} \left[F_x\Big(U(x_{i+1/2}, y, t^n)\Big) - F_x\Big(U(x_{i-1/2}, y, t^n)\Big) \right] dy \\ &- \frac{\Delta t}{\Delta x_i \Delta y_j} \int_{x_{i-1/2}}^{x_{i+1/2}} \left[F_y\Big(U(x, y_{j+1/2}, t^n)\Big) - F_y\Big(U(x, y_{j-1/2}, t^n)\Big) \right] dx. \end{aligned} \tag{2.7}$$

The numerical fluxes are defined by

$$\begin{aligned} F_{x,i+1/2,j}^{n} &= \frac{1}{\Delta y_j} \int_{y_{j-1/2}}^{y_{j+1/2}} F_x\Big(U(x_{i+1/2}, y, t^n)\Big) dy, \\ F_{y,i,j+1/2}^{n} &= \frac{1}{\Delta x_i} \int_{x_{i-1/2}}^{x_{i+1/2}} F_y\Big(U(x, y_{j+1/2}, t^n)\Big) dx. \end{aligned}$$

Those numerical fluxes are obtained with a Riemann type scheme in the numerical tests. Finally, the finite volume method for this 2-D cell-centered geometry is

$$U_{i,j}^{n+1} = U_{i,j}^{n} - \frac{\Delta t}{\Delta x_i} \left(F_{x,i+1/2,j}^{n} - F_{x,i-1/2,j}^{n} \right) - \frac{\Delta t}{\Delta y_j} \left(F_{y,i,j+1/2}^{n} - F_{y,i,j-1/2}^{n} \right).$$

In this case, the CFL condition is given by

$$\lambda_{max} \frac{\Delta t}{h_{min}} \leq 1.$$

There are a large various ways of choosing the coefficient λ_{max} [12, 31, 74]. For instance, this coefficient λ_{max} can be defined as the maximum of wave all over the computational domain. Indeed, for a cell $\Omega_{i,j}$, we denote

$$\lambda_{max,i,j} = \max_{\lambda \in Sp(A_{i,j}^n)} (|\lambda|), \;\; A_{i,j}^n = \partial_U F(U_{i,j}^n).$$

Then we have

$$\lambda_{max} = \max_{i=1..N_x, j=1..N_y} (\lambda_{max,i,j}). \tag{2.8}$$

The variable h_{min} is given by

$$h_{min} = \min(\Delta x_{min}, \Delta y_{min}), \;\; \Delta x_{min} = \min_{i=1..N_x} (\Delta x_i), \;\; \Delta y_{min} = \min_{j=1..N_y} (\Delta y_j).$$

In Chapter 4, the numerical tests are also performed at the second order in space for the cell-centered approaches. Here, the second order is based on MUSCL-type method [76, 41]. It consists to use a piecewise linear reconstruction of the solution U instead of a piecewise constant solution. Figure 2.2 gives a 1-D example of such a reconstruction. In 2-D Cartesian geometry, then the linear solution on the control cell $\Omega_{i,j}$ is given by

$$U_{i,j}(x,y) = U^n_{i,j} + (x - x_i)\delta_x U_{i,j} + (y - y_j)\delta_y U_{i,j},$$

with

$$\left\{ \begin{array}{rcl} \delta_x U_{i,j} & = & \dfrac{U^n_{i+1,j} - U^n_{i-1,j}}{x_{i+1} - x_{i-1}}, \\ \\ \delta_y U_{i,j} & = & \dfrac{U^n_{i,j+1} - U^n_{i,j-1}}{y_{j+1} - y_{j-1}}. \end{array} \right. \tag{2.9}$$

At the first order in space, the numerical fluxes $F^n_{i+1/2,j}$ and $F^n_{i,j+1/2}$ are computed with Riemann-type flux. In other words, to determine $F^n_{i+1/2,j}$ at the interface $(x_{i+1/2}, y_j)$ we consider the Riemann problem $(U^n_{i,j}, U^n_{i+1,j})$. At second order in space, the left and right state of the Riemann problem are now $(U^-_{i+1/2,j}, U^+_{i+1/2,j})$ where

$$\left\{ \begin{array}{rcccl} U^-_{i+1/2,j} & = & U_{i,j}(x_{i+1/2}, y_j) & = & U^n_{i,j} + \dfrac{\Delta x_i}{2}\delta_x U_{i,j}, \\ \\ U^+_{i+1/2,j} & = & U_{i+1,j}(x_{i+1/2}, y_j) & = & U^n_{i+1,j} - \dfrac{\Delta x_{i+1}}{2}\delta_x U_{i+1,j}. \end{array} \right.$$

However, some physical properties, such as the positivity of densities and pressures, have to be preserved during the reconstruction of the solution. Then, we use the *minmod* limiter: the coefficient $\partial_x U_{i,j}$ of (2.9) is re-computed with

$$\partial_x U_{i,j} = minmod\left(\partial_x U_{i,j}, \frac{U^n_{i+1,j} - U^n_{i,j}}{x_{i+1} - x_i}, \frac{U^n_{i,j} - U^n_{i-1,j}}{x_i - x_{i-1}}\right),$$

where the *minmod* function is

$$minmod(a,b,c) = \min(0, \max(a,b,c)) + \max(0, \min(a,b,c)).$$

Likewise the x-direction, the two states at the interface $(x_i, y_{j+1/2})$ are denoted $U^-_{i,j+1/2}$, and $U^+_{i,j+1/2}$ and are given by

$$\left\{ \begin{array}{rcccl} U^-_{i,j+1/2} & = & U_{i,j}(x_i, y_{j+1/2}) & = & U^n_{i,j} + \dfrac{\Delta y_j}{2}\delta_y U_{i,j}, \\ \\ U^+_{i,j+1/2} & = & U_{i,j+1}(x_i, y_{j+1/2}) & = & U^n_{i,j+1} - \dfrac{\Delta y_{j+1}}{2}\delta_y U_{i,j+1}. \end{array} \right.$$

where we also limit $\delta_y U_{i,j}$ with the *minmod* function

$$\delta_y U_{i,j} = minmod\left(\delta_y U_{i,j}, \frac{U^n_{i,j+1} - U^n_{i,j}}{y_{j+1} - y_j}, \frac{U^n_{i,j} - U^n_{i,j-1}}{y_j - y_{j-1}}\right).$$

Usually, a second order in space scheme is also coupled to a second order time method. In the numerical implementation, we use the following second order Runge-Kutta-type method for the time integration. Knowing the solution U^n_i at the time t^n, we first compute

$U_i^{'}$ with (2.7). Then, we re-use this formula (2.7) in which we have replaced U_i^n by $U_i^{'}$ and the numerical fluxes are obtained from the states $U_i^{'}$. The result of this second step is called $U_i^{''}$. Finally, the solution U_i^{n+1} at the time t^{n+1} is given by

$$U_i^{n+1} = \frac{1}{2}\left(U_i^n + U_i^{''}\right).$$

Remark: For the ideal MHD equations, the equations on the x and y-components of the magnetic field are given by:

$$\left\{\begin{array}{lcccl} \partial_t B_x & & + & \partial_y(vB_x - uB_y) & = 0, \\ \partial_t B_y & + \partial_x(uB_y - vB_x) & & & = 0. \end{array}\right.$$

Since B_x, respectively B_y does not have a x-derivative, respectively an y-one, then, the variable B_x, respectively B_y is not reconstructed in the x-direction, respectively the y-direction.

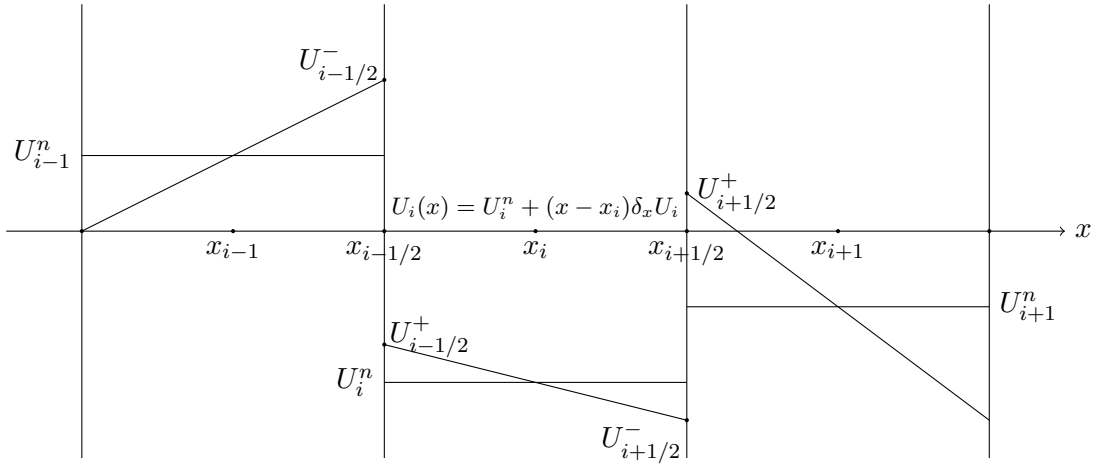

Figure 2.2: Piecewise linear reconstruction for the 1-D case.

I.3 2-D vertex-centered finite volume on a triangular mesh

Here, we consider a triangulation of the computational domain. We denote N_τ the number of triangles and N_p the number of points in the mesh. For the vertex-centered approach [41, 78, 45], the control cells are constructed in the following way. Let us first consider a vertex i, with $i = 1..N_p$, the control cell associated is denoted Ω_i. Then,

$$\Omega_i = \bigcup_{\tau \in \mathcal{V}^\tau(i)} \Omega_i^\tau,$$

where $\mathcal{V}^\tau(i)$ is the set of the triangles in which i is a vertex, and Ω_i^τ is a subset of the triangle τ. To build Ω_i^τ, the triangle τ is divided in six equal triangles, which means that those triangles are formed with the three medians of the triangle. Then, Ω_i^τ is given by the two resulting triangles which share the vertex i (see Figure 2.3). Thus the surface of the control cell is

$$|\Omega_i| = \frac{1}{3}\sum_{\tau \in \mathcal{V}^\tau(i)} |\tau|, \tag{2.10}$$

where $|\tau|$ is the surface of the triangle τ.

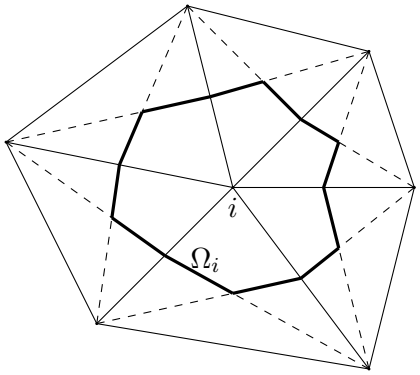

Figure 2.3: Representation of a control cell Ω_i in the vertex-centered approach.

Concerning the flux term of (2.4), we have

$$\int_{\Omega_i} \nabla \cdot F\Big(U(\mathbf{x}, t^n)\Big) d\Omega = \int_{\partial\Omega_i} F(U)\mathbf{n} d(\partial\Omega),$$

where $\partial\Omega_i$ is the boundary of the control cell Ω_i. According to the Figure 2.3, $\partial\Omega_i$ is

$$\partial\Omega_i = \bigcup_{j\in\mathcal{V}(i)} \partial\Omega_{ij},$$

where $\mathcal{V}(i)$ is the set of the neighbor point of i, and

$$\partial\Omega_{ij} = \Omega_i \bigcap \Omega_j, \ j \in \mathcal{V}(i).$$

Hence we have

$$\int_{\Omega_i} \nabla \cdot F\Big(U(\mathbf{x}, t)\Big) d\Omega = \sum_{j\in\mathcal{V}(i)} \int_{\partial\Omega_{ij}} F(U)\mathbf{n} d(\partial\Omega).$$

The numerical flux is defined as

$$F_{ij}(U_i^n, U_j^n, \mathbf{n}_{ij}) = \frac{1}{|\partial\Omega_{ij}|} \int_{\partial\Omega_{ij}} F(U)\mathbf{n} d(\partial\Omega), \ |\partial\Omega_{ij}| = \int_{\partial\Omega_{ij}} d(\partial\Omega),$$

where

$$\mathbf{n}_{ij} = \frac{1}{\| \int_{\partial\Omega_{ij}} \mathbf{n} d\partial\Omega \|} \int_{\partial\Omega_{ij}} \mathbf{n} d\partial\Omega. \tag{2.11}$$

Finally the finite volume scheme for this vertex-centered approach is

$$U_i^{n+1} = U_i^n - \sum_{j\in\mathcal{V}(i)} \frac{\Delta t |\partial\Omega_{ij}|}{|\Omega_i|} F(U_i^n, U_j^n, \mathbf{n}_{ij}),$$

where the numerical fluxes are computed with a Riemann type scheme. The CFL condition is given by

$$\lambda_{max} \max_{i,j=1..N_p} \left(\frac{|\partial\Omega_{ij}|}{|\Omega_i|} \right) \Delta t \leq 1.$$

Likewise the cell-centered approach, the numerical tests using the vertex-centered approach have been performed at the second order in space. To do so, we still base the reconstruction method on a MUSCL-type method. According to [45], for i and j two

neighboring points, the initial data (U_{ij}^-, U_{ji}^+) used to compute the numerical fluxes at the interface are given by

$$\begin{cases} U_{ij}^- &= U_i^n + \dfrac{1}{2}(\nabla U)_i \cdot (\overrightarrow{ij}), \\ U_{ji}^+ &= U_j^n - \dfrac{1}{2}(\nabla U)_j \cdot (\overrightarrow{ij}). \end{cases}$$

It exists several ways to compute the gradient $(\nabla U)_i$, in numerical simulations the average nodal gradient is chosen:

$$(\nabla U)_i = \frac{1}{|\Omega_i|} \sum_{\tau \in \mathcal{V}^\tau(i)} \nabla U|_\tau |\tau|.$$

Finally, the *minmod* limiter is applied to correct the gradient and to insure positive densities and pressures. Once again, a second order Runge-Kutta method is used for the time integration.

II Cell-centered approach for cylindrical coordinates

By keeping in mind the tokamak application, we are now interested in the adaptation of the cell-centered approach to the cylindrical coordinates. All the computations of this section are given for the ideal MHD equations (1.96) case.

II.1 Ideal MHD equations in cylindrical coordinates

In Figure 2.4, the cylindrical coordinates are denoted (R, φ, Z), the canonical basis is $(\mathbf{e}_R, \mathbf{e}_\varphi, \mathbf{e}_Z)$, and a vector $\mathbf{A}$ is represented by

$$\mathbf{A} = A_R \mathbf{e}_R + A_\varphi \mathbf{e}_\varphi + A_Z \mathbf{e}_Z.$$

Let us now consider two vectors $\mathbf{A}$ and $\mathbf{B}$, the tensorial product is given by

$$\mathbf{A} \otimes \mathbf{B} = \begin{bmatrix} A_R B_R & A_R B_\varphi & A_R B_Z \\ A_\varphi B_R & A_\varphi B_\varphi & A_\varphi B_Z \\ A_Z B_R & A_Z B_\varphi & A_Z B_Z \end{bmatrix}.$$

Let $\overline{\overline{T}}$ be a tensor given by

$$\overline{\overline{T}} = \begin{bmatrix} T_{RR} & T_{R\varphi} & T_{RZ} \\ T_{\varphi R} & T_{\varphi\varphi} & T_{\varphi Z} \\ T_{ZR} & T_{Z\varphi} & T_{ZZ} \end{bmatrix},$$

then, the divergence of tensor is

$$\begin{cases} \left(\nabla \cdot \overline{\overline{T}}\right)_R &= \dfrac{1}{R}\partial_R(RT_{RR}) + \dfrac{1}{R}\partial_\varphi T_{R\varphi} + \partial_Z T_{RZ} - \dfrac{1}{R}T_{\varphi\varphi}, \\ \left(\nabla \cdot \overline{\overline{T}}\right)_\varphi &= \dfrac{1}{R}\partial_R(RT_{\varphi R}) + \dfrac{1}{R}\partial_\varphi T_{\varphi\varphi} + \partial_Z T_{\varphi Z} + \dfrac{1}{R}T_{R\varphi}, \\ \left(\nabla \cdot \overline{\overline{T}}\right)_Z &= \dfrac{1}{R}\partial_R(RT_{ZR}) + \dfrac{1}{R}\partial_\varphi T_{Z\varphi} + \partial_Z T_{ZZ}. \end{cases} \tag{2.12}$$

The translation invariance $\partial_Z \cdot = 0$ is assumed, then the ideal MHD equations (1.96) writes

$$\begin{cases} \partial_t(R\rho) + \partial_R(R\rho u_R) + \partial_\varphi(\rho u_\varphi) = 0, \\ \partial_t(R\rho u_R) + \partial_R\left[R\left(\rho u_R^2 + p_T - B_R^2\right)\right] + \partial_\varphi\left[\rho u_R u_\varphi - B_R B_\varphi\right] = \rho u_\varphi + p_T - B_\varphi^2, \\ \partial_t(R\rho u_\varphi) + \partial_R\left[R\left(\rho u_R u_\varphi - B_R B_\varphi\right)\right] + \partial_\varphi\left[\rho u_\varphi + p_T - B_\varphi^2\right] = -\left(\rho u_R u_\varphi - B_R B_\varphi\right), \\ \partial_t(R\rho u_Z) + \partial_R\left[R\left(\rho u_R u_Z - B_R B_Z\right)\right] + \partial_\varphi\left[\rho u_\varphi u_Z - B_\varphi B_Z\right] = 0, \\ \partial_t(R\mathcal{E}_T) + \partial_R\Big[R\Big((\mathcal{E}_T + p_T)u_R - (\mathbf{u}\cdot\mathbf{B})B_R\Big)\Big] + \partial_\varphi\Big[(\mathcal{E}_T + p_T)u_\varphi - (\mathbf{u}\cdot\mathbf{B})B_\varphi\Big] = 0, \\ \partial_t(RB_R) + \partial_\varphi\left(u_\varphi B_R - u_R B_\varphi\right) = 0, \\ \partial_t(RB_\varphi) + \partial_R\left[R\left(u_R B_\varphi - u_\varphi B_R\right)\right] = u_R B_\varphi - u_\varphi B_R, \\ \partial_t(RB_Z) + \partial_R\left[R\left(u_R B_Z - u_Z B_R\right)\right] + \partial_\varphi\left(u_\varphi B_Z - u_Z B_\varphi\right) = 0. \end{cases} \tag{2.13}$$

This system has some artificial source terms, and in order to suppress some of them, the tangential momentum equation is multiplied by R and yields to

$$\partial_t(R^2\rho u_\varphi) + \partial_R\left[R^2\left(\rho u_R u_\varphi - B_R B_\varphi\right)\right] + \partial_\varphi\left[R\left(\rho u_\varphi^2 + p_T - B_\varphi\right)\right] = 0. \tag{2.14}$$

By developing the R-derivative in the tangential magnetic field equation, we also obtain a source term-free equation

$$\partial_t B_\varphi + \partial_R(u_R B_\varphi - B_\varphi u_R) = 0. \tag{2.15}$$

Up to our knowledge, a process to suppress the source term of the radial momentum equation can not be applied. By replacing, the tangential momentum and tangential magnetic field equations of (2.13) by the equations (2.14) and (2.15), we obtain the following system

$$\begin{cases} \partial_t(R\rho) + \partial_R(R\rho u_R) + \partial_\varphi(\rho u_\varphi) = 0, \\ \partial_t(R\rho u_R) + \partial_R\left[R\left(\rho u_R^2 + p_T - B_R^2\right)\right] + \partial_\varphi\left[\rho u_R u_\varphi - B_R B_\varphi\right] = \rho u_\varphi + p_T - B_\varphi^2, \\ \partial_t(R^2\rho u_\varphi) + \partial_R\left[R^2\left(\rho u_R u_\varphi - B_R B_\varphi\right)\right] + \partial_\varphi\left[R\left(\rho u_\varphi^2 + p_T - B_\varphi\right)\right] = 0, \\ \partial_t(R\rho u_Z) + \partial_R\left[R\left(\rho u_R u_Z - B_R B_Z\right)\right] + \partial_\varphi\left[\rho u_\varphi u_Z - B_\varphi B_Z\right] = 0, \\ \partial_t(R\mathcal{E}_T) + \partial_R\Big[R\Big((\mathcal{E}_T + p_T)u_R - (\mathbf{u}\cdot\mathbf{B})B_R\Big)\Big] + \partial_\varphi\Big[(\mathcal{E}_T + p_T)u_\varphi - (\mathbf{u}\cdot\mathbf{B})B_\varphi\Big] = 0, \\ \partial_t(RB_R) + \partial_\varphi\left(u_\varphi B_R - u_R B_\varphi\right) = 0, \\ \partial_t B_\varphi + \partial_R\left(u_R B_\varphi - u_\varphi B_R\right) = 0, \\ \partial_t(RB_Z) + \partial_R\left[R\left(u_R B_Z - u_Z B_R\right)\right] + \partial_\varphi\left(u_\varphi B_Z - u_Z B_\varphi\right) = 0. \end{cases} \tag{2.16}$$

The previous system is written in the following form

$$\partial_t U + \partial_R F_R(U) + \partial_\varphi F_\varphi(U) = S(U),$$

where

$$\left\{\begin{array}{rcl} U & = & \begin{bmatrix} R\rho \\ R\rho u_R \\ R^2\rho u_\varphi \\ R\rho u_Z \\ R\mathcal{E}_T \\ RB_R \\ B_\varphi \\ RB_Z \end{bmatrix}, \qquad F_R(U) \;=\; \begin{bmatrix} R\rho u_R \\ R(\rho u_R^2 + p_T - B_R^2) \\ R^2(\rho u_R u_\varphi - B_R B_\varphi) \\ R(\rho u_R u_Z - B_R B_Z) \\ R[(\mathcal{E}_T + p_T)u_R - (\mathbf{u}\cdot\mathbf{B})B_R] \\ 0 \\ u_R B_\varphi - u_\varphi B_R \\ R(u_R B_Z - u_Z B_R) \end{bmatrix}, \\ S(U) & = & \begin{bmatrix} 0 \\ \rho u_\varphi^2 + p_T - B_\varphi^2 \\ 0 \\ 0 \\ 0 \\ 0 \\ 0 \\ 0 \end{bmatrix}, \quad F_\theta(U) \;=\; \begin{bmatrix} \rho u_\varphi \\ \rho u_R u_\varphi - B_R B_\varphi \\ R(\rho u_\varphi^2 + p_T - B_\varphi^2) \\ \rho u_\varphi u_Z - B_\varphi B_Z \\ (\mathcal{E}_T + p_T)u_\varphi - (\mathbf{u}\cdot\mathbf{B})B_\varphi \\ u_\varphi B_R - u_R B_\varphi \\ 0 \\ u_\varphi B_Z - u_Z B_\varphi \end{bmatrix}. \end{array}\right. \tag{2.17}$$

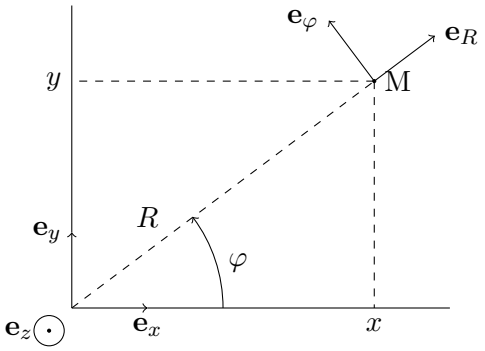

Figure 2.4: Cartesian and cylindrical basis representation.

II.2 Cell-centered approach in a circular mesh

After writing the ideal MHD equations in the cylindrical coordinate system, a finite volume-type method using the cell-centered approach is designed to approximate the solution of the MHD system. The computational domain is now a disc still meshed with quadrangle elements aligned with the R and φ-directions. N_R represents the number of cells in the R-direction and N_φ is the φ-one. Then a typical control cell $\Omega_{i,j}$ is shown in Figure 2.5 for $i = 1..N_R$, and $j = 1..N_\varphi$. The vertex of the control cells are denoted $\left(R_{i+1/2}\right)_{0\le i\le N_R}$, and $\left(\varphi_{j+1/2}\right)_{0\le j\le N_\varphi}$ where

$$\begin{array}{ccccccccccccc} 0 & \le & R_{1/2} & \le & \cdots & \le & R_{i+1/2} & \le & \cdots & \le & R_{N_R+1/2}, & & \\ 0 & = & \varphi_{1/2} & \le & \cdots & \le & \varphi_{j+1/2} & \le & \cdots & \le & \varphi_{N_\varphi+1/2} & = & 2\pi, \end{array}$$

where periodic boundary conditions are used in the φ-direction. Using the definition (2.5), the cell center in cylindrical coordinates is given by

$$\left\{\begin{array}{rcll} R_i & = & \dfrac{R_{i-1/2} + R_{i+1/2}}{2}, & i = 1..N_R, \\ \varphi_j & = & \dfrac{\varphi_{j-1/2} + \varphi_{j+1/2}}{2}, & j = 1..N_\varphi. \end{array}\right.$$

According to (2.16), the 2-D ideal MHD equations in cylindrical coordinates can be written in three different forms

$$\left\{\begin{array}{lcll} \partial_t u + \partial_R f_R(u) + \partial_\varphi f_\varphi(u) & = & s(u), & u = B_\varphi, \\ \partial_t (Ru) + \partial_R (R f_R(u)) + \partial_\varphi f_\varphi(u) & = & s(u), & u \in \{\rho, \rho u_R, \rho u_Z, \mathcal{E}_T, B_R, B_Z\}, \\ \partial_t (R^2 u) + \partial_R (R^2 f_R(u)) + \partial_\varphi (R f_\varphi(u)) & = & s(u), & u = \rho u_\varphi, \end{array}\right. \tag{2.18}$$

where $f_R(u)$, $f_\varphi(u)$, and $s(u)$ are the corresponding values given in (2.17). The three forms of the cylindrical equations leads us to define the space increments by

$$\left\{\begin{array}{lcl} (\Delta R)_{i,k} & = & \displaystyle\int_{R_{i-1/2}}^{R_{i+1/2}} R^k dR, \quad i = 1...N_R, \quad k = 0...2, \\ (\Delta\varphi)_j & = & \varphi_{j+1/2} - \varphi_{j-1/2}, \quad j = 1...N_\varphi. \end{array}\right. \tag{2.19}$$

The first equation of (2.18), has the same form as a Cartesian one with a source term. Then, by integrating this equation over $\Omega_{i,j} \times [t^n, t^{n+1}]$ for $i = 1...N_R$ and $j = 1...N_\varphi$, we have

$$(\Delta R)_{i,0}(\Delta\varphi)_j (u_{i,j}^{n+1} - u_{i,j}^n) + \Delta t (\Delta\varphi)_j \left[f_{R,i+1/2,j}^n(u) - f_{R,i-1/2,j}^n(u) \right]$$

$$+\Delta t (\Delta R)_{i,0} \left[f_{\varphi,i,j+1/2}^n(u) - f_{\varphi,i,j-1/2}^n(u) \right] = \int_{\Omega_{i,j}} \int_{t^n}^{t^{n+1}} s\Big(u(R,\varphi,t)\Big) dt dR d\varphi,$$

where the average solution $u_{i,j}^n$ and the numerical fluxes $f_{R,i+1/2,j}^n$ and $f_{\varphi,i,j+1/2}^n$ are given by

$$\left\{\begin{array}{lcl} u_{i,j}^n & = & \displaystyle\frac{1}{(\Delta R)_{i,0}(\Delta\varphi)_j} \int_{\Omega_{i,j}} u(R,\varphi,t^n) dR d\varphi, \\ f_{R,i+1/2,j}^n(u) & = & \displaystyle\frac{1}{(\Delta\varphi)_j} \int_{\varphi_{j-1/2}}^{\varphi_{j+1/2}} f_R\Big(u(R_{i+1/2},\varphi,t^n)\Big) d\varphi, \\ f_{\varphi,i,j+1/2}(u) & = & \displaystyle\frac{1}{(\Delta R)_{i,0}} \int_{R_{i-1/2}}^{R_{i+1/2}} f_\varphi\Big(u(R,\varphi_{j+1/2},t^n)\Big) dR. \end{array}\right. \tag{2.20}$$

The time integral of the source term is evaluated in t^n, then we have

$$s_{i,j}^n(u) = \frac{1}{(\Delta R)_{i,0}(\Delta\varphi)_j} \int_{\Omega_{i,j}} s\Big(u(R,\varphi,t^n)\Big) dR d\varphi. \tag{2.21}$$

Finally, the finite volume method in cylindrical coordinates writes

$$\begin{array}{rcl} u_{i,j}^{n+1} = u_{i,j}^n & - & \displaystyle\frac{\Delta t}{(\Delta R)_{i,0}} \left[f_{R,i+1/2,j}^n(u) - f_{R,i-1/2,j}^n(u) \right] \\ & - & \displaystyle\frac{\Delta t}{(\Delta\varphi)_j} \left[f_{\varphi,i,j+1/2}^n(u) - f_{\varphi,i,j-1/2}^n(u) \right] + \Delta t \; s_{i,j}^n(u). \end{array} \tag{2.22}$$

Let us now focus on the second equation of (2.18), we integrate it over $\Omega_{i,j} \times [t^n, t^{n+1}]$

$$\int_{\Omega_{i,j}} \int_{t^n}^{t^{n+1}} R \partial_t u(R,\varphi,t) dt dR d\varphi + \int_{t^n}^{t^{n+1}} \int_{\Omega_{i,j}} \partial_R \Big(R f_R\Big(u(R,\varphi,t)\Big) \Big) dR d\varphi dt$$

$$\int_{t^n}^{t^{n+1}} \int_{\Omega_{i,j}} \partial_\varphi f_\varphi\Big(u(R,\varphi,t)\Big) dR d\varphi dt = \int_{t^n}^{t^{n+1}} \int_{\Omega_{i,j}} s\Big(u(R,\varphi,t)\Big) dR d\varphi dt.$$

Then, we have for explicit numerical fluxes:

$$\int_{\Omega_{i,j}} u(R,\varphi,t^{n+1})RdRd\varphi - \int_{\Omega_{i,j}} u(R,\varphi,t^{n})RdRd\varphi$$

$$+\Delta t \int_{\varphi_{j-1/2}}^{\varphi_{j+1/2}} \Big[R_{i+1/2} f_R\Big(u(R_{i+1/2},\varphi,t^n)\Big) - R_{i-1/2} f_R\Big(u(R_{i-1/2},\varphi,t^n)\Big)\Big] d\varphi$$

$$+\Delta t \int_{R_{i-1/2}}^{R_{i+1/2}} \Big[f_\varphi\Big(u(R,\varphi_{j+1/2},t)\Big) - f_\varphi\Big(u(R,\varphi_{j-1/2},t)\Big)\Big] dR$$

$$= \int_{t^n}^{t^{n+1}} \int_{\Omega_{i,j}} s\Big(u(R,\varphi,t)\Big) dRd\varphi dt.$$

In this case, we deduce that the average solution $u_{i,j}^n$ is

$$u_{i,j}^n = \frac{1}{(\Delta R)_{i,1}(\Delta\varphi)_j} \int_{\Omega_{i,j}} u(R,\varphi,t^n)RdRd\varphi.$$

The explicit numerical fluxes and the source term are still defined by the relation (2.20) and (2.21).Finally, the numerical scheme writes

$$\begin{aligned} u_{i,j}^{n+1} = u_{i,j}^n \quad &- \quad \frac{\Delta t}{(\Delta R)_{i,1}}\Big[R_{i+1/2} f_{R,i+1/2,j}(u) - R_{i-1/2} f_{R,i-1/2,j}(u)\Big] \\ &- \quad \frac{\Delta t}{(\Delta\varphi)_j}\frac{(\Delta R)_{i,0}}{(\Delta R)_{i,1}}\Big[f_{\varphi,i,j+1/2}(u) - f_{\varphi,i,j-1/2}(u)\Big] \\ &+ \quad \Delta t \frac{(\Delta R)_{i,0}}{(\Delta R)_{i,1}} s_{i,j}^n(u). \end{aligned} \tag{2.23}$$

For the last equation of (2.18), we use the same method as the two previous ones. We obtain that the finite volume method is

$$\begin{aligned} u_{i,j}^{n+1} = u_{i,j}^n \quad &- \quad \frac{\Delta t}{(\Delta R)_{i,2}}\Big[R_{i+1/2}^2 f_{R,i+1/2,j}^n(u) - R_{i-1/2}^2 f_{R,i-1/2,j}^n(u)\Big] \\ &- \quad \frac{\Delta t}{(\Delta\varphi)_j}\frac{(\Delta R)_{i,1}}{(\Delta R)_{i,2}}\Big[f_{\varphi,i,j+1/2}^n(u) - f_{\varphi,i,j-1/2}^n(u)\Big] \\ &+ \quad \Delta t \frac{(\Delta R)_{i,0}}{(\Delta R)_{i,2}} s_{i,j}^n(u), \end{aligned} \tag{2.24}$$

where

$$\begin{cases} u_{i,j}^n & = \dfrac{1}{(\Delta R)_{i,2}(\Delta\varphi)_j} \displaystyle\int_{\Omega_{i,j}} u(R,\varphi,t^n)R^2 dRd\varphi, \\ f_{\varphi,i,j+1/2}^n(u) & = \dfrac{1}{(\Delta R)_{i,1}} \displaystyle\int_{R_{i-1/2}}^{R_{i+1/2}} f_\varphi\Big(u(R,\varphi_{j+1/2},t^n)\Big) RdR, \end{cases}$$

the radial numerical flux $f_{R,i+1/2,j}^n(u)$, and the source term $s_{i,j}^n(u)$ are given by (2.20) and (2.21).

The relations (2.22)-(2.24) can be generalized with the following formula

$$\begin{aligned} u_{i,j,k}^{n+1} = u_{i,j,k}^{n} \quad &- \quad \frac{\Delta t}{(\Delta R)_{i,k}} \left[R_{i+1/2}^{k} f_{R,i+1/2,j}^{n}(u) - R_{i-1/2}^{k} f_{R,i-1/2,j}^{n}(u) \right] \\ &- \quad \mu_{i,k} \frac{\Delta t}{(\Delta \varphi)_j} \left[f_{\varphi,i,j+1/2,k}^{n}(u) - f_{\varphi,i,j-1/2,k}^{n}(u) \right] \\ &+ \quad \Delta t \frac{(\Delta R)_{i,0}}{(\Delta R)_{i,k}} s_{i,j}^{n}(u), \;\; k = 0..2, \end{aligned} \tag{2.25}$$

where the average solution on $\Omega_{i,j}$ is

$$u_{i,j,k}^{n} = \frac{1}{(\Delta R)_{i,k}(\Delta \varphi)_j} \int_{R_{i-1/2}}^{R_{i+1/2}} \int_{\varphi_{j-1/2}}^{\varphi_{j+1/2}} u\left(R, \varphi, t^n\right) R^k dR d\varphi.$$

The numerical fluxes are given by

$$f_{R,i+1/2,j}^{n}(u) = \frac{1}{(\Delta \varphi)_j} \int_{\varphi_{j-1/2}}^{\varphi_{j+1/2}} f_R\Big(u(R_{i+1/2}, \varphi, t^n)\Big) d\varphi,$$

$$f_{\varphi,i,j+1/2,k}^{n}(u) = \begin{cases} \dfrac{1}{(\Delta R)_{i,0}} \displaystyle\int_{R_{i-1/2}}^{R_{i+1/2}} f_\varphi\Big(u(R, \varphi_{j+1/2}, t^n)\Big) dR, & k = 0, \\ \dfrac{1}{(\Delta R)_{i,k-1}} \displaystyle\int_{R_{i-1/2}}^{R_{i+1/2}} f_\varphi\Big(u(R, \varphi_{j+1/2}, t^n)\Big) R^{k-1} dR, & k = 1, 2. \end{cases}$$

The source term is

$$s_{i,j}^{n}(u) = \frac{1}{(\Delta R)_{i,0}(\Delta \varphi)_j} \int_{R_{i-1/2}}^{R_{i+1/2}} \int_{\varphi_{j-1/2}}^{\varphi_{j+1/2}} s\Big(u\left(R, \varphi, t^n\right)\Big) dR d\varphi.$$

Finally, the function $\mu_{i,k}$ is defined by

$$\mu_{i,k} = \begin{cases} 1, & k = 0, \\ \dfrac{(\Delta R)_{i,k-1}}{(\Delta R)_{i,k}}, & k = 1, 2. \end{cases}$$

According to (2.25), the CFL condition is given by

$$\lambda_{max} \frac{\Delta t}{h_{min}} \leq 1,$$

where λ_{max} is the one of relation (2.8), and h_{min} is

$$h_{min} = \min_{i=1..N_R, j=1..N_\varphi, k=0..2} \left((\Delta R)_{i,k}, \frac{(\Delta \varphi)_j}{\mu_{i,k}} \right).$$

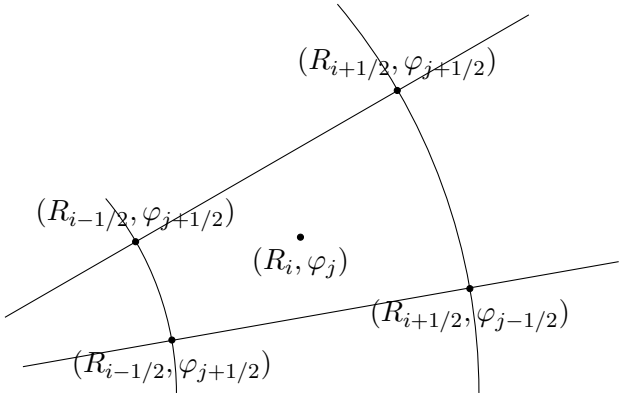

Figure 2.5: Representation of a cell $\Omega_{i,j}$ in the cylindrical coordinates for the cell-centered approach.

III Vertex-centered approach for the toroidal geometry

After presenting the adaptation of the cell-centered approach to the cylindrical coordinates, we now focus to write a vertex-centered finite volume-type method for a fully 3-D toroidal geometry. First, the mathematical and geometrical properties of a torus are used to design the 3-D mesh. Finally, we give the computations related to volume, surface, and unitary normal necessary to write the finite volume method.

III.1 Cylindrical coordinates for toroidal problem and divergence form

The toroidal geometry is particularly useful for simulations taking place in a tokamak. Indeed, a tokamak can be modeled as a 2-D plane in rotation about an axis [18]. The 2-D plane is named poloidal plane. Hence, the axisymetric feature of a tokamak makes pertinent to use cylindrical coordinates.

Let us consider the Cartesian coordinates of a tokamak point $\mathbf{x} = (x, y, z)^T$. The relation between its Cartesian coordinates and its cylindrical coordinates $(R, Z, \varphi)^T$ is given by

$$\left\{ \begin{array}{rcl} x & = & R\cos\varphi, \\ y & = & R\sin\varphi, \\ z & = & Z, \end{array} \right.$$

where $R \in \mathbb{R}_+^*$, $\varphi \in [0, 2\pi[$, and $Z \in \mathbb{R}$.

The mapping $\Psi : \mathbb{R}^3 \to \mathbb{R}^3$, $\mathbf{x} = (x, y, z)^T \mapsto (R, Z, \varphi)^T$ leads to the following covariant basis:

$$\left\{ \begin{array}{rcl} \widetilde{\mathbf{e}}_R & = & \partial_R x\ \mathbf{e}_x + \partial_R y\ \mathbf{e}_y + \partial_R z\ \mathbf{e}_z, \\ \widetilde{\mathbf{e}}_Z & = & \partial_Z x\ \mathbf{e}_x + \partial_Z y\ \mathbf{e}_y + \partial_Z z\ \mathbf{e}_z, \\ \widetilde{\mathbf{e}}_\varphi & = & \partial_\varphi x\ \mathbf{e}_x + \partial_\varphi y\ \mathbf{e}_y + \partial_\varphi z\ \mathbf{e}_z, \end{array} \right.$$

where $(\mathbf{e}_x, \mathbf{e}_y, \mathbf{e}_z)$ is the canonical base of $\mathbb{R}^3$. The Jacobian determinant of Ψ is

$$\widetilde{\mathbf{e}}_R \cdot (\widetilde{\mathbf{e}}_\varphi \times \widetilde{\mathbf{e}}_Z) = R > 0,$$

which means that the transformation Ψ is one-to-one. The scaled covariant basis is useful and is given by

$$\mathbf{e}_R = \frac{\widetilde{\mathbf{e}}_R}{\|\widetilde{\mathbf{e}}_R\|},\ \mathbf{e}_Z = \frac{\widetilde{\mathbf{e}}_Z}{\|\widetilde{\mathbf{e}}_Z\|},\ \mathbf{e}_\varphi = \frac{\widetilde{\mathbf{e}}_\varphi}{\|\widetilde{\mathbf{e}}_\varphi\|}.$$

It is also worthwhile to define the contravariant basis associated to the transformation Ψ. The contravariant basis $(\widetilde{\mathbf{e}}^R, \widetilde{\mathbf{e}}^Z, \widetilde{\mathbf{e}}^\varphi)$ is defined by duality relations

$$\widetilde{\mathbf{e}}_k.\widetilde{\mathbf{e}}^l = \delta_k^l,$$

where δ_k^l is the Kronecker's symbol and $k, l = R, Z, \varphi$.

In cylindrical coordinates, the divergence operator writes for a vector $\mathbf{V} = V_R\mathbf{e}_R + V_Z\mathbf{e}_Z + V_\varphi\mathbf{e}_\varphi$

$$\nabla \cdot \mathbf{V} = \frac{1}{R}\partial_R(RV_R) + \partial_Z V_z + \frac{1}{R}\partial_\varphi V_\varphi.$$

We re-call that for a tensor

$$\overline{\overline{T}} = \begin{bmatrix} T_{RR} & T_{RZ} & T_{R\varphi} \\ T_{ZR} & T_{ZZ} & T_{Z\varphi} \\ T_{\varphi R} & T_{\varphi Z} & T_{\varphi\varphi} \end{bmatrix},$$

the divergence operator writes

$$\begin{aligned}
(\nabla \cdot \overline{\overline{T}})_R &= \frac{1}{R}\partial_R(RT_{RR}) + \frac{1}{R}\partial_\varphi T_{R\varphi} + \partial_Z T_{RZ} - \frac{1}{R}T_{\varphi\varphi}, \\
(\nabla \cdot \overline{\overline{T}})_Z &= \frac{1}{R}\partial_R(RT_{ZR}) + \frac{1}{R}\partial_\varphi T_{Z\varphi} + \partial_Z T_{ZZ}, \\
(\nabla \cdot \overline{\overline{T}})_\varphi &= \frac{1}{R}\partial_R(RT_{\varphi R}) + \frac{1}{R}\partial_\varphi T_{\varphi\varphi} + \partial_Z T_{\varphi Z} + \frac{1}{R}T_{R\varphi}.
\end{aligned}$$

The projection onto the cylindrical base $(\mathbf{e}_R, \mathbf{e}_Z, \mathbf{e}_\varphi)$ of the vectorial equation

$$\partial_t \mathbf{V} + \nabla \cdot \overline{\overline{T}} = 0,$$

gives

$$\left\{ \begin{array}{lcl}
\partial_t(RV_R) + \partial_R(RT_{RR}) + \partial_Z(RT_{RZ}) + \partial_\varphi T_{R\varphi} &=& T_{\varphi\varphi}, \\
\partial_t(RV_z) + \partial_R(RT_{ZR}) + \partial_Z(RT_{ZZ}) + \partial_\varphi T_{Z\varphi} &=& 0, \\
\partial_t(RV_\varphi) + \partial_R(RT_{\varphi R}) + \partial_Z(RT_{\varphi Z} + \partial_\varphi T_{\varphi\varphi} &=& -T_{R\varphi}.
\end{array} \right.$$

Then, artificial source terms are created by the spatial variation of the local basis. This remark has also been made in the previous Section for the case of the ideal MHD equations. Therefore, to keep the strong conservative form of (2.1), we use the general definition of the divergence operator as it has been done in [18, 21]

$$\nabla \cdot \mathbf{V} = \frac{1}{R}\partial_k \left(R\mathbf{V} \cdot \widetilde{\mathbf{e}}^k \right),$$

where $\mathbf{V}$ is either a vector or a tensor. In this formula, the Einstein summation convention is used. Taking $\mathbf{V} = U$ and $\overline{\overline{T}} = F(U)$, using the above definition of the divergence operator and considering R time independent lead to a conservative form of (2.1) which writes:

$$\partial_t(RU) + \partial_k \left(RF(U) \cdot \widetilde{\mathbf{e}}^k \right) = 0. \tag{2.26}$$

Finally, the finite volume-type method is applied to this equation.

III.2 Mesh design and adaptation to the finite volume method

To design the 3-D toroidal mesh, the axisymmetry of toroidal geometry, we start from a 2-D mesh which represents the mesh of a section (R, Z) of the torus [18, 21], also known as poloidal plane. The 3-D elements are obtained by the rotation of the poloidal ones around the Z-axis. Therefore, the φ or toroidal direction is modeled by the interval $[0, 2\pi]$. This interval is then divided by N_{plan} segments by the points $(\varphi_{j+1/2})_{0\leq j\leq N_{plan}}$ where $\varphi_{1/2} = \varphi_{N_{plan}+1/2} = 0$ with a 2π-periodicity where the centers are given by

$$\varphi_j = \frac{\varphi_{j-1/2} + \varphi_{j+1/2}}{2},\ j = 1...N_{plan}.$$

For practical implementation, we only need the 2-D mesh of the poloidal plane. To construct a typical 3-D curved control cell, we first use the global numbering

$$i = (i_{2D} - 1)N_{plan} + j,\ i_{2D} = 1..N_{2D},\ j = 1..N_{plan}.$$

where N_{2D} is the number of point in the initial 2-D mesh, i_{2D} represent the number of the 2-D control cell $\Omega^{2D}_{i_{2D}}$ in the poloidal plane, and j locate this plane in the toroidal direction. Then, the 3-D control cell Ω_i obtained by the rotation of $\Omega^{2D}_{i_{2D}}$ around the Z-axis between the toroidal angles $\varphi = \varphi_{j-1/2}$ and $\varphi = \varphi_{j+1/2}$:

$$\Omega_i = \Omega^{2D}_{i_{2D}} \times [\varphi_{j-1/2}, \varphi_{j+1/2}].$$

According to this description, we have coupled a 2-D vertex-centered approach to a cell-centered one in the third direction. All of this is summarized in Figure 2.6 where R_0 is the major radius of the torus. Then the radial coordinate can be rewritten as

$$R = R_0 + r,\ r \in \mathbb{R}^+,$$

In numerical simulation, r is the first coordinate of the 2-D initial mesh to which we add the major radius value to obtained the right radial coordinate in the torus.

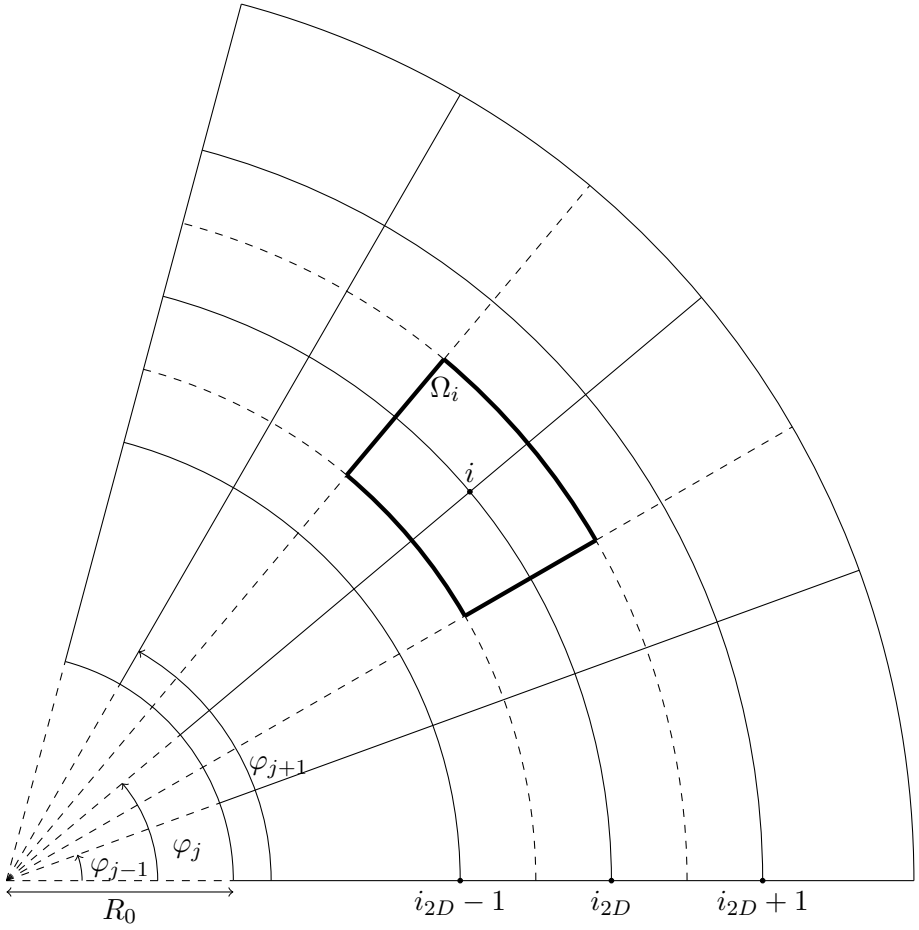

Figure 2.6: Projection on $\mathbf{e}_\varphi$ of the Ω_i cell control.

The finite volume method for the hyperbolic system (2.26) using explicit time integration writes

$$\begin{aligned}&\int_{\Omega_i} RU(R,Z,\varphi,t^{n+1})dRdZd\varphi - \int_{\Omega_i} RU(R,Z,\varphi,t^n)dRdZd\varphi \\ &+\Delta t \int_{\Omega_i} \partial_k \left[RF\Big(U(R,Z,\varphi,t^n)\Big)\cdot \tilde{\mathbf{e}}^k \right] d\Omega = 0.\end{aligned} \tag{2.27}$$

Hence, the average value U_i^n is given by

$$U_i^n = \frac{1}{|\Omega_i|}\int_{\Omega_i} RU(R,Z,\varphi,t^n)dRdZd\varphi,\ |\Omega_i| = \int_{\Omega_i} RdRdZd\varphi.$$

According to the mesh design, the expression of the cell control volume writes

$$|\Omega_i| = \left(\int_{\Omega^{2D}_{i_{2D}}} RdRdZ\right)\left(\int_{\varphi_{j-1/2}}^{\varphi_{j+1/2}} d\varphi\right) = |\Omega^{2D}_{i_{2D}}|\Delta\varphi_j,$$

where $\Delta\varphi_j = \varphi_{j+1/2} - \varphi_{j-1/2}$, $j = 1...N_{plan}$. The surface $|\Omega^{2D}_{i_{2D}}|$ is given by

$$|\Omega^{2D}_{i_{2D}}| = \frac{1}{6}\sum_{\tau\in\mathcal{V}^\tau(i_{2D})} R^\tau_{i_{2D}}|\tau|,$$

with

$$R^{\tau}_{i_{2D}} = \frac{11}{9} R_{i_{2D}} + \frac{7}{18}(R_{l_{2D}} + R_{m_{2D}}),$$

with l_{2D} and m_{2D} are the two other vertices of the triangle τ, and $\mathcal{V}^{\tau}(i_{2D})$ is the 2-D set of the triangle having i_{2D} as a vertex.

The last term of (2.27) writes

$$\int_{\Omega_i} \partial_k \left[RF\Big(U(R,Z,\varphi,t^n)\Big) \cdot \widetilde{\mathbf{e}}^k \right] d\Omega = \int_{\partial\Omega_i} R \left[F\Big(U(R,Z,\varphi,t^n)\Big) \cdot \widetilde{\mathbf{e}}^k \right] \Big(\mathbf{n} \cdot \widetilde{\mathbf{e}}^k\Big)\, d\partial\Omega.$$

Writing that $\partial\Omega_i = \bigcup \partial\Omega_i^b$ where $\partial\Omega_i^b$ are boundaries of the cell Ω_i, we have

$$\int_{\partial\Omega_i} R \left[F\Big(U(R,Z,\varphi,t^n)\Big) \cdot \widetilde{\mathbf{e}}^k \right] \big(\mathbf{n} \cdot \widetilde{\mathbf{e}}^k\big)\, d\partial\Omega = \sum_{\partial\Omega_i^b \in \partial\Omega_i} \int_{\partial\Omega_i^b} \left[RF\Big(U(R,Z,\varphi,t^n)\Big) \cdot \widetilde{\mathbf{e}}^k \right] \big(\mathbf{n} \cdot \widetilde{\mathbf{e}}^k\big)\, d\partial\Omega.$$

In the rest of this subsection, $(\mathbf{e}_{R,j}, \mathbf{e}_Z, \mathbf{e}_{\varphi,j})$ is the cylindrical basis at the angle φ_j. In order to approach correctly flux integrals, we present here the different types of boundary surfaces and the computation linked to it. The boundary surfaces $\partial\Omega_i^b$ can be divided into three types:

- The surfaces $\partial\Omega_i^+$ of outgoing normal $\mathbf{n} = \mathbf{e}_{\varphi,j+1/2}$,
- The surfaces $\partial\Omega_i^-$ of outgoing normal $\mathbf{n} = -\mathbf{e}_{\varphi,j-1/2}$,
- The curved surfaces $\mathcal{S}_i$ directed along the toroidal direction $\mathbf{e}_{\varphi}$,

with $\partial\Omega_i = \partial\Omega_i^+ \bigcup \partial\Omega_i^- \bigcup \mathcal{S}_i$. To be more precise, the two first types of surfaces are similar and we have

$$\partial\Omega_i^{\pm} = \Omega_{i_{2D}}^{2D},$$

and

$$\int_{\partial\Omega_i^{\pm}} R \left[F(U,R,Z,\varphi,t^n) \cdot \widetilde{\mathbf{e}}^k \right] (\mathbf{n} \cdot \widetilde{\mathbf{e}}^k) d\partial\Omega = F\left(U_i^n, U_l^n, \pm\mathbf{e}_{\varphi_{j\pm1/2}}\right) \int_{\Omega_{i_{2D}}^{2D}} dRdZ.$$

We deduce from (2.10) that

$$|\partial\Omega_i^{\pm}| = \frac{1}{3} \sum_{\tau \in \mathcal{V}^{\tau}(i_{2D})} |\tau|,$$

and

$$\int_{\partial\Omega_i^{\pm}} R \left[F(U,R,Z,\varphi,t^n) \cdot \widetilde{\mathbf{e}}^k \right] (\mathbf{n} \cdot \widetilde{\mathbf{e}}^k) d\partial\Omega = |\partial\Omega_i^{\pm}| F\left(U_i^n, U_l^n \pm \mathbf{e}_{\varphi,j\pm1/2}\right),$$

where $l = i + N_{plan}$ for $\partial\Omega_i^+$ and $l = i - N_{plan}$ for $\partial\Omega_i^-$ are the two neighbors of i in the φ-direction.

Finally, the surface $\mathcal{S}_i$ is the rest of the boundary surfaces. It can be described as

$$S_i = \bigcup_{l \in \mathcal{V}^{2D}(i)} S_{il},$$

where $\mathcal{V}^{2D}(i)$ is the set of the neighbors of i in the poloidal plane. For $l \in \mathcal{V}^{2D}(i)$, the surface S_{il} is given by

$$S_{il} = \prod_{\varphi \in [\varphi_{j-1/2}, \varphi_{j+1/2}]} \mathcal{R}_{\varphi}\left(S_{il}^{2D}\right), \; S_{il}^{2D} = \Omega_{i_{2D}}^{2D} \bigcap \Omega_{l_{2D}}^{2D},$$

where i_{2D} and l_{2D} are the poloidal number of i and l, and the operator $\mathcal{R}_\varphi(S_{il}^{2D})$ is the rotation of S_{il}^{2D} around the Z-axis about the angle φ. To compute the numerical flux over the surface S_{il}, we write its unitary normal in the Cartesian coordinates

$$\mathbf{n} = \begin{bmatrix} n_R \cos\varphi \\ n_R \sin\varphi \\ n_Z \end{bmatrix}.$$

Then we have

$$\int_{\mathcal{S}_{il}} \left[RF\Big(U(R,Z,\varphi)\Big) \cdot \widetilde{\mathbf{e}}^k \right] \left(\mathbf{n} \cdot \widetilde{\mathbf{e}}^k \right) d\mathcal{S} = |\mathcal{S}_{il}| F\left(U_i^n, U_l^n, \mathbf{n}_{il}\right),$$

where $F(U_i^n, U_l^n, \mathbf{n}_{il})$ is the numerical flux determined with a Riemann-type scheme, and $\mathbf{n}_{il}$ is the average unitary normal of $\mathcal{S}_{il}$ given by the definition (2.11)

$$\begin{aligned} \mathbf{n}_{il} &= \frac{1}{|\mathcal{S}_{il}|} \int_{\mathcal{S}_{il}} \mathbf{n} d\mathcal{S} = \frac{1}{|\mathcal{S}_{il}|} \int_{\mathcal{S}_{il}^{2D}} R d\mathcal{S}^{2D} \int_{\varphi_{j-1/2}}^{\varphi_{j+1/2}} \begin{bmatrix} n_R \cos\varphi \\ n_R \sin\varphi \\ n_Z \end{bmatrix} d\varphi, \\ &= \frac{|\mathcal{S}_{il}^{2D}|}{|\mathcal{S}_{il}|} \begin{bmatrix} 2n_R \sin\dfrac{\Delta\varphi_j}{2} \cos\varphi_j \\ 2n_R \sin\dfrac{\Delta\varphi_j}{2} \sin\varphi_j \\ n_Z \Delta\varphi_j \end{bmatrix}, \end{aligned}$$

where

$$|\mathcal{S}_{il}^{2D}| = \int_{\mathcal{S}_{il}^{2D}} R d\mathcal{S}^{2D}, |\mathcal{S}_{il}| = \int_{\mathcal{S}_{il}} R d\mathcal{S}.$$

Using the form of $\mathcal{S}_{il}$, we deduce that

$$|\mathcal{S}_{il}| = \Delta\varphi_j |\mathcal{S}_{il}^{2D}|.$$

Then, the normal $\mathbf{n}_{il}$ becomes

$$\mathbf{n}_{il} = \begin{bmatrix} \beta_j n_R \cos\varphi_j \\ \beta_j n_R \sin\varphi_j \\ n_Z \end{bmatrix}_{(\mathbf{e}_x, \mathbf{e}_y, \mathbf{e}_z)} = \begin{bmatrix} \beta_j n_R \\ n_Z \\ 0 \end{bmatrix}_{(\mathbf{e}_{R,j}, \mathbf{e}_Z, \mathbf{e}_{\varphi,j})}, \ \beta_j = \frac{\sin\dfrac{\Delta\varphi_j}{2}}{\dfrac{\Delta\varphi_j}{2}},$$

Finally, the finite volume method for the toroidal geometry writes

$$\begin{aligned} U_i^{n+1} = U_i^n &- \sum_{l \in \mathcal{V}^{2D}(i)} \left(\frac{|S_{il}|}{|\Omega_i|} F(U_i^n, U_l^n, \mathbf{n}_{il}) \right) \\ &- \frac{|\partial\Omega_i^{\pm}|}{|\Omega_i|} \left[F\left(U_i^n, U_{i+N_{plan}}^n, \mathbf{e}_{\varphi,j+1/2}\right) - F\left(U_{i-N_{plan}}^n, U_i^n, \mathbf{e}_{\varphi,j-1/2}\right) \right]. \end{aligned}$$

For a scalar variable u, its average value over a control cell Ω_i is given by

$$u_i = \frac{1}{|\Omega_i|} \int_{\Omega_i} R u d\Omega.$$

The one of a vectorial variable $\mathbf{u}$ is

$$\mathbf{u}_i = \frac{1}{|\Omega_i|}\int_{\Omega_i} R \left[\begin{array}{c} u_R \\ u_Z \\ u_\varphi \end{array}\right]_{(\mathbf{e}_R,\mathbf{e}_Z,\mathbf{e}_\varphi)} d\Omega.$$

As the cylindrical basis is moving in the control cell Ω_i and the finite volume method is applied to the entire vector, we have also to compute the average value of this basis in Ω_i. Hence, we have

$$\left\{\begin{array}{rcccl} \widetilde{\mathbf{e}}_{R,j} & = & \dfrac{1}{|\Omega_i|}\displaystyle\int_{\Omega_i} R\mathbf{e}_R d\Omega & = & \beta_j \mathbf{e}_{R,j}, \\ \widetilde{\mathbf{e}}_{Z,j} & = & \dfrac{1}{|\Omega_i|}\displaystyle\int_{\Omega_i} R\mathbf{e}_Z d\Omega & = & \mathbf{e}_{Z,j}, \\ \widetilde{\mathbf{e}}_{\varphi,j} & = & \dfrac{1}{|\Omega_i|}\displaystyle\int_{\Omega_i} R\mathbf{e}_\varphi d\Omega & = & \beta_j \mathbf{e}_{\varphi,j}. \end{array}\right.$$

Thus the average value of the vector $\mathbf{u}$ on Ω_i is

$$\mathbf{u}_i = \left[\begin{array}{c} \beta_j u_{R,i} \\ u_{Z,i} \\ \beta_j u_{\varphi,i} \end{array}\right].$$

We define the function μ_j^k

$$\mu_j^k = \left\{\begin{array}{ll} \beta_j & \text{if} \quad k = R, \varphi, \\ 1 & \text{if} \quad k = Z. \end{array}\right.$$

Then, the finite volume method for each component of the vector $\mathbf{u}$ writes

$$\begin{aligned} \mathbf{u}_{k,i}^{n+1} = \mathbf{u}_{k,i}^n \quad & - \quad \sum_{l\in\mathcal{V}^{2D}(i)} \left(\frac{|S_{il}|}{\mu_j^k|\Omega_i|} F(U_i^n, U_l^n, \mathbf{n}_{il})\right) \\ & - \quad \frac{|\partial\Omega_i^{\pm}|}{\mu_j^k|\Omega_i|}\left[F\left(U_i^n, U_{i+N_{plan}}^n, \widetilde{\mathbf{e}}_{\varphi,j+1/2}\right) - F\left(U_{i-N_{plan}}^n, U_i^n, \widetilde{\mathbf{e}}_{\varphi,j-1/2}\right)\right]. \end{aligned}$$

This finite volume method for toroidal geometry has also been tested at the second order in space. To compute the gradient in this 3-D geometry, we have used the method presented in subsection I.3 for its poloidal part: (R, Z)-coordinates. As the mesh of the toroidal direction is cell-centered, we will use the method of subsection I.2 to determine the gradient the φ-direction. However, we have to be careful with the toroidal direction of the gradient: since the local basis is moving, then for a vectorial variable we have to take into account the derivative in φ-direction. To be more precise, by using the relations

$$\partial_\varphi \mathbf{e}_R = \mathbf{e}_\varphi, \ \partial_\varphi \mathbf{e}_Z = 0, \ \text{and} \ \partial_\varphi \mathbf{e}_\varphi = -\mathbf{e}_R,$$

we obtain that the variation in the toroidal direction of each component of a vector $\mathbf{u}$ is

$$\delta_\varphi \mathbf{u} = \left[\begin{array}{c} \delta_\varphi u_R + u_\varphi \\ \delta_\varphi u_Z \\ \delta_\varphi u_\varphi - u_R \end{array}\right],$$

the notation δ_φ represent the variation of a variable in the toroidal direction.

IV Conclusions

In this chapter, we have presented two different 2-D approaches of finite volume-type methods in Cartesian geometry. Then, the cell-centered approach is adapted to the cylindrical coordinates under the translation invariance $\partial_Z \cdot = 0$ assumption. I, the case of the ideal MHD equations, the projection of the vectorial variable equations on the cylindrical basis creates artificial source terms. We have suppress as much as possible those terms in the equations and proposed a finite volume method adapted to the new ideal MHD system equations. The numerical results of this methods are given in Chapter 4.
Finally, a fully 3-D finite volume method is designed by coupling a 2-D vertex-centered approach in the poloidal plane (R, Z) to a cell-centered one in the toroidal direction φ. In order to avoid artificial source terms, the divergence operator is written in its original definition [18, 21]. This method will be tested for the bi-temperature Euler equations in Chapter 3.

Chapter 3

Relaxation scheme for the bi-temperature Euler model

In this chapter, a numerical scheme is designed to solve the bi-temperature Euler conservative equations (1.76). Using the rotational invariance of this system, a relaxation scheme is built for the 1-D equations. The numerical scheme and the numerical experiments are presented for the mono-atomic case (1.43).

I Presentation of the scheme

Let us first give the principle of the proposed relaxation-type scheme which is based on the relaxation one of the mono-temperature Euler equations [22, 53, 73, 15, 14]. For the bi-temperature Euler equations, this scheme has been written for the non-conservative system in [7]. Here, we detail the scheme for the conservative one. The system is relaxed one the electronic and ionic pressures which are replaced by the two relaxation variables π_e, and π_i in the equations. Thus, the relaxed system writes

$$\left\{\begin{array}{lcl} \partial_t\rho + \partial_x(\rho u) & = & 0, \\ \partial_t(\rho u) + \partial_x(\rho u^2 + \pi_e + \pi_i) & = & 0, \\ \partial_t(\rho v) + \partial_x(\rho uv) & = & 0, \\ \partial_t(\rho w) + \partial_x(\rho uw) & = & 0, \\ \partial_t\mathcal{E} + \partial_x\left[(\mathcal{E} + \pi_e + \pi_i)\,u\right] & = & 0, \\ \partial_t(\rho_e S_e) + \partial_x(\rho_e S_e u) & = & (\gamma-1)\nu_{ei}^{\mathcal{E}}\rho_e^{1-\gamma}(T_i - T_e), \\ \\ \partial_t\pi_e + \dfrac{a^2 c_e}{\rho}\partial_x u + u\partial_x\pi_e & = & \nu\left(p_e - \pi_e\right), \\ \\ \partial_t\pi_i + \dfrac{a^2 c_i}{\rho}\partial_x u + u\partial_x\pi_i & = & \nu\left(p_i - \pi_i\right). \end{array}\right.$$

According to [7], the parameter a has to satisfy the following stability condition

$$a \geq \rho \max(c_{s,e}, c_{s,i}),\ \ c_{s,\alpha} = \sqrt{\frac{\gamma p_\alpha}{\rho_\alpha}},\ \ \alpha = e, i,$$

known as Whitham subs-characteristic condition. In order to have a more precise solution, the parameter a can be chosen as non-uniform variable solution of a transport equation.

Therefore, the relaxed system becomes

$$\begin{cases} \partial_t \rho + \partial_x(\rho u) &= 0, \\ \partial_t(\rho u) + \partial_x(\rho u^2 + \pi_e + \pi_i) &= 0, \\ \partial_t(\rho v) + \partial_x(\rho u v) &= 0, \\ \partial_t(\rho w) + \partial_x(\rho u w) &= 0, \\ \partial_t \mathcal{E} + \partial_x\left[(\mathcal{E} + \pi_e + \pi_i)\, u\right] &= 0, \\ \partial_t(\rho_e S_e) + \partial_x(\rho_e S_e u) &= (\gamma - 1)\nu_{ei}^{\mathcal{E}} \rho_e^{1-\gamma}(T_i - T_e), \\ \partial_t \pi_e + \dfrac{a^2 c_e}{\rho}\partial_x u + u\partial_x \pi_e &= \nu\left(p_e - \pi_e\right), \\ \partial_t \pi_i + \dfrac{a^2 c_i}{\rho}\partial_x u + u\partial_x \pi_i &= \nu\left(p_i - \pi_i\right), \\ \partial_t(\rho a) + \partial_x(\rho a u) &= 0. \end{cases}$$

The system is now written in the hyperbolic conservative form

$$\partial_t U + \partial_x F(U) = S_\nu(U),$$

where

$$U = \begin{bmatrix} \rho \\ \rho u \\ \rho v \\ \rho w \\ \mathcal{E} \\ \rho_e S_e \\ \rho \pi_e \\ \rho \pi_i \\ \rho a \end{bmatrix}, \; F(U) = \begin{bmatrix} \rho u \\ \rho u^2 + \pi_e + \pi_i \\ \rho u v \\ \rho u w \\ (\mathcal{E} + \pi_e + \pi_i)\, u \\ \rho_e S_e u \\ (\rho \pi_e + a^2 c_e) u \\ (\rho \pi_i + a^2 c_i) u \\ \rho a u \end{bmatrix}, \; S_\nu(U) = \begin{bmatrix} 0 \\ 0 \\ 0 \\ 0 \\ 0 \\ (\gamma - 1)\nu_{ei}^{\mathcal{E}} \rho_e^{1-\gamma}(T_i - T_e) \\ \nu(p_e - \pi_e) \\ \nu(p_i - \pi_i) \\ 0 \end{bmatrix}.$$

The relaxation scheme is divided in two steps: a transport step and a projection one. During the transport step, the system

$$\partial_t U + \partial_x F(U) = 0, \tag{3.1}$$

is solved with a Riemann-type scheme. Then, for the projection step, we take the limit $\dfrac{1}{\nu} \to 0$ and solve

$$\partial_t U = S_\nu(U). \tag{3.2}$$

II Transport step

In this Section, we give the properties of the relaxed system (3.1). Then, to compute the relaxation flux, we solve the Riemann problem at the interfaces.

II.1 Properties of the relaxed system

In this part, we construct the numerical flux of the Godunov scheme for the system (3.1). First, the system is rewritten in the form

$$\partial_t U + A(U)\partial_x U = 0,$$

where $A(U)$ is the Jacobian of $F(U)$ and is given by

$$A(U) = \begin{bmatrix} 0 & 1 & 0 & 0 & 0 & 0 & 0 & 0 & 0 \\ -(u^2 + \frac{\pi_e+\pi_i}{\rho}) & 2u & 0 & 0 & 0 & 0 & \frac{1}{\rho} & \frac{1}{\rho} & 0 \\ -uv & v & u & 0 & 0 & 0 & 0 & 0 & 0 \\ -uw & w & 0 & u & 0 & 0 & 0 & 0 & 0 \\ -\frac{u}{\rho}\left[\mathcal{E} + 2(\pi_e + \pi_i)\right] & \frac{1}{\rho}\left(\mathcal{E} + \pi_e + \pi_i\right) & 0 & 0 & u & 0 & \frac{u}{\rho} & \frac{u}{\rho} & 0 \\ -c_e u S_e & c_e S_e & 0 & 0 & 0 & u & 0 & 0 & 0 \\ -u\left(\pi_e + 3c_e\frac{a^2}{\rho}\right) & \pi_e + c_e\frac{a^2}{\rho} & 0 & 0 & 0 & 0 & u & 0 & 2c_e\frac{au}{\rho} \\ -u\left(\pi_i + 3c_i\frac{a^2}{\rho}\right) & \pi_i + c_i\frac{a^2}{\rho} & 0 & 0 & 0 & 0 & 0 & u & 2c_i\frac{au}{\rho} \\ -au & a & 0 & 0 & 0 & 0 & 0 & 0 & u \end{bmatrix}.$$

Hence, the matrix $A(U)$ has three different eigenvalues given by

$$\begin{cases} \lambda_1 &= u - \dfrac{a}{\rho}, \\ \lambda_2 &= u, \\ \lambda_3 &= u + \dfrac{a}{\rho}. \end{cases}$$

where λ_2 has an order 7 of multiplicity. The eigenvectors obtained are

$$R_1 = \begin{bmatrix} 1 \\ u - \dfrac{a}{\rho} \\ v \\ w \\ \dfrac{1}{\rho}(\mathcal{E} + \pi_e + \pi_i - au) \\ c_e S_e \\ \pi_e + c_e\dfrac{a^2}{\rho} \\ \pi_i + c_i\dfrac{a^2}{\rho} \\ a \end{bmatrix}, \; R_2 = \begin{bmatrix} 1 \\ u \\ 1 \\ 1 \\ 1 \\ 1 \\ \pi_e \\ \pi_i \\ a \end{bmatrix}, R_3 = \begin{bmatrix} 1 \\ u + \dfrac{a}{\rho} \\ v \\ w \\ \dfrac{1}{\rho}(\mathcal{E} + \pi_e + \pi_i + au) \\ c_e S_e \\ \pi_e + c_e\dfrac{a^2}{\rho} \\ \pi_i + c_i\dfrac{a^2}{\rho} \\ a \end{bmatrix}.$$

The three waves are linearly degenerated hence, they are contact discontinuities. The Riemann invariants are

$$\begin{aligned}
(u-\frac{a}{\rho})-\text{wave} \quad &: \quad u-\frac{a}{\rho},\ v,\ w,\ a,\ S_e,\ \pi_e+c_e\frac{a^2}{\rho},\ \pi_i+c_i\frac{a^2}{\rho},\\
&\qquad \text{and } \varepsilon-\frac{1}{2c_e a^2}\pi_e^2-\frac{1}{2c_i a^2}\pi_i^2,\\
u-\text{wave} \quad &: \quad u,\ \text{and } \pi_e+\pi_i,\\
(u+\frac{a}{\rho})-\text{wave} \quad &: \quad u+\frac{a}{\rho},\ v,\ w,\ a,\ S_e,\ \pi_e+c_e\frac{a^2}{\rho},\ \pi_i+c_i\frac{a^2}{\rho},\\
&\qquad \text{and } \varepsilon-\frac{1}{2c_e a^2}\pi_e^2-\frac{1}{2c_i a^2}\pi_i^2,
\end{aligned}$$

where ε is the total internal energy defined by

$$\rho\varepsilon=\rho_e\varepsilon_e+\rho_i\varepsilon_i,\ \rho_\alpha\varepsilon_\alpha=(\gamma-1)p_\alpha,\ \alpha=e,i.$$

In [7], the Riemann invariants are almost the same ones. Indeed, for the $(u-\frac{a}{\rho})$ and $(u+\frac{a}{\rho})$-waves, instead of giving the Riemann invariants on the internal energy of each species, we give the ones on the electronic entropy and on the total internal energy. This difference comes from the fact that we have considered the conservative system instead of the non-conservative one.

II.2 Relaxation flux

After computing the Riemann invariants of each waves, we have now to solve the Riemann (U_L, U_R) to determine the numerical fluxes at the interface of control cells. First, let us compute the two intermediate states U_L^*, and U_R^* shown in Figure 3.1. Since the three waves are contact discontinuities, then the Riemann invariants are used to obtain the two intermediate states. For example, u and $(\pi_e+\pi_i)$ are the invariants of the 2-wave then we have

$$\left\{\begin{array}{lcll} u_L^* & = & u_R^* & = u^*,\\ \pi_{e,L}^*+\pi_{i,L}^* & = & \pi_{e,R}^*+\pi_{i,R}^* & = \pi^*. \end{array}\right. \tag{3.3}$$

For the rest of the Riemann invariants we obtain the following system for the 1-wave

$$\left\{\begin{array}{lcl} u_L-\dfrac{a_L}{\rho_L} & = & u^*-\dfrac{a_L}{\rho_L^*},\\[2ex] \pi_{e,L}+c_e\dfrac{a_L^2}{\rho_L} & = & \pi_{e,L}^*+c_e\dfrac{a_L^2}{\rho_L^*},\\[2ex] \pi_{i,L}+c_i\dfrac{a_L^2}{\rho_L} & = & \pi_{i,L}^*+c_i\dfrac{a_L^2}{\rho_L^*},\\[2ex] \varepsilon_L-\dfrac{1}{2c_e a_L^2}\pi_{e,L}^2-\dfrac{1}{2c_i a_L^2}\pi_{i,L}^2 & = & \varepsilon_L^*-\dfrac{1}{2c_e a_L^2}(\pi_{e,L}^*)^2-\dfrac{1}{2c_i a_L^2}(\pi_{i,L}^*)^2. \end{array}\right. \tag{3.4}$$

The 3-wave Riemann invariants give the last system

$$\begin{cases} u_R + \dfrac{a_R}{\rho_R} & = & u^* - \dfrac{a_R}{\rho_R^*}, \\ \pi_{e,R} + c_e \dfrac{a_L^2}{\rho_R} & = & \pi_{e,R}^* + c_e \dfrac{a_R^2}{\rho_R^*}, \\ \pi_{i,R} + c_i \dfrac{a_L^2}{\rho_R} & = & \pi_{i,R}^* + c_i \dfrac{a_R^2}{\rho_R^*}, \\ \varepsilon_R - \dfrac{1}{2c_e a_R^2}\pi_{e,R}^2 - \dfrac{1}{2c_i a_R^2}\pi_{i,R}^2 & = & \varepsilon_R^* - \dfrac{1}{2c_e a_R^2}(\pi_{e,R}^*)^2 - \dfrac{1}{2c_i a_R^2}(\pi_{i,R}^*)^2. \end{cases} \tag{3.5}$$

By solving simultaneously the three previous systems (3.3)-(3.5), we obtain

$$\frac{1}{\rho_L^*} = \frac{1}{\rho_L} + \frac{a_R(u_R - u_L) + (\pi_{e,L} + \pi_{i,L}) - (\pi_{e,R} + \pi_{i,R})}{a_L(a_L + a_R)},$$

$$\frac{1}{\rho_R^*} = \frac{1}{\rho_R} + \frac{a_L(u_R - u_L) + (\pi_{e,R} + \pi_{i,R}) - (\pi_{e,L} + \pi_{i,L})}{a_R(a_L + a_R)},$$

$$u^* = \frac{a_L u_L + a_R u_R + (\pi_{e,L} + \pi_{i,L}) - (\pi_{e,R} + \pi_{i,R})}{a_L + a_R},$$

$$\pi_{\alpha,L}^* = \pi_{\alpha,L} - c_\alpha a_L \frac{a_R(u_R - u_L) + (\pi_{e,L} + \pi_{i,L}) - (\pi_{e,R} + \pi_{i,R})}{a_L + a_R}, \ \alpha = e, i,$$

$$\pi_{\alpha,R}^* = \pi_{\alpha,R} - c_\alpha a_R \frac{a_L(u_R - u_L) + (\pi_{e,R} + \pi_{i,R}) - (\pi_{e,L} + \pi_{i,L})}{a_L + a_R}, \ \alpha = e, i,$$

$$\varepsilon_K^* = \varepsilon_K + \frac{1}{2c_e a_K^2}\left[(\pi_{e,K}^*)^2 - \pi_{e,K}^2\right] + \frac{1}{2c_i a_K^2}\left[(\pi_{i,K}^*)^2 - \pi_{i,K}^2\right], \ K = L, R.$$

Hence, the two intermediate state U_L^*, and U_R^* can be computed and, the solution of the Riemann problem is given by

$$U^* = \begin{cases} U_L & \text{if} \quad 0 \le \lambda_1, \\ U_L^* & \text{if} \quad \lambda_1 \le 0 \le \lambda_2, \\ U_R^* & \text{if} \quad \lambda_2 \le 0 \le \lambda_3, \\ U_R & \text{if} \quad \lambda_3 \le 0. \end{cases}$$

Finally, the flux of the relaxation scheme is

$$F^* = F(U^*).$$

To keep a physical result with positive densities and positive internal energies, the parameter a has to fulfill the following conditions

$$\begin{cases} a_L(a_L + a_R) & \ge & \rho_L\left[(\pi_{e,R} + \pi_{i,R}) - (\pi_{e,L} + \pi_{i,L}) - a_R(u_R - u_L)\right], \\ a_R(a_L + a_R) & \ge & -\rho_R\left[(\pi_{e,R} + \pi_{i,R}) - (\pi_{e,L} + \pi_{i,L}) + a_L(u_R - u_L)\right]. \end{cases}$$

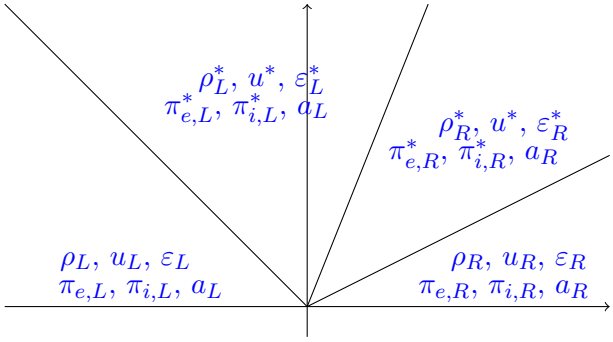

Figure 3.1: Riemann fan for the relaxed system (3.1).

III Projection step

After taking the limit $\frac{1}{\nu} \to 0$ in the equations (3.2), the resulting system is re-written as function of the physical variables $(\rho, u, v, w, \pi_e, \pi_u, T_e, T_i)^T$

$$\begin{cases} \partial_t \rho &= 0, \\ \partial_t u &= 0, \\ \partial_t v &= 0, \\ \partial_t w &= 0, \\ \pi_e &= p_e, \\ \pi_i &= p_i, \\ \partial_t T_e &= \nu_{ei}(T_i - T_e), \\ \partial_t T_i &= -\nu_{ie}(T_i - T_e), \end{cases} \tag{3.6}$$

where the temperature is in electron-Volt (eV). The coefficient $\nu_{\alpha\beta}$ is related to the coefficient $\nu_{ei}^{\mathcal{E}}$ defined in (1.19)

$$\nu_{\alpha\beta} = (\gamma - 1)\frac{\nu_{ei}^{\mathcal{E}}}{n_\alpha k_B}, \ \alpha = e, i.$$

For practical implementation, we use the value of the coefficient $\nu_{\alpha\beta}$ given by the NRL formulary [48] at the page 34

$$\nu_{\alpha\beta} = 1.8 \times 10^{-19} \frac{\sqrt{m_e m_i} n_\beta \lambda_{ei}}{(m_i T_e + m_e T_i)^{3/2}} s^{-1}, \tag{3.7}$$

and λ_{ei} is the Coulomb logarithm also defined by the NRL formulary [48] given at the same page

$$\lambda_{ei} = \begin{cases} 23 - \ln\left(\dfrac{\sqrt{n_e}}{T_e^{3/2}}\right), & \dfrac{m_e}{m_i} T_i < T_e < 10eV, \\ \\ 24 - \ln\left(\dfrac{\sqrt{n_e}}{T_e}\right), & \dfrac{m_e}{m_i} T_i < 10eV < T_e. \end{cases} \tag{3.8}$$

In (3.7) and (3.8), the temperatures T_e, and T_i are in eV, the mass are expressed in g, and n_e is in cm^{-3}.

The final temperatures T_e^{n+1} and T_i^{n+1} are given by

$$\begin{cases} T_e^{n+1} &= -\dfrac{\nu_{ei}}{\nu_{ei}+\nu_{ie}}(T_i^n - T_e^n)e^{-(\nu_{ei}+\nu_{ie})\Delta t} + \dfrac{\nu_{ie}T_e^n + \nu_{ei}T_i^n}{\nu_{ei}+\nu_{ie}}, \\ T_i^{n+1} &= \dfrac{\nu_{ie}}{\nu_{ei}+\nu_{ie}}(T_i^n - T_e^n)e^{-(\nu_{ei}+\nu_{ie})\Delta t} + \dfrac{\nu_{ie}T_e^n + \nu_{ei}T_i^n}{\nu_{ei}+\nu_{ie}}. \end{cases}$$

where T_e^n and T_i^n are the temperatures obtained with the transport step. We then get the relaxation time t_{relax} given by

$$t_{relax} = \frac{1}{\nu_{ei}+\nu_{ie}}. \tag{3.9}$$

At this end, we compute the new total energy and the new electronic entropy with (1.27), (1.44), and (1.49) in the S.I. units. To do so, the temperatures need to be express in Kelvin (K). The relation between the temperature T^{eV} in eV and the temperature T^K in K is given by

$$T^K = 1.1604 \times 10^4 T^{eV}.$$

According to (3.6), the difference between the two temperatures $(T_i - T_e)$ is solution of the equation

$$\partial_t(T_i - T_e) = -(\nu_{ei}+\nu_{ie})(T_i - T_e).$$

Therefore, at the end of the projection step, the difference $T_i - T_e$ is

$$T_i^{n+1} - T_e^{n+1} = (T_i^n - T_e^n)e^{-(\nu_{ei}+\nu_{ie})\Delta t}.$$

It means that if at the beginning of the projection step, the electronic and ionic temperatures are equals, then this thermal equilibrium $T_i = T_e$ is preserved during this step.

IV Numerical tests

For all numerical tests, the computations have been done with a second order in time and space scheme. The time integration has used a second order the Runge-Kutta while second order in space space used a MUSCL method on non-structured meshes described in [45] and re-called in Chapter 2.

IV.1 Shock tube

This test case is inspired by the well-known Sod's tube for Euler equations [70] and intends to test the transport step of the proposed numerical method. This test has been run in a 2-D setting on a square $[0,1] \times [0,1]$ meshed with 200×5 points. The computation is carried out until $t = 8.6289 \times 10^{-8} s$. The initial data writes

$$U(x,y) = \begin{cases} U_L, & \text{if} \quad x < 0.5, \\ U_R, & \text{if} \quad x \geq 0.5, \end{cases}$$

where U_L and U_R are given in Table 3.1. The initial data of the density are the usual ones, and the initial temperatures are chosen in order to keep as in [70] a ratio of 10 between the pressures of the left and right states.

	ρ	**u**	T_e(K)	T_i(K)
U_L	1	0	1.04436×10^8	1.27644×10^8
U_R	0.125	0	8.1228×10^7	1.04436×10^8

Table 3.1: Initial data for the shock tube problem.

This solution of this problem contains three different waves: one rarefaction, one contact discontinuity, and one shock.

In order to test the transport part of the numerical method, the simulation is first realized without any source term: $\nu_{ei} = \nu_{ie} = 0$. The results are given in Figure 3.2. As expected, the solution is 1-D, and although the simulation has been done on a 2D mesh, the numerical scheme does not generate transverse velocities. The density follows correctly the three waves. We observe an overshoot of temperatures at the beginning of the contact discontinuity around $x = 0.64$. With respect to the entropies, it is seen that as it has been shown by the mathematical study of the bi-temperature Euler equations, the electronic entropy is constant across the shock wave at $x \approx 0.84$ in Figure 3.2 while on the opposite the ionic entropy jumps across the shock.

In a second simulation, we now add the temperature relaxation source terms where ν_{ei} and ν_{ie} are given by (3.7). The obtained results on the electronic and ionic temperatures, pressures, and entropy are given in Figure 3.3 again for $t = 8.6289 \times 10^{-8} s$. According to Table 3.1, the equilibrium times for the left and the right states are

$$\begin{cases} t_{eq,L} &= 2.39 \times 10^{-8} s, \\ t_{eq,R} &= 1.21 \times 10^{-7} s, \end{cases}$$

and therefore, the computation is stopped before the time where the two temperatures should have attained a common value. This time is also called thermal equilibrium time and corresponds to the relaxation time (3.9) denoted t_{eq}. Actually, the results show that on the left side where the relaxation time is smaller the thermal equilibrium is reached before the contact discontinuity while the two temperatures are still significantly different on the right side.

We can also see that the temperature relaxation modifies the entropies and that the electronic entropy is not any more constant across the shock wave. By comparing Figures 3.2 and 3.3, this effect is less apparent for the ionic entropy that seems to be less affected by the temperature relaxation. One can suspect that this behavior is probably a direct consequence of the large difference of mass between the two species.

The numerical method gives satisfactory results on this problem and thus validate the numerical treatment of the transport step.

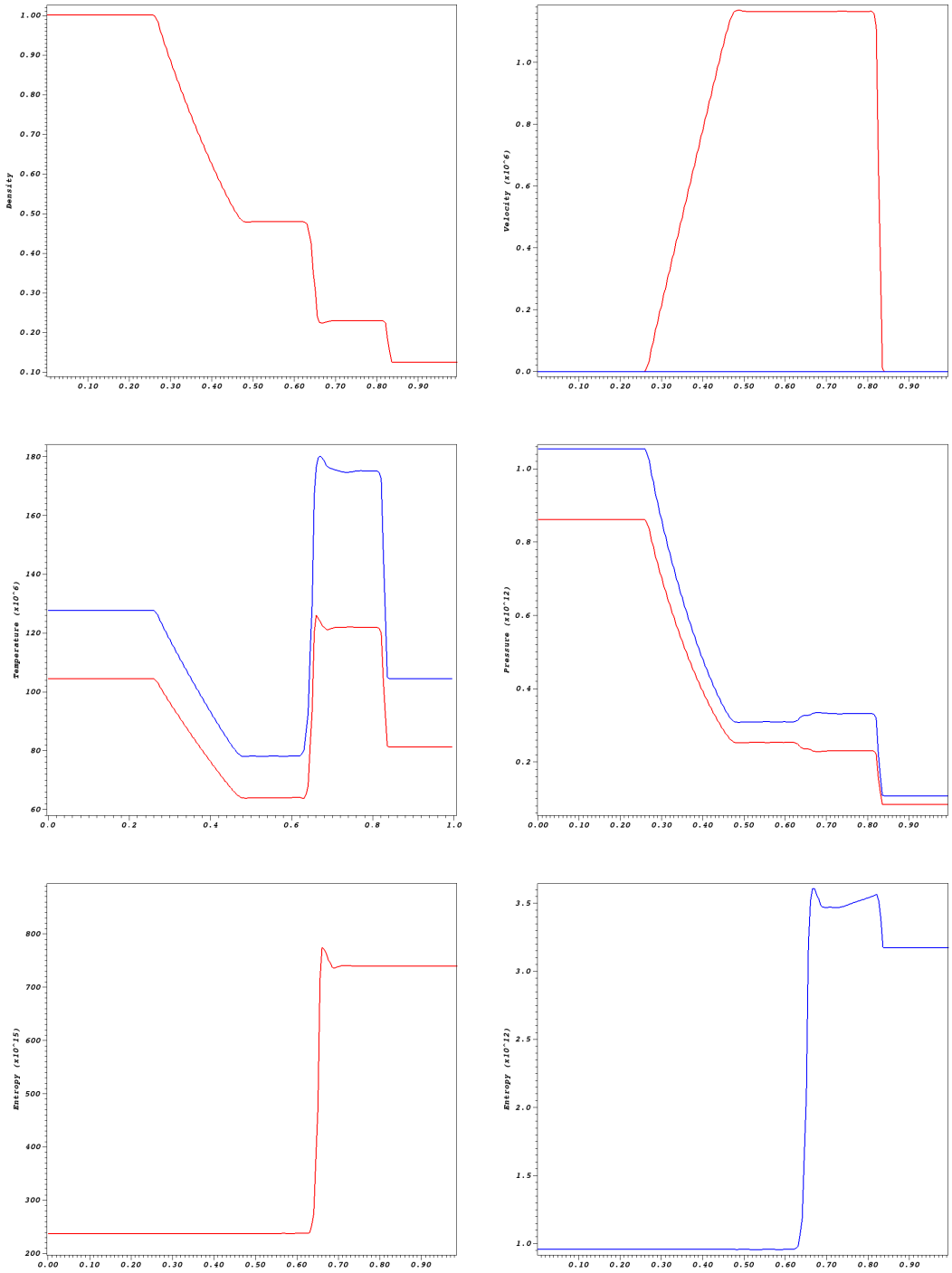

Figure 3.2: Shock tube problem at $t = 8.6289 \times 10^{-8} s$ with $\nu_{ei} = \nu_{ie} = 0$. Solution at $y = 0.5$. Left-Top: Density, Right-Top: x-velocity in red, and y-velocity in blue, Left-Center: Electronic (red) and ionic (blue) temperatures, Right-Center: Electronic (red) and ionic(blue) pressures, Left-Bottom: Electronic entropy, Right-Bottom: Ionic entropy.

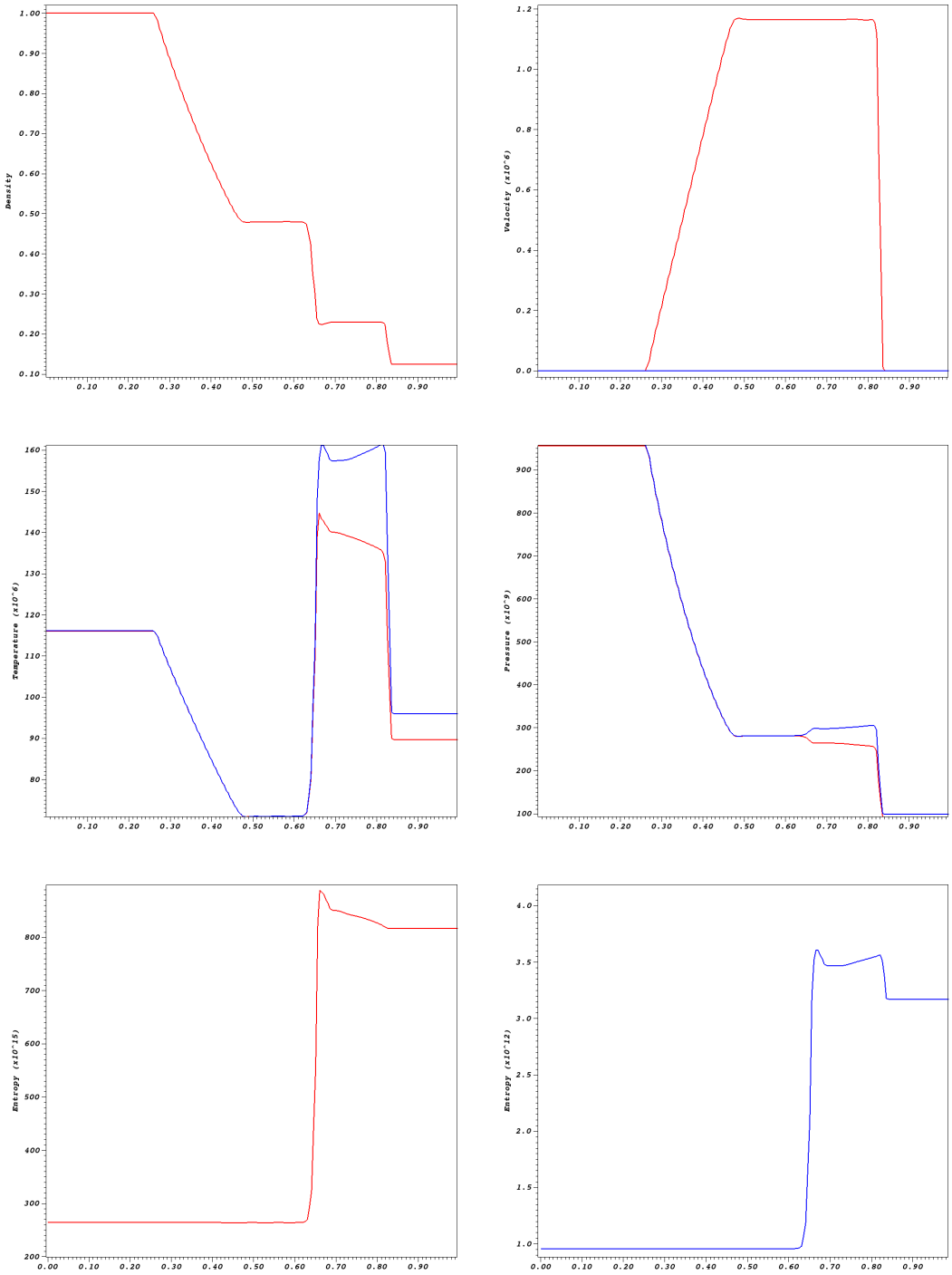

Figure 3.3: Shock tube problem at $t = 8.6289 \times 10^{-8} s$ with $\nu_{ei} \neq 0$, $\nu_{ie} \neq 0$. Solution at $y = 0.5$. Left-Top: Density, Right-Top: x-velocity in red, and y-velocity in blue, Left-Center: Electronic (red) and ionic (blue) temperatures, Right-Center: Electronic (red) and ionic(blue) pressures, Left-Bottom: Electronic entropy, Right-Bottom: Ionic entropy.

IV.2 Implosion

This test case is inspired from [28] and adapted to the bi-temperature Euler equations. Indeed, the density and velocity initial data are the same as the ones used in [28]. The physical motivation of this test is to simulate a laser beam shooting a target in order to initiate a fusion reaction. Then, for this test, the temperatures are chosen in order to be in the laser plasma domain given in page 41 of the NRL formulary [48]. From a computational point of view, we test in this simulation the capability of the numerical scheme to handle shock focusing and reflection leading to a large and fast increase of the density. The initial data is given by

$$U(x,y) = \begin{cases} U_L, & \text{if} \quad R < 0.5, \\ U_R, & \text{if} \quad R \geq 0.5, \end{cases}, \quad R = \sqrt{x^2+y^2}.$$

where the data U_L and U_R are given in Table 3.2.

This test has been computed in a 2-D Cartesian geometry on a simulation domain equal to a quarter of disc of radius equal to 1 meshed by 33153 points. The mesh is a refined version of the mesh presented in Figure 3.4. Since we want to compute the reflection of the shock wave at the origin, it has not been possible to use a polar grid that contains very small cells at the origin and thus implies the use of very small time steps. The mesh used is a good approximation of a polar mesh: the constant radius lines are almost mesh lines. However, this is not exactly true and will lead to some numerical artefacts.

This problem contains three cylindrical waves propagating towards the origin: first a shock, followed by a contact discontinuity leaving behind it a rarefaction wave. After interacting with the origin the shock will be reflected back and will propagate towards the exterior. Eventually, the reflected shock will interact with the contact discontinuity that is still propagating towards the center. At the initial time, the equilibrium temperature times for the left and the right states are

$$\begin{cases} t_{eq,L} &= 1.34 \times 10^{-10} s, \\ t_{eq,R} &= 2.97 \times 10^{-9} s, \end{cases}$$

that are quite small. Figures 3.5 and 3.6 present the results obtained at the time $t_1 = 4.0901 \times 10^{-7} s$ before the interaction of the shock with the origin. Since t_1 is significantly larger than the temperature relaxation times, the electronic and ionic temperatures had time to relax to a common value as shown on the color plot of Figure 3.5 and the 1-D plot of Figure 3.6 and the electronic and ionic pressures and temperatures are the same.

Since the initial data depends only on R, we expect a 1-D solution in a cylindrical coordinates system R, φ. As shown in Figures 3.5 and 3.7, this property is satisfied by the simulation except on the contact discontinuity where small wiggles appears. These wiggles grow along time. This loss of the 1-D character of the solution is not seen on the propagation of the shock wave but appears on the contact discontinuity. It is likely that these wiggles are initiated by the fact that the mesh is not exactly aligned with the initial data and that they are amplified by some kind of Richtmyer-Meshkov type instability although we do not claim that they have a physical origin.

Figures 3.7 and 3.8 present the results at $t = t_2 = 6.22 \times 10^{-7} s$ shortly after the reflection of the shock. The density and pressure at the origin have increased by a factor ten and a zone of positive velocity can be noticed while the contact discontinuity is still moving towards the center.

Finally at $t = t_3 = 8.4973 \times 10^{-7} s$ the shock begins to interact with the contact discontinuity. In Figure 3.9 are displayed the evolution of the density contours at times t_1, t_2, t_3, that show the development of instabilities on the contact discontinuity with mushroom shapes. However the mesh resolution for this computation is too coarse to pretend to capture a true physical instability and the contact is smeared over several cells. This is a well-know problem in the computation of linearly degenerate-waves by Eulerian methods and is often taken as an argument to prefer Lagrangian methods for multi-material problems and specially for ICF simulations [57, 58, 40].

	ρ	$\mathbf{u}$	T_e(K)	T_i(K)
U_L	1	0	2.3×10^6	1.7406×10^6
U_R	1	0	2.3×10^7	1.7406×10^7

Table 3.2: Initial data for the implosion problem.

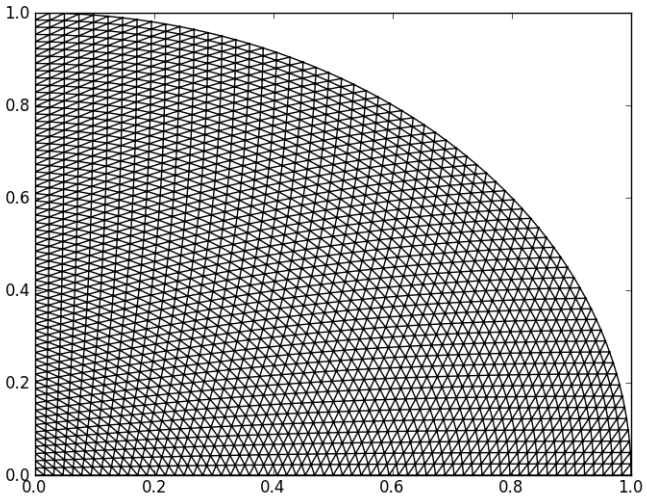

Figure 3.4: Implosion problem, Similar mesh with 2145 points as the one used in numerical simulation. The mesh used in Section IV.2 has been obtained by a refinement of a factor 4 from the present one and contains 33153 ($\approx 4 \times 4 \times 2145$).

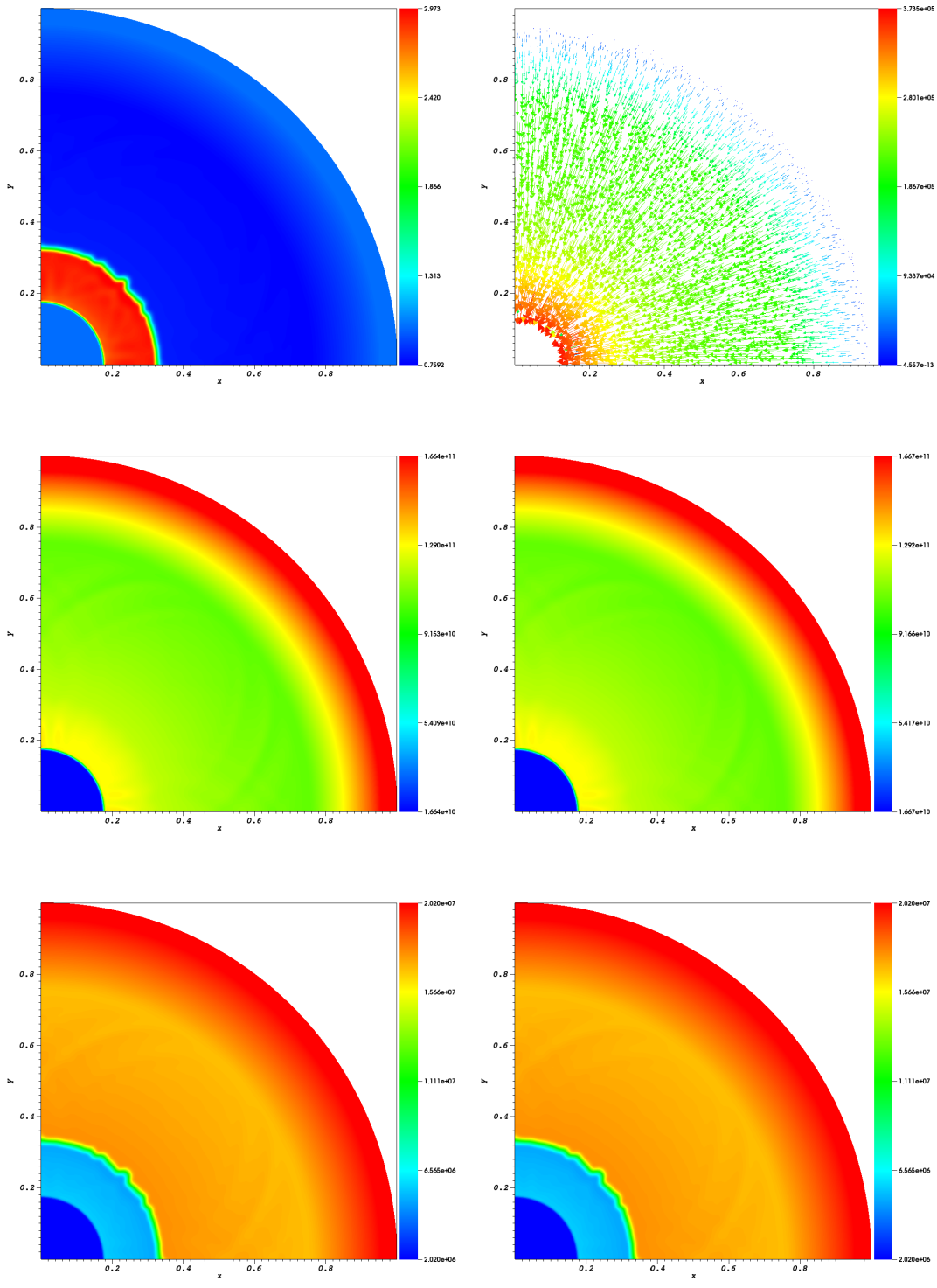

Figure 3.5: Implosion problem at $t_1 = 4.0901 \times 10^{-7} s$. 2-D fields of Left-Top: Density, Right-Top: Velocity, Left-Center: Electronic pressure, Right-Center: Ionic pressure, Left-Bottom: Electronic temperature, Right-Bottom: Ionic temperature.

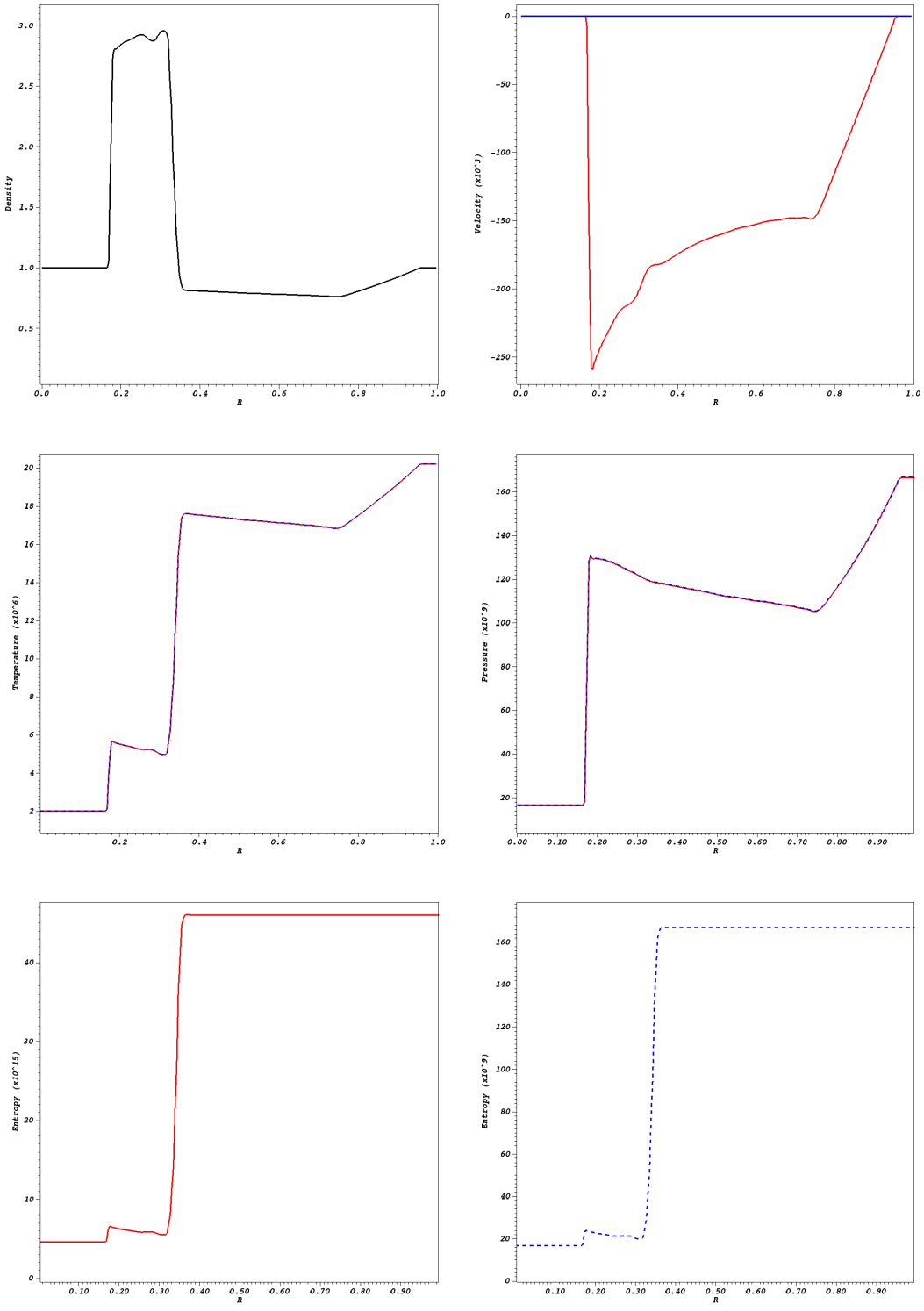

Figure 3.6: Implosion problem at $t_1 = 4.0901 \times 10^{-7} s$. 1-D fields at $y = x$ of Left-Top: Density, Right-Top: Radial (red) and tangential (blue) velocities, Left-Center: Electronic (red) and ionic (blue) temperatures, Right-Center: Electronic (red) and ionic (blue) pressures, Left-Bottom: Electronic entropy, Right-Bottom: Ionic entropy.

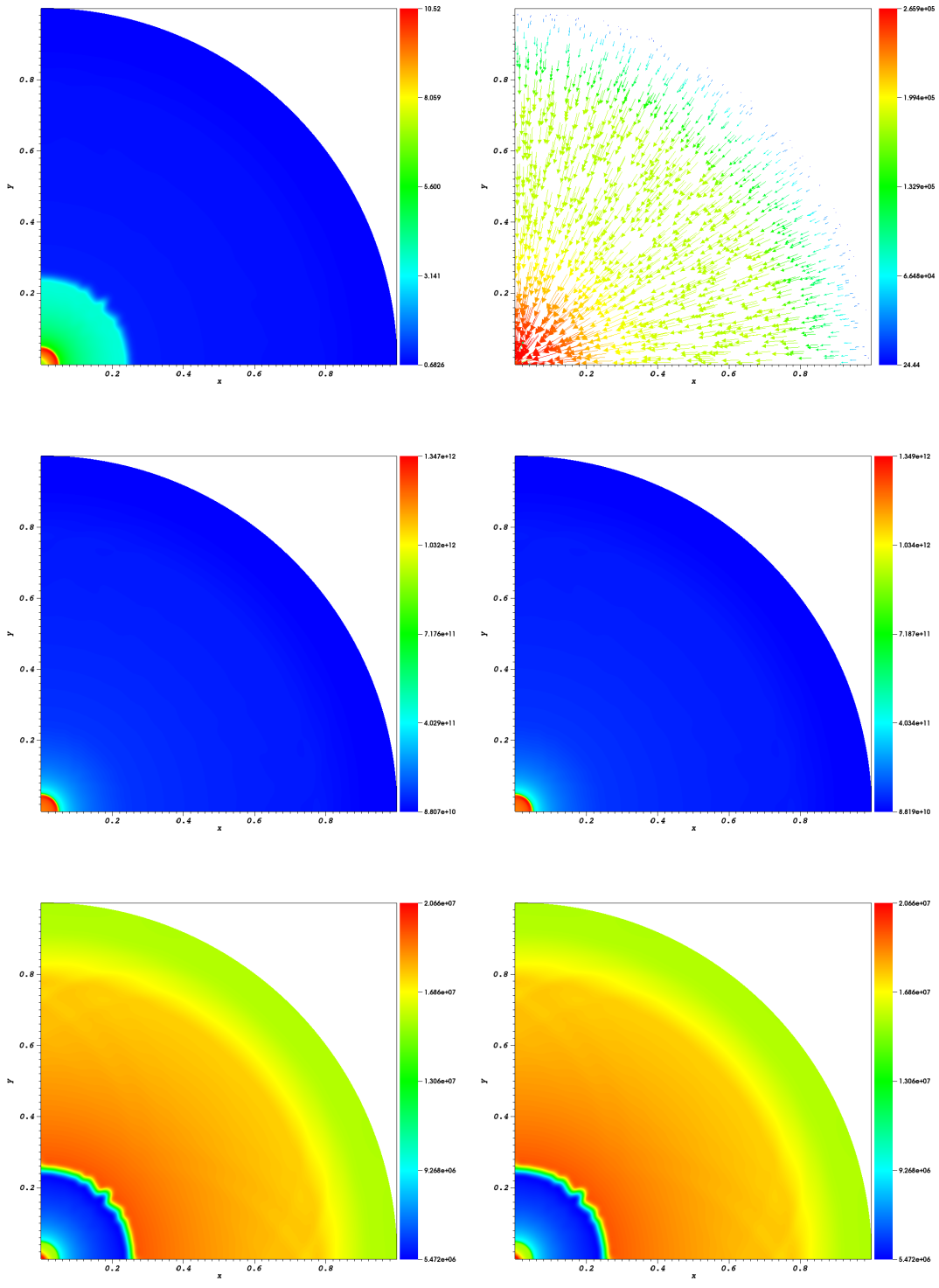

Figure 3.7: Implosion problem at $t_2 = 6.22 \times 10^{-7} s$. 2-D fields of Left-Top: Density, Right-Top: Velocity, Left-Center: Electronic pressure, Right-Center: Ionic pressure, Left-Bottom: Electronic temperature, Right-Bottom: Ionic temperature.

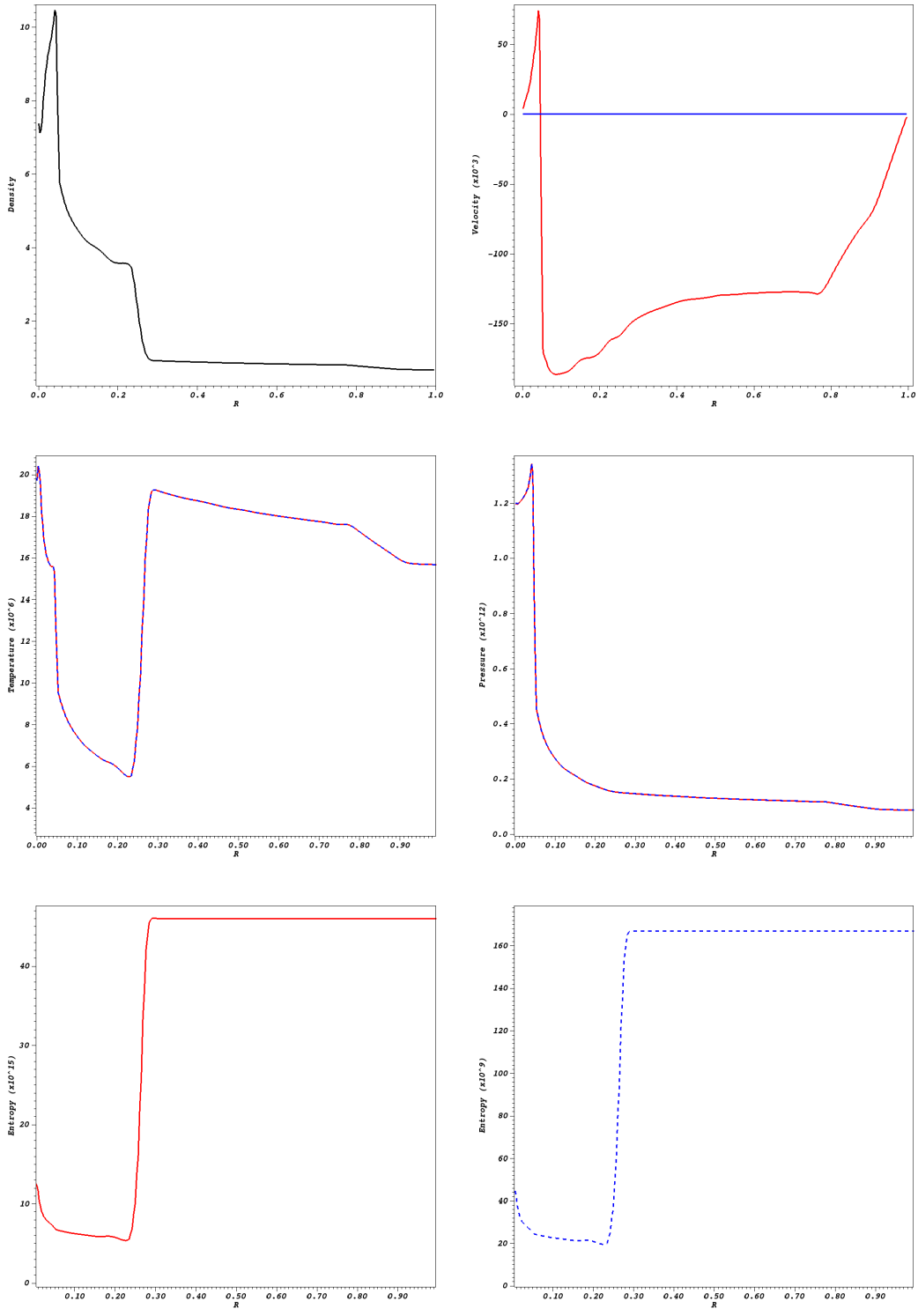

Figure 3.8: Implosion problem at $t_2 = 6.22 \times 10^{-7} s$. 1-D fields at $y = x$ of Left-Top: Density, Right-Top: Radial (red) and tangential (blue) velocities, Left-Center: Electronic (red) and ionic (blue) temperatures, Right-Center: Electronic (red) and ionic (blue) pressures, Left-Bottom: Electronic entropy, Right-Bottom: Ionic entropy.

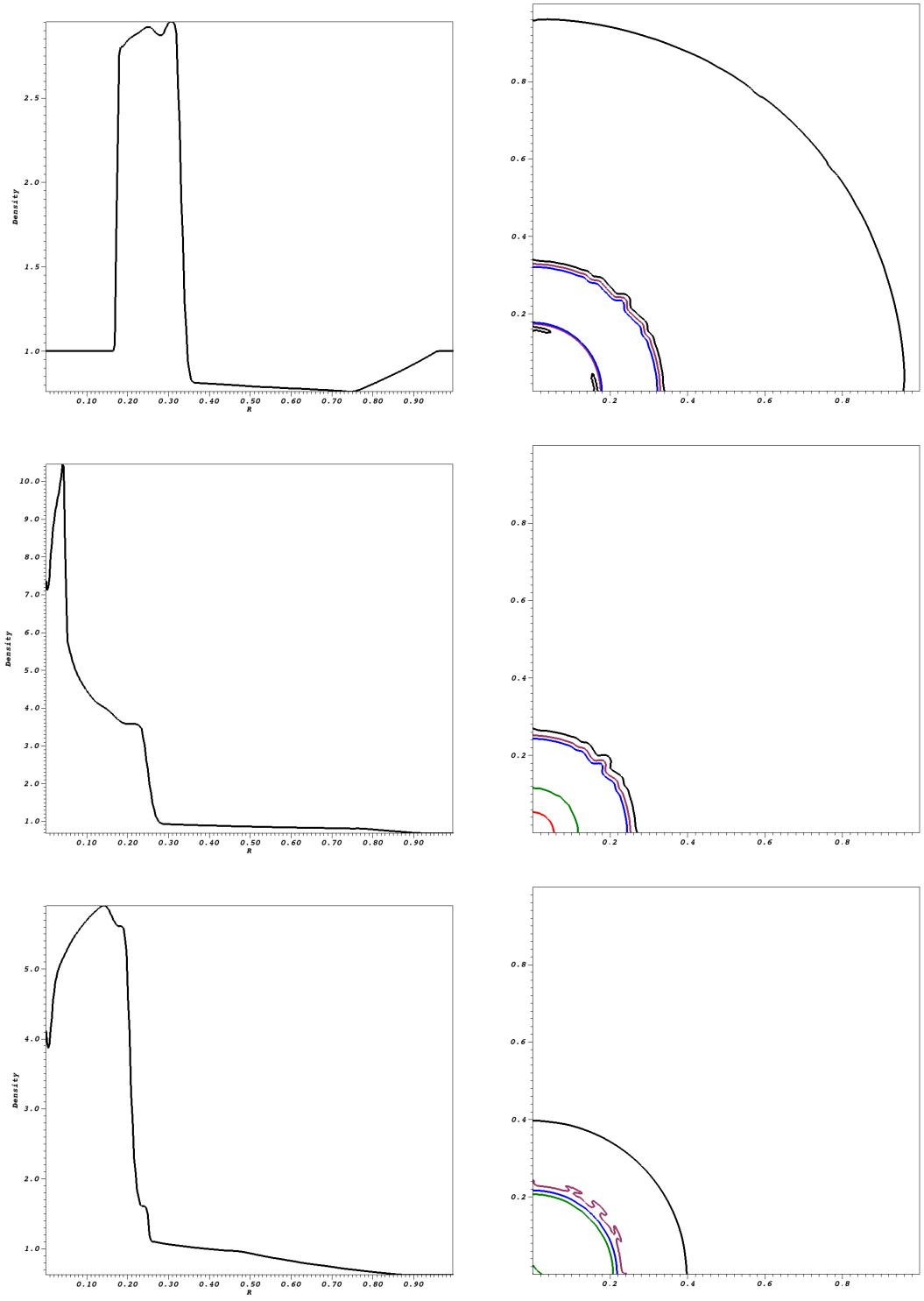

Figure 3.9: Implosion problem, Density, Left: 1-D fields at $y = x$, Right: 2-D isolines at $\rho = 1$ (black), $\rho = 1.585$ (violet), $\rho = 2.369$ (blue), $\rho = 4.259$ (green), and $\rho = 6.047$ (red). Top: $t_1 = 4.0901 \times 10^{-7}s$, Middle: $t_2 = 6.22 \times 10^{-7}s$, Bottom: $t_3 = 8.4973 \times 10^{-7}s$.

IV.3 Sedov injection in 2-D Cartesian geometry

For this test case, a Sedov problem is considered in a uniform medium with cylindrical axisymmetry. It consists the deposit of an intense energy spot in the center of the disc of the uniform medium. Here, we adapt this test from [57, 58] to the bi-temperature model with

$$\left\{ \begin{array}{rcl} T_e & = & 1.7406 \times 10^7 K, \\ T_i & = & 5.802 \times 10^6 K, \end{array} \right.$$

the injection temperature of the electrons and the ions. The temperatures of the rest of the domain are

$$T_e = T_i = 2.901 \times 10^4 K.$$

The rest of the data is given by

$$\left\{ \begin{array}{rcl} \rho & = & 1, \\ \mathbf{u} & = & 0. \end{array} \right.$$

In [57, 58], the domain is a quarter of disc of radius equal to 1. In this simulation, the computational domain is a complete disc of radius equal to 1 meshed with 8321 points with a mesh similar to the one of Figure 3.4. Such a mesh has the property that the points are almost aligned in the R-direction but avoid small cells at the center of the domain. Note also that in contrast with polar meshes, the origin is not a singular point and therefore, since the computation is done on the whole disc, there is no boundary conditions to enforce at the center of the disc which is an interior point. The injection of energy takes place in the cell containing the disc center. The final time of the computation is chosen in order to compare the results to the ones obtained in [57]. Figures 3.10 shows the computed results at $t = 9.7634 \times 10^{-6} s$ that consists of an expanding shock wave. Likewise the implosion problem, the initialization is 2-D in the Cartesian coordinates and the expected solution is 1-D in cylindrical coordinates. As shown in Figure 3.10, the numerical solution respects this property. This is what was expected from the previous test since the loss of the cylindrical symmetry of the computation was shown to occur on contact discontinuity but not on propagating shock waves. Figure 3.11 presents the results of the density and temperatures at three different times.

In Figure 3.11, at the final time, the maximum of density is about 1.2, whereas in [58] the density reaches a maximum around 3.5 and it is shown in [40] that the exact density reaches a maximum of 6. This is due to the fact that the mesh used here is not fine enough.

Concerning the equilibrium between the electronic and ionic temperatures, at the initialization and at the end of the simulation, the relaxation times to reach the same temperature at the injection cell are

$$\left\{ \begin{array}{rcl} t_{init} & = & 1.3 \times 10^{-9} s, \\ t_{end} & = & 2.2 \times 10^{-9} s. \end{array} \right.$$

Therefore, the equilibrium is reached soon after the beginning of the simulation. Figure 3.11 gives a zoom near the origin of the 1-D profiles of the two temperatures at two different times in the beginning of the simulation: The two temperatures attain rapidly a common value on the whole domain as the expanding shock propagates from the disc center.

This test has shown that the numerical method is able to compute a strong expanding shock wave on a 2D Cartesian mesh with no loss of the 1-D cylindrical character of the solution.

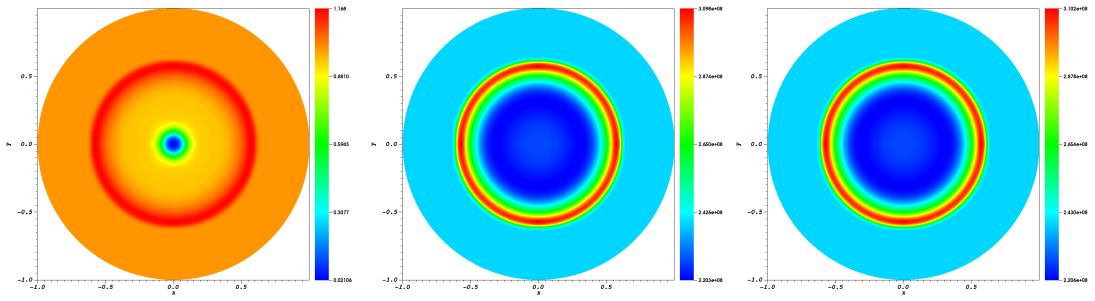

Figure 3.10: Sedov injection in 2-D Cartesian geometry at $t = 9.7634 \times 10^{-6}s$. Left: Density, Center: Electronic pressure, Right: Ionic pressure.

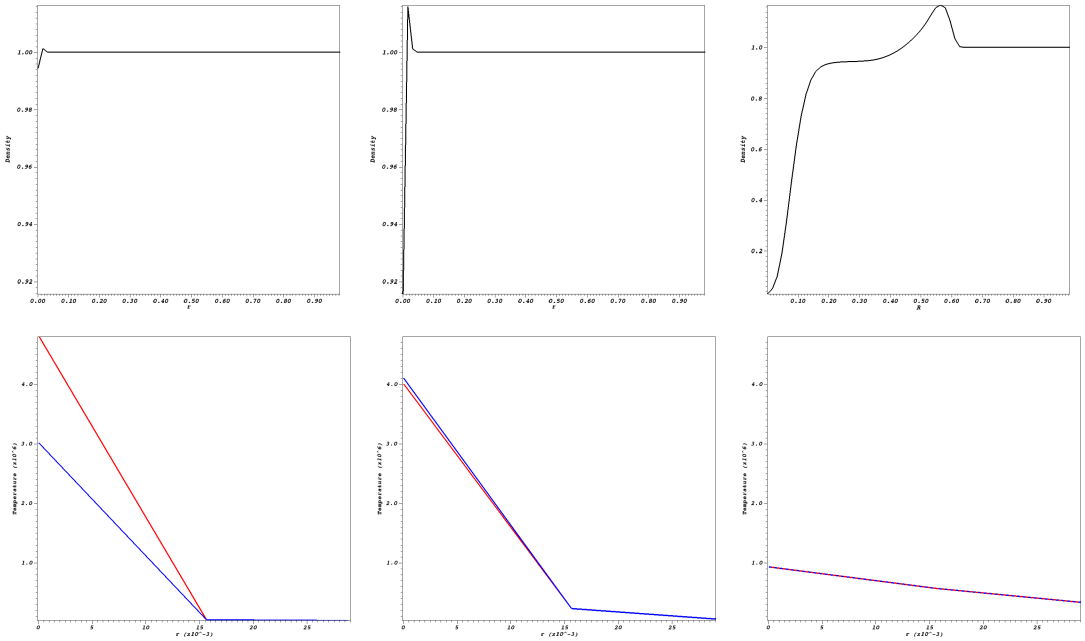

Figure 3.11: Sedov injection in 2-D Cartesian geometry. 1-D profiles at Left: $t = 6.73 \times 10^{-10}s$, Middle: $t = 6.73 \times 10^{-9}s$, Right: $t = 9.7634 \times 10^{-6}s$, Top: Density. Bottom: Electronic (red) and Ionic (blue) temperatures.

IV.4 Sedov injection in a poloidal plane of a torus with axisymmetry initialization

We are now interested in testing the 3D numerical method in cylindrical (R, Z, φ) geometry that we have presented in Section III of Chapter 2. For this, we re-run the previous test where now the considered disc is contained in the poloidal plane of a torus. We assume that the major radius of the torus is 5 and consider two simulations. The first one is a 2D one where we assume that all derivatives in the φ-direction are zero and therefore we use only one poloidal plane to define the computational domain. The second simulation is a true 3D computation where 20 poloidal planes have been used to discretize the toroidal direction. In this case, the initial conditions are axisymmetric in the φ-direction, and do not depend on φ. Therefore, we expect the solution to be axisymmetric for all $t > 0$. The goal of this test is to check that the numerical method does not generate artificial toroidal velocities and does not destroy the axisymmetric character of the solution.

The results are presented at $t = 9.7634 \times 10^{-6} s$ in Figures 3.12.

With respect to the previous simulation, we observe that in a toroidal geometry, the solution is not anymore 1-D in a R, φ-coordinate system. Indeed, we can see that the wave is moving faster on the center of the torus side than on the exterior side. This phenomenon is due to the centripetal force in the torus. On the maximum value of the pressures and the density, we note small differences: the maximum density in the Cartesian case, respectively in the axisymmetric case, is 1.168, respectively 1.145. Then time when the ionic and electronic temperatures become equal is also slightly changed: it is now of $5.5 \times 10^{-8} s$ instead of $5 \times 10^{-8} s$ in the Cartesian case.

As shown in Figure 3.12, the 3-D results are extremely close to the 2-D ones. Indeed there is only a difference of 1×10^{-3} on the extrema of the density of each cases. Moreover, no toroidal velocities has been generated in the 3-D as shown in Figure 3.13 and the solution remains axisymmetric.

We find in the last three runs that our numerical method is able to handle both Cartesian and cylindrical geometries. Indeed, we obtain comparable solutions between the two 2-D runs and the difference observed in the cylindrical runs is due to force created in this geometry. Finally, the 3-D toroidal numerical method has also been validated in getting really close results to the 2-D axisymmetric run.

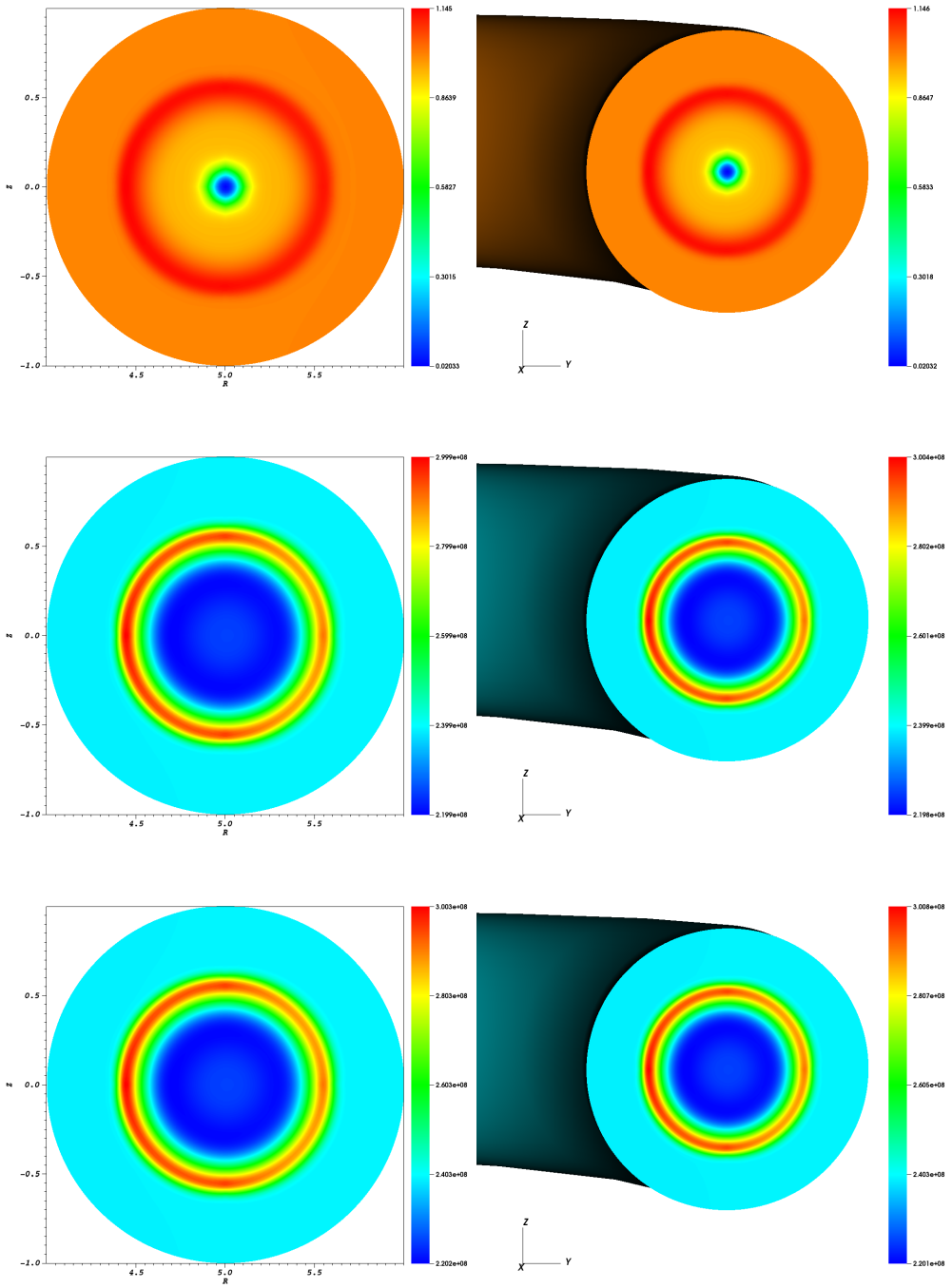

Figure 3.12: Sedov injection in axisymmetric toroidal geometry at $t = 9.7634 \times 10^{-6} s$. Comparison of the 2-D axisymmetric and 3D computations. Left: 2-D run, Right: 3-D run, Top: Density, Center: Electronic pressure, Bottom: Ionic pressure.

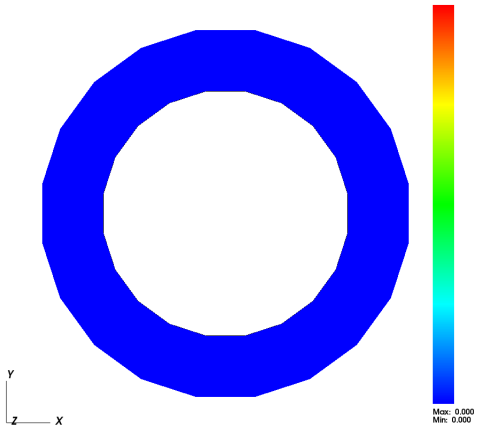

Figure 3.13: Sedov injection in 3-D toroidal geometry, toroidal velocity u_φ at $t = 9.7634 \times 10^{-6} s$ along $Z = 0$.

IV.5 Triple point problem in a rectangular computational domain

The goal of this next experiment is to emphasize that in absence of temperature relaxation, the solution of the bi-temperature model is not identical to the solution of a single temperature model even if the electronic and ionic temperatures are initially equal.

Then, we consider a three state problem, inspired by the test case carried out in [40] and compare their results to the ones of the relaxation scheme. The electronic and ionic pressures are chosen to be equal and correspond to the same total pressure as the one fixed in [40]. The other difference between the two tests is that in our test, the adiabatic index γ is uniform and set equal to $5/3$.

The computational domain is the rectangle $[0,7]\times[-3,3]$ meshed with 70×60 points with symmetric elements around the x-axis. The domain is divided in three different sub-domains Ω_1, Ω_2, and Ω_3. The sub-domain Ω_1 is given by the rectangle $[1,7]\times[-1.5,1.5]$ and contains a high-density and low-pressure fluid. The sub-domain Ω_2 corresponds to the rectangle $[0,1]\times[-3,3]$ and is composed of a high-density and high-pressure fluid. Finally, the sub-domain Ω_3 is the rest of the domain and contains a low-density and low-pressure fluid. This description is summarized in Figure 3.14. In this test, the pressures, time, and density are not express in the S.I. units and have been scale to agree with ICF characteristic ones.

In [40], the evolution of this three-state problem is described: the intersections of the three sub-domains Ω_1, Ω_2, and Ω_3 are located at $(1,-1.5)^T$ and $(1,1.5)^T$, those two points are named triple points. Let us first consider a point located on the interface between Ω_2 and Ω_1 far from the triple points, the initial data generate three waves which are a contact discontinuity, a rightward shock, and a leftward rarefaction. This is also the case for a point on the interface between Ω_2 and Ω_3 far from the triple points. In the case of the interface between Ω_1 and Ω_3, it produces a contact discontinuity. Around the triple points, the situation is quite tricky. Since the different waves are interacting together it leads to a complex 2-D fluid flow. As it is pointed out in [40], the two rightward shock waves of Ω_1 and Ω_3 are not moving at the same sound speed due to their difference of density. Indeed we have $\rho_3 c_{s,3} < \rho_1 c_{s,1}$, then the rightward shock of Ω_3 is moving faster than the Ω_1 one. This creates a strong shear leading to a Kelvin-Helmholtz instability and to the formation of a vortex.

In our simulation, we set $\nu_{ei} = \nu_{ie} = 0$ and leave the ionic and electronic temperatures evolve independently. In Figure 3.15, we compare the results of the internal energy of the mixture given by

$$\varepsilon = \frac{1}{\gamma-1}\frac{p_e+p_i}{\rho},$$

at the time 3.5 and 5 with the results of [40]. We can see that at $t=3.5$ the results obtained with the relaxation scheme for the bi-temperature Euler equations are quite different from the ones of [40] (note that in Figure 3.15 the results of [40] are obtained by two different numerical methods, this is why their results are not symmetric with respect to the $y=0$ axis.) Indeed, Figure 3.16 displays the ratio $\dfrac{T_i-T_e}{T_e}$ at two successive times which shows that the temperatures do not remain identical although $T_i = T_e$ at the initialization, and without the use of thermal exchange in the equations. The same result can be inferred from Figure 3.17 that shows the density, the electronic temperature, and the ionic one at $t=3.5$ and $t=5.0$. This is due to the fact that in the transport step, the electronic entropy jump is assumed to be zero across a shock. Therefore the discontinuous solutions of the two-temperature model are not the same than the ones of the mono-fluid Euler equations

and even if the initial temperatures are equal, in the presence of discontinuous solutions, the bi-temperature Euler model is not equivalent to the mono-fluid Euler model. As we show in Section III, the projection step insure the preservation of the thermal equilibrium.

Likewise the shock tube, we then re-run this test with the thermal exchange terms. As expected, the electronic and ionic temperatures stay equal during all the simulation. In Figure 3.18, we give the final temperature of the case with thermal exchange which we compare to the electronic and ionic temperatures of the case without thermal exchange, those 2-D plots are given at the same scale for each time. In all the cases, the final shape of the temperatures are close to each other. Moreover, the balanced temperature is approximately the average of the electronic and ionic temperatures of the first test. We also compare their densities in Figure 3.19. Likewise, the results are close to each other. Indeed, in the case with thermal exchange, the extrema of the density at $t = 3.5$ are 0.2119 and 3.456 instead of 0.2120 and 3.442 for the case $\nu_{ei} = \nu_{ie} = 0$.

Then this numerical test has shown the importance of the thermal exchange terms in the equations. Indeed, it seems that the balanced temperature corresponds to an average of the electronic and ionic temperatures when those ones are computed without thermal exchange.

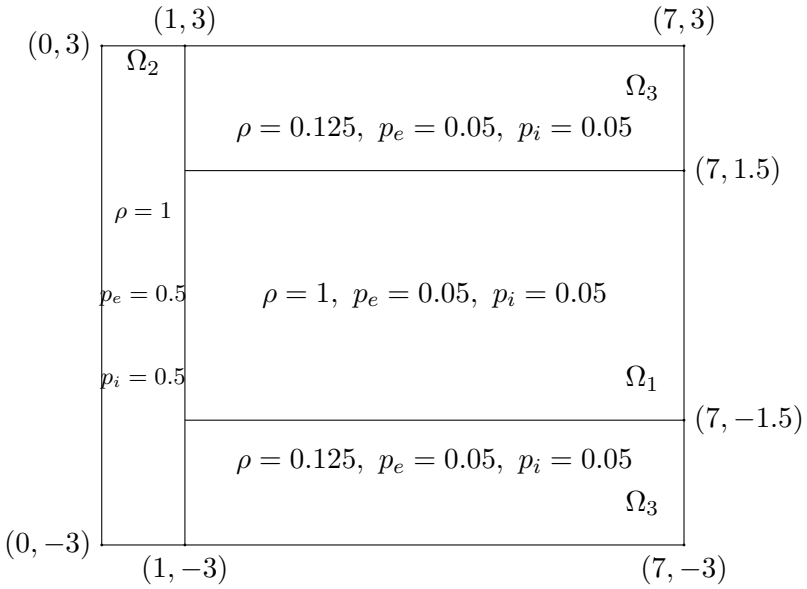

Figure 3.14: Initialization of the triple point problem in a rectangle.

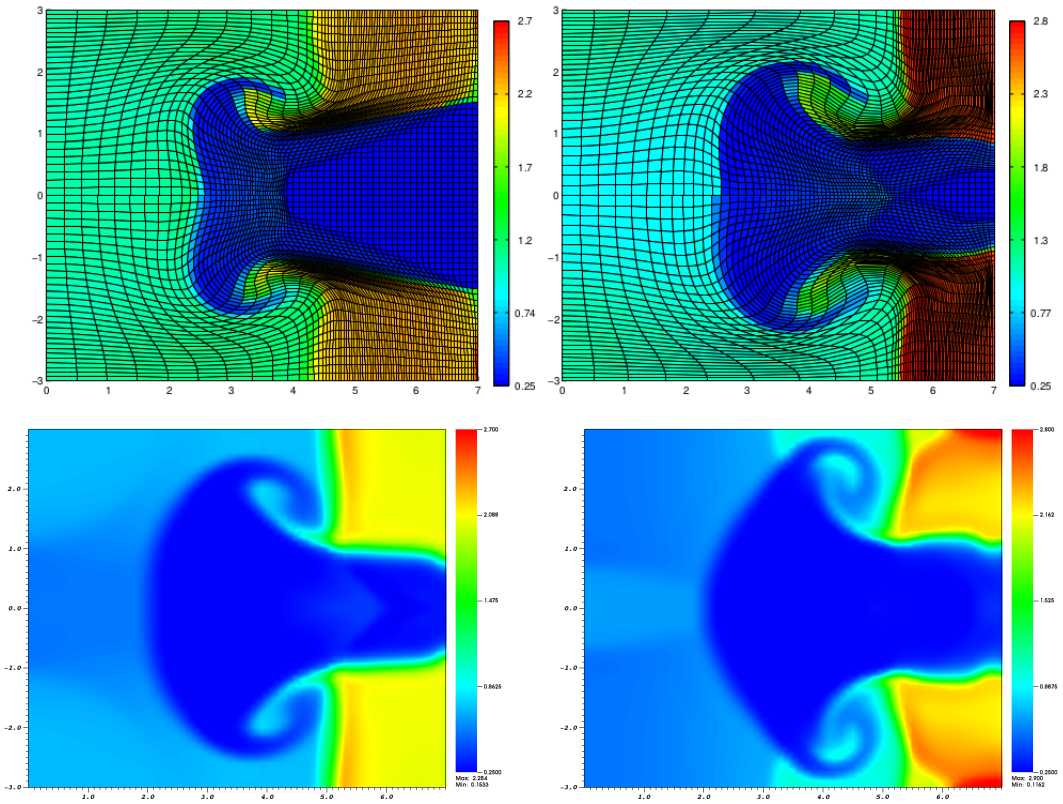

Figure 3.15: Triple point problem total internal energy at $t = 3.5$ (left) and at $t = 5.0$ (right), Top: Results from [40] for mono-temperature Euler equations where the top of the domain is obtained with the Volume of Fluid method and the bottom of the domain with the concentration equations, Bottom: Relaxation scheme for bi-temperature Euler equations with $\nu_{ei} = \nu_{ie} = 0$.

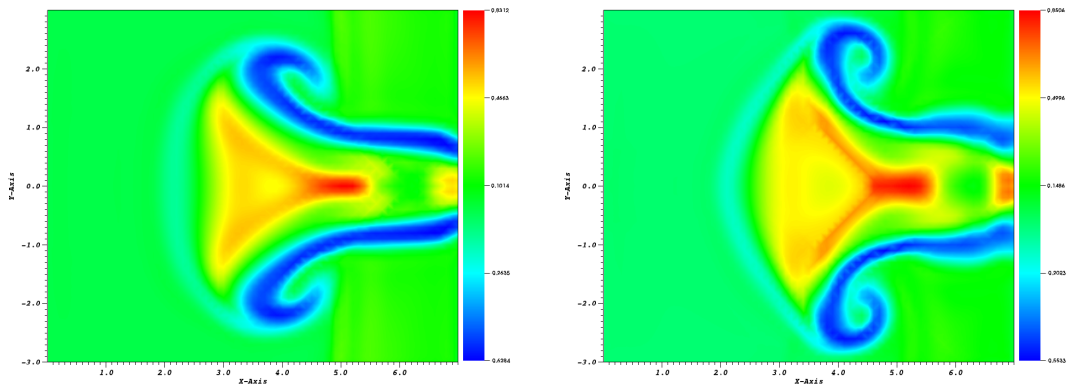

Figure 3.16: Triple point problem without thermal exchange, $\nu_{ei} = \nu_{ie} = 0$, $\dfrac{T_i - T_e}{T_e}$ 2-D field at $t = 3.5$ (Left), and $t = 5.0$ (Right).

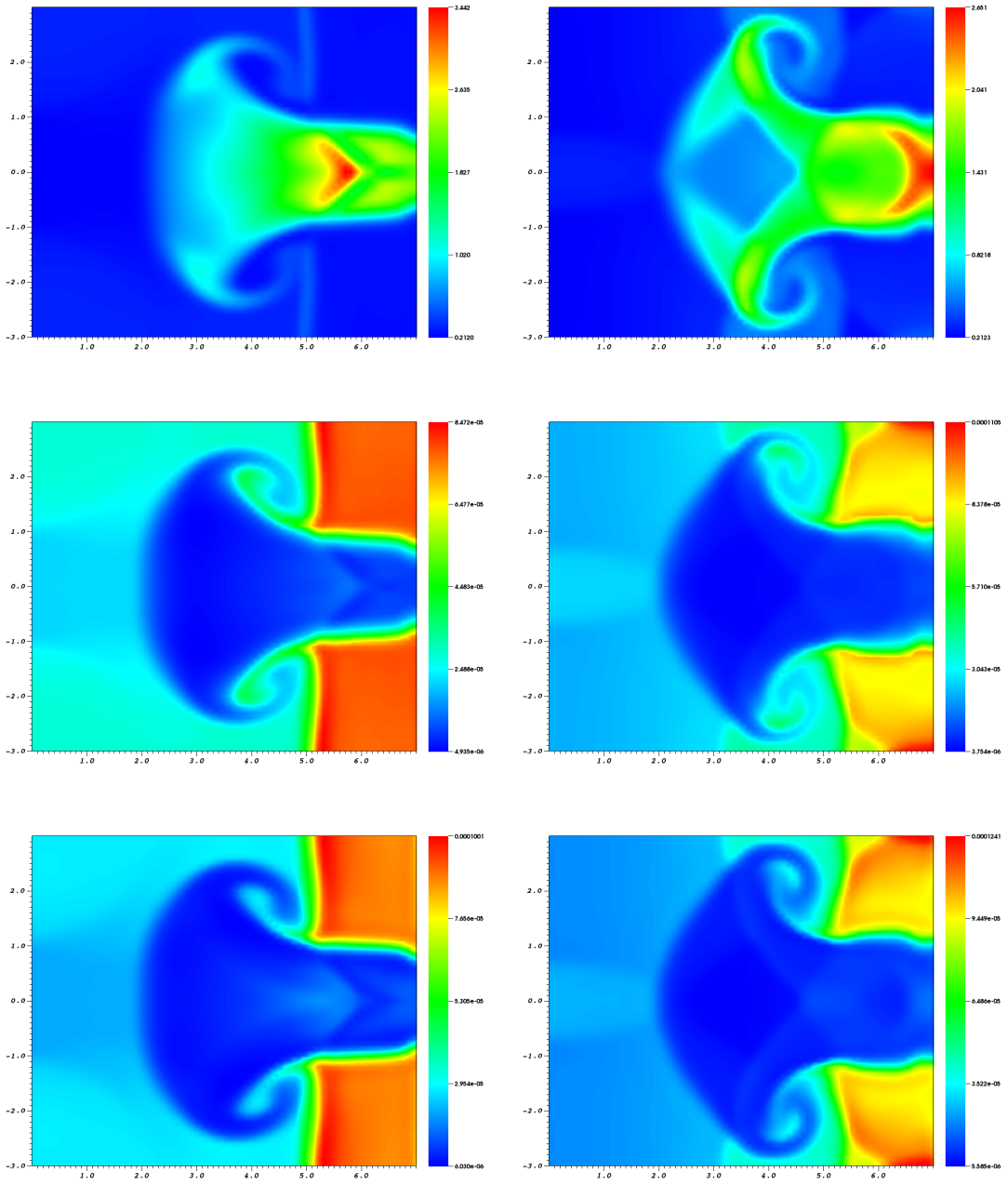

Figure 3.17: Triple point problem with $\nu_{ei} = \nu_{ie} = 0$ at $t = 3.5$ (Left), and $t = 5$ (Right). 2-D fields of Top: Density, Middle: Electronic temperature, Bottom: Ionic temperature.

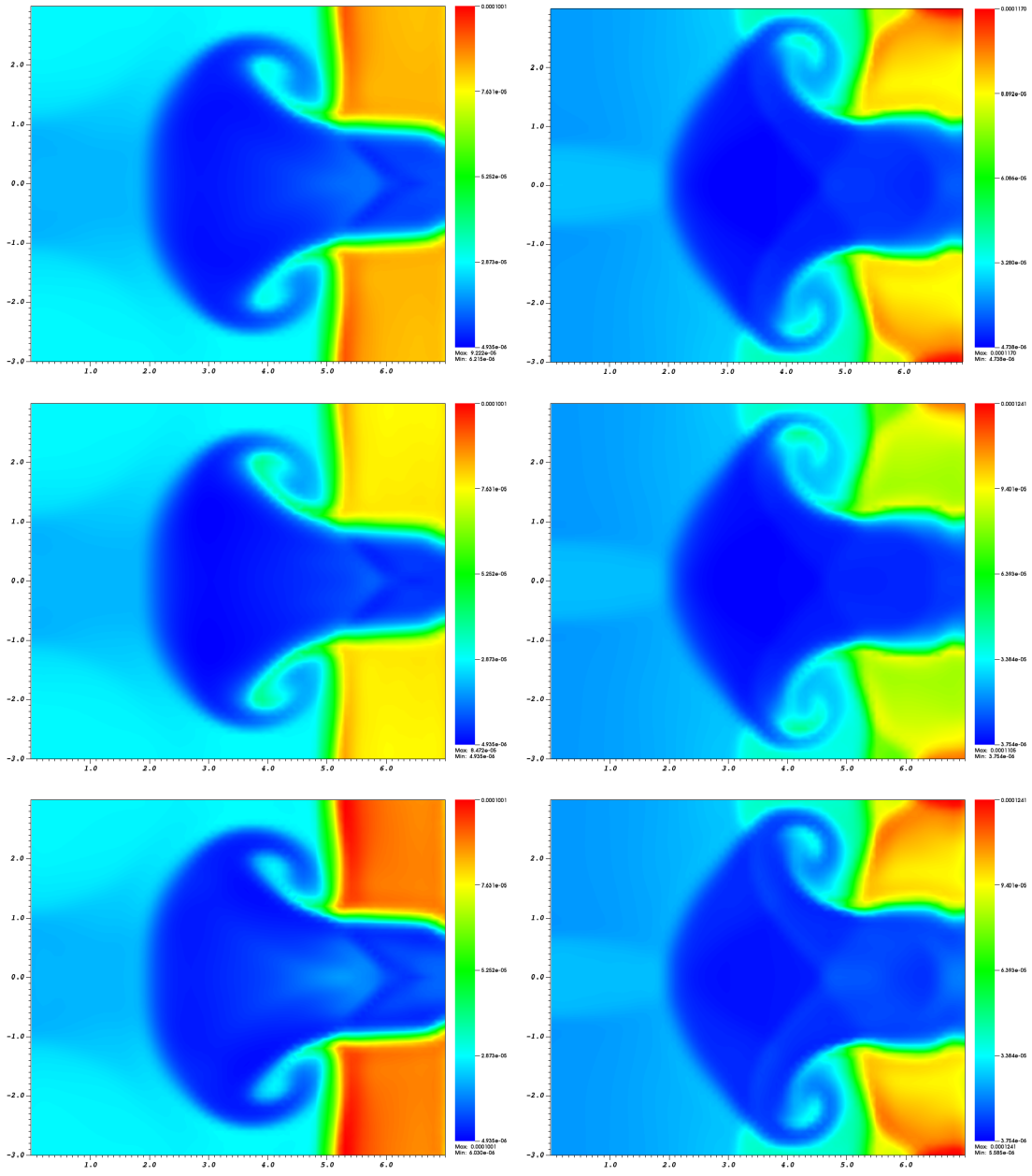

Figure 3.18: Triple point in a rectangular domain at $t = 3.5$ (left) and $t = 5.0$ (right). Comparison between the temperature of the case $\nu_{ei} \neq 0$ and $\nu_{ie} \neq 0$ (Top) and the electronic (middle) and ionic (bottom) temperatures of the case $\nu_{ei} = \nu_{ie} = 0$.

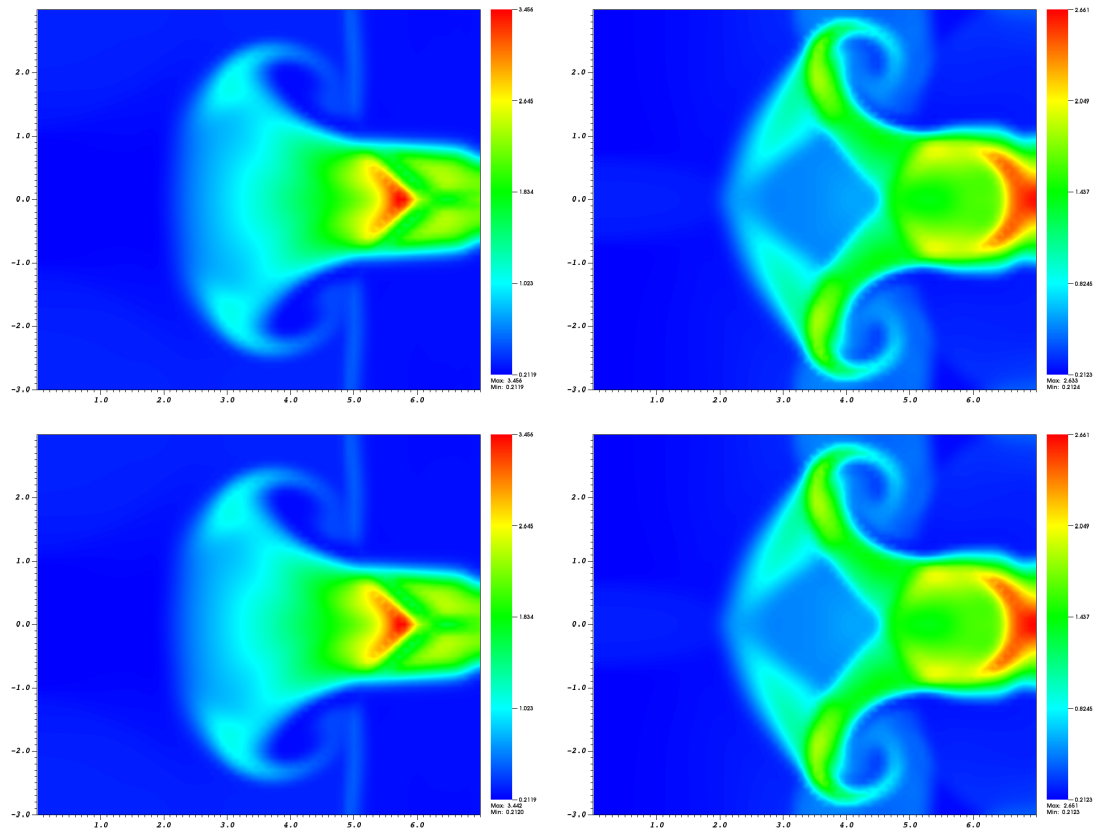

Figure 3.19: Triple point in a rectangular domain at $t = 3.5$ (left) and $t = 5.0$ (right). Comparison between the density of the case $\nu_{ei} \neq 0$ and $\nu_{ie} \neq 0$ (Top) and the one of the case $\nu_{ei} = \nu_{ie} = 0$ (Bottom).

IV.6 Triple point problem in a disc in 2-D Cartesian geometry

Here we consider a triple point problem in a different geometry as a preliminary test for studying some problems of injection in tokamaks where very cold and dense cryogenic Deuterium/Tritium mixtures known as pellets are injected in a hot plasma. We first consider a problem in Cartesian geometry. The computational domain is now a disc of radius 1 meshed with 1435 cells. Figure 3.20 and Table 3.3 summarize the setting of the problem: the sub-domain Ω_1 is initially a domain of high density and low temperatures, it is given by the disc of radius 0.1414 of center point $(0.5, -0.5)$. The sub-domain Ω_3 is characterized by a low density and high temperatures and defined by the disc of center $(0, 0)$ and radius equal to 0.707 without the part Ω_1 of this disc. Finally, the sub-domain Ω_2 is the rest of the computational domain, its density and temperatures are chosen to be between the density and temperatures of the other two domains.

	ρ	$\mathbf{u}$	T_e(K)	T_i(K)	$p_e + p_i(Pa)$
Ω_1	3	0	3.4812×10^6	2.3208×10^6	1.4348×10^{11}
Ω_2	1	0	2.78496×10^7	1.85664×10^7	3.8262×10^{11}
Ω_3	0.5	0	3.4812×10^7	2.3208×10^7	2.3914×10^{11}

Table 3.3: Initial data of the three states of the triple points problem.

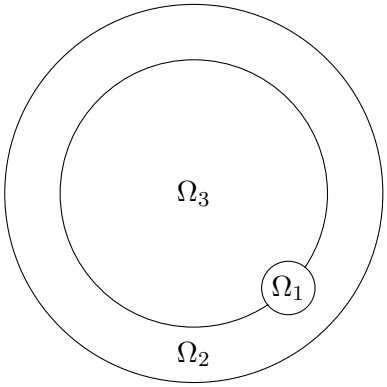

Figure 3.20: The three domain of the triple point problem in the (R, Z) plane.

We first comment on the differences in ionic and electronic temperatures for this test case. According to the formula (3.7) giving the temperature relaxation times, the equilibrium time varies as $T^{3/2}$. More precisely, at time $t = 0$, the temperature relaxation times in the three domains are

$$\begin{cases} t_{\Omega_1} &= 8.51 \times 10^{-11} s, \\ t_{\Omega_2} &= 3.86 \times 10^{-9} s, \\ t_{\Omega_3} &= 1.00 \times 10^{-8} s. \end{cases} \tag{3.10}$$

Hence we expect temperature equilibrium to be reached rapidly in domain Ω_1 while domain Ω_3 will be the last one where temperature equilibrium will occur.

Figure 3.21 displays the ratio $\dfrac{T_i - T_e}{T_e}$ at three different times.

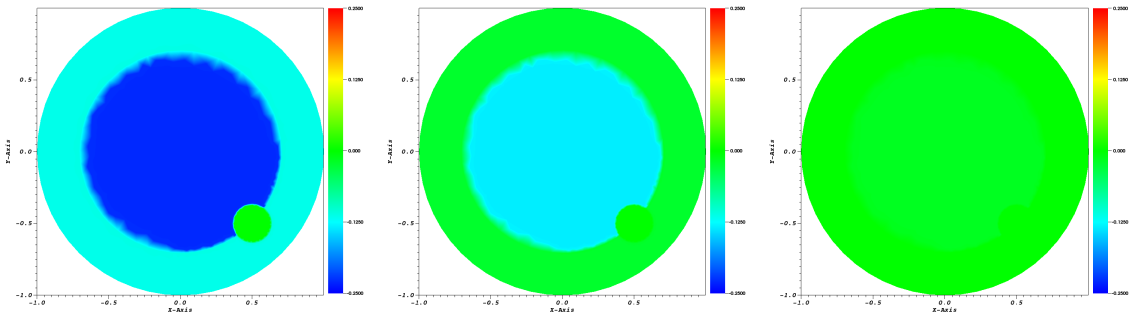

Figure 3.21: Triple point problem in Cartesian geometry. $\dfrac{T_i - T_e}{T_e}$ 2-D fields at $t = 2.1 \times 10^{-9} s$ (left), $t = 4.7 \times 10^{-9} s$ (middle), and $t = 1.35 \times 10^{-8} s$ (right).

At $t = 2.1 \times 10^{-9} s$, we can see that only the sub-domain Ω_1 gets equal temperatures. Then, at $t = 4.7 \times 10^{-9} s$, the cold and the intermediate sub-domains have reached the equilibrium. Finally, after $t = 1.35 \times 10^{-8} s$, the electronic and the ionic temperatures are equal in all the domain.

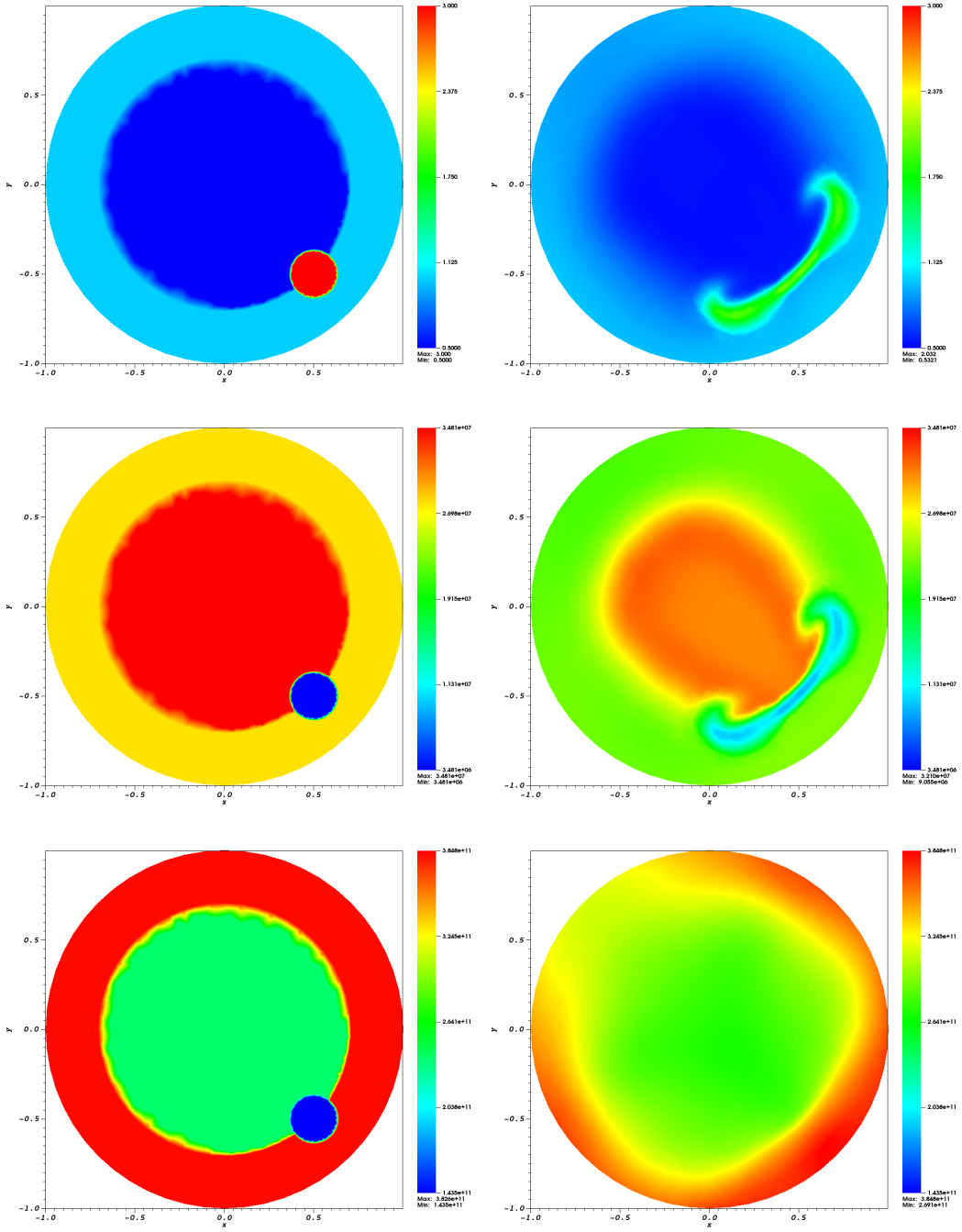

Figure 3.22: Triple point problem in Cartesian geometry. Initial data (Left) and solution at $t = 1.1574 \times 10^{-5} s$ (Right). Top: Density, Center: Electronic temperature, Bottom: Total pressure.

The results are at $t = 1.1574 \times 10^{-5} s$, and are given in Figure 3.22. The initial cold and dense domain Ω_1 corresponds to a zone of low pressure. Therefore it has been crushed by the high pressure neighboring zones and has expanded mainly in the angular direction. Another noticeable result is that at this time, the density and temperatures have been smoothed out: while the initial density was in the interval $[0.5, 3]$, it is now between 0.5321 and 2.032 and the same smoothing effect can be noticed for the temperature. This effect is mainly due to pressure reflection on the boundary of the domain. Indeed, a rough estimate of the sound speed at time $t = 0$ ($c_s \approx 8.92816 \times 10^5 m.s^{-1}$) shows that at $t = 1.1574 \times 10^{-5} s$, pressure waves have crossed the domain around 5 times leading to a smoothing of the density and temperature fields.

IV.7 Triple point problem in the plane of a torus with axisymmetry initialization

As in Section IV.4 we now reproduce the previous test case in the geometry of a torus. The aim of this test case is to see the influence of the geometry. We set the major radius of the torus at 3. As in Section IV.4, we have performed two simulations: the first one is a pure 2-D axisymmetric computation while the second is a true 3-D one where the toroidal direction has been discretized with 20 planes. As in Section IV.4 we have checked that the 3-D runs maintain the 2-D axisymmetric character of the solution and that no toroidal velocities have been created.

Since the results between the 3-D and the 2-D axisymmetric are extremely close, we present only the ones of the 2-D axisymmetric simulation.

The results are given in Figure 3.23. We see that the average domain Ω_2 expends more to the initial hot domain in the area closer to the center of the torus. This phenomenon can be due to centripetal or centrifugal forces. Moreover, the final temperatures are quite different of the 2-D Cartesian case. Indeed, for the cold domain, we obtain $8.738 \times 10^6 K$ for the electronic and ionic temperatures of the cold domain instead of $9.055 \times 10^6 K$. Then, we can suppose that the evolution is slower in the cylindrical case than in the Cartesian one. We also remark, that the final shape of the cold domain Ω_1 is not anymore symmetric and the temperature is hotter closer to torus center than to the exterior side. Likewise, the density is higher in the torus center zone than the exterior, and the final value of the domain Ω_1 is 2.092 instead of 2.032. In fact, the cold domain seems to move to the exterior of the torus. At the end of the simulation, as expected the electronic and ionic temperatures are balanced. In Figure 3.24, we compare the velocity in the poloidal plane (R, Z) to the one of the Cartesian run. We can see that for the cylindrical geometry, the velocity is around twice the maximum of velocity of the Cartesian run. Indeed, around the border between the hot domain and the average domain closer to the center of the torus, the velocity of the axisymmetric run is about four times the one of the Cartesian geometry.

It follows from the above two last numerical tests that the geometry is an important input, since it largely modifies quantitatively and qualitatively the behavior of the velocity field, and this the whole set of results.

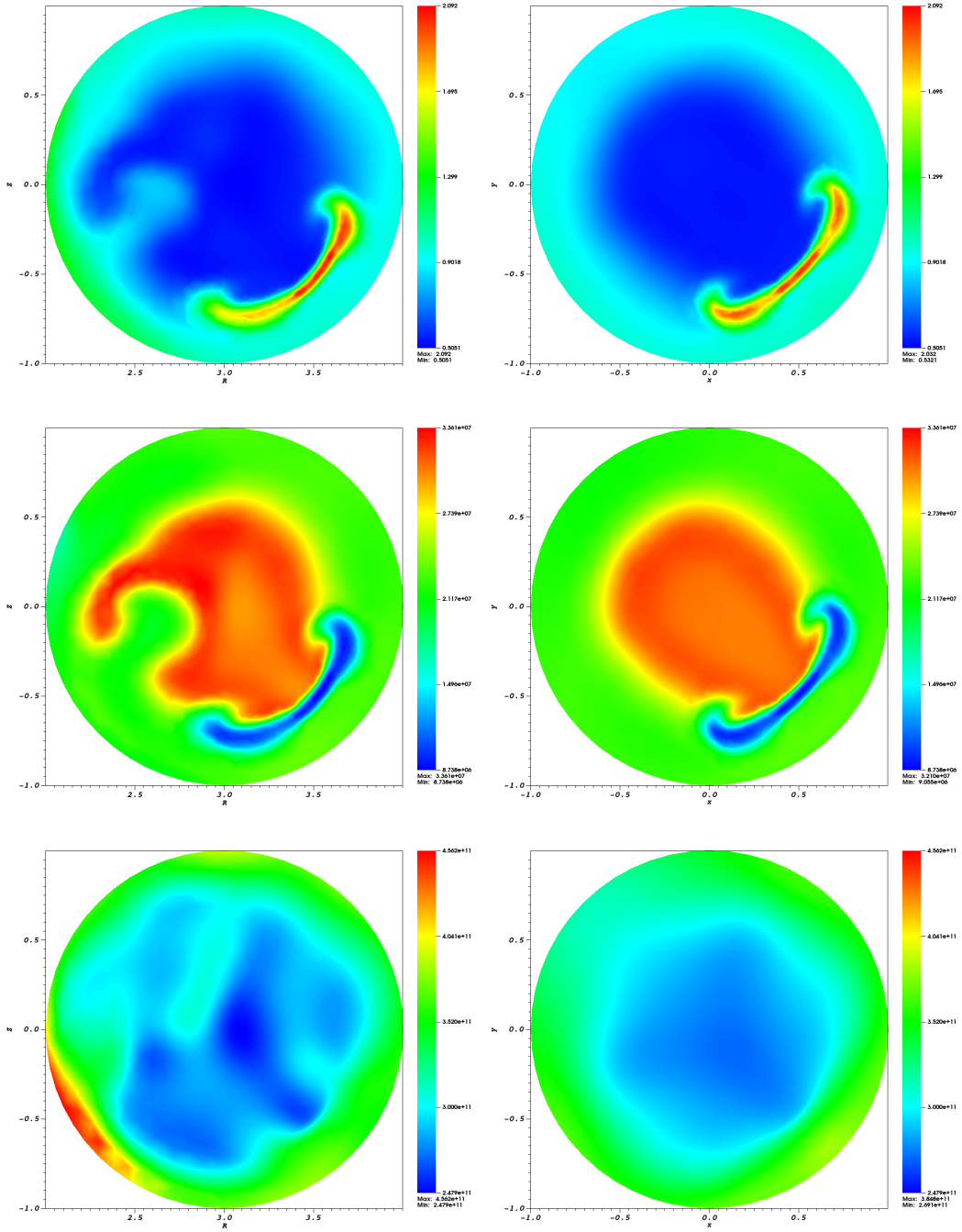

Figure 3.23: Triple point problem at $t = 1.1574 \times 10^{-5} s$. Comparison of the results obtained in Cartesian geometry and in a torus. Left: 2-D axisymmetric run, Right: 2-D Cartesian run. Top: Density, Center: Electronic temperature, Bottom: Total pressure.

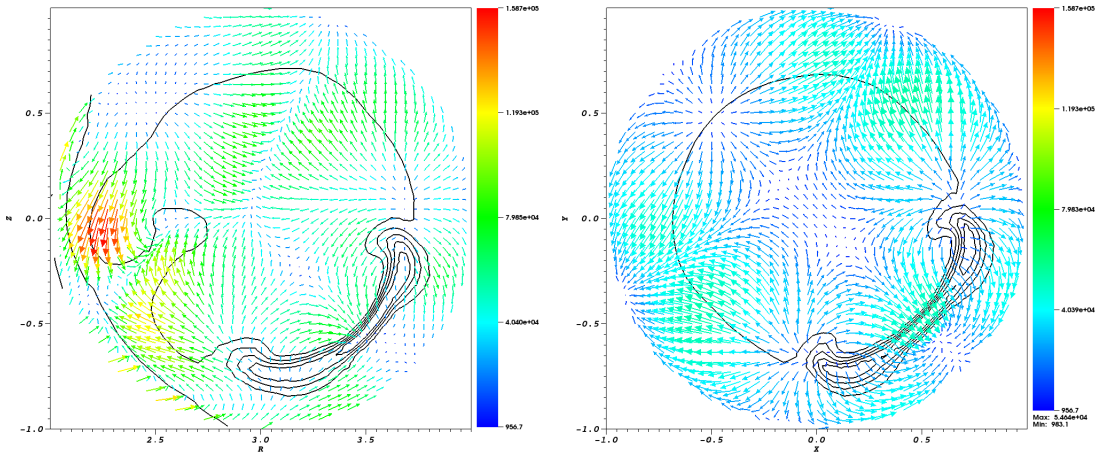

Figure 3.24: Triple point problem at $t = 1.1574 \times 10^{-5} s$. Comparison of the results obtained in Cartesian geometry and in a torus. Velocity vectors with density contours. Left: 2-D axisymmetric run, Right: 2-D Cartesian run.

IV.8 Triple point problem in 3-D toroidal geometry

Here, we propose a fully 3-D numerical test in toroidal geometry. This test is based on the two previous cases, but instead of having an axisymmetric initialization, we consider that the initial cold and dense zone is a small cylinder. The periodic toroidal direction is meshed in a regular manner with 20 points and we assume that the zone where the cylinder is localized corresponds to the angular domain $[0, 3 \times 2\pi/20]$. In the domain where the cylinder is localized, a three state initialization is used while in the rest of the domain the fields are described by two different states. The different domains of the poloidal plans are described in Figures 3.25 and 3.26, and the initialization used for the domain Ω_1, Ω_2, and Ω_3 is given in Table 3.3. The three poloidal planes that intersect the cylinder as numbered as the poloidal planes 1, 2, and 3. Then, the two neighboring planes are numbered the planes 4 and 20.

Figure 3.27 to Figure 3.29 display the results in the planes 1 to 3, 4 and 20 and 10. Its shows that the extrema are reduced with respect to the 2D case. For instance, in the 3D case, the extrema are 0.46 and 1.867 instead of 0.5051 and 2.092 in the 2D axisymmetric case. But, globally, the evolution of the solution is similar to the one described for an axisymmetric initial state except for the total pressure. We can however note that we have a 3 dimensional effect in the toroidal direction leading to a increased smoothing of the extrema in the 3D case although this effect seems to be weak, up to this time. Such a computation would require a much denser mesh in the toroidal direction to give meaningful results.

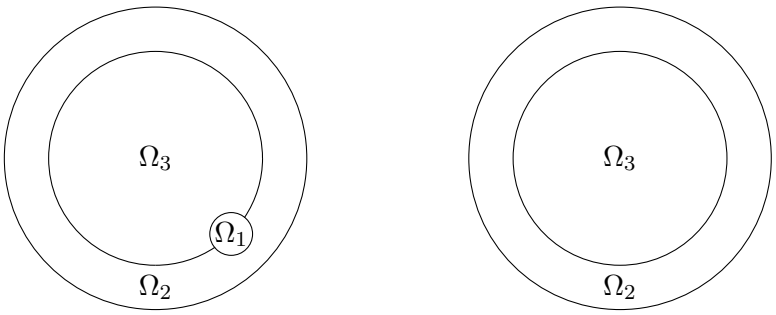

Figure 3.25: Triple point problem initial domain in 3-D toroidal geometry. Left: for the poloidal planes 1 to 3. Right: for the rest of the poloidal planes (4 to 20).

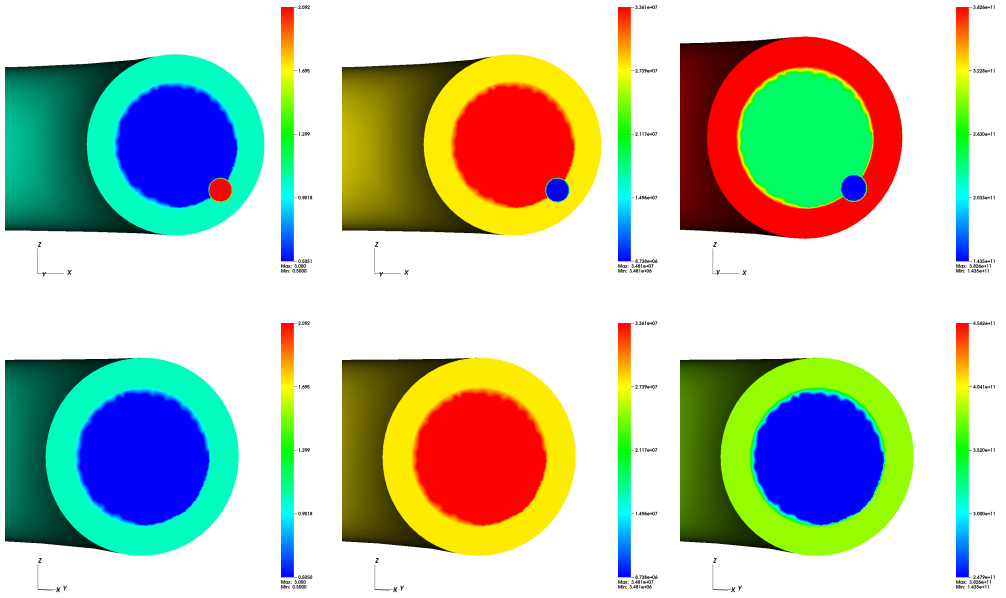

Figure 3.26: Triple point problem initialization. Top: Poloidal planes 1 to 3, Bottom: Poloidal planes 4 to 20. Left: Density, Center: Electronic temperature, Right: Total pressure.

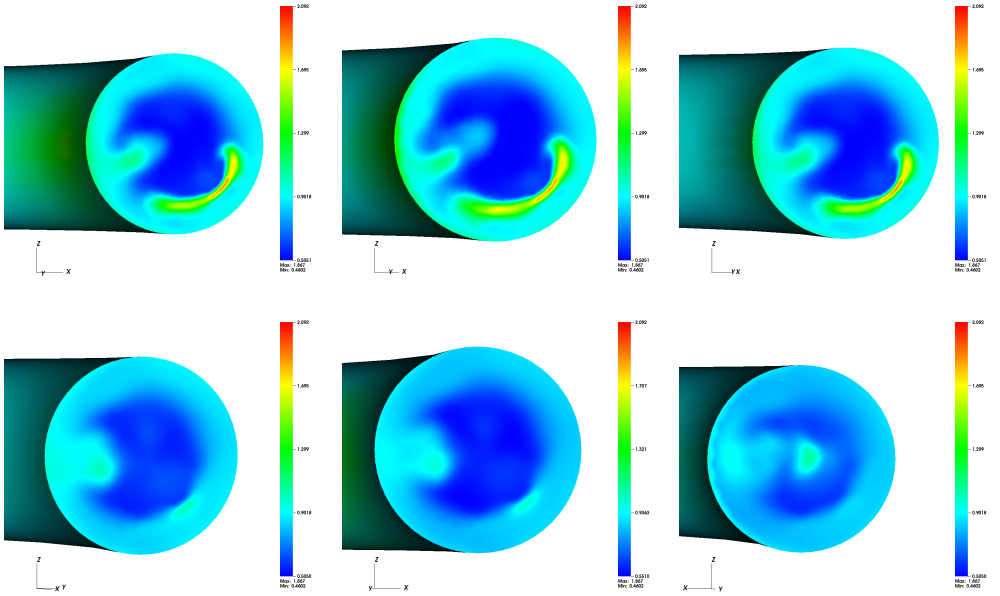

Figure 3.27: Triple point problem in 3-D toroidal geometry. Density at $t = 1.1574 \times 10^{-5} s$. Top-Left: Plane 1, Top-Center: Plane 2, Top-Right: Plane 3, Bottom-Left: Plane 4, Bottom-Center: Plane 20, Bottom-Right: Plane 10.

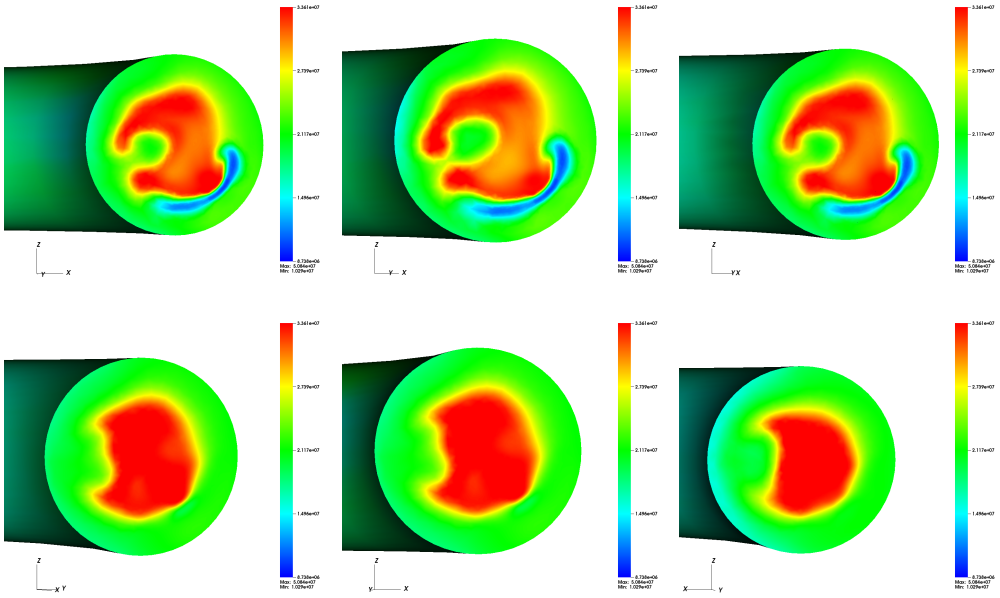

Figure 3.28: Triple point problem in 3-D toroidal geometry. Electronic temperature at $t = 1.1574 \times 10^{-5} s$. Top-Left: Plane 1, Top-Center: Plane 2, Top-Right: Plane 3, Bottom-Left: Plane 4, Bottom-Center: Plane 20, Bottom-Right: Plane 10.

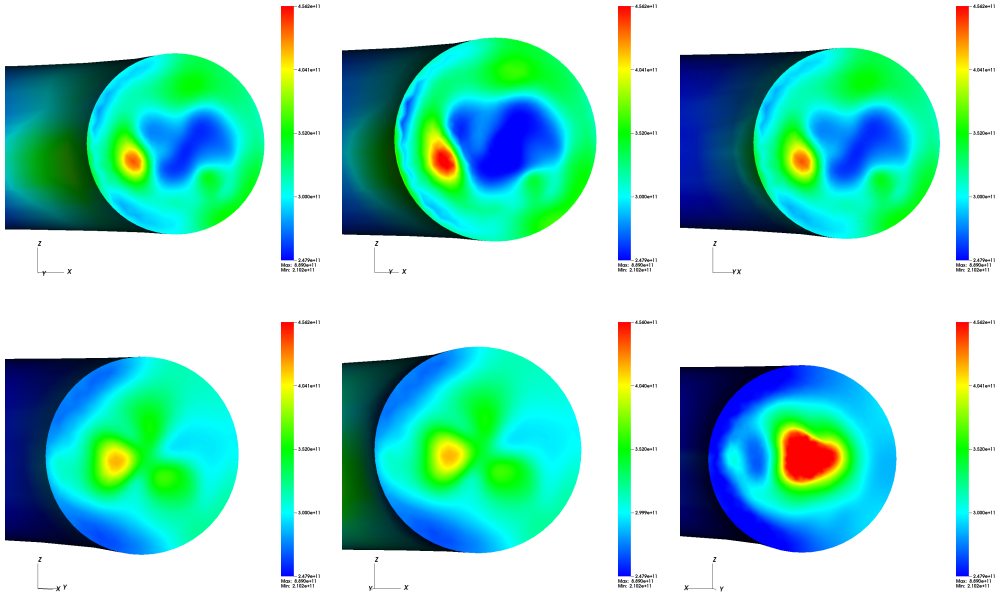

Figure 3.29: Triple point problem in 3-D toroidal geometry. Total pressure at $t = 1.1574 \times 10^{-5} s$. Top-Left: Plane 1, Top-Center: Plane 2, Top-Right: Plane 3, Bottom-Left: Plane 4, Bottom-Center: Plane 20, Bottom-Right: Plane 10.

V Conclusions

In this Chapter, we have studied a numerical scheme for the approximation of T_i-T_e model of Chapter 1. This model considers the ion-electron mixture as a single fluid but retains two temperature or energy equations to describe the thermodynamics of the mixture. We have proposed a relaxation scheme to solve the bi-temperature Euler equations in Cartesian as well as in cylindrical coordinates by a finite volume method. The interest for cylindrical coordinate system is motivated by possible future applications to MCF and tokamaks.

Finally, we have presented several different numerical tests using the two coordinate systems and different geometries. The results have shown that the numerical scheme is able to simulate problems with large densities and pressure differences as well as fast phenomena. In the geometry of a torus, the proposed finite volume method has been tested on 3D test cases and has demonstrated its capability to respect the axisymmetric character of the solutions which is an important point for MCF applications. Future work on this topic will involve its extension to bounded plasma β parameter and the introduction of magnetic field and dissipative terms.

Chapter 4

On Euler potential for MHD models

The aim of this Chapter is to built a numerical strategy able to solve the ideal and resistive MHD equations and to maintain the $\nabla \cdot \mathbf{B} = 0$ constraint. There exists a lot of strategies dealing with the divergence-free constraint and we re-call some of them in a first part. Using those methods, we propose a numerical scheme for the ideal and resistive MHD models and finally we test it with well-known MHD numerical tests both for Cartesian and cylindrical coordinates.

I Issues on the divergence-free constraint

We have seen in Chapter 1 that the MHD equations are a combination of the hydrodynamic equations and of the Maxwell's one (1.35). By taking the divergence of the Maxwell-Faraday equations we obtain

$$\partial_t(\nabla \cdot \mathbf{B}) = -\nabla \cdot (\nabla \times \mathbf{E}) = 0,$$

that shows that if

$$\nabla \cdot \mathbf{B} = 0, \text{ at } t = 0 \ \Rightarrow \forall t, \ \nabla \cdot \mathbf{B}(t) = 0.$$

This equation is a main issue in the numerical approximation of solutions of MHD equations. It has been reported in [11, 23, 42], that without cautions, the errors on $\nabla \cdot \mathbf{B}$ grow in time leading to an nonphysical system.

Nowadays, there exists two families of methods to solve the divergence-free problem: vector potential $\mathbf{A}$, and divergence cleaning-type methods.

I.1 Vector potential A method

This method consists to use the property $\nabla \cdot (\nabla \times \cdot) = 0$ in order to re-write the magnetic field $\mathbf{B}$ under the form of the curl of a vector potential $\mathbf{A}$:

$$\mathbf{B} = \nabla \times \mathbf{A}.$$

In [42], the magnetic field $\mathbf{B}$ is replaced by $\mathbf{A}$ in the ideal MHD system (1.96), the resulting system is then given by

$$\begin{cases} \partial_t \rho + \nabla \cdot (\rho \mathbf{u}) & = & 0, \\ \partial_t (\rho \mathbf{u}) + \nabla \cdot [\rho \mathbf{u} \otimes \mathbf{u} - (\nabla \times \mathbf{A}) \otimes (\nabla \times \mathbf{A})] + \nabla \left[p + \frac{1}{2} (\nabla \times \mathbf{A})^2 \right] & = & 0, \\ \partial_t \mathcal{E}_T + \nabla \cdot \left[\left(\mathcal{E} + p + (\nabla \times \mathbf{A})^2 \right) \mathbf{u} - [\mathbf{u} \cdot (\nabla \times \mathbf{A})] \nabla \times \mathbf{A} \right] & = & 0, \\ \partial_t \mathbf{A} - \mathbf{u} \times (\nabla \times \mathbf{A}) & = & -\nabla U, \end{cases}$$

where U is the electric potential.

With this method, we insure to maintain the divergence-free constraint. However, as we can see in the previous system the spatial derivative order has increased of one order, and in the induction equation, the electric potential U appears and has to be computed by the choice of a gauge condition. As it is pointed out in [42], the boundary conditions have to be evaluated for $\mathbf{A}$ instead of $\mathbf{B}$ in ghost cells. This problem is not so obvious however it can be solved by imposing the flux at the boundary interfaces. Finally, for numerical scheme using Riemann solver, it can be difficult to use the vector potential $\mathbf{A}$ as a basic variable instead of the magnetic field $\mathbf{B}$.

I.2 Powell's source term

Originally presented in [66], in this method a source term proportional to the divergence of the magnetic field is added to ideal MHD equations. The result is given by

$$\begin{cases} \partial_t \rho + \nabla \cdot (\rho \mathbf{u}) & = & 0, \\ \partial_t (\rho \mathbf{u}) + \nabla \cdot [\rho \mathbf{u} \otimes \mathbf{u} - \mathbf{B} \otimes \mathbf{B}] + \nabla p_T & = & -(\nabla \cdot \mathbf{B}) \mathbf{B}, \\ \partial_t \mathcal{E}_T + \nabla \cdot [(\mathcal{E}_T + p_T) \mathbf{u} - (\mathbf{u} \cdot \mathbf{B}) \mathbf{B}] & = & -(\nabla \cdot \mathbf{B}) \mathbf{u} \cdot \mathbf{B}, \\ \partial_t \mathbf{B} + \nabla \cdot [\mathbf{B} \otimes \mathbf{u} - \mathbf{u} \otimes \mathbf{B}] & = & -(\nabla \cdot \mathbf{B}) \mathbf{u}. \end{cases} \tag{4.1}$$

In this method the source term is coming from the transformation of the MHD equations into conservative form and then (1.96) and (4.1) are equivalent.

According to [75], this method can generate incorrect jump across discontinuities. This problem can be solved by using the source term only in the Maxwell-Faraday equations and leaves the momentum and energy equations source term-free, as proposed in [42]. Moreover, in [67], it has been shown that this strategy is easily incorporated for grid-adaptive computations.

I.3 Generalized Lagrange Multiplier

Among the existing methods dealing with the $\nabla \cdot \mathbf{B} = 0$ constraint, we have also the Generalized Lagrange Multiplier, shortly named GLM, presented in [30, 63]. In the Maxwell-Faraday equation, the Lagrange Multiplier Ψ is added leading to

$$\partial_t \mathbf{B} + \nabla \cdot [\mathbf{B} \otimes \mathbf{u} - \mathbf{u} \otimes \mathbf{B}] + \nabla \Psi = 0. \tag{4.2}$$

The divergence-free constraint becomes

$$\mathcal{D}(\Psi) + \nabla \cdot \mathbf{B} = 0, \tag{4.3}$$

where $\mathcal{D}$ is a linear differential operator chosen in order that the initial and boundary condition of Ψ is a good numerical approximation of (4.2) and (4.3). Then, the operator $\mathcal{D}$ is given by

$$\mathcal{D}(\Psi) = \frac{1}{c_h^2} \partial_t \Psi + \frac{1}{c_p^2} \Psi,$$

where c_h and c_p are respectively hyperbolic and parabolic correctors.

Likewise the Powell's source term method, the GLM one is easily incorporated in computations with Riemann type fluxes. In this method, the divergence is set to zero for one approximation, but as we have seen in the previous method, $\nabla \cdot \mathbf{B}$ appears several times.

I.4 Contrained transport method

Another strategy dealing with divergence-free constraint consists to maintain $\nabla \cdot \mathbf{B} = 0$ in one discretization by insisting on the *machine precision accuracy* [42]. This method is named constrained transport and was originally presented in [33]. This method has been re-used in many MHD codes [11, 77].

In [11], a 3-D cell-centered finite volume method, where the control cells are aligned with the x, y, and z-directions, is developed. Writing the Maxwell-Faraday equations over a control cell $\mathcal{S}$

$$\partial_t \int_{\mathcal{S}} \mathbf{B} d\mathcal{S} = - \oint_{\partial \mathcal{S}} \mathbf{E} d\partial\mathcal{S},$$

the different components of $\mathbf{B}$ are computed at different locations of the control cell. All this explanation is summarized in Figure 4.1. The constrained transport method can be used for more general systems owning a divergence-free equation on one of its physical variables. In this frame, examples of procedure have been developed in [35] for 2-D geometries.
This method gets the same advantages than the two previous one, but the adaptation of this strategy to unstructured meshes can be tricky.

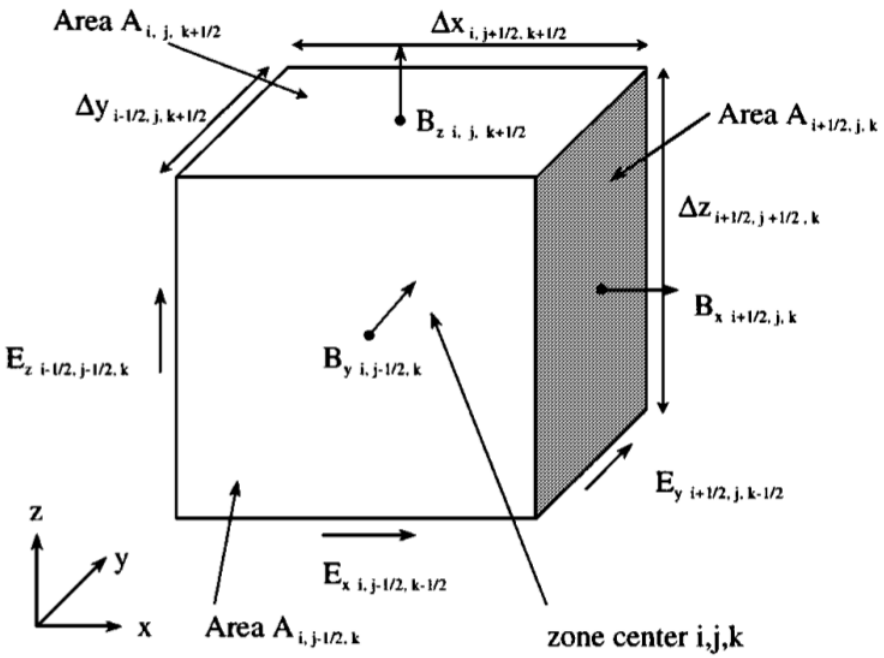

Figure 4.1: Localization of the magnetic and electric fields for the contrained transport method. Source: [11].

II An alternate method for divergence-free problem

This section proposes an alternate method to the ones presented in the previous section. The representation of the magnetic field in term of vector potential $\mathbf{A}$ is then used with $\mathbf{A} = \alpha\nabla\beta$ and we get [71]:

$$\mathbf{B} = \nabla\alpha \times \nabla\beta,$$

where α, and β are named Euler potentials. It has been shown in [71] that the Euler potentials are solutions of simple transport equations in the case of ideal MHD model:

$$\left\{ \begin{array}{rcl} \partial_t\alpha + \mathbf{u}\cdot\nabla\alpha &=& 0, \\ \partial_t\beta + \mathbf{u}\cdot\nabla\beta &=& 0. \end{array} \right.$$

This strategy designed is presented here only for 2-D geometry under the translation invariance $\partial_z\cdot = 0$ assumption. With this hypothesis, the magnetic field can be re-written in the following form:

$$\mathbf{B} = B_z\mathbf{e}_z + \mathbf{e}_z \times \nabla\psi, \tag{4.4}$$

where ψ is an Euler potential, and B_z is a constant. Therefore, the Maxwell-Faraday equation of (1.35) can be written in the following form

$$\nabla \times [\mathbf{E} - \partial_t\psi\mathbf{e}_z] = 0.$$

Hence, we have

$$\partial_t\psi\mathbf{e}_z - \mathbf{E} = \nabla U.$$

According to the translation invariance $\partial_z\cdot = 0$, we have

$$\partial_t\psi - E_z = 0.$$

We now replace the z-component of the electric by the ideal Ohm's law (1.95) and the resistive one (1.90)

$$\left\{ \begin{array}{lrcl} \text{Ideal MHD:} & \partial_t\psi + \mathbf{u}\cdot\nabla\psi &=& 0, \\ \text{Resistive MHD:} & \partial_t\psi + \mathbf{u}\cdot\nabla\psi &=& \eta\nabla^2\psi. \end{array} \right.$$

Those equations are rewritten in the conservative form

$$\left\{ \begin{array}{lrcl} \text{Ideal MHD:} & \partial_t(\rho\psi) + \nabla\cdot(\rho\psi\mathbf{u}) &=& 0, \\ \text{Resistive MHD:} & \partial_t(\rho\psi) + \nabla\cdot(\rho\psi\mathbf{u}) &=& \rho\eta\nabla^2\psi. \end{array} \right. \tag{4.5}$$

The main idea of the method that we design in this chapter is to solve the extended system composed of the MHD equations and the Euler potential one to built a numerical scheme based on the relaxation-type method. First, this numerical strategy is presented for the ideal MHD model in the next Section. Next, we adapt the scheme for the resistive MHD model in Section IV. Finally, those two numerical schemes using Euler potentials are tested for both Cartesian and cylindrical geometry in Section V.

III Numerical resolution of ideal MHD equations with Euler potential

The numerical scheme designed in this Section is called *scheme with projection*.

III.1 Presentation of the scheme

Let us consider the ideal MHD equations (1.96) coupled to the corresponding Euler potential equation (4.5)

$$\left\{\begin{array}{lcl} \partial_t \rho + \nabla \cdot (\rho \mathbf{u}) & = & 0, \\ \partial_t (\rho \mathbf{u}) + \nabla \cdot (\rho \mathbf{u} \otimes \mathbf{u} - \mathbf{B} \otimes \mathbf{B}) + \nabla p_T & = & 0, \\ \partial_t \mathcal{E}_T + \nabla \cdot \Big[(\mathcal{E}_T + p_T)\, \mathbf{u} - (\mathbf{u} \cdot \mathbf{B}) \mathbf{B} \Big] & = & 0, \\ \partial_t \mathbf{B} + \nabla \cdot (\mathbf{B} \otimes \mathbf{u} - \mathbf{u} \otimes \mathbf{B}) & = & 0, \\ \partial_t (\rho \psi) + \nabla \cdot (\rho \psi \mathbf{u}) & = & 0. \end{array}\right. \tag{4.6}$$

This system is redundant: the last equation of the previous system is equivalent to the ones on the two first components of the magnetic field. We propose a two-step scheme similar to the one presented in Chapter 3. The two step of the scheme with projection are given by:

- Transport step: During this step, the system (4.6) is solved with a finite volume-type method.
- Projection step: Using the definition (4.4), the magnetic field $\mathbf{B}$ is projected on the gradient of ψ.

The detail of the computations made in those two steps are given in the two next subsections.

III.2 Transport step

As the system (4.6) is invariant by rotation, we limit ourselves to the 1-D ideal MHD equations in the x-direction:

$$\partial_t U + \partial_x F(U) = 0,$$

where

$$U = \begin{bmatrix} \rho \\ \rho u \\ \rho v \\ \rho w \\ \mathcal{E}_T \\ B_y \\ B_z \\ \rho \psi \end{bmatrix}, \quad F(U) = \begin{bmatrix} \rho u \\ \rho u^2 + p_T - B_x^2 \\ \rho u v \\ \rho u w \\ (\mathcal{E}_T + p_T) u - (\mathbf{u} \cdot \mathbf{B}) B_x \\ u B_y - v B_x \\ u B_z - w B_x \\ \rho \psi u \end{bmatrix}.$$

Since the x-magnetic field equation in this 1-D case is $\partial_t B_x = 0$, then this variable does not evolve during the transport step, thus we do not report this equation in the previous system. To solve this system, we use the cell-centered finite volume method of Chapter 2 where the numerical fluxes are obtained with one of those three Riemann-type scheme: Rusanov, HLL, and HLLD fluxes.

i Rusanov flux

In [49], the Riemann problem (U_L, U_R) with one intermediate state U^* is used to compute the Rusanov flux, as shown in Figure 4.2. First, the maximal wave speed $\lambda_{\max}$ is defined as follow:

$$\lambda_{\max} = \max(u_L, u_R) + \max(c_{f,L}, c_{f,R}),$$

where c_f has been defined in (1.97). The slopes S_L and S_R of Figure 4.2 are chosen to be symmetric:

$$S_R = -S_L = \lambda_{\max}.$$

Finally, the Rankine-Hugoniot relation is used to obtain the flux of the intermediate state which corresponds to the Rusanov flux:

$$F^{Rusanov} = \frac{1}{2}\left(F_L + F_R\right) - \frac{\lambda_{max}}{2}\left(U_R - U_L\right),$$

where

$$F_K = F(U_K),\ K = L, R.$$

Since the Euler potential equation is a simple transport one, then its Rusanov flux is replaced by an upwind one

$$F(\rho\psi) = \begin{cases} \rho_L\psi_L u_L, & F^{Rusanov}(\rho) > 0, \\ \rho_R\psi_R u_R, & F^{Rusanov}(\rho) < 0. \end{cases} \tag{4.7}$$

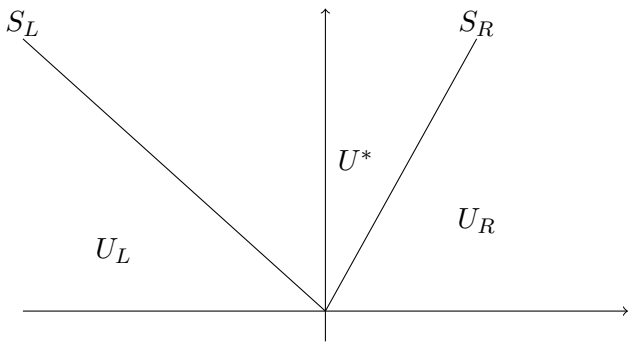

Figure 4.2: Riemann fan with one intermediate state.

ii HLL flux

Likewise the Rusanov flux, the HLL flux , originally presented in [46], is a Riemann solver with one intermediate state, but the two slopes of this problem are not anymore symmetric. Then, the slopes S_L and S_R of Figure 4.2 are now:

$$\begin{cases} S_L &= \min(u_L, u_R) - \max(c_{f,L}, c_{f,R}), \\ S_R &= \max(u_L, u_R) + \max(c_{f,L}, c_{f,R}). \end{cases} \tag{4.8}$$

We denote by F_L and F_R the fluxes $F(U_L)$ and $F(U_R)$. In [46], by using Rankine-Hugoniot relation, the intermediate state U^* is given by

$$U^* = \frac{S_R U_R - S_L U_L - (F_R - F_L)}{S_R - S_L}, \tag{4.9}$$

then its flux is

$$F^* - F_L = S_L(U^* - U_L),$$

where F^* is the flux of the intermediate state U^*. The previous relation leads to

$$F^* = \frac{S_L S_R(U_R - U_L) - S_L F_R + S_R F_L}{S_R - S_L}.$$

Then, the HLL flux is determined by

$$F^{HLL} = \begin{cases} F_L, & 0 < S_L, \\ F^*, & S_L \leq 0 < S_R, \\ F_R, & S_R \leq 0. \end{cases} \tag{4.10}$$

By denoting

$$\begin{cases} S_L^- &= \min(0, S_L), \\ S_R^+ &= \max(0, S_R), \end{cases}$$

the HLL flux (4.10) can be generalized with

$$F^{HLL} = \frac{S_R^+ F_L - S_L^- F_R + S_R^+ S_L^-(U_R - U_L)}{S_R^+ - S_L^-}.$$

Likewise the Rusanov flux, the HLL one of the Euler potential ψ is replaced by the upwind flux (4.7).

iii HLLD flux

In [61], Miyoshi and Kusano design a Riemann solver with four intermediate states for the ideal MHD equations. The left and right states of the Riemann problem are denoted (U_L, U_R), and the four intermediate states $(U_L^*, U_L^{**}, U_R^{**}, U_R^*)$, this problem is represented in Figure 4.3. In this paper, we give the computation of all the variables of the four intermediate states [61].

Likewise the HLL flux, the slope S_L and S_R are given by the relation (4.8). The choice of the middle wave S_M is based on the HLL scheme, then using the result (4.9) for the density and the normal momentum we have

$$S_M = \frac{(S_R - u_R)\rho_R u_R - (S_L - u_L)\rho_L u_L - [(p_T)_R - (p_T)_L]}{(S_R - u_R)\rho_R - (S_L - u_L)\rho_L}.$$

The velocity u is chosen constant along all the intermediate states with

$$u^* = S_M = u_L^{**} = u_L^* = u_R^* = u_R^{**}.$$

A similar assumption is made for the total pressure

$$\begin{aligned} p_T^* &= p_{T,L}^{**} = p_{T,L}^* = p_{T,R}^* = p_{T,R}^{**} \\ &= \frac{(S_R - u_R)\rho_R p_{T,L} - (S_L - u_L)\rho_L p_{T,R} + \rho_L\rho_R(S_R - u_R)(S_L - u_L)(u_R - u_L)}{(S_R - u_R)\rho_R - (S_L - u_L)\rho_L}. \end{aligned}$$

We are now interested in determine the intermediate states U_L^* and U_R^*. For $K = L, R$, we use the Rankine-Hugoniot relation at the speed $S = S_K$

$$S_K(U_K^* - U_K) = F_K^* - F_K,$$

which is equivalent to

$$\left\{\begin{array}{lcl}
S_K(\rho_K^* - \rho_K) &=& \rho_K^* u^* - \rho_K u_K, \\
S_K(\rho_K^* v_K^* - \rho_K v_K) &=& (\rho_K^* u^* v_K^* - B_x B_{y,K}^*) - (\rho_K u_K v_K - B_x B_{y,K}), \\
S_K(\rho_K^* w_K^* - \rho_K w_K) &=& (\rho_K^* u^* w_K^* - B_x B_{z,K}^*) - (\rho_K u_K w_K - B_x B_{z,K}), \\
S_K(\mathcal{E}_{T,K}^* - \mathcal{E}_{T,K}) &=& \left[\left(\mathcal{E}_{T,K}^* + p_T^*\right) u^* + (\mathbf{u}_K^* \cdot \mathbf{B}_K^*)\, B_x\right] \\
&& - \left[(\mathcal{E}_{T,K} + p_{T,K})\, u_K - (\mathbf{u}_K \cdot \mathbf{B}_K)\, B_x\right], \\
S_K(B_{y,K}^* - B_{y,K}) &=& (B_{y,K}^* u^* - B_x v_K^*) - (B_{y,K} u_K - B_x v_K), \\
S_K(B_{z,K}^* - B_{z,K}) &=& (B_{z,K}^* u^* - B_x w_K^*) - (B_{z,K} u_K - B_x w_K), \\
S_K(\rho_K^* \psi_K^* - \rho_K \psi_K) &=& \rho_K^* \psi_K^* u^* - \rho_K \psi_K u_K.
\end{array}\right.$$

The solution is then given by

$$\left\{\begin{array}{lcllcl}
\rho_K^* &=& \rho_K \dfrac{S_K - u_K}{S_K - u^*}, & \psi_K^* &=& \psi_K, \\
v_K^* &=& v_K - B_x \dfrac{B_{y,K}^* - B_{y,K}}{\rho_K (S_K - u_K)}, & w_K^* &=& w_K - B_x \dfrac{B_{z,K}^* - B_{z,K}}{\rho_K (S_K - u_K)}, \\
B_{y,K}^* &=& B_{y,K} \dfrac{(S_K - u_K)^2 - c_{a,K}^2}{(S_K - u^*)(S_K - u_K) - c_{a,K}^2}, & B_{z,K}^* &=& B_{z,K} \dfrac{(S_K - u_K)^2 - c_{a,K}^2}{(S_K - u^*)(S_K - u_K) - c_{a,K}^2},
\end{array}\right.$$

$$\mathcal{E}_{T,K}^* = \mathcal{E}_{T,K} \frac{S_K - u_K}{S_K - u^*} + \frac{p_T^* u^* - p_{T,K} u_K - B_x \left[(\mathbf{u}_K^* \cdot \mathbf{B}_K^*) - (\mathbf{u}_K \cdot \mathbf{B}_K)\right]}{S_K - u^*}.$$

In the case of $(S_K - u^*)(S_K - u_K) - c_{a,K}^2 \approx 0$, the choice of the tangential velocities and magnetic fields are given by

$$v_K^* = v_K,\ w_K^* = w_K,\ B_{y,K}^* = B_{y,K},\ B_{z,K}^* = B_{z,K}.$$

The slopes S_L^* and S_R^* are chosen to correspond with the two Alfvén waves of the ideal MHD equations

$$S_L^* = u^* - c_{a,L}^*,\ S_R^* = u^* + c_{a,R}^*.$$

The Rankine-Hugoniot relation in S_M leads to

$$\left\{\begin{array}{lcllcl}
B_{y,L}^{**} &=& B_{y,R}^{**} &=& B_y^{**}, \\
B_{z,L}^{**} &=& B_{z,R}^{**} &=& B_z^{**}, \\
v_L^{**} &=& v_R^{**} &=& v^{**}, \\
w_L^{**} &=& w_R^{**} &=& w^{**}.
\end{array}\right.$$

For $K = L, R$, the Rankine-Hugoniot relation in S_K^* leads to

$$\begin{cases} \rho_K^{**} &= \rho_K^*, \\ \psi_K^{**} &= \psi_K^* = \psi_K, \\ v^{**} &= \dfrac{\sqrt{\rho_R^*}v_R^* - \sqrt{\rho_L^*}v_L^* + sgn(B_x)(B_{y,R}^* - B_{y,L}^*)}{\sqrt{\rho_L^*} + \sqrt{\rho_R^*}}, \\ w^{**} &= \dfrac{\sqrt{\rho_R^*}w_R^* - \sqrt{\rho_L^*}w_L^* + sgn(B_x)(B_{z,R}^* - B_{z,L}^*)}{\sqrt{\rho_L^*} + \sqrt{\rho_R^*}}, \\ \mathcal{E}_{T,L}^{**} &= \mathcal{E}_{T,L}^* + sgn(B_x)\sqrt{\rho_L^*}\left[(\mathbf{u}^{**}\cdot\mathbf{B}^{**}) - (\mathbf{u}_L^*\cdot\mathbf{B}_L^*)\right], \\ \mathcal{E}_{T,R}^{**} &= \mathcal{E}_{T,R}^* - sgn(B_x)\sqrt{\rho_R^*}\left[(\mathbf{u}^{**}\cdot\mathbf{B}^{**}) - (\mathbf{u}_R^*\cdot\mathbf{B}_R^*)\right], \\ B_y^{**} &= \dfrac{\sqrt{\rho_R^*}B_{y,R}^* - \sqrt{\rho_L^*}B_{y,L}^* + sgn(B_x)\sqrt{\rho_L^*\rho_R^*}(v_R^* - v_L^*)}{\sqrt{\rho_L^*} + \sqrt{\rho_R^*}}, \\ B_z^{**} &= \dfrac{\sqrt{\rho_R^*}B_{z,R}^* - \sqrt{\rho_L^*}B_{z,L}^* + sgn(B_x)\sqrt{\rho_L^*\rho_R^*}(w_R^* - w_L^*)}{\sqrt{\rho_L^*} + \sqrt{\rho_R^*}}, \end{cases}$$

where $sgn(B_x)$ is the sign function defined by

$$sgn(B_x) = \begin{cases} 1, & B_x > 0, \\ -1, & B_x < 0. \end{cases}$$

Finally, the four intermediate fluxes are given by

$$\begin{cases} F_L^* &= F_L + S_L(U_L^* - U_L), \\ F_L^{**} &= F_L + S_L^*U_L^{**} - (S_L^* - S_L)U_L^* - S_LU_L, \\ F_R^{**} &= F_R + S_R^*U_R^{**} - (S_R^* - S_R)U_R^* - S_RU_R, \\ F_R^* &= F_R + S_R(U_R^* - U_R). \end{cases} \tag{4.11}$$

Therefore, the HLLD flux is

$$F^{HLLD} = \begin{cases} F_L, & 0 < S_L, \\ F_L^*, & S_L \le 0 < S_L^*, \\ F_L^{**}, & S_L^* \le 0 < S_M, \\ F_R^{**}, & S_M \le 0 < S_R^*, \\ F_R^*, & S_R^* \le 0 < S_R, \\ F_R, & S_R \le 0. \end{cases}$$

According to the previous computations, the Euler potential in the intermediate states are $\psi_K^{**} = \psi_K^* = \psi_K$ for $K = L, R$. Then, the relation (4.11) gives that the HLLD flux of the conservative variable $\rho\psi$ is:

$$F^{HLLD}(\rho\psi) = F^{HLLD}(\rho)\begin{cases} \psi_L, & 0 < u^*, \\ \psi_R, & u^* \le 0. \end{cases}$$

This flux corresponds to an upwind flux. Then, we do not need to change the flux of the Euler potential as it has been done for the Rusanov and HLL flux.

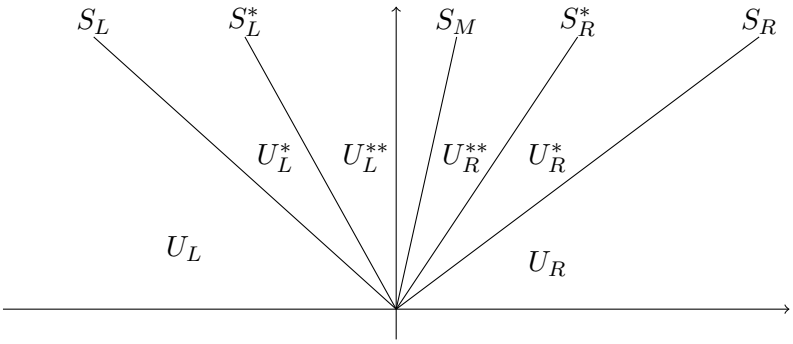

Figure 4.3: Riemann fan with four intermediate states.

III.3 Projection step

At the end of the transport step, the intermediate solution is denoted $U^{n+1/2}$. To obtain the final solution U^{n+1} of the scheme with projection, it remains to project the magnetic field $\mathbf{B}$ on the gradient of the Euler potential $\nabla\psi$ with the definition (4.4). This step is written in function of the physical variables $(\rho, \mathbf{u}, p, \mathbf{B}, \psi)^T$:

$$\left\{\begin{array}{lcl} \rho^{n+1} & = & \rho^{n+1/2}, \\ \mathbf{u}^{n+1} & = & \mathbf{u}^{n+1/2}, \\ p^{n+1/2} & = & p^{n+1}, \\ \psi^{n+1} & = & \psi^{n+1/2}, \\ \mathbf{B} & = & B_z^{n+1/2}\mathbf{e}_z + \mathbf{e}_z \times (\nabla\psi)^{n+1/2}, \end{array}\right. \tag{4.12}$$

In numerical experiments, we use the cell-centered approach with a uniform mesh both for Cartesian and for cylindrical coordinates.

i Cartesian coordinates

In order to evaluate the gradient of ψ, we use a second order central finite difference. Then, for Cartesian coordinates, we have

$$(\nabla\psi)_{i,j} = \begin{bmatrix} (\partial_x\psi)_{i,j} \\ (\partial_y\psi)_{i,j} \\ 0 \end{bmatrix} = \begin{bmatrix} \dfrac{\psi_{i+1,j} - \psi_{i-1,j}}{2\Delta x} \\ \dfrac{\psi_{i,j+1} - \psi_{i,j-1}}{2\Delta y} \\ 0 \end{bmatrix}, \ i = 1..N_x, \ j = 1..N_y, \tag{4.13}$$

where Δx and Δy are the uniform space steps in the x and y-directions. Using the definition (4.4) in Cartesian coordinates we have

$$\mathbf{B} = \begin{bmatrix} -\partial_y\psi \\ \partial_x\psi \\ B_z \end{bmatrix}. \tag{4.14}$$

Therefore, using the results (4.13) and (4.14), the system (4.12) becomes for $i = 1..N_x$, $j = 1..N_y$

$$\begin{cases} \rho_{i,j}^{n+1} &= \rho_{i,j}^{n+1/2}, \\ \mathbf{u}_{i,j}^{n+1} &= \mathbf{u}_{i,j}^{n+1/2}, \\ p_{i,j}^{n+1} &= p_{i,j}^{n+1/2}, \\ \psi_{i,j}^{n+1} &= \psi_{i,j}^{n+1/2}, \\ B_{x,i,j}^{n+1} &= -\dfrac{\psi_{i,j+1}^{n+1} - \psi_{i,j-1}^{n+1}}{2\Delta y}, \\ B_{y,i,j}^{n+1} &= \dfrac{\psi_{i+1,j}^{n+1} - \psi_{i-1,j}^{n+1}}{2\Delta x}, \\ B_{z,i,j}^{n+1} &= B_{z,i,j}^{n+1/2}. \end{cases}$$

ii Issue for cylindrical coordinates

In cylindrical coordinates, the gradient of the Euler potential writes

$$\nabla\psi = \begin{bmatrix} \partial_R\psi \\ \dfrac{1}{R}\partial_\varphi\psi \\ 0 \end{bmatrix}.$$

Likewise the Cartesian coordinates, we use central finite differences to evaluate the gradient in the center of the control cell $\Omega_{i,j}$, $i = 1..N_R$, $j = 1..N_\varphi$. Therefore the system (4.12) writes

$$\begin{cases} \rho_{i,j}^{n+1} &= \rho_{i,j}^{n+1/2}, \\ \mathbf{u}_{i,j}^{n+1} &= \mathbf{u}_{i,j}^{n+1/2}, \\ p_{i,j}^{n+1} &= p_{i,j}^{n+1/2}, \\ \psi_{i,j}^{n+1} &= \psi_{i,j}^{n+1/2}, \\ B_{R,i,j}^{n+1} &= -\dfrac{\psi_{i,j+1}^{n+1} - \psi_{i,j-1}^{n+1}}{2R_i\Delta\varphi}, \\ B_{\varphi,i,j}^{n+1} &= \dfrac{\psi_{i+1,j}^{n+1} - \psi_{i-1,j}^{n+1}}{2\Delta R}, \\ B_{Z,i,j}^{n+1} &= B_{Z,i,j}^{n+1/2}, \end{cases}$$

where ΔR and $\Delta\varphi$ are defined in (2.19) in the uniform case with $k = 0$.

IV Numerical resolution of resistive MHD equations

After writing the scheme with projection for the ideal MHD equations we are now interested to adapt this scheme to the resistive MHD model. The notations are the same as the ones used in the previous section.

IV.1 Presentation of the proposed scheme

The scheme with projection for the resistive MHD consider the system (1.94) coupled to the second equation of (4.5)

$$\left\{\begin{array}{lcll} \partial_t\rho + \nabla\cdot(\rho\mathbf{u}) & = & 0, & \\ \partial_t(\rho\mathbf{u}) + \nabla\cdot(\rho\mathbf{u}\otimes\mathbf{u} - \mathbf{B}\otimes\mathbf{B}) + \nabla p_T & = & 0, & \\ \partial_t\mathcal{E}_T + \nabla\cdot[(\mathcal{E}_T + p_T)\mathbf{u} - (\mathbf{u}\cdot\mathbf{B})\mathbf{B}] & = & \eta\nabla\cdot[\mathbf{B}\times(\nabla\times\mathbf{B})], & (4.15)\\ \partial_t\mathbf{B} + \nabla\cdot(\mathbf{B}\otimes\mathbf{u} - \mathbf{u}\otimes\mathbf{B}) & = & \eta\nabla^2\mathbf{B}, & \\ \partial_t(\rho\psi) + \nabla\cdot(\rho\psi\mathbf{u}) & = & \rho\eta\nabla^2\psi. & \end{array}\right.$$

We propose a method based on the one for ideal MHD equations given in Section III. Indeed, we construct a three step scheme:

- Transport step: this step is identical to the corresponding one of Section III.
- Resistive step: it consists to solve with an implicit scheme the resistive source terms of (4.15).
- Projection step: this step is identical to the corresponding one of Section III.

IV.2 Presentation of the resistive step

This part is devoted to the computations made for the resistive step in the scheme with projection step. It consists to solve the following system

$$\left\{\begin{array}{lcll} \partial_t\rho & = & 0, & \\ \partial_t(\rho\mathbf{u}) & = & 0, & \\ \partial_t\mathcal{E}_T & = & \eta\nabla\cdot[\mathbf{B}\times(\nabla\times\mathbf{B})], & (4.16)\\ \partial_t\mathbf{B} & = & \eta\nabla^2\mathbf{B}, & \\ \partial_t(\rho\psi) & = & \rho\eta\nabla^2\psi. & \end{array}\right.$$

We recall that the system (4.16) is a redundant system. In this step, since the next one is the projection step then we will not modify the two first components of $\mathbf{B}$. Likewise the projection step, we will not work with the conservative variables $(\rho, \rho\mathbf{u}, \mathcal{E}_T, \mathbf{B}, \rho\psi)^T$ but with the following physical variables $(\rho, \mathbf{u}, p, B_z, \psi)^T$. Then, the system (4.16) becomes:

$$\left\{\begin{array}{lcl} \partial_t\rho & = & 0, \\ \partial_t\mathbf{u} & = & 0, \\ \partial_t p & = & (\gamma-1)\eta\left[(\nabla B_z)^2 + (\nabla^2\psi)^2\right], \\ \partial_t B_z & = & \nabla^2 B_z, \\ \partial_t\psi & = & \nabla^2\psi. \end{array}\right.$$

Then, the solution of the resistive step is obtained with an implicit step. The time step Δt is the same one of the one of the transport step. We now denote $U^{n+1/3}$ the solution of the transport step and $U^{n+2/3}$ the one of the resistive step. Finally, the previous system is approximated with

$$\left\{\begin{array}{lcl} \rho^{n+2/3} & = & \rho^{n+1/3}, \\ \mathbf{u}^{n+2/3} & = & \mathbf{u}^{n+1/3}, \\ p^{n+2/3} & = & p^{n+1/3} + (\gamma-1)\eta\Delta t\left[(\nabla B_z)^{n+2/3}\right]^2 \\ & & +(\gamma-1)\eta\Delta t\left[\left(\nabla^2\psi\right)^{n+2/3}\right]^2, \\ B_z^{n+2/3} - \eta\Delta t\left(\nabla^2 B_z\right)^{n+2/3} & = & B_z^{n+1/3}, \\ \psi^{n+2/3} - \eta\Delta t\left(\nabla^2\psi\right)^{n+2/3} & = & \psi^{n+1/3}, \end{array}\right. \quad (4.17)$$

where $(\rho^{n+2/3}, \mathbf{u}^{n+2/3}, p^{n+2/3}, B_z^{n+2/3}, \psi^{n+2/3})^T$ is the solution of the resistive step.

IV.3 Resistive step in Cartesian coordinates

Let us first detail the resistive step for the Cartesian coordinates. Under the hypothesis of translation invariance $\partial_z \cdot = 0$, the gradient and the Laplacian of a scalar f write

$$\nabla f = \begin{bmatrix} \partial_x f \\ \partial_y f \\ 0 \end{bmatrix}, \ \nabla^2 f = \partial_x^2 f + \partial_y^2 f.$$

This step has been developed at the second and the fourth order in space. In this Subsection, we focus on the three last equations of (4.17).

i Order 2

We consider a control cell $\Omega_{i,j}$, $i = 1..N_x$, $j = 1..N_y$, then the first and second derivatives at the second order in space of a scalar f are given by the approximations

$$\begin{cases} (\partial_x f)_{i,j} & \approx & \dfrac{f_{i+1,j} - f_{i-1,j}}{2\Delta x}, \\ (\partial_x^2 f)_{i,j} & \approx & \dfrac{f_{i-1,j} - 2f_{i,j} + f_{i+1,j}}{\Delta x^2}. \end{cases} \tag{4.18}$$

Therefore the three last equations of (4.17) can be rewritten in the form

$$\begin{aligned} f_{i,j}^{n+1/3} = f_{i,j}^{n+2/3} & - \eta \frac{\Delta t}{\Delta x^2} \left[f_{i-1,j}^{n+2/3} - 2f_{i,j}^{n+2/3} + f_{i+1,j}^{n+2/3} \right] \\ & - \eta \frac{\Delta t}{\Delta y^2} \left[f_{i,j-1}^{n+2/3} - 2f_{i,j}^{n+2/3} + f_{i,j+1}^{n+2/3} \right], \ f \in \{\psi, B_z\}, \end{aligned} \tag{4.19}$$

$$\begin{aligned} p_{i,j}^{n+2/3} = p^{n+1/3} & + \eta(\gamma-1) \frac{\Delta t}{4\Delta x^2} \left[B_{z,i+1,j}^{n+2/3} - B_{z,i-1,j}^{n+2/3} \right]^2 \\ & + \eta(\gamma-1) \frac{\Delta t}{4\Delta y^2} \left[B_{z,i,j+1}^{n+2/3} - B_{z,i,j-1}^{n+2/3} \right]^2 \\ & + (\gamma-1)\eta\Delta t \Big[\frac{1}{\Delta x^2} \left(\psi_{i-1,j}^{n+2/3} - 2\psi_{i,j}^{n+2/3} + \psi_{i+1,j}^{n+2/3} \right) \\ & \quad + \frac{1}{\Delta y^2} \left(\psi_{i,j-1}^{n+2/3} - 2\psi_{i,j}^{n+2/3} + \psi_{i,j+1}^{n+2/3} \right) \Big]^2, \end{aligned} \tag{4.20}$$

By using the global numbering

$$k = (i-1)N_y + j, \ i = 1..N_x, \ j = 1..N_y,$$

and by writing

$$f = (f_k)_{1 \le k \le N_x N_y} = (f_{i,j})_{1 \le i \le N_x, \ 1 \le j \le N_y}, \ f \in \{B_z, \psi\},$$

the equation (4.19) can be rewritten in the following vectorial form

$$f^{n+1/3} + BC_f = (I + A) f^{n+2/3}, \tag{4.21}$$

where the matrix I is the identity one, and A is given by

$$A = \begin{bmatrix} D & B & & \\ B & \ddots & \ddots & \\ & \ddots & \ddots & B \\ & & B & D \end{bmatrix}, \; D = \begin{bmatrix} \alpha & -\beta_y & & \\ -\beta_y & \ddots & \ddots & \\ & \ddots & \ddots & -\beta_y \\ & & -\beta_y & \alpha \end{bmatrix}, \; B = -\beta_x I,$$

with

$$\begin{cases} \alpha &= 2(\beta_x + \beta_y), \\ \beta_x &= \dfrac{\eta \Delta t}{\Delta x^2}, \\ \beta_y &= \dfrac{\eta \Delta t}{\Delta y^2}. \end{cases}$$

In the equation (4.21), the vector BC_f represents the boundary conditions of the variable $f \in \{B_z, \psi\}$ in the ghost cells of the mesh, and writes

$$BC_f = BC_{f,x} + BC_{f,y}, \; BC_{f,x} = \begin{bmatrix} BC_{f,x}^1 \\ 0 \\ \vdots \\ 0 \\ BC_{f,x}^{N_x} \end{bmatrix}, \; BC_{f,y} = \begin{bmatrix} BC_{f,y}^1 \\ \vdots \\ BC_{f,y}^{N_x} \end{bmatrix},$$

where

$$BC_{f,x}^1 = \beta_x \begin{bmatrix} f_{0,1} \\ \vdots \\ f_{0,N_y} \end{bmatrix}, \; BC_{f,x}^{N_x} = \beta_x \begin{bmatrix} f_{N_x+1,1} \\ \vdots \\ f_{N_x+1,N_y} \end{bmatrix},$$

$$BC_{f,y}^i = \beta_y \begin{bmatrix} f_{i,0} \\ 0 \\ \vdots \\ 0 \\ f_{i,N_y+1} \end{bmatrix}, \; i = 1..N_x,$$

where for $i = 1..N_x$ and $j = 1..N_y$, $f_{0,j}$, $f_{N_x+1,j}$, $f_{i,0}$, and f_{i,N_y+1} are the boundary conditions of f given in the ghost cell shown in Figure 4.4.

As the matrix A is a diagonally dominant and symmetric, we are a sure to obtain a solution of the equation (4.21) by using the conjugate gradient method. Then, we have the new Euler potential $\psi^{n+2/3}$ and the new z-magnetic field $B_z^{n+2/3}$. Therefore, we can now compute the final pressure $p^{n+2/3}$ by using the formula (4.20).

ii Order 4

The computations of the solution of the resistive step have also been tested at the fourth order in space. Let us first write the approximations of the first and second order derivatives in the x-direction for a scalar f

$$\begin{cases} (\partial_x f)_{i,j} &\approx \dfrac{1}{12\Delta x}\Big[f_{i-2,j} - 8f_{i-1,j} + 8f_{i+1,j} - f_{i+2,j}\Big], \\ (\partial_x f)_{i,j} &\approx \dfrac{1}{12\Delta x^2}\Big[-f_{i-2,j} + 16f_{i-1,j} - 30f_{i,j} + 16f_{i,j} - f_{i+2,j}\Big]. \end{cases} \tag{4.22}$$

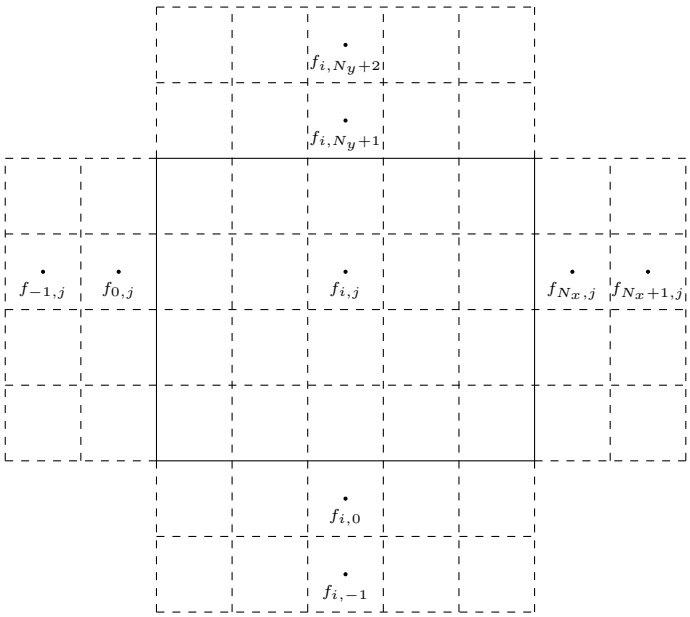

Figure 4.4: Representation of the ghost cells for a Cartesian mesh.

Then, the equation on the z-magnetic field and the Euler potential in the system (4.17) writes at the fourth order in space

$$\begin{aligned} f_{i,j}^{n} = f_{i,j}^{n+2/3} &- \frac{\eta\Delta t}{12\Delta x^2}\Big[- f_{i-2,j}^{n+2/3} + 16 f_{i-1,j}^{n+2/3} - 30 f_{i,j}^{n+2/3} + 16 f_{i+1,j}^{n+2/3} - f_{i+2,j}^{n+2/3}\Big] \\ &- \frac{\eta\Delta t}{12\Delta y^2}\Big[f_{i,j-2}^{n+2/3} + 16 f_{i,j-1}^{n+2/3} - 30 f_{i,j}^{n+2/3} + 16 f_{i,j+1}^{n+2/3} - f_{i,j+2}^{n+2/3}\Big], \\ f \in \{B_z, \psi\}. & \end{aligned} \tag{4.23}$$

By using the same method as the second order, the previous equation can be written in the form (4.21) where the matrix A is now

$$A = \begin{bmatrix} D & B & C & & & \\ B & \ddots & \ddots & \ddots & & \\ C & \ddots & \ddots & \ddots & \ddots & \\ & \ddots & \ddots & \ddots & \ddots & C \\ & & \ddots & \ddots & \ddots & B \\ & & & C & B & D \end{bmatrix}, \qquad \begin{cases} B &= -16\beta_x I, \\ C &= \beta_x I, \end{cases}$$

$$D = \begin{bmatrix} \alpha & -16\beta_y & \beta_y & & & \\ -16\beta_y & \ddots & \ddots & \ddots & & \\ \beta_y & \ddots & \ddots & \ddots & \ddots & \\ & \ddots & \ddots & \ddots & \ddots & \beta_y \\ & & \ddots & \ddots & \ddots & -16\beta_y \\ & & & \beta_y & -16\beta_y & \alpha \end{bmatrix}, \qquad \begin{cases} \alpha &= 30(\beta_x + \beta_y), \\ \beta_x &= \dfrac{\eta\Delta t}{12\Delta x^2}, \\ \beta_y &= \dfrac{\eta\Delta t}{12\Delta y^2}. \end{cases}$$

The boundary conditions on the ghost cells are given by

$$BC_f = BC_{f,x} + BC_{f,y},\ BC_{f,x} = \begin{bmatrix} BC_{f,x}^1 \\ \\ BC_{f,x}^2 \\ \\ 0 \\ \vdots \\ 0 \\ \\ BC_{f,x}^{N_x-1} \\ \\ BC_{f,x}^{N_x} \end{bmatrix},\ BC_{f,y} = \begin{bmatrix} BC_{f,y}^1 \\ \vdots \\ BC_{f,y}^{N_x} \end{bmatrix},$$

with

$$BC_{f,x}^1 = \beta_x \begin{bmatrix} -f_{-1,1} + 16 f_{0,1} \\ \vdots \\ -f_{-1,N_y} + 16 f_{0,N_y} \end{bmatrix},\quad BC_{f,x}^2 = -\beta_x \begin{bmatrix} f_{0,1} \\ \vdots \\ f_{0,N_y} \end{bmatrix},$$

$$BC_{f,x}^{N_x-1} = -\beta_x \begin{bmatrix} f_{N_x+1,1} \\ \vdots \\ f_{N_x+1,N_y} \end{bmatrix},\qquad BC_{f,x}^{N_x} = \beta_x \begin{bmatrix} 16 f_{N_x+1,1} - f_{N_x+2,1} \\ \vdots \\ 16 f_{N_x+1,N_y} - f_{N_x+2,N_y} \end{bmatrix}.$$

In the y-direction, the boundary conditions are

$$BC_{f,y}^i = \beta_y \begin{bmatrix} -f_{i,-1} + 16 f_{i,0} \\ -f_{i,0} \\ 0 \\ \vdots \\ 0 \\ -f_{i,N_y+1} \\ 16 f_{i,N_y+1} - f_{i,N_y+2} \end{bmatrix},\ i = 1..N_x.$$

Likewise the second order, the matrix A keeps the property of diagonally dominant symmetric matrix, then we still solve the system (4.21) with a conjugate gradient solver. To

determine the pressure $p^{n+2/3}$, at the fourth order the equation (4.20) becomes

$$\begin{aligned} p_{i,j}^{n+2/3} = p_{i,j}^{n+1/3} \quad &+ \quad (\gamma-1)\Delta t\left[\frac{-\psi_{i-2,j}^{n+2/3}+16\psi_{i-1,j}^{n+2/3}-30\psi_{i,j}^{n+2/3}+16\psi_{i+1,j}^{n+2/3}-\psi_{i+2,j}^{n+2/3}}{12\Delta x^2}\right. \\ &\left. +\frac{-\psi_{i,j-2}^{n+2/3}+16\psi_{i,j-1}^{n+2/3}-30\psi_{i,j}^{n+2/3}+16\psi_{i,j+1}^{n+2/3}-\psi_{i,j+2}^{n+2/3}}{12\Delta y^2}\right]^2 \\ &+ \quad \frac{(\gamma-1)\eta\Delta t}{144\Delta x^2}\left[B_{z,i-2,j}^{n+2/3}-8B_{z,i-1,j}^{n+2/3}+8B_{z,i+1,j}^{n+2/3}-B_{z,i+2,j}^{n+2/3}\right]^2 \\ &+ \quad \frac{(\gamma-1)\eta\Delta t}{144\Delta y^2}\left[B_{z,i,j-2}^{n+2/3}-8B_{z,i,j-1}^{n+2/3}+8B_{z,i,j+1}^{n+2/3}-B_{z,i,j+2}^{n+2/3}\right]^2. \end{aligned} \tag{4.24}$$

IV.4 Resistive step in cylindrical coordinates

In cylindrical coordinates, with the translation invariance $\partial_Z \cdot = 0$, the gradient and the Laplacian of a scalar write

$$\nabla f = \begin{bmatrix} \partial_R f \\ \frac{1}{R}\partial_\varphi f \\ 0 \end{bmatrix}, \quad \nabla^2 f = \frac{1}{R}\partial_R\left(R\partial_R f\right) + \frac{1}{R^2}\partial_\varphi^2 f.$$

Likewise the Cartesian coordinates, we give the resolution of the resistive step at the second and the fourth order in space.

i Order 2

First, we focus on the R-derivative approximation in the Laplacian. By developing the R-derivative terms in the Laplacian, we have

$$\frac{1}{R}\partial_R\left(R\partial_R f\right) = \frac{1}{R}\partial_R f + \partial_R^2 f. \tag{4.25}$$

By using the formula (4.18), we obtain for $i = 1..N_x$ and $j = 1..N_y$

$$\left(\frac{1}{R}\partial_R\left(R\partial_R f\right)\right)_{i,j} = \frac{1}{R_i\Delta R^2}\left[R_{i-1/2}f_{i,j} - 2R_i f_{i,j} + R_{i+1/2}f_{i,j}\right].$$

Therefore, the approximation of the Laplacian at the second order in the case of cylindrical coordinates is

$$\left(\nabla^2 f\right)_{i,j} = \frac{1}{R_i\Delta R^2}\left[R_{i-1/2}f_{i,j} - 2R_i f_{i,j} + R_{i+1/2}f_{i,j}\right] + \frac{1}{R_i^2\Delta\varphi^2}\left[f_{i,j-1} - 2f_{i,j} + f_{i,j+1}\right].$$

In the system (4.17), the solution for the Z-magnetic field and the Euler potential is then given by

$$\begin{aligned} f_{i,j}^{n+1/3} = f_{i,j}^{n+2/3} \quad &- \quad \frac{\eta\Delta t}{R_i\Delta R^2}\left[R_{i-1/2}f_{i-1,j}^{n+2/3} - 2R_i f_{i,j}^{n+2/3} + R_{i+1/2}f_{i+1,j}^{n+2/3}\right] \\ &- \quad \frac{\eta\Delta t}{R_i^2\Delta\varphi^2}\left[f_{i,j-1}^{n+2/3} - 2f_{i,j}^{n+2/3} + f_{i,j}^{n+2/3}\right], \\ f \in \{B_Z, \psi\}. & \end{aligned} \tag{4.26}$$

For $i = 1..N_R$, we denote by α_i, $\beta_{R,i}$, and $\beta_{\varphi,i}$ the parameters

$$\begin{cases} \alpha_i &= 2(\beta_{R,i} + \beta_{\varphi,i}), \\ \beta_{R,i} &= \dfrac{\eta \Delta t}{R_i \Delta R^2}, \\ \beta_{\varphi,i} &= \dfrac{\eta \Delta t}{R_i^2 \Delta \varphi^2}. \end{cases}$$

By using the global numbering

$$k = (i-1)N_\varphi + j, \ i = 1..N_R, \ j = 1..N_\varphi,$$

the equation (4.26) can be rewritten in the general form

$$f^{n+1/3} + BC_f = (I + A) f^{n+2/3}, \tag{4.27}$$

where $f^{n+1/3} = (f_k^{n+1/3})_{1 \le k \le N_R N_\varphi}$, and $f^{n+2/3} = (f_k^{n+2/3})_{1 \le k \le N_R N_\varphi}$. The boundary conditions are given by ghost cells, and we have

$$BC_f = BC_{f,R} + BC_{f,\varphi}, \ BC_{f,R} = \begin{bmatrix} BC_{f,R}^1 \\ 0 \\ \vdots \\ 0 \\ BC_{f,R}^{N_R} \end{bmatrix}, \ BC_{f,\varphi} = \begin{bmatrix} BC_{f,\varphi}^1 \\ \vdots \\ BC_{f,\varphi}^{N_\varphi} \end{bmatrix},$$

with

$$BC_{f,R}^1 = \beta_{R,1} R_{1/2} \begin{bmatrix} f_{0,1} \\ \vdots \\ f_{0,N_\varphi} \end{bmatrix}, \ BC_{f,R}^{N_R} = \beta_{R,N_R} R_{N_R+1/2} \begin{bmatrix} f_{N_R+1,1} \\ \vdots \\ f_{N_R+1,N_\varphi} \end{bmatrix},$$

for the φ-direction we have

$$BC_{f,\varphi}^i = \beta_{\varphi,i} \begin{bmatrix} f_{i,0} \\ 0 \\ \vdots \\ 0 \\ f_{i,N_\varphi+1} \end{bmatrix}, \ i = 1..N_R.$$

In the system (4.27), the matrix A is given by

$$A = \begin{bmatrix} D_1 & B_1 & & \\ \widetilde{B}_2 & \ddots & \ddots & \\ & \ddots & \ddots & B_{N_R-1} \\ & & \widetilde{B}_{N_R} & D_{N_R} \end{bmatrix},$$

where the different blocks of this matrix are given by

$$D_i = \begin{bmatrix} \alpha_i & -\beta_{\varphi,i} & & \\ -\beta_{\varphi,i} & \ddots & \ddots & \\ & \ddots & \ddots & -\beta_{\varphi,i} \\ & & -\beta_{\varphi,i} & \alpha_i \end{bmatrix}, \ i = 1..N_R,$$

$$\left\{\begin{array}{rcll} B_i & = & R_{i+1/2}\beta_{R,i}I, & i=1..N_R-1, \\ \widetilde{B}_i & = & R_{i-1/2}\beta_{R,i}I, & i=2..N_R. \end{array}\right.$$

Contrary to the Cartesian case, the matrix A for the cylindrical coordinates is not anymore symmetric. Therefore, the conjugate gradient method can not be used anymore to solve the system (4.27). In the numerical tests presented in section V, we have restricted ourselves to Cartesian geometries. A poibility is the GMRES method.

Let us now consider the computation of the pressure given in system (4.17), by using the expression of the Laplacian and the gradient in cylindrical coordinates, we have

$$\begin{aligned} p_{i,j}^{n+2/3} = p_{i,j}^{n+1/3} \quad + \quad & (\gamma-1)\eta\Delta t\left[\frac{R_{i-1/2}\psi_{i-1,j}^{n+2/3}-2R_i\psi_{i,j}^{n+2/3}+R_{i+1/2}\psi_{i+1,j}^{n+2/3}}{R_i\Delta R^2}\right. \\ & \left.+\frac{\psi_{i,j-1}^{n+2/3}-2\psi_{i,j}^{n+2/3}+\psi_{i,j+1}}{R_i^2\Delta\varphi^2}\right]^2 \\ + \quad & \frac{(\gamma-1)\eta\Delta t}{4\Delta R^2}\left[B_{Z,i+1,j}^{n+2/3}-B_{Z,i-1,j}^{n+2/3}\right]^2 \\ + \quad & \frac{(\gamma-1)\eta\Delta t}{4R_i^2\Delta\varphi^2}\left[B_{Z,i,j+1}^{n+2/3}-B_{Z,i,j-1}^{n+2/3}\right]^2. \end{aligned}$$

ii Order 4

In this part, we adapt the four order Cartesian resistive step to the cylindrical coordinates. Likewise the second order, we use the form (4.25) to approximate the R-derivative of the Laplacian with the fourth order formula (4.22). Then, for a scalar f, we have

$$\begin{aligned} \left(\nabla^2 f\right)_{i,j} \quad = \quad & \frac{-R_{i-1}f_{i-2,j}+16R_{i-1/2}f_{i-1,j}-30R_if_{i,j}+16R_{i+1/2}f_{i+1,j}-R_{i+1}f_{i+2,j}}{12R_i\Delta R^2} \\ & +\frac{-f_{i,j-2}+16f_{i,j-1}-30f_{i,j}+16f_{i,j+1}-f_{i,j+2}}{R_i^2\Delta\varphi^2}. \end{aligned}$$

Therefore, in the cylindrical coordinates the results (4.23) becomes for $f\in\{B_Z,\psi\}$

$$\begin{aligned} f_{i,j}^{n+1/3} = f_{i,j}^{n+2/3} \quad & +\frac{\eta\Delta t}{12R_i\Delta R^2} \quad \left[-R_{i-1}f_{i-2,j}^{n+2/3}+16R_{i-1/2}f_{i-1,j}^{n+2/3}-30R_if_{i,j}^{n+2/3}\right. \\ & \qquad \left.+16R_{i+1/2}f_{i+1,j}^{n+2/3}-R_{i+1}f_{i+2,j}^{n+2/3}\right] \\ & +\frac{\eta\Delta t}{12R_i^2\Delta\varphi^2} \quad \left[-f_{i,j-2}^{n+2/3}+16f_{i,j-1}^{n+2/3}-30f_{i,j}^{n+2/3}+16f_{i,j+1}^{n+2/3}-f_{i,j+2}^{n+2/3}\right]. \end{aligned}$$

We write this equation into the vectorial form (4.21), where the matrix A is now

$$A=\begin{bmatrix} D_1 & B_1 & C_1 & & & \\ \widetilde{B}_2 & \ddots & \ddots & \ddots & & \\ \widetilde{C}_3 & \ddots & \ddots & \ddots & \ddots & \\ & \ddots & \ddots & \ddots & \ddots & C_{N_R-2} \\ & & \ddots & \ddots & \ddots & B_{N_R-1} \\ & & & \widetilde{C}_{N_R} & \widetilde{B}_{N_R} & D_{N_R} \end{bmatrix}, \quad \left\{\begin{array}{rcll} B_i & = & -16\beta_{R,i}R_{i+1/2}I, & i=1..N_R-1, \\ \widetilde{B}_i & = & -16\beta_{R,i}R_{i-1/2}I, & i=2..N_R, \\ C_i & = & \beta_{R,i}R_{i+1}I, & i=1..N_R-2, \\ \widetilde{C}_i & = & \beta_{R,i}R_{i+1/2}I, & i=3..N_R, \end{array}\right.$$

for $i = 1..N_R$, we have

$$D_i = \begin{bmatrix} \alpha_i & -16\beta_{\varphi,i} & \beta_{\varphi,i} & & & & \\ -16\beta_{\varphi,i} & \ddots & \ddots & \ddots & & & \\ \beta_{\varphi,i} & \ddots & \ddots & \ddots & \ddots & & \\ & \ddots & \ddots & \ddots & \ddots & \beta_{\varphi,i} & \\ & & \ddots & \ddots & \ddots & -16\beta_{\varphi,i} & \\ & & & \beta_{\varphi,i} & -16\beta_{\varphi,i} & \alpha_i & \end{bmatrix}, \begin{cases} \alpha_i &=& 30(R_i\beta_{R,i} + \beta_{\varphi,i}), \\ \beta_{R,i} &=& \dfrac{\eta\Delta t}{12R_i\Delta R^2}, \\ \beta_{\varphi,i} &=& \dfrac{\eta\Delta t}{12R_i^2\Delta\varphi^2}. \end{cases}$$

The boundary conditions are given by

$$BC = BC_{f,R} + BC_{f,\varphi},\ BC_{f,R} = \begin{bmatrix} BC_{f,R}^1 \\ BC_{f,R}^2 \\ 0 \\ \vdots \\ 0 \\ BC_{f,R}^{N_R-1} \\ BC_{f,R}^{N_R} \end{bmatrix},\ BC_{f,\varphi} = \begin{bmatrix} BC_{f,\varphi}^1 \\ \vdots \\ BC_{f,\varphi}^{N_R} \end{bmatrix},$$

with

$$\begin{aligned} BC_{f,R}^1 &= \beta_{R,1} \begin{bmatrix} -R_0 f_{-1,1} + 16R_{1/2} f_{0,1} \\ \vdots \\ -R_0 f_{-1,N_\varphi} + 16R_{1/2} f_{0,N_\varphi} \end{bmatrix}, \\ BC_{f,R}^2 &= \beta_{R,2} R_1 \begin{bmatrix} -f_{0,1} \\ \vdots \\ -f_{0,N_\varphi} \end{bmatrix}, \\ BC_{f,R}^{N_R-1} &= \beta_{R,N_R-1} R_{N_R} \begin{bmatrix} -f_{N_R+1,1} \\ \vdots \\ -f_{N_R+1,N_\varphi} \end{bmatrix}, \\ BC_{f,R}^{N_R} &= \beta_{R,N_R} \begin{bmatrix} 16R_{N_R+1/2} f_{N_R+1,1} - R_{N_R+1} f_{N_R+2,1} \\ \vdots \\ 16R_{N_R+1/2} f_{N_R+1,N_\varphi} - R_{N_R+1} f_{N_R+2,N_\varphi} \end{bmatrix}, \\ R_0 &= R_1 - \Delta R, \\ R_{N_R+1} &= R_{N_R} + \Delta R. \end{aligned}$$

Finally, the boundary conditions in the φ-direction are

$$BC^i_{f,\varphi} = \beta_{\varphi,i} \begin{bmatrix} -f_{i,-1} + 16 f_{i,0} \\ -f_{i,0} \\ 0 \\ \vdots \\ 0 \\ -f_{i,N_\varphi+1} \\ 16 f_{i,N_\varphi+1} - f_{i,N_\varphi+2} \end{bmatrix}, \; i = 1..N_R.$$

By using the same method as the fourth order for the Cartesian coordinates, the results (4.24) giving the new pressure $p^{n+2/3}$ becomes for the cylindrical coordinates

$$\begin{aligned} p^{n+2/3}_{i,j} = p^{n+1/3}_{i,j} \quad & + \frac{(\gamma-1)\eta\Delta t}{144\Delta R^2} \left[B^{n+2/3}_{Z,i-2,j} - 8B^{n+2/3}_{Z,i-1,j} + 8B^{n+2/3}_{Z,i+1,j} - B^{n+2/3}_{Z,i+2,j} \right]^2 \\ & + \frac{(\gamma-1)\eta\Delta t}{144R_i^2\Delta\varphi^2} \left[B^{n+2/3}_{Z,i,j-2} - 8B^{n+2/3}_{Z,i,j-1} + 8B^{n+2/3}_{Z,i,j+1} - B^{n+2/3}_{Z,i,j+2} \right]^2 \\ & + (\gamma-1)\eta\Delta t \left[\frac{1}{12R_i\Delta R^2} \Big(- R_{i-1}\psi^{n+2/3}_{i-2,j} + 16R_{i-1/2}\psi^{n+2/3}_{i-1,j} \right. \\ & \qquad \left. -30R_i\psi^{n+2/3}_{i,j} + 16R_{i+1/2}\psi^{n+2/3}_{i+1,j} - R_{i+1}\psi^{n+2/3}_{i+2,j} \Big) \right. \\ & \qquad \left. + \frac{-\psi^{n+2/3}_{i,j-2} + 16\psi^{n+2/3}_{i,j-1} - 30\psi^{n+2/3}_{i,j} + 16\psi^{n+2/3}_{i,j+1} - \psi^{n+2/3}_{i,j+2}}{12R_i^2\Delta\varphi^2} \right]^2. \end{aligned}$$

In this Section, we have presented two different numerical methods to solve the resistive step in cylindrical coordinates. For now, those method have not yet been implemented for numerical tests.

V Numerical results

This section is devoted to the numerical tests made for ideal and resistive MHD. In the results, the scheme with projection for ideal and resistive MHD is compared to scheme without the projection step. For all the tests, we have set the adiabatic index to $\frac{5}{3}$.

V.1 Brio-Wu problem for ideal MHD

Originally presented by Brio-Wu [25] for the 1-D ideal MHD equations, this numerical test is based on the Sod's tube [70] for Euler equations. Indeed, it contains the same hydrodynamics initialization as the one of [70] and a magnetic field is added. The initial condition writes

$$U(x) = \begin{cases} U_L, & x < 0.5, \\ U_R, & x > .0.5. \end{cases}$$

where U_L and U_R are given in Table 4.1. This experiments permits to observe how the different schemes are able to capture the different waves of the problem: shocks, rarefactions, and contact discontinuities. In the results a 1-D reference solution has been computed with the HLLD scheme without projection where the domain $[0, 1]$ is meshed with 2000 cells.

	ρ	$\mathbf{u}$	p	B_x	B_y	B_z
U_L	1	0	1	0.75	1	0
U_R	0.125	0	0.1	0.75	-1	0

Table 4.1: Initial data of Brio-Wu problem.

First, the simulations are run in 1-D Cartesian geometry on the domain $[0, 1]$. Then, the definition (4.4) rewrites

$$\mathbf{B} = B_x \mathbf{e}_x + \partial_x \psi \mathbf{e}_y + B_z \mathbf{e}_z.$$

Therefore, the Euler potential equation becomes

$$\partial_t(\rho\psi) + \partial_x(\rho\psi u) = B_x \rho v.$$

In the numerical experiments reported below, this source term is computed using a simple numerical quadrature. We deduce from Table 4.1 that the initialization of the Euler potential is given by

$$\psi(x) = \begin{cases} x, & x < 0.5, \\ 1 - x, & x > 0.5. \end{cases} \tag{4.28}$$

The computations are performed over $[0, 1]$ meshed by 100 points until $t = 0.1$. Figures 4.5 to 4.10 compare the scheme with and without projection for the Rusanov, HLL, and HLLD fluxes at the first order in time and space and the second order too.

At the first order in time and space, the Rusanov scheme with and without projection is not able to capture precisely enough the solution. The same remark can also be made for the HLL scheme with and without projection. Moreover, the HLL flux shows oscillations between $x = 0.35$ and $x = 0.9$ specially for the scheme with projection. The HLLD schemes with and without projection have the closest results solution to the reference solution but those results are not precise enough. For the y-magnetic field, for the three different fluxes, the schemes without projection get better results than the scheme with projection. This phenomenon is due to the fact that for the 1-D MHD equations, the magnetic field $\mathbf{B}$ is always satisfying the divergence-free constraint. Then, in the scheme with projection, B_y is evaluated with two numerical approximations: first, the Euler potential is computed in the transport step, and in a second time from the Euler potential approximation, we evaluate with finite differences B_y. Whereas, in the scheme without projection, B_y is only computed in the transport step, then we have made only one approximation.

As the results of the first order in time and space are not good enough, we re-run the test at the second order in time and space. Those new results are referred in Figures 4.8 to 4.10. The Rusanov schemes have the less precise results. Indeed, for the density the wave located at $x = 0.55$ is not captured at all. The oscillations of the HLL schemes are smaller and happen in a smaller domain: between $x = 0.35$ and $x = 0.6$. Finally, for the HLLD schemes, the results are really better than the two other fluxes. We can see that the HLLD scheme with projection present some overshoot around $x = 0.5$ for the pressure and the y-velocity.

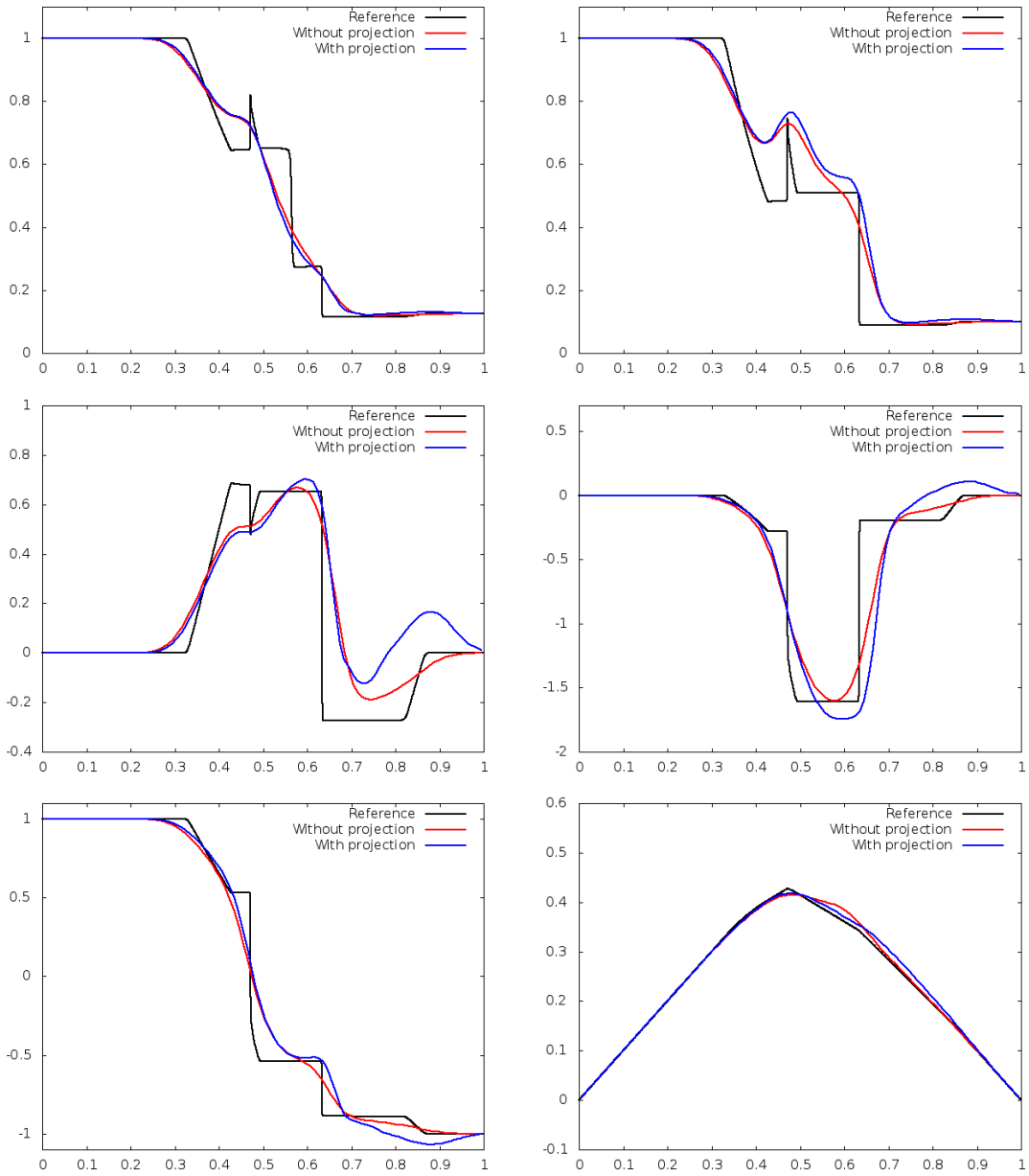

Figure 4.5: 1-D Brio-Wu problem, Solution at $t = 0.1$, O(1) Rusanov flux with and without projection, Top-Left: Density, Top-Right: Pressure, Middle-Left: x-velocity, Middle-Right: y-velocity, Bottom-Left: y-magnetic field, Bottom-Right: Euler potential.

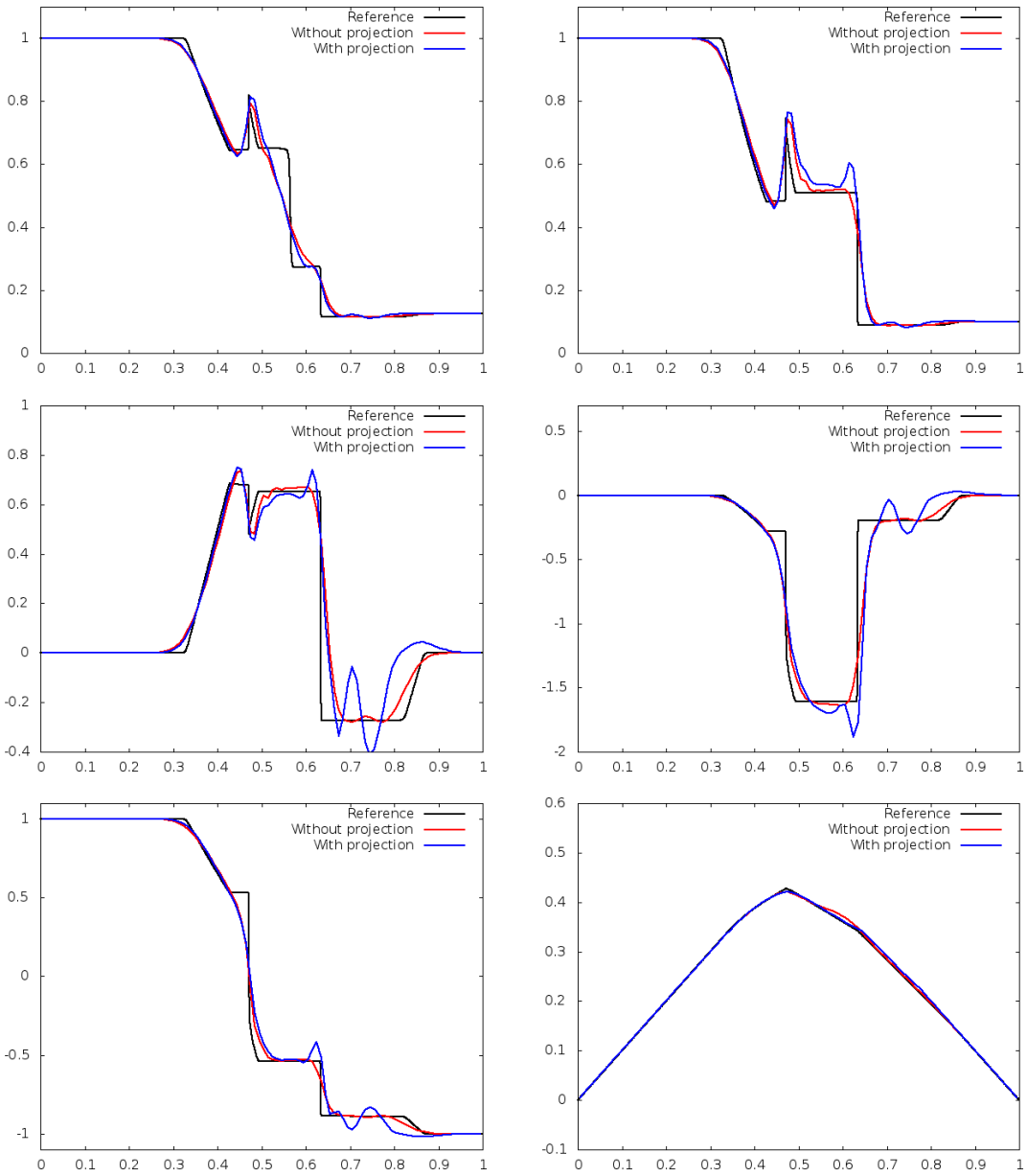

Figure 4.6: 1-D Brio-Wu problem, Solution at $t = 0.1$, O(1) HLL flux with and without projection, Top-Left: Density, Top-Right: Pressure, Middle-Left: x-velocity, Middle-Right: y-velocity, Bottom-Left: y-magnetic field, Bottom-Right: Euler potential.

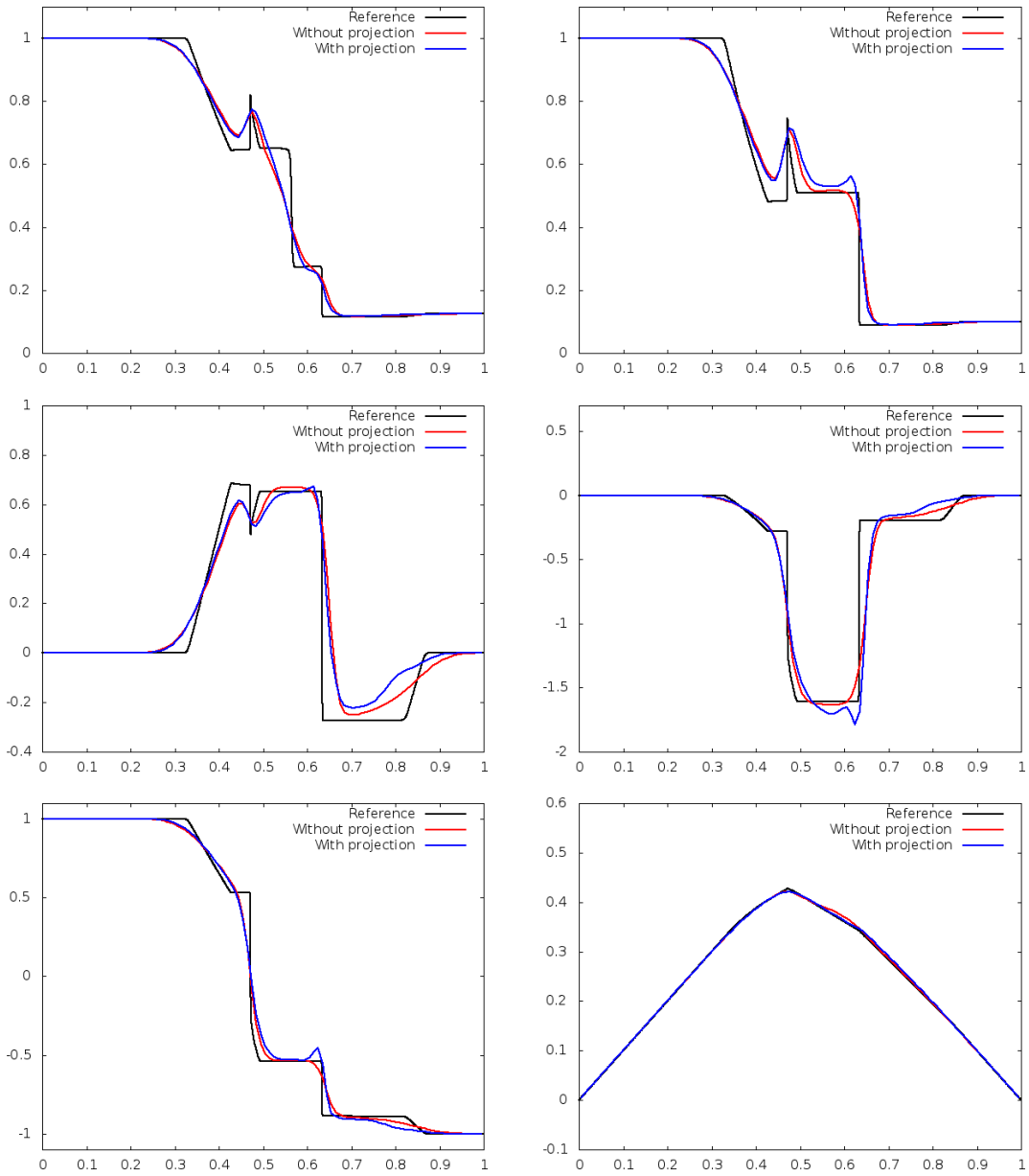

Figure 4.7: 1-D Brio-Wu problem, Solution at $t = 0.1$, O(1) HLLD flux with and without projection, Top-Left: Density, Top-Right: Pressure, Middle-Left: x-velocity, Middle-Right: y-velocity, Bottom-Left: y-magnetic field, Bottom-Right: Euler potential.

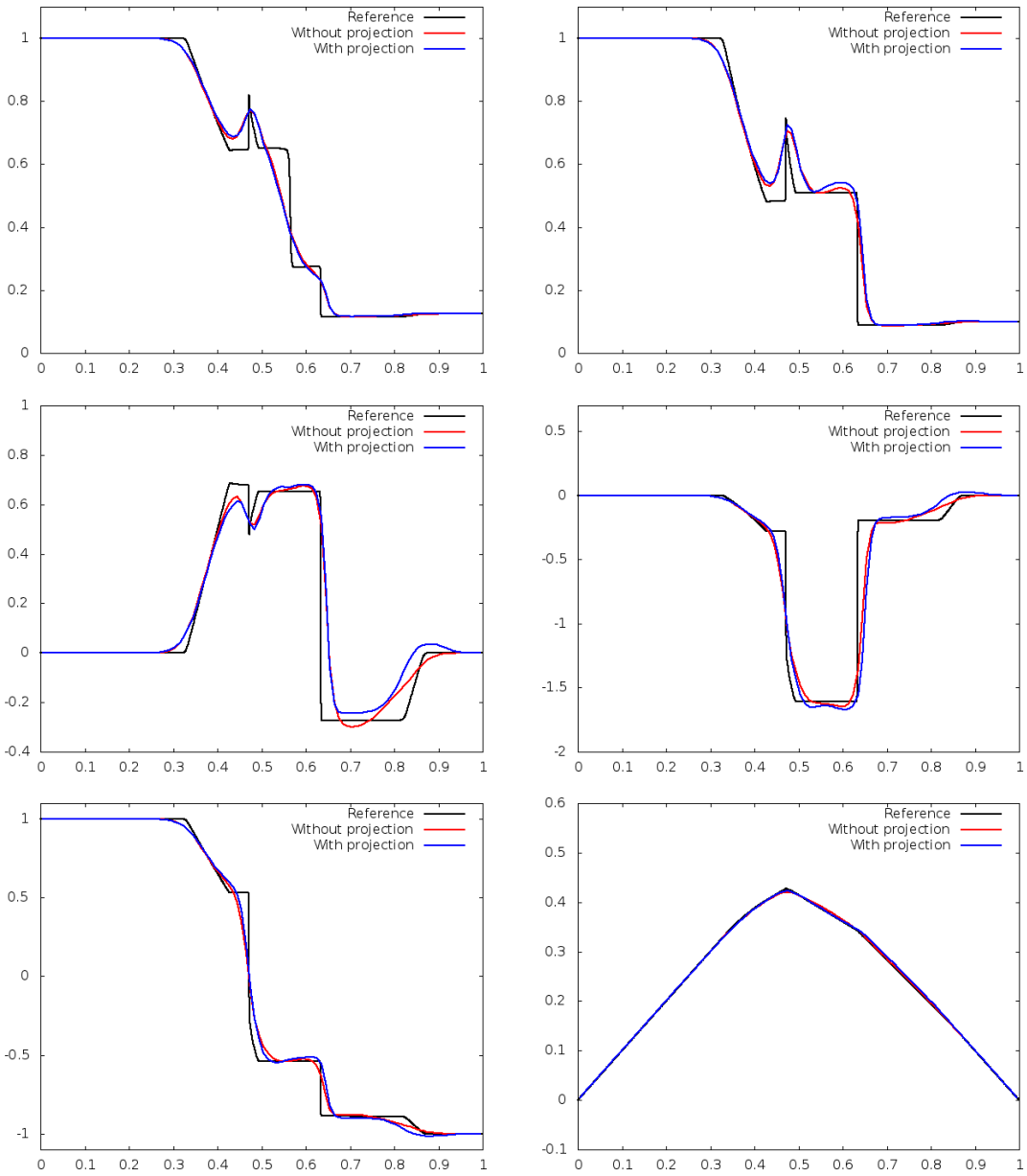

Figure 4.8: 1-D Brio-Wu problem, Solution at $t = 0.1$, O(2) Rusanov flux with and without projection, Top-Left: Density, Top-Right: Pressure, Middle-Left: x-velocity, Middle-Right: y-velocity, Bottom-Left: y-magnetic field, Bottom-Right: Euler potential.

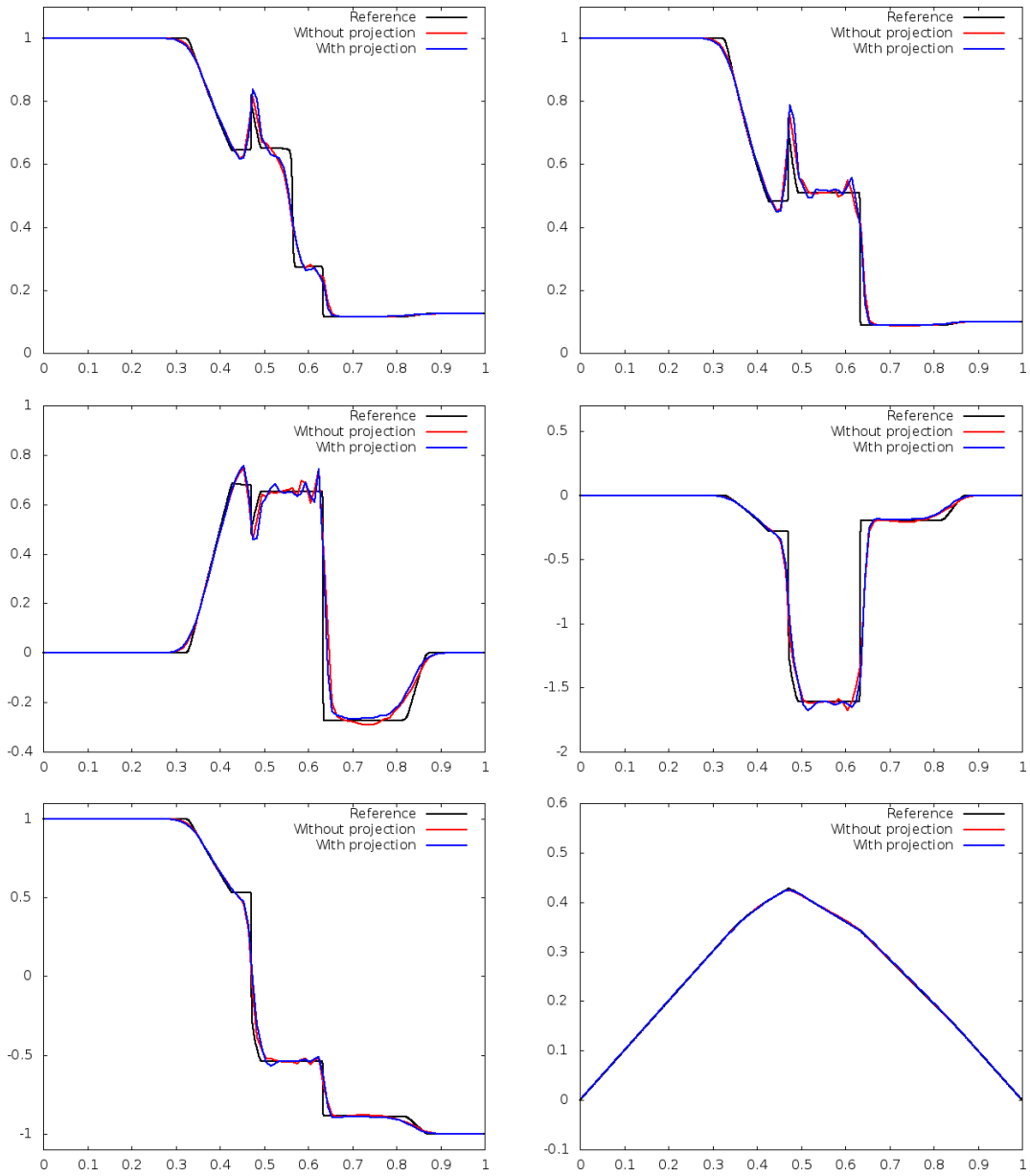

Figure 4.9: 1-D Brio-Wu problem, Solution at $t = 0.1$, O(2) HLL flux with and without projection, Top-Left: Density, Top-Right: Pressure, Middle-Left: x-velocity, Middle-Right: y-velocity, Bottom-Left: y-magnetic field, Bottom-Right: Euler potential.

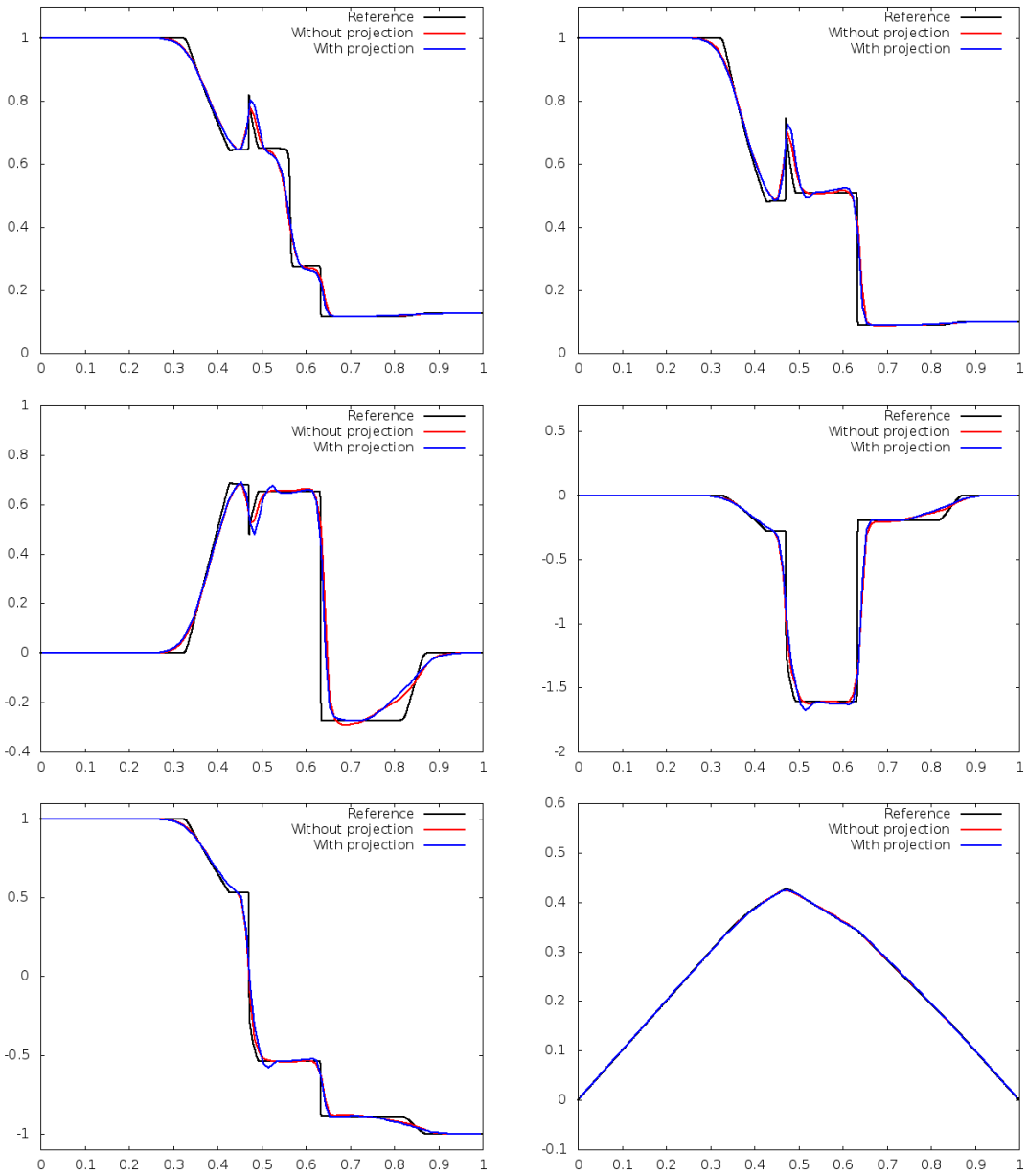

Figure 4.10: 1-D Brio-Wu problem, Solution at $t = 0.1$, O(2) HLLD flux with and without projection, Top-Left: Density, Top-Right: Pressure, Middle-Left: x-velocity, Middle-Right: y-velocity, Bottom-Left: y-magnetic field, Bottom-Right: Euler potential.

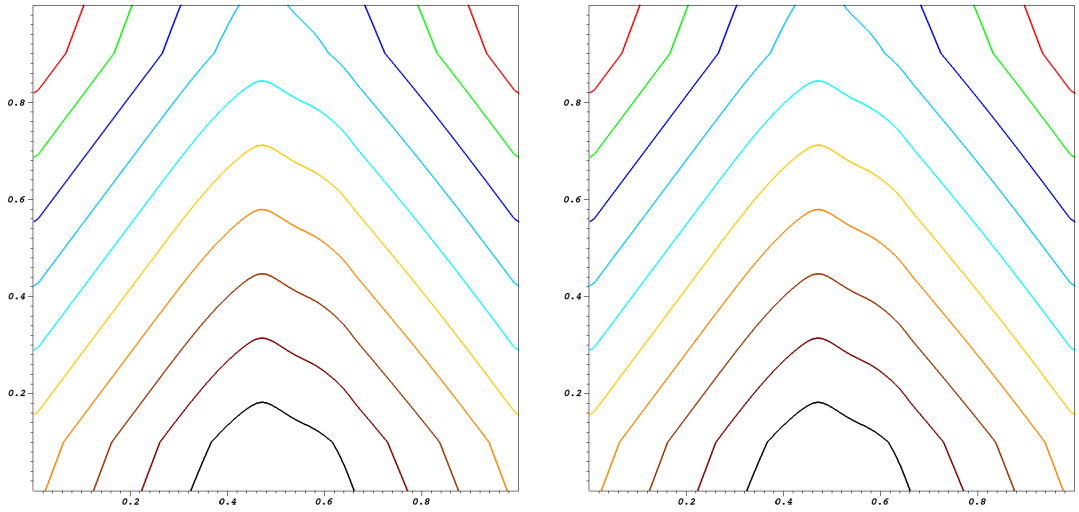

Figure 4.11: 2-D Brio-Wu problem, Euler potential ψ at $t = 0.1$. HLLD flux with projection, Left: Order 1 in time and space, Right: Order 2 in time and space.

As the x-magnetic field is not zero, then according to (4.4), ψ should depend of the x and y coordinates. Then, we re-run this test in 2-D in the square $[0, 1] \times [0, 1]$ meshed with 100×10 cells. According to Table 4.1, the new Euler potential is given by

$$\psi(x, y) = \psi(x) - 0.75y,$$

where $\psi(x)$ is the initialization of ψ in the 1-D run given in (4.28). As expected, all the physical variables except the Euler potential obtained the same results as the 1-D case. Its new final solution is given in Figure 4.11 for the HLLD scheme with projection at the first and second order in time and space. We observe that both of schemes keep a linear relation between the different isolines in the y-direction.

Finally, we have shown that the HLLD schemes at the second order in time and space obtain the best results. Thus, in the rest of the numerical test, we will only use this numerical flux.

V.2 Orszag-Tang problem for ideal MHD

The Orszag-Tang problem is a classical 2-D test for ideal MHD. In this test, we can observe shock waves and this test permits to test the robustness of a scheme as it is shown in [59, 61, 77]. The initial data are the same as the ones of [59] and are referred in Table 4.2. The computation domain is the square $[0, 1] \times [0, 1]$ meshed by 512×512 cells with periodic boundary conditions. According to Table 4.2, the Euler potential is initialized with

$$\psi(x, y) = -\frac{1}{2\pi}\cos(2\pi y) - \frac{1}{4\pi}\cos(4\pi x).$$

The computations are performed until $t = 0.5$ and $t = 1.0$ with the HLLD flux at the second order in time and space. In order to keep physicals results, the pressure and the density are forced to be strictly positive. Moreover, for the second order in space, the normal component of the magnetic field is kept at the first order in space. In this test, we compare the scheme with projection to the one without projection.

ρ	$u(x,y)$	$v(x,y)$	w	$p(x,y)$	$B_x(x,y)$	$B_y(x,y)$	B_z
γ^2	$-\sin(2\pi y)$	$\sin(2\pi x)$	0	γ	$-\sin(2\pi y)$	$\sin(4\pi x)$	0

Table 4.2: Initial data of Orszag-Tang 2-D problem.

Figure 4.12 compares the scheme with projection to the one without projection at $t = 0.5$ for the density and the pressure. We observe that for the scheme without projection, the pressure need to be forced to stay positive, and the results of this scheme are not satisfying. For the scheme with projection we can see that we do not need the criteria to enforce strictly positive density and pressure. Density and pressure remain positive during the time of the simulation. In Figure 4.13, we plot the pressure along $y = 0.3125$ at $t = 0.5$. We observe that the scheme without projection show large oscillations around shock waves at $x = 0.25$ and $x = 0.7$. Moreover, in Figure 4.14 we observe that $\nabla \cdot \mathbf{B}$ has blown up leading to the crash of the simulation before $t = 1.0$. By comparing our results to the ones of [77] with contrained transport method of Balsara and Spicer [11], we see that we obtain similar results.

Figure 4.15 presents the pressure and the density field at $t = 1.0$ by the scheme with projection. We observe that we get a similar results to the one of [77] but we do not get the same value at the center of the computational domain: 4.7 for the pressure instead of 6 in [77].

In Figure 4.14, we compare the 2-D field of $\nabla \cdot \mathbf{B}$ for the two schemes at $t = 0.5$, we also give the evolution of the L^2 and L^∞ norms of the divergence of the magnetic field. Those two norms are given by

$$\|\nabla \cdot \mathbf{B}\|_{L^2} = \sqrt{\sum_{i=1}^{Nx}\sum_{j=1}^{N_y} |C_{i,j}| \left[(\nabla \cdot \mathbf{B})_{i,j}\right]^2}, \quad \|\nabla \cdot \mathbf{B}\|_\infty = \max_{i=1..N_x, j=1..N_y} \left[(\nabla \cdot \mathbf{B})_{i,j}\right].$$

We can see that for the scheme with projection, the divergence of $\mathbf{B}$ stay really close to zero during all the simulation, meanwhile the scheme without projection has a blow-up of the divergence leading to an nonphysical results.

We have shown that only the scheme with projection is able to give comparable results to the ones of [77]. This scheme get satisfactory results by comparing with the ones of [77].

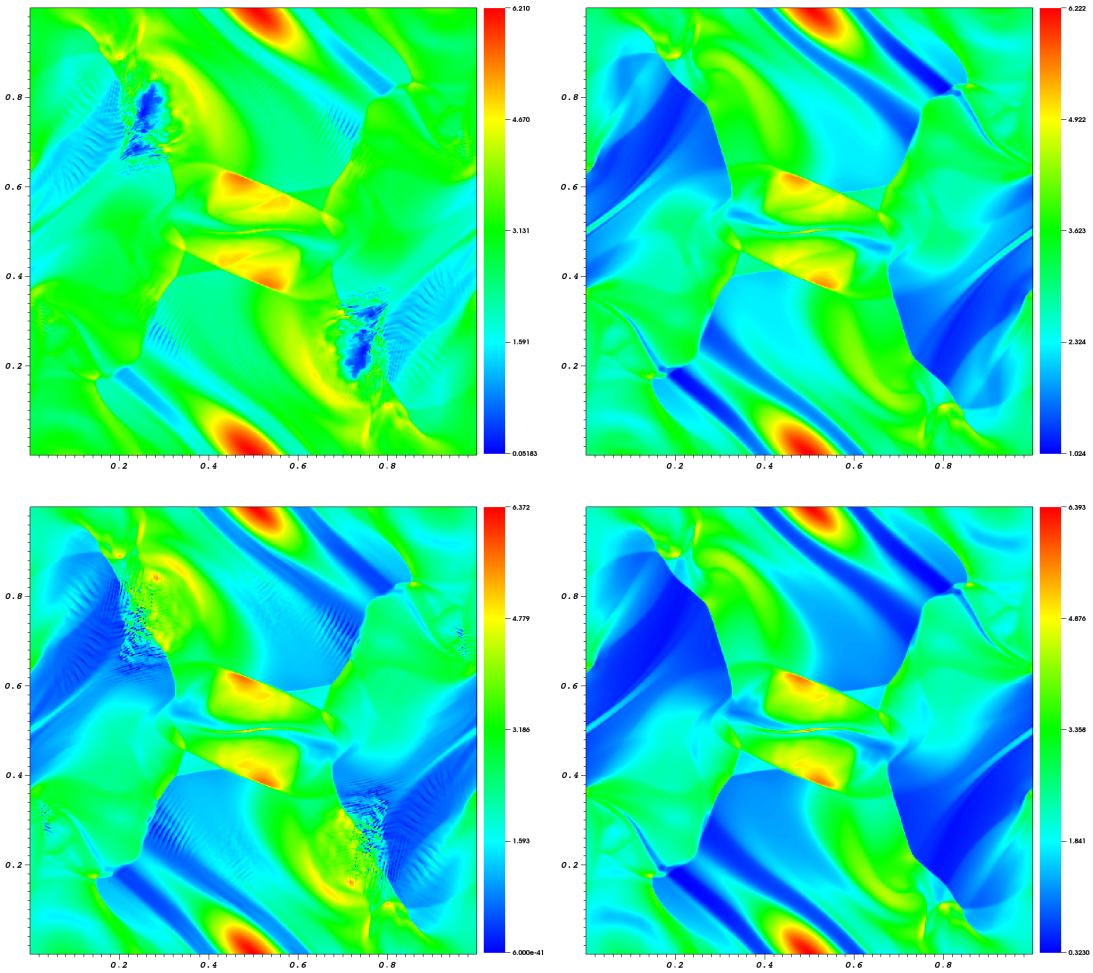

Figure 4.12: Orszag-Tang problem, HLLD O(2), $t = 0.5$, Top: Density field, Bottom: Pressure field, Left: Scheme without projection, Right: Scheme with projection.

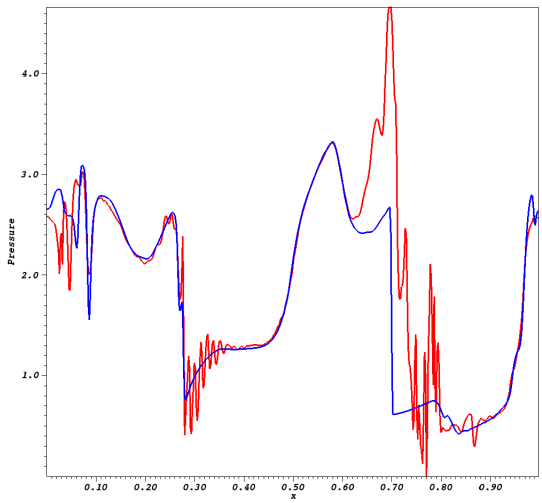

Figure 4.13: Orszag-Tang problem, HLLD O(2), $t = 0.5$, Pressure along $y = 0.3125$, Red: Scheme without projection, Blue: Scheme with projection.

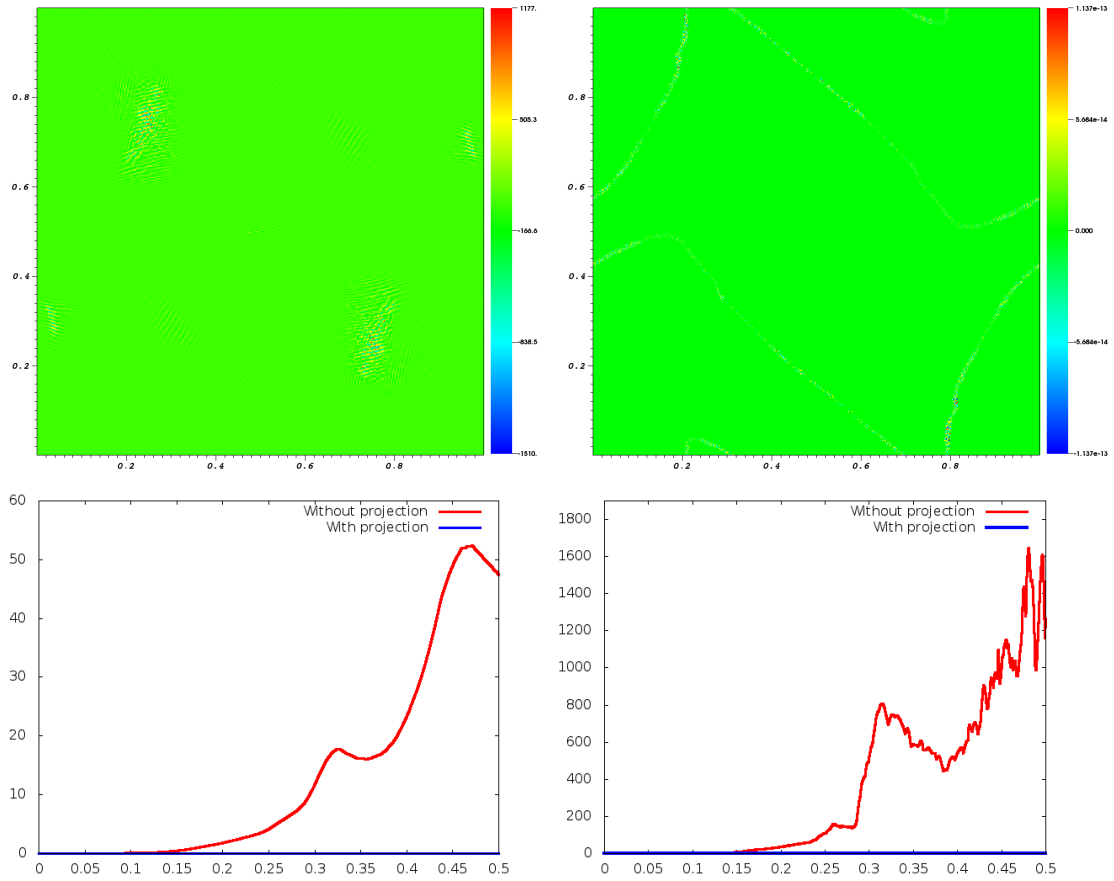

Figure 4.14: Orszag-Tang problem, HLLD O(2), Top-Left: $\nabla \cdot \mathbf{B}$ field at $t = 0.5$ scheme without projection, Top-Right: $\nabla \cdot \mathbf{B}$ field at $t = 0.5$ scheme with projection, Bottom-Left: $\|\nabla \cdot \mathbf{B}\|_{L^2}(t)$, Bottom-Right: $\|\nabla \cdot \mathbf{B}\|_{\infty}(t)$,

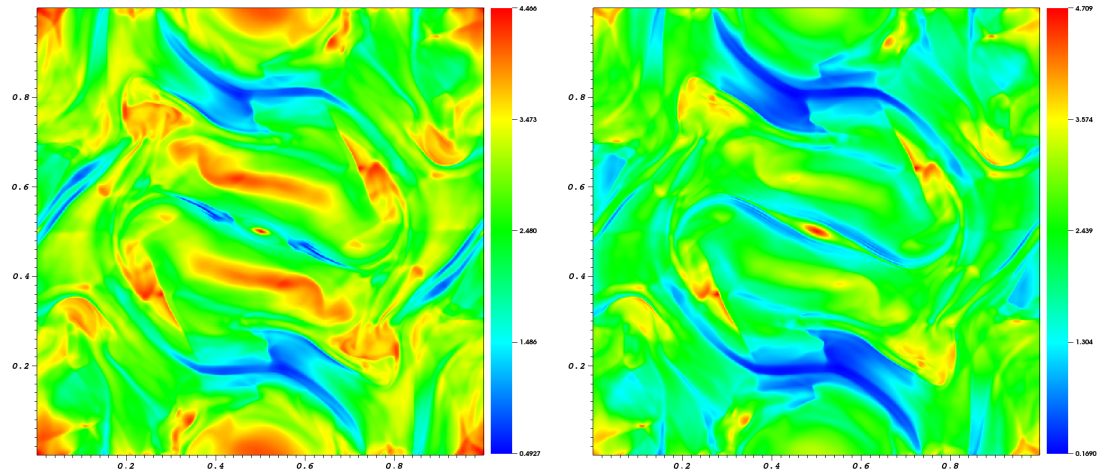

Figure 4.15: Orszag-Tang problem, HLLD O(2) with projection, $t = 1.0$, Left: Density field, Right: Pressure field.

V.3 Kelvin-Helmholtz instabilities for ideal MHD

The Kelvin-Helmholtz instabilities [59] show a nonlinear evolution of the 2-D MHD equations and are resulting from velocity shears. The initial data are the same one as the one of [77] and are given in Table 4.3 where the Mach number is $M = 1$, the width of the region of large sleep shear velocity gradient is $y_0 = 0.05$, and $c_a = 0.1$ is the Alfvén speed. At $t = 0$, a single-mode perturbation is added to the tangential velocity v

$$v_p(x, y) = 0.01 \sin(2\pi x) \exp\left(-\frac{y^2}{\sigma^2}\right), \ \sigma = 0.01.$$

The aim of this test is to see how the different schemes make evolve the perturbation into turbulence flows and maintain the divergence-free constraint. The computational domain is the rectangle $[0, 1] \times [-1, 1]$. At the top and the bottom of the domain, the boundary conditions are reflecting ones. For the left and right boundaries, there are set to periodic boundaries. We also introduce the ratio of the poloidal magnetic field over the toroidal one by

$$\frac{B_{pol}}{B_{tor}} = \frac{\sqrt{B_x^2 + B_y^2}}{B_z}.$$

ρ	$u(x, y)$	v	w	p	B_x	B_y	B_z	$\psi(x, y)$
1	$\frac{M}{2} \tanh(\frac{y}{y_0})$	0	0	$\frac{1}{\gamma}$	$c_a \cos\left(\frac{\pi}{3}\right) \sqrt{\rho}$	0	$c_a \sin(\frac{\pi}{3})\sqrt{\rho}$	$-c_a \cos(\frac{\pi}{3})\sqrt{\rho} y$

Table 4.3: Initial data of Kelvin-Helmholtz instabilities.

First, we compare the schemes with and without projection at four different times: $t = 5.0$, $t = 8.0$, $t = 12.0$, and $t = 20.0$. the computation domain is meshed with 256×512 cells. The results are given in Figure 4.16. We can see that for the scheme without projection that at $t = 5.0$ some instabilities began to appear leading to a non-exploitable results for the rest of the simulation. Concerning the scheme with projection, we observe that there is no such instabilities and then we can observe the turbulence in the computation domain the four different time. By comparing our results to the ones of Vides [77], we observe that for $t = 5.0$ we have similar results as the ones of the constrained transport method, but for the rest of the visualization time, the turbulence of the scheme with projection are not developing in the same way.

In Figure 4.17, we present the evolution of $\|\nabla \cdot \mathbf{B}\|_{L^2}$ and $\|\nabla \cdot \mathbf{B}\|_\infty$ in function of time, we observe that only the scheme with projection is able to keep the divergence-free constraint of the magnetic field. Likewise the Orszag-Tang problem, the divergence of $\mathbf{B}$ for the scheme without projection has blown up leading to non-satisfactory results.

Finally, we re-run the test for two meshes: 64×128 cells, and 128×256 cells. We give the solution for the scheme with projection at $t = 5.0$, $t = 8.0$, $t = 12.0$, and $t = 20.0$ and compare the results in Figure 4.18. We can see for the 64×128 cells mesh no turbulence effect are captured. In fact, more the mesh is precise more the turbulence can be captured.

(a) Without projection

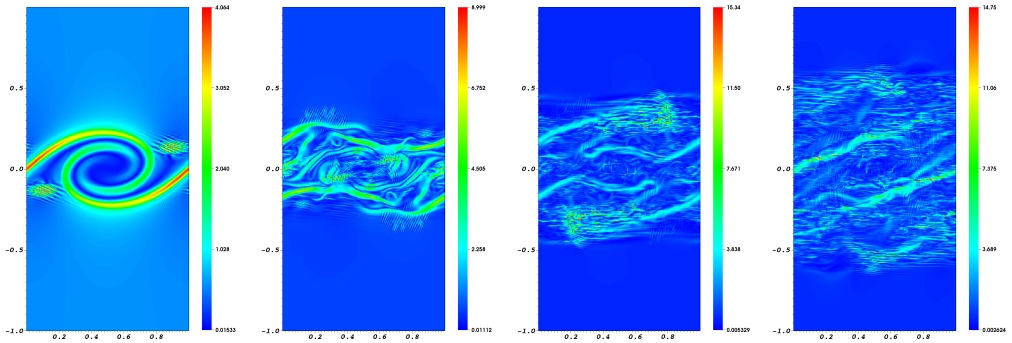

(b) With projection

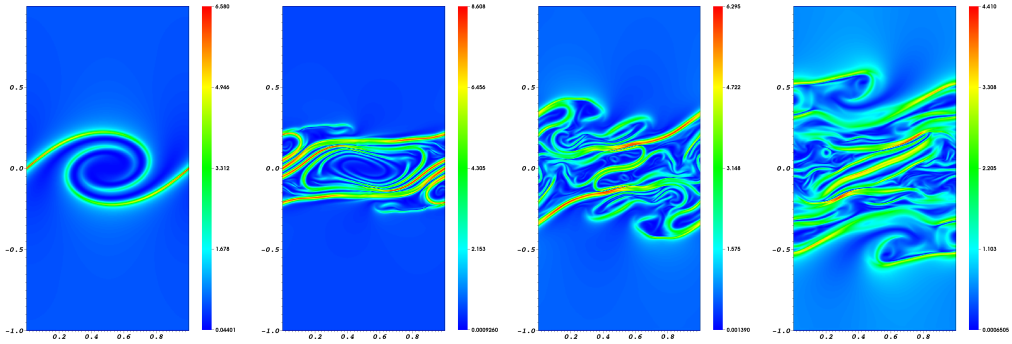

Figure 4.16: Kelvin-Helmholtz instabilities for ideal MHD, Ratio $\frac{B_{pol}}{B_{tor}}$, 256×512 mesh, O(2) HLLD flux. Column 1: $t = 5.0$, Column 2: $t = 8.0$, Column 3: $t = 12.0$, Column 4: $t = 20.0$.

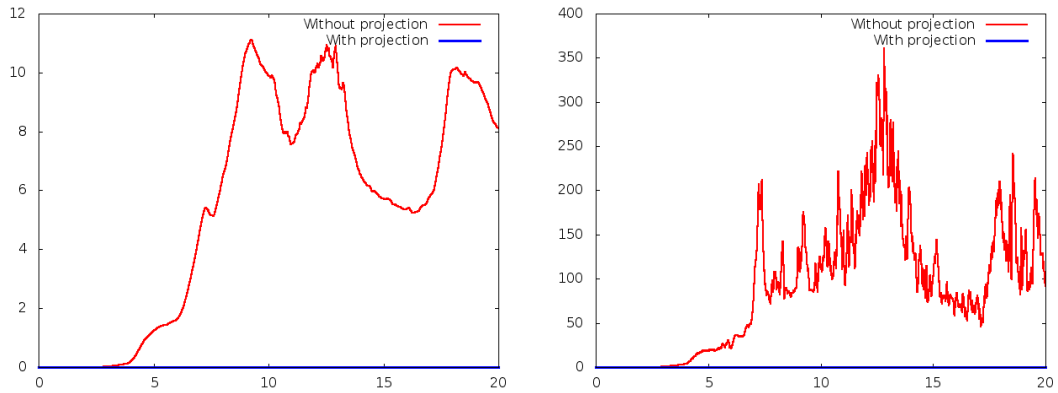

Figure 4.17: Kelvin-Helmholtz instabilities for ideal MHD, 256×512 mesh, O(2) HLLD flux. Left: $||\nabla \cdot \mathbf{B}||_{L^2}||(t)$, Right: $||\nabla \cdot \mathbf{B}||_{\infty}(t)$.

(a) 64×128 mesh grid

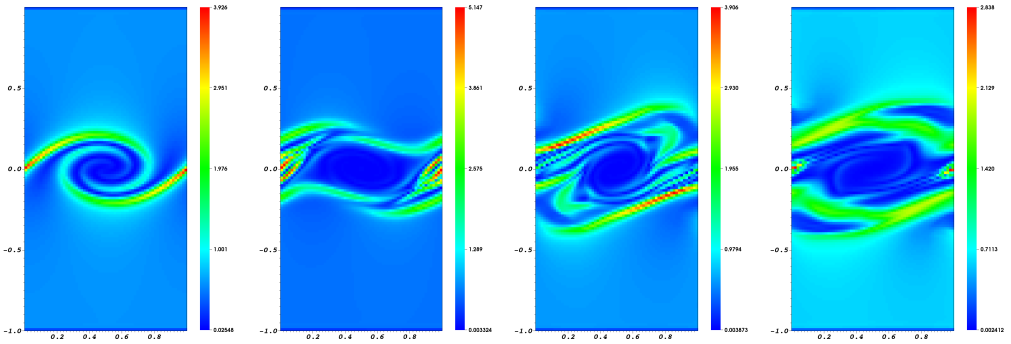

(b) 128×256 mesh grid

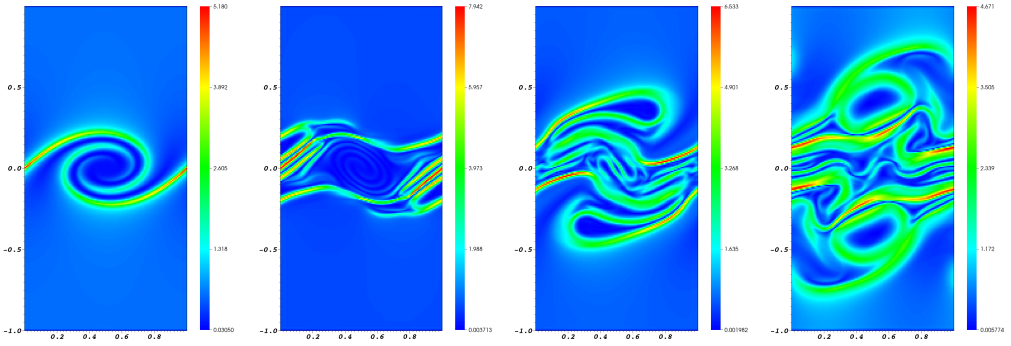

(c) 256×512 mesh grid

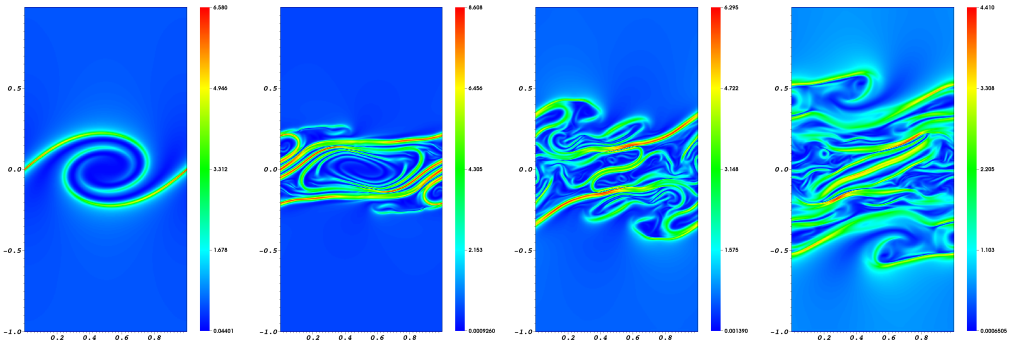

Figure 4.18: Kelvin-Helmholtz instabilities for ideal MHD, Ratio $\frac{B_{pol}}{B_{tor}}$, O(2) HLLD flux with projection. Column 1: $t = 5.0$, Column 2: $t = 8.0$, Column 3: $t = 12.0$, Column 4: $t = 20.0$.

V.4 Kelvin-Helmholtz instabilities for resistive MHD

We are now interested to compare our resistive step at the second and the fourth order for the scheme with projection. Therefore, we re-run the previous case for the resistive MHD equations as it has been done in [60]. The initial data are the same as the previous test, and given by Table 4.3. We have run this test for $\eta = 5 \times 10^{-4}$ and $\eta = 10^{-3}$.

Figure 4.19 presents the results of $\frac{B_{pol}}{B_{tor}}$ for $\eta = 5 \times 10^{-4}$. This Figure compares the scheme with projection at the second order and the fourth order of the resistive step. We observe that the shape of the solution for the two order are similar for each time.

Nevertheless, we can observe some differences between the extrema of the ratio $\frac{B_{pol}}{B_{tor}}$. Indeed at $t = 5.0$, the extrema of the fourth order are 0.01153 and 2.759, instead of 0.1221 and 2.762 for the second order. At the final time of the simulation, this difference is bigger, 1.280 and 0.001084 are the extrema of the fourth order, and the second order get 1.296 and 0.0003226 for the extrema. We also observe that the fact to add the resistive term in the MHD equations for this test reduce the turbulence that we have observed in the case of ideal MHD.

The Figure 4.20 shows the results for $\eta = 1.0 \times 10^{-3}$, and we observe a huge difference with the case $\eta = 5.0 \times 10^{-4}$. Indeed, we do not observe anymore the shear effect in the center of the computational domain, at $t = 20.0$ that we were able to see in the first case. Let us now compare the fourth and the second order of the resistive step of the scheme with projection. At $t = 5.0$, the ratio $\frac{B_{pol}}{B_{tor}}$ evolved between 0.009043 and 2.249 for the fourth order and between 0.009202 and 2.250 for the second one. Likewise the case $\eta = 5.0 \times 10^{-4}$, this difference grows with time along the simulation, indeed at $t = 20.0$, the extrema of the fourth order are 0.004414 and 1.041, and the ones of the second order are 0.004267 and 1.050.

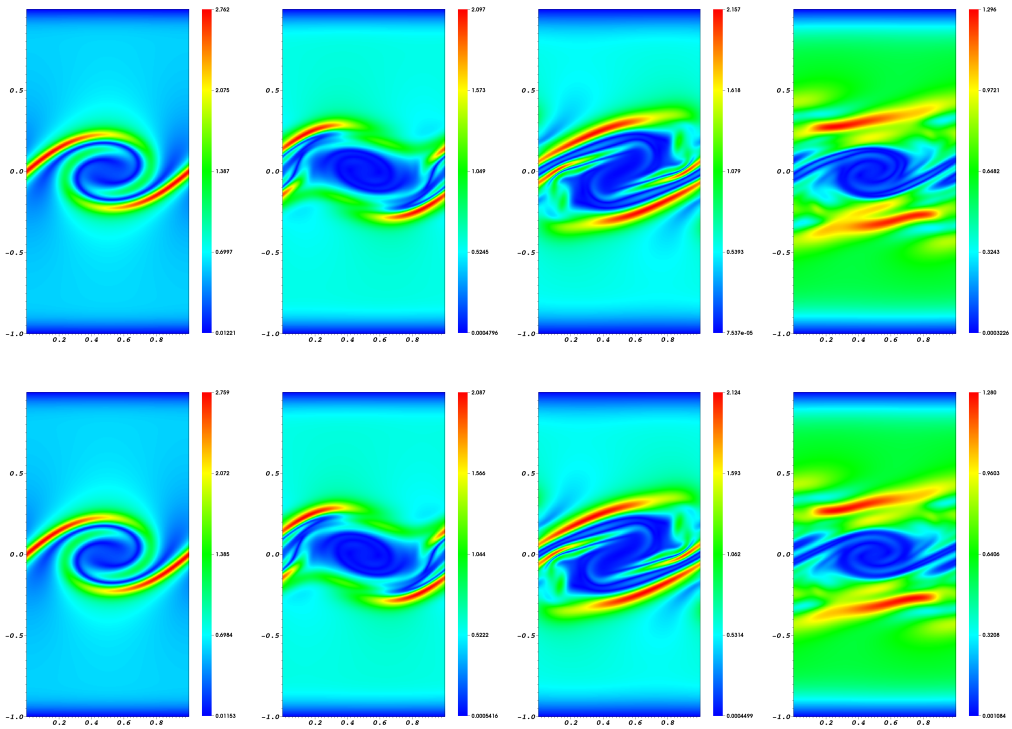

Figure 4.19: Kelvin-Helmholtz instabilities for resistive MHD, $\eta = 5 \times 10^{-4}$, Ratio $\frac{B_{pol}}{B_{tor}}$, HLLD O(2), Top: Order 2 for the resistive step, Bottom: Order 4 for the resistive step, Column 1: $t = 5.0$, Column 2: $t = 8.0$, Column 3: $t = 12.0$, Column 4: $t = 20.0$.

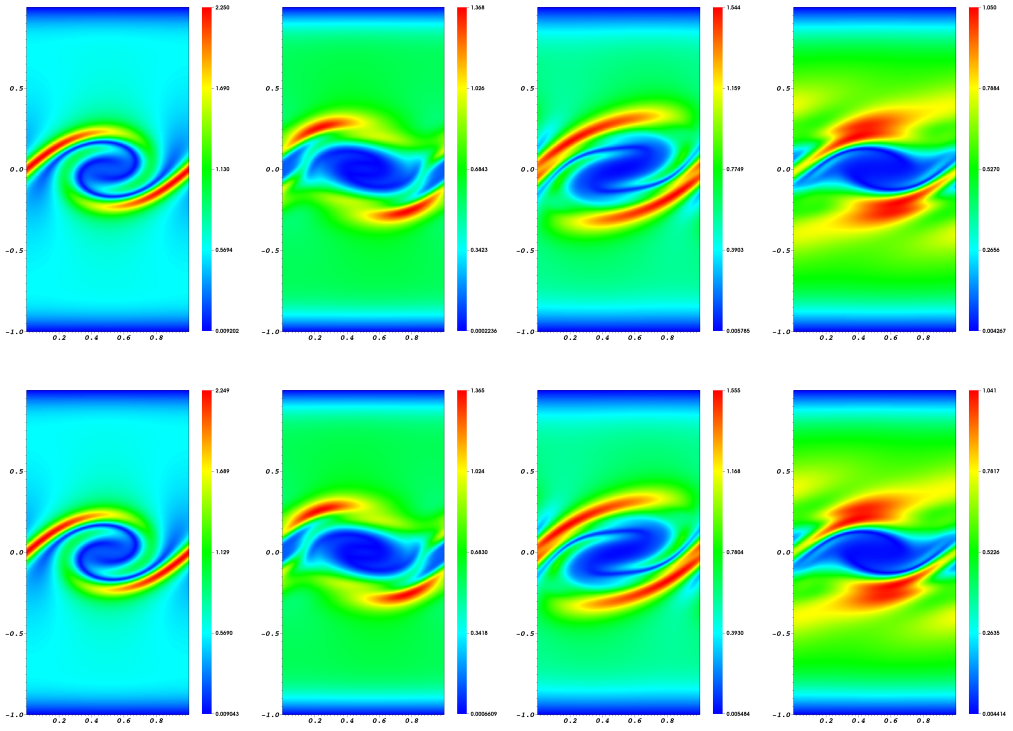

Figure 4.20: Kelvin-Helmholtz instabilities for resistive MHD, $\eta = 10^{-3}$, Ratio $\frac{B_{pol}}{B_{tor}}$, HLLD O(2), Top: Order 2 for the resistive step, Bottom: Order 4 for the resistive step, Column 1: $t = 5.0$, Column 2: $t = 8.0$, Column 3: $t = 12.0$, Column 4: $t = 20.0$.

V.5 Screw pinch equilibrium with uniform density in cylindrical coordinates for ideal MHD

The screw pinch equilibrium corresponds to a fusion plasma test. It consists to maintain a stationary solution and to observe how the numerical scheme is able to keep it. All the theory of this test is explained by Fiedberg in Chapter 5 of [38]. Here, we suppose that the solution is only depending on the radial coordinates R and that there is no radial magnetic field B_R, and no velocity $\mathbf{u}$. The Z-component of the magnetic field is chosen constant. Hence, the only remaining equation from the MHD equations is the radial momentum equation given by

$$\partial_R(Rp_T) = p_T - B_\varphi^2.$$

One solution of this equilibrium is given in Table 4.4 where $R_0 = 10$ and it is represented in Figure 4.21. The computation domain is the disc of radius equal to 1 meshed with $[100 \times 10]$ cells aligned with the R and φ-directions.

The simulation is ended when a steady state is reached or after 10^5 time iterations. The steady state is defined by $\dfrac{Res}{Res0} < 10^{-3}$ where

$$\begin{cases} Res0 &= \|(\rho u_R)^1 - (\rho u_R)^0\|_{L^2}, \\ Res &= \|(\rho u_R)^{n+1} - (\rho u_R)^n\|_{L^2}. \end{cases}$$

Figures 4.22 to 4.24 present the results obtained for the Rusanov, HLL, and HLLD fluxes at the first order in time and space, and compare the scheme with projection to the one without projection. We observe that for the Rusanov and the HLL fluxes the scheme with projection get the closest result. Indeed, Figure 4.25 shows that only the scheme with projection has reached the steady state and then the solution of the Rusanov and HLL scheme without projection are given after 10^5 time iterations. For the one without projection, there were around 30000 time iterations. For the HLLD flux, we can see in Figure 4.24 that the scheme with and without projection get really close results, then to determine which one of the two scheme get the best results we present the evolution of the residu and the one of B_φ relative error in Figure 4.26. The relative error is defined by

$$Err = \frac{\|B_\varphi^n - B_\varphi^{exact}\|_{L^2}}{\|B_\varphi^{exact}\|_{L^2}}.$$

The HLLD scheme with and without projection has converged after the same number of time iterations. But the relative error on the tangential magnetic field show that the scheme without projection is more precise than the one with projection. One reason is that the solution is 1-D in the radial direction, therefore the divergence stays free: For the scheme without projection B_φ is evaluated only with the HLLD flux, whereas with the one with projection we first evaluate ψ with the HLLD flux then we approximate $\partial_R\psi$ to get B_φ.

We now re-run the test at the second order in time and space. The results are given in Figures 4.27 to 4.29. First, for the Rusanov and the HLL schemes, the scheme without projection gets much better results than at the first order but it still less precise than the one with projection. The residu of the Rusanov and HLL schemes shows that the scheme without projection still does not reach the convergence criteria. The HLL scheme with projection also does not attain the criteria as it is shown in Figure 4.30 but it get stable after 10^4 time iterations. For the HLLD flux, the two schemes still get close results and Figure 4.31 shows that the scheme without projection is the most precise.

ρ	$\mathbf{u}$	$p(R)$	B_R	$B_\varphi(R)$	B_Z	$\psi(R)$
1	0	$\frac{1}{6R_0^2(3R^2+1)^2}$	0	$\frac{R}{R_0(3R^2+1)}$	1	$\frac{1}{6R_0}\ln(3R^2+1)$

Table 4.4: Initial data of screw pinch equilibrium.

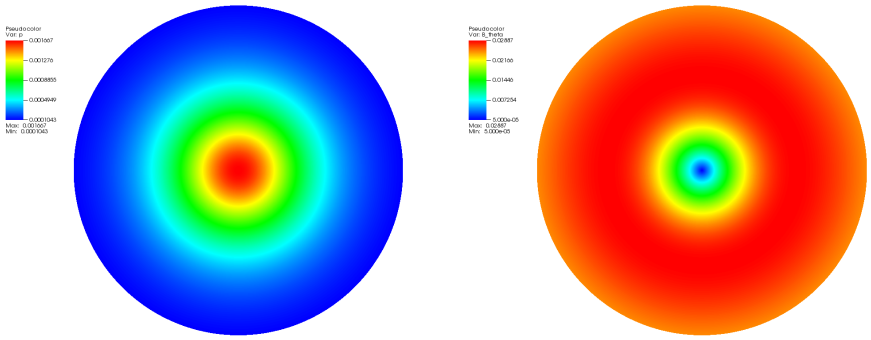

Figure 4.21: Screw pinch equilibrium: Exact solution. Left: Pressure, Right: φ-magnetic field.

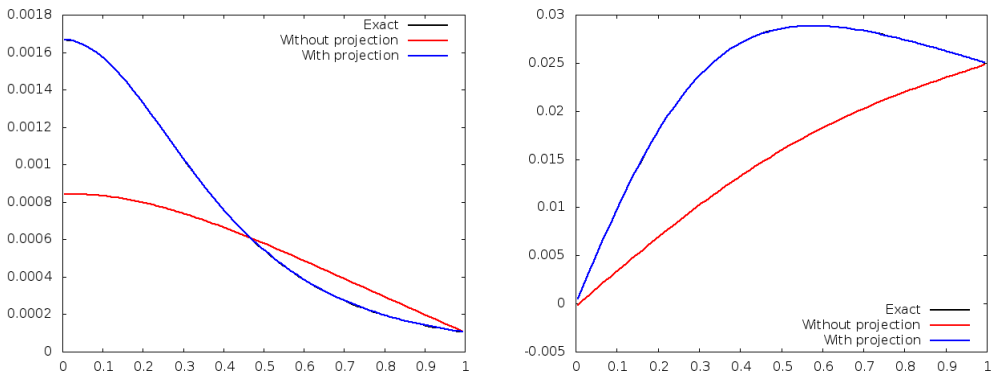

Figure 4.22: Screw pinch equilibrium in cylindrical coordinates, All R. Rusanov O(1). Left: Pressure, Right: B_φ.

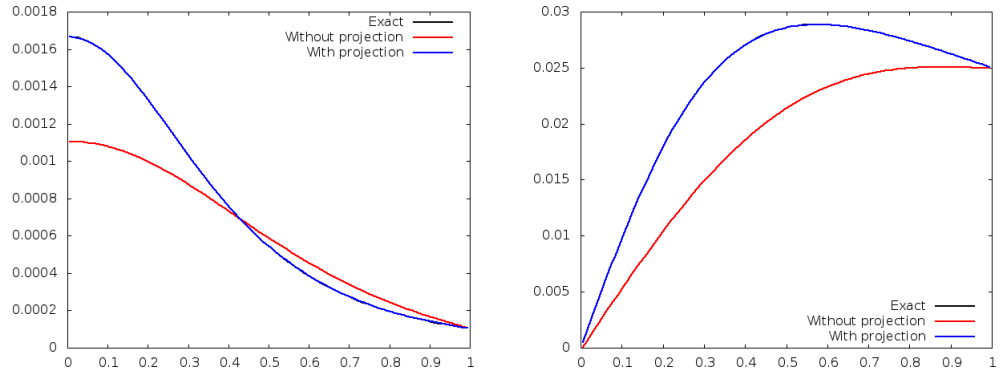

Figure 4.23: Screw pinch equilibrium in cylindrical coordinates, All R. HLL O(1). Left: Pressure, Right: B_φ.

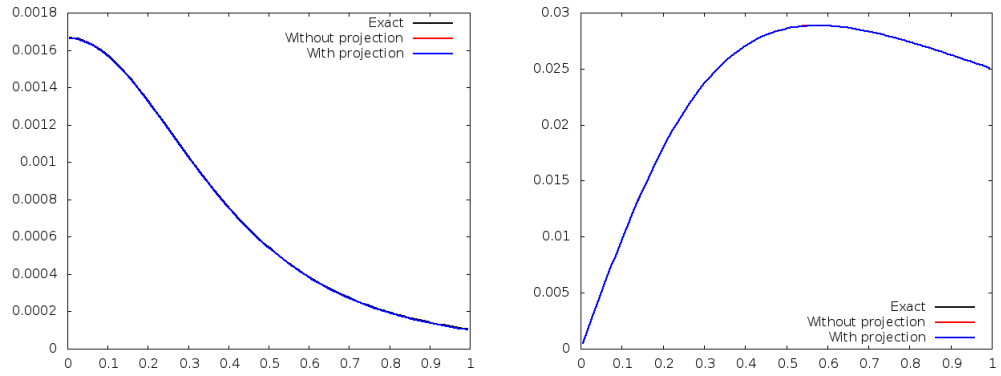

Figure 4.24: Screw pinch equilibrium in cylindrical coordinates, All R. HLLD O(1). Left: Pressure, Right: B_φ.

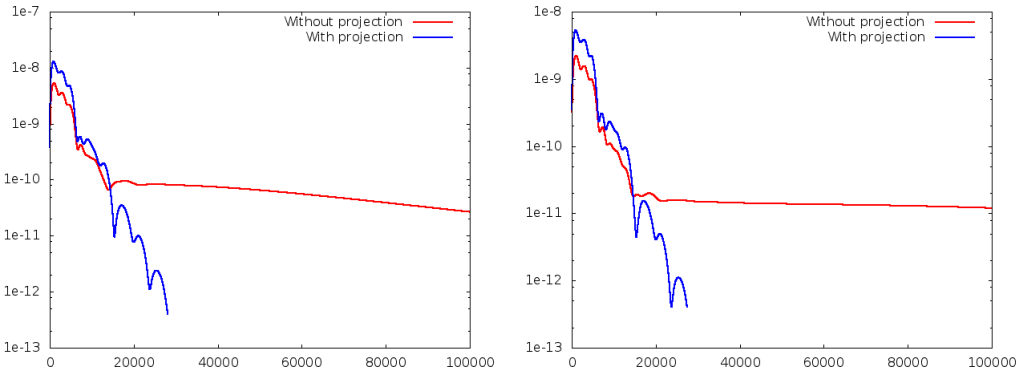

Figure 4.25: Screw pinch equilibrium in cylindrical coordinates. First order in time and space. Comparison of the scheme with projection and of the one without projection. Left: Rusanov flux, Right: HLL flux.

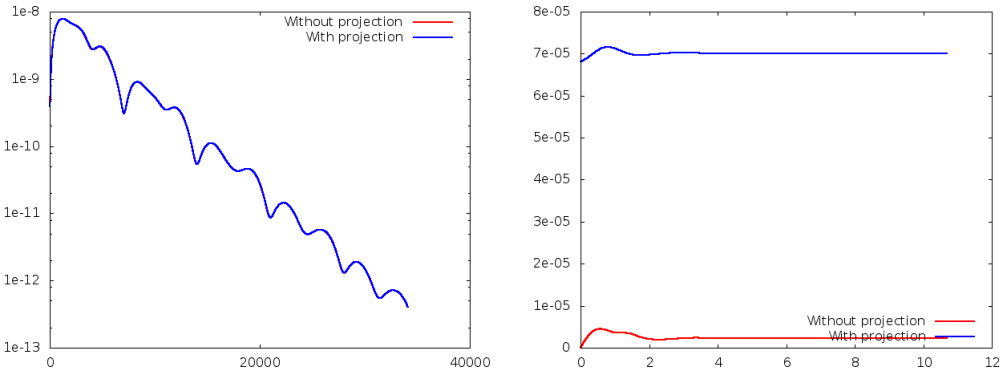

Figure 4.26: Screw pinch equilibrium in cylindrical coordinates. O(1) HLLD flux. Evolution of Left: the Residu in function time iteration. Right: Relative error of B_φ in function of time.

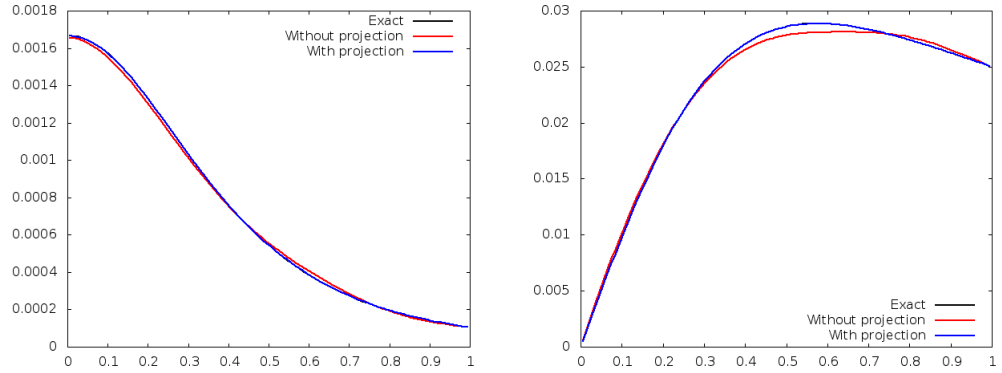

Figure 4.27: Screw pinch equilibrium in cylindrical coordinates, All R. Rusanov O(2). Left: Pressure, Right: B_φ.

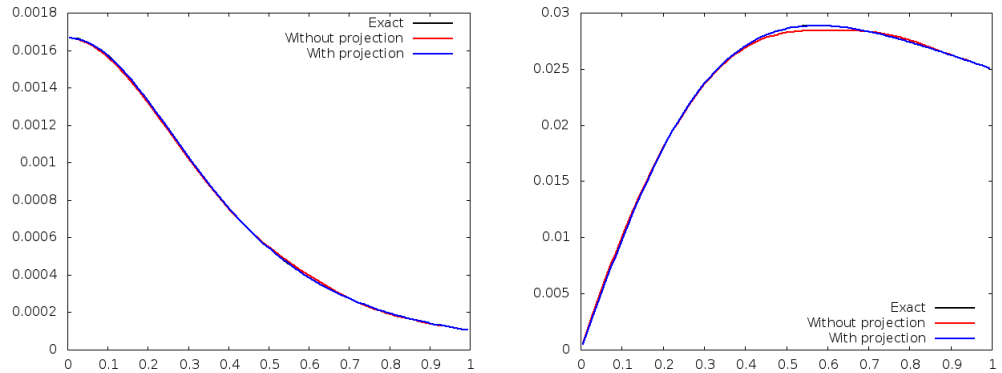

Figure 4.28: Screw pinch equilibrium in cylindrical coordinates, All R. HLL O(2). Left: Pressure, Right: B_φ.

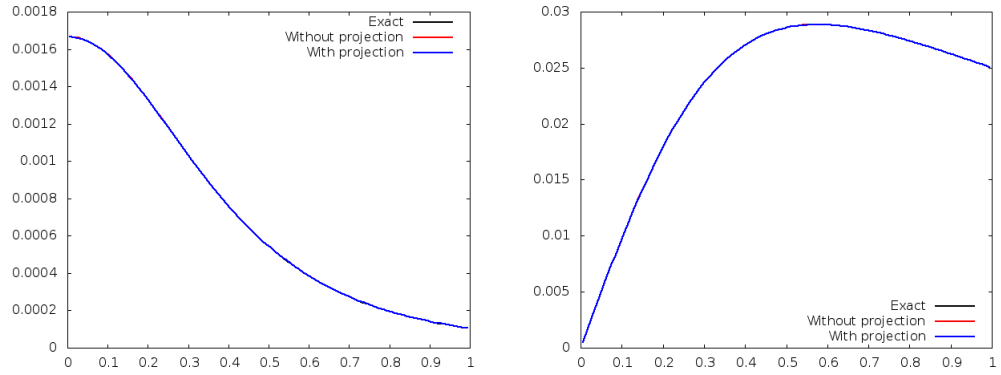

Figure 4.29: Screw pinch equilibrium in cylindrical coordinates, All R. HLLD O(2). Left: Pressure, Right: B_φ.

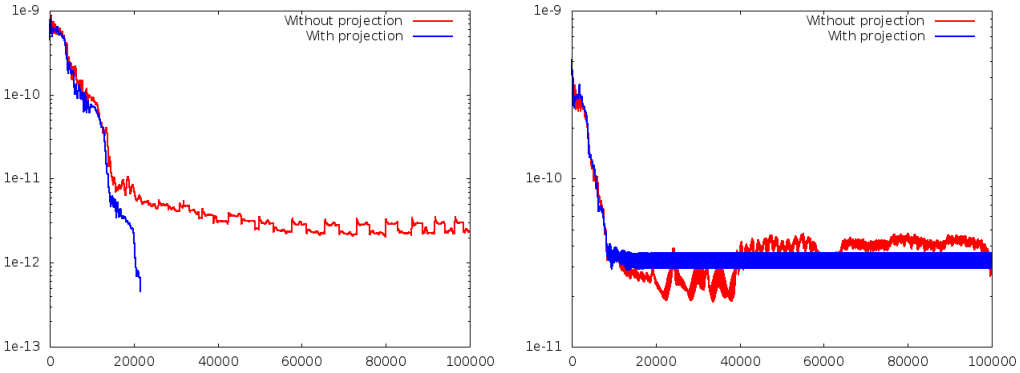

Figure 4.30: Screw pinch equilibrium in cylindrical coordinates. Second order in time and space. Comparison of the scheme with projection and of the one without projection. Left: Rusanov flux, Right: HLL flux.

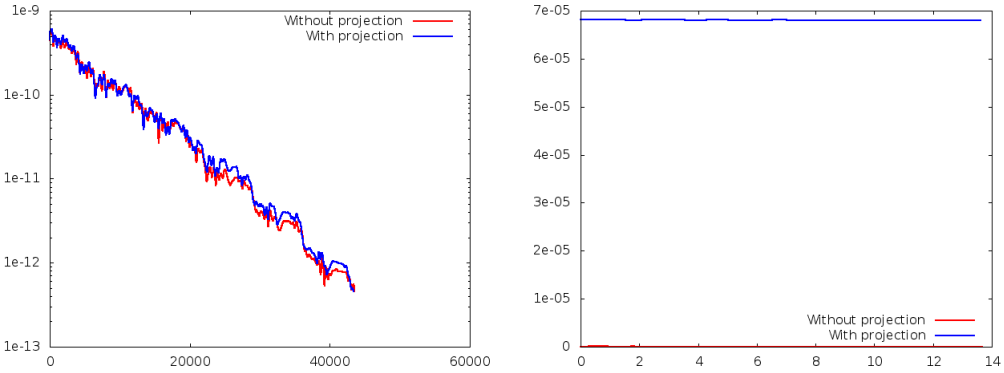

Figure 4.31: Screw pinch equilibrium in cylindrical coordinates. O(2) HLLD flux. Evolution of Left: the Residu in function time iteration. Right: Relative error of B_φ in function of time.

V.6 Screw pinch equilibrium with uniform density in Cartesian coordinates for ideal MHD

We are now interested in re-running the test of subsection V.5 but this time we use the Cartesian coordinates. The new computational domain is the square $[-1,1]\times[-1,1]$ meshed by 200×200 cells. According to Table 4.4, the magnetic field $\mathbf{B}$ in Cartesian coordinates is

$$\mathbf{B}(x,y)=\begin{bmatrix} -\dfrac{y}{R_0(3R^2+1)} \\ \dfrac{x}{R_0(3R^2+1)} \\ 1 \end{bmatrix}_{(\mathbf{e}_x,\mathbf{e}_y,\mathbf{e}_z)}, \quad R^2=x^2+y^2,\ R_0=10.$$

As in Section V.5 the HLLD scheme gets the best results, we test here only the HLLD scheme at the second order in time and space and compare the scheme with projection to the one without projection. The aim of this test is to see how many time iterations the two schemes are able to maintain the screw pinch equilibrium by using the Cartesian coordinates.

Figure 4.32 gives the evolution of the relative error of the pressure in function of Alfvén time. To define the Alfvén time, we re-call the definition of Alfvén speed (1.82)

$$u_0=\frac{B_0/\sqrt{\mu_0}}{\sqrt{n_0(m_e+m_i)}}.$$

Then, the Alfvén time is defined by

$$t_A=\frac{L_0}{u_0}.$$

In the simulation, B_0 and L_0 are set with the following values

$$\begin{cases} B_0 &= 1T, \\ L_0 &= 1m. \end{cases}$$

Figure 4.32 shows that the scheme without projection has crashed in the beginning of the simulation around 15 Alfvén times and after 7500 time iterations. Indeed the pressure relative error has grown up to 100. Meanwhile the scheme with projection run the simulation until 2000 Alfvén time which corresponds to $0.91ms$ after 9×10^5 time iterations. As we can observe in Figure 4.33 that none of those two schemes were able to keep physical results, indeed both of them must use the same criteria as the one used in subsection V.2 to have a strictly positive pressure. However, we observe that the scheme without projection seems to get a 1-D solution in the cylindrical geometry as we expected. For the scheme with projection, the solution present some oscillations leading to the loss of the 1-D character in the cylindrical geometry. This can be explained by the fact that the scheme without projection has done less time iterations than the one with projection and then the solution does not have time to smooth by the first scheme.

This test has shown the influence of the geometry and of the mesh to maintain an 1-D equilibrium in function of the R coordinates. Indeed, by using a mesh aligned with the cylindrical (R,φ) coordinates the two schemes converge to a steady solution close to the exact one. But, for a Cartesian mesh aligned with the x and y-directions, none of the

schemes maintains a suitable solution. Moreover, the 2-D Cartesian computations have shown that the scheme with projection keep more time a physical solution around $0.91ms$. In practice, we want a scheme able to maintain this equilibrium several ms then, we have to find a way to improve the scheme with projection.

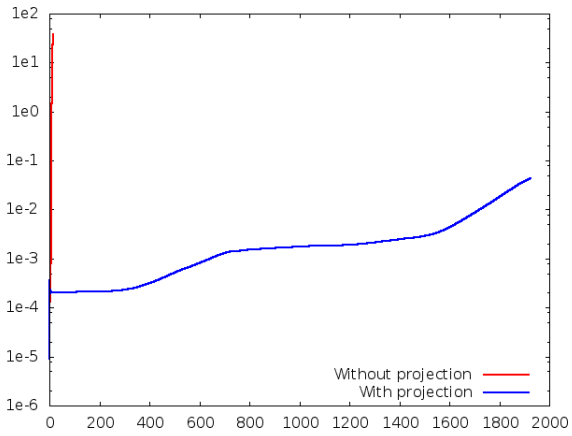

Figure 4.32: Screw pinch in Cartesian geometry. Comparison of the HLLD scheme with and without projection at the second order in time and space. Relative error of the pressure in function of Alfvén time.

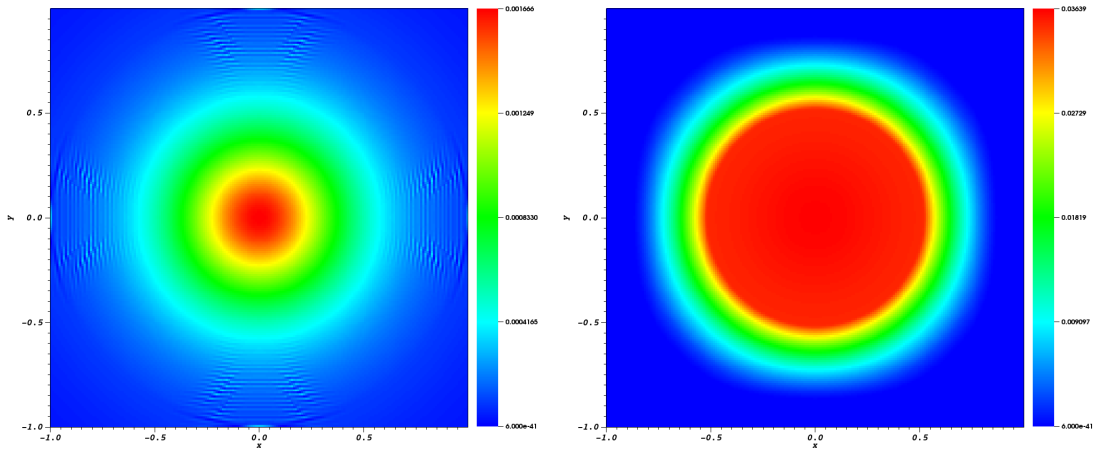

Figure 4.33: Screw pinch equilibrium in Cartesian geometry for ideal MHD. Comparison of the HLLD schemes with and without projection. Final pressure field, Left: Scheme with projection, Right: Scheme without projection.

V.7 Screw pinch equilibrium with uniform density in Cartesian coordinates for resistive MHD

We next reproduce the test of subsection V.6 but this time we run it for the resistive MHD equations to see if the scheme is able to keep the equilibrium on a longer time simulation. We still set the maximum of time iteration at 2.5×10^6. The computational domain is the same as the previous test. For the resistivity, in [34] the authors set the resitivity between 10^{-4} and 10^{-6} then we choose to take $\eta = 10^{-6}$. We still use the HLLD schemes at the second order in time and space.

For the resistive MHD model, the solution is not stationary. However, by using the equation containing the resistive terms, we get that the resistive time is defined by:

$$t_\eta = \frac{L_0}{\eta_0},$$

where L_0 is the reference lengths given in the previous test, and η_0 is the reference resistivity given by the following relation:

$$\eta_0 = 6.5 \times 10^{-8} \frac{1}{T_e^{3/2}},$$

where T_e is in keV. To determine η_0, we use the data of Table 1.1 in the center of the tokamak with $T_e = 11.2keV$. We obtain that the resistive time is

$$t_\eta = 5.77 \times 10^8 s,$$

whereas with the Alfvén time given in the previous test is

$$t_A = 4.58^{\times} 10^{-7} s.$$

Since we have $t_\eta >> t_A$, then the solution should stay close to the initial solution during the simulation.

For this simulation, all the schemes have performed 2.5×10^6 time iterations, and the results are presented in Figures 4.34 and 4.35. Globally, we observe that the use of the resistive MHD equations give better results that the ones obtained with the ideal MHD equations.

Figure 4.34 compares the pressure relative errors of the scheme with and without projection and the second and fourth order of the resistive step. First, we observe that the two orders of resistive step get close results to each other. For the scheme without projection, we see in Figure 4.34 that the simulation ended around 250 Alfvén time. Meanwhile with the same number of time iterations the scheme with projection almost reaches 3500 Alfvén time $\approx 1.6ms$. Both of these schemes have a final relative error around 1.

The final pressure of the four simulations is given in Figure 4.35. Likewise we have said before the results between the two orders of the resistive step does not change the results a lot. The main differences are coming from the use of the projection step or not. Indeed, the final shape of the pressure are totally different between the scheme with projection and the one without. Moreover, the scheme without projection seems to have lot of oscillations closer to the center of the computational domain than at its exterior. At the second order in the resistive step, the extrema of the pressure are 2.759×10^{-14} and 0.00285 for the scheme without projection instead of 1.352×10^{-6} and 0.001910 for the one with projection. The final shape of the scheme with projection show some issue in

the four corners of the computation domain and around the points $(0, -1)$, $(0, 1)$, $(-1, 0)$, and $(1, 0)$.

Using the resistive MHD equations instead of the ideal MHD ones improves the results. The use of the Cartesian coordinates yields to the loss of the 1-D character of the equilibrium. One solution could be to add the Hall effect in the Ohm's law. To go further, it will be interested to re-do this test in the (R, Z) planes as it has be done in [34].

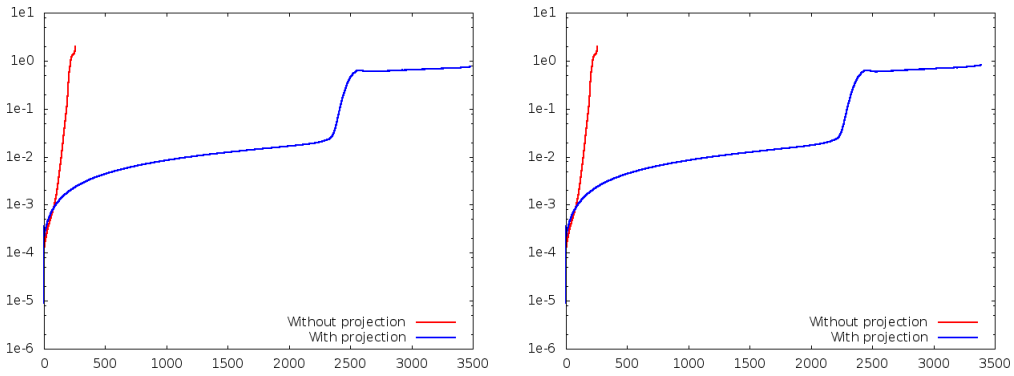

Figure 4.34: Screw pinch in Cartesian geometry for resistive MHD with $\eta = 1.0 \times 10^{-6}$. Comparison of the HLLD scheme with and without projection at the second order in time and space. Relative error of the pressure in function of Alfvén time. Left: Resistive step at the second order, Right: Resistive step at the fourth order.

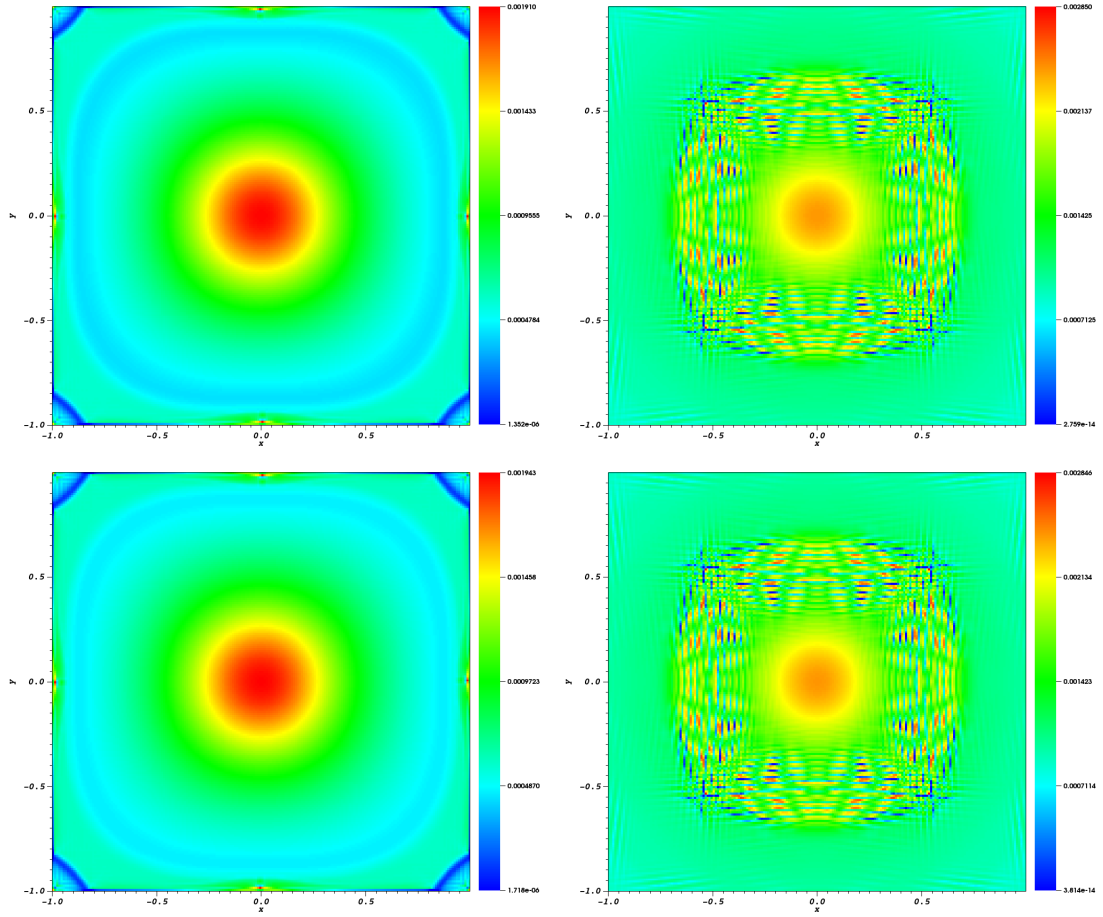

Figure 4.35: Screw pinch equilibrium in Cartesian geometry for resistive MHD. $\eta = 1.0 \times 10^{-6}$. Comparison of the HLLD schemes with and without projection. Final pressure field, Left: Scheme with projection, Right: Scheme without projection. Top: Resistive step at the second order, Bottom: Resistive step at the fourth order.

VI Conclusions

In this Chapter, we have designed a numerical scheme for the ideal and resistive MHD models of Chapter 1. This numerical scheme deals with a strategy to treat the divergence-free constraint. This method is a mixture of the vector potential and divergence cleaning-type methods [42, 30, 66, 63]. Indeed, we have a redundant system containing equations on the magnetic field and on the vector potential. We have used the cell-centered finite volume method both in Cartesian and cylindrical coordinates.

Finally, we have performed numerical tests using the two coordinate systems. The results have shown that the scheme with projection is able to maintain $\nabla \cdot \mathbf{B} = 0$ for 2-D tests and is able to handle instabilities as the Kelvin-Helmholtz ones. The last test of this Chapter consists in observing how the numerical method is able to keep the screw pinch equilibrium. We have noticed that only the cylindrical case converges to a final solution close to the equilibrium. For the Cartesian geometry, the use of the resistive terms in the equations allow a more long time simulation than the ideal MHD equations for the scheme with projection.

One future work will be to adapt this method to the vertex-centered finite volume method of Chapter 2 which has been tested for bi-temperature Euler model in Chapter 3 in order to perform more MCF tests in a torus.

Conclusions

The work presented in this thesis deals the simulations of fusion plasma applied to toroidal geometry. The behavior of plasma involves different physical phenomena at different time scale, then we have to take it into account in the choice of the model to simulate a plasma.

In Chapter 1, we have obtained the bi-temperatures Euler model and the MHD models based on the same kinetic model. The bi-temperature Euler model is mono-fluid model in which the electrons and the ions are distinguished by their temperatures or energies. This model describes phenomena where the magnetic effects are neglected in front of the hydrodynamics ones, then this models correspond better to the Inertial Confinement Fusion point of view. However, for Magnetic Confinement Fusion which is the method use for tokamak devices, the magnetic effects can not be anymore neglected. Then, we have shown the assumptions yielding to the ideal and resistive magnetohydrodynamic models. Those two models are also mono-fluid models but the two species are not anymore distinguishes with their temperatures or energies. During the derivation of the bi-fluid magnetohydrodynamic models, we have never used the hypothesis of weak electron mass as it is usually done [37, 43, 51]. Moreover, the kinetic model has been coupled with the four Maxwell's equations and has taken into account the magnetic field, then the obtention of the bi-temperature Euler model is more general than the one of [7].

Next, Chapter 2 has presented the finite volume method used to approximate solutions of the three models with two 2-D different approaches: the cell-centered one, and the vertex-centered one. The cell-centered approach has been adapted to the cylindrical coordinates. The use of cylindrical coordinates introduces some artificial terms when the vectorial equations are projected on its basis. Then, we have shown a process to remove as much as possible those terms in the ideal magnetohydrodynamic equations. Finally, to model a torus, we have presented the derivation of the 2-D vertex-centered approach to obtain a 3-D finite-volume method adapted to the toroidal geometry. To avoid to deal with artificial source terms in the numerical, we have used the strong conservative form of the equations as it has been done in [18, 21]. Both approaches have been extended to the second order in space and time scheme. The second space order is based on MUSCL-type method, meanwhile the time integration uses a second order Runge-Kutta method.

Chapter 3 was devoted to the design of a numerical method to approximate solution of the bi-temperature Euler equations. We have proposed a relaxation-type scheme based on the one for Euler equations. In a first step, by using relaxation variables instead of the two pressures, the transport part of the system is solved by using an exact Riemann solver to compute the numerical fluxes. Then, during the second and last step of the scheme, we have treated the thermal exchange and given some properties on the equilibrium of the temperatures. Finally, this numerical scheme has been tested for Cartesian and cylindrical geometries. The results have been compared to the ones of the literature and discussed.

Finally, in Chapter 4 we have developed a numerical scheme to solve the two monofluid magnetohydrodynamic models for 2-D geometries. In this numerical scheme, the condition $\nabla \cdot \mathbf{B} = 0$ has been taking into account. Indeed, by introducing the Euler potential and to add its equations in the initial system, we have worked with a redundant system. First, the proposed numerical method for ideal magnetohydrodynamic equations is based on the relaxation schemes, indeed, the two first components of the magnetic field have played the role of the relaxation variables since their are re-evaluated with the Euler potential during a projection step. Then, this numerical method is adapted to the resistive MHD equations. In fact, we have added an implicit step in the scheme to deals with the resistive terms of the model. Those two schemes have been tested and discussed.

Conclusions

Le travail présenté dans cette thèse traite de la simulation de plasma de fusion adapté à la géométrie toroïdale. Le comportement du plasma fait intervenir différent phénomènes physiques à différentes échelle de temps que nous avons du prendre en compte dans le choix des modèles pour modéliser le plasma.

Dans le chapitre 1, nous avons obtenus le modèle d'Euler bi-températures et les modèles MHD à partir du même modèle cinétiques. Le modèle d'Euler bi-températures est un modèle mono-fluide dans lequel les électrons et les ions sont distingués par leur température ou énergies. Ce modèle décrit des phénomènes dans lesquels les effets du champs magnétiques sont négligeables par rapport à les effets hydrodynamiques, ainsi ce modèle s'adapte plus à la fusion par confinement inertiel. Cependant, pour la fusion par confinement magnétiques qui est la méthode utilisée dans les tokamaks, les effets magnétiques ne peuvent pas être négligés. Ainsi, on a donné les hypothèses permettant d'obtenir les modèles de MHD idéales et résistives. Ces deux modèles sont des modèles mono-fluides où les deux espèces ne plus distinguées par leurs températures. Lors de la transformation du modèle magnétohydrodynamique bi-fluide, nous n'avons jamais supposé que la masse des électrons est petite comme cela a été fait dans [37, 43, 51]. De plus, le modèle cinétique a été couplé aux quatre équations de Maxwell prenant en compte le champs magnétiques lors de l'obtention du modèle d'Euler bi-températures ce qui est plus général que la méthode utilisée dans [7].

Ensuite, le chapitre 2 a présenté la méthode volume finis utilisée pour approximer les solutions des trois modèles avec deux approches différentes : l'approche cell-centered, et l'approche vertex-centered. L'approche cell-centered a été adaptée aux coordonnées cylindriques. Leur utilisation introduit des termes sources artificiels dans les équations vectorielles lorsque celles-ci sont projetés sur sa base. Ensuite, nous avons montré un procédé pour supprimer autant que possible ces termes. Finalement, nous avons adapté l'approche 2-D vertex-centered pour obtenir une méthode volume finis 3-D pour la géométrie toroïdale. Afin d'éviter d'avoir des termes sources artificiels, nous avons utilisés la formulation conservative forte des équations comme cela avait été fait dans [18, 21]. Ces deux méthodes numériques ont aussi été formulées pour le second ordre en espace et en temps. Le second ordre en espace s'est servi du méthode du type MUSCL pendant que l'intégration en temps a été approchée par une méthode Runge-Kutta d'ordre 2.

Le chapitre 3 a été consacré à la construction d'une méthode numérique pour approximer les solutions des équations d'Euler bi-températures. Nous avons proposé un schéma du type relaxation basé sur celui pour les équations d'Euler. Duant une première étape en utlisant des variables de relaxation à la place des deux pressions, la partie transport dans les équations est résolue en utilisant un solveur de Riemann exact pour calculer les flux numériques. Ensuite, lors d'une seconde et dernière étape du schéma, nous avons traité les

termes d'échanges thermiques et donné des propriétés de l'équilibre des températures. Finalement, le schéma numérique a été testé pour les géométries cartésiennes et cylindrique. Les résultats obtenus ont été comparés à ceux obtenus dans la littérature et discutés.

Enfin, dans le chapitre 4, nous avons développé un schéma numérique pour résoudre les deux modèles magnétohydrodynamiques mono-fluide pour des géométries 2-D. Dans ce schéma numérique, la condition $\nabla \cdot \mathbf{B} = 0$ est prise en compte. En effet, eb définissant le potentiel d'Euler et ajoutant son équation au système initial, nous avons travaillé avec un système redondant. Tout d'abord, la méthode numérique proposée pour les équations de la MHD idéale s'est basée sur celle des schéma de relaxation où les différentes composantes du champs magnétique ont joué le rôle des variables de relaxation puisqu'elles sont réévaluées à chaque pas de temps à partir du potentiel d'Euler. Ensuite, on l'a adaptée aux équations de la MHD résistive. En fait, nous avons ajouté une étape intermédiaire implicite au premier schéma pour traiter les termes résistifs du modèle. Ces deux schémas ont été testés et commentés.

Bibliography

[1] http://fusionforenergy.europa.eu/understandingfusion/.

[2] https://en.wikipedia.org/wiki/File:Inertial_confinement_fusion.svg.

[3] https://lasers.llnl.gov/science/icf/how-icf-works.

[4] http://petal.aquitaine.fr/Schema-de-l-Allumage-Rapide,87.html.

[5] https://www.euro-fusion.org/2011/09/tokamak-principle-2/.

[6] http://fusionwiki.ciemat.es/wiki/File:ITER.jpg.

[7] D. Aregba-Driolet, J. Breil, S. Brull, B. Dubroca, and E. Estibals. Modelling and numerical approximation for the nonconservative bitemperature Euler model. *Accepted*, 2017.

[8] S. Atzeni and J. Meyer-Ter-Vehn. *The Physics of Intertial Fusion*. Oxford University Press, 2004.

[9] R. Balescu. *Classical Transport*, volume 1 of *Transport Processes in Plasmas*. North-Holland, Amsterdam, 1988.

[10] R. Balescu. *Classical Transport*, volume 2 of *Transport Processes in Plasmas*. North-Holland, Amsterdam, 1988.

[11] D. Balsara and D. Spicer. A Staggered Mesh Algorithm Using High Order Godunov Fluxes to Ensure Solenoidal Magnetic Fields in Magnetohydrodynamic Simulations. *Journal of Computational Physics*, 149:270–292, 1999.

[12] P. Batten, N. Clarke, C. Lambert, and D.M. Causson. On the Choice of Wavespeeds for the HLLC Riemann Solver. *SIAM Journal of Scientific Computing*, 18:1553–1570, 1997.

[13] C. Berthon, F. Coquel, and P.G. LeFloch. Why many theories of shock waves are necessary: kinetic relations for non-conservative systems. *Proceedings of the Royal Society of Edinburgh: Section A Mathematics*, 142(1):1–37, 2012.

[14] C. Berthon, B. Dubroca, and A. Sangam. A Local Entropy Minimum Principle for Deriving Entropy Preserving Schemes. *SIAM Journal on Numerical Analysis*, 50(2):468–491, 2012.

[15] C. Berthon, B. Dubroca, and A. Sangam. An Entropy Preserving Relaxation Scheme For Ten-Moments Equations with Source Terms. *Communications in Mathematical sciences*, 13(8):2119–2154, 2015.

[16] A. Bettinger and M. Decroisette. Laser megajoule project and impact on the inertial fusion program. *Fusion Engineering and Design*, 46:457–460, 1999.

[17] P.L. Bhatnagar, E. P. Gross, and K. Krook. A model for collision processes in gases. *Physical Review*, 94:511–524, 1954.

[18] M. Bilanceri, L. Combe, H. Guillard, and A. Sangam. A 3D finite volume scheme for the simulation of edge plasma in tokamaks. *ESAIM: Proceedings*, 43:164–179, 2013.

[19] J. Blum. *Numerical Simulation and Optimal Control in Plasma Physics.* Series in Applied Mathematics. Wiley and Gauthier-Villars, 1989.

[20] A. Bonnement. *Modélisation numérique par approximation fluide du plasma de bord des tokamaks (projet ITER).* PhD thesis, Ecole Doctorale en Sciences Fondamentales et Appliquées, Université Nice-Sophia Antipolis, France, 2012.

[21] A. Bonnement, T. Fajraoui, H. Guillard, M. Martin, B. Nkonga, and A. Sangam. Finite volume method in curvilinear coordinates for hyperbolic conservation laws. *ESAIM: Proceedings*, 32:163–176, 2011.

[22] F. Bouchut. *Nonlinear Stability of Finite Volume Methods for hyperbolic Conservation Laws and Well-Balanced Schemes for Sources.* Birkhäuser, 2004.

[23] J.U. Brackbill and D.C. Barnes. Note: The effect of nonzero $\nabla \cdot \mathbf{B}$ on the numerical solution of the magnetohydrodynamic equations. *Journal of Computational Physics*, 35:426–430, 1980.

[24] S. I. Braginskii. Transport processes in a plasma. *Reviews of Plasma Physics*, 1:205–311, 1965. Translated from the Russian.

[25] M. Brio and C.C. Wu. An Upwind Differencing Scheme for the Equations of Ideal Magnetohydrodynamics. *Journal of Computational Physics*, 75:400–422, 1988.

[26] F Coquel and C Marmignon. Numerical methods for weakly ionized gas. *Astrophysics and Space Science*, 260(1-2):15–27, 1998.

[27] R. Dautray and J.-P. Watteau. *La Fusion Thermonucléaire Inertielle par Laser, Partie 2, les Techniques Expérimentales et Numériques, Volume 3.* Eyrolles, Paris, 1993.

[28] Dante De Santis, Gianluca Geraci, and Alberto Guardone. Finite Volume and Finite Element Schemes for the Euler Equation in Cylindrical and Spherical Coordinates. *Journal of Computational and Applied Mathematics*, 236:4827–4839, 2012.

[29] A. Decoster. *Fluid equations and transport coefficients of plasmas, in Modelling of collisions.* Masson, ed. by P.-A. Raviart edition, 1997.

[30] A. Dedner, D. Kröner, C.-D. Munz, T. Schnitzer, and M. Wesenberg. Hyperbolic Divergence Cleaning for the MHD equations. *Journal of Computational Physics*, 175:645–673, 2002.

[31] B. Einfeldt, C.D Munz, P.L Roe, and B. Sjögreen. On Godunov-type methods near low densities. *Journal of Computational Physics*, 92(2):273–295, 1991.

[32] Élise Estibals, Hervé Guillard, and Afeintou Sangam. Bi-temperature Euler Equations Modeling for Fusion Plasma. Research Report RR-9026, INRIA Sophia-Antipolis, France, February 2017.

[33] C.R. Evans and J.F. Hawley. Simulation of magnetohydrodynamics flows: a constrained transport method. *Astrophys. J.*, 322:659–677, 1988.

[34] N.M. Ferraro and S.C. Jardin. Calculations of two-fluid magnetohydrodynamic axisymmetric steady states. *Journal of Computational Physics*, 228:7742–7770, 2009.

[35] M. Fey and M. Torrilhon. *A Constrained Transport Upwind Scheme for Divergence-free Advection*, pages 529–538. Springer Berlin Heidelberg, 2003.

[36] R. Fitzpatrick. *Plasma physics: an introduction.* CRC Press, 2014.

[37] J. P. Freidberg. *Plasma Physics and Fusion.* Cambridge University Press, 2007.

[38] J. P. Freidberg. *Ideal MHD.* Cambridge University Press, 2014.

[39] D. Furfaro and R. Saurel. A simple HLLC-type Riemann solver for compressible non-equilibrium two-phase flows. *Computers & Fluids*, 111:159–178, 2015.

[40] S. Galera, P.-H. Maire, and J. Breil. A two-dimensional unstructured cell-centered multi-material ALE scheme using VOF interface reconstruction. *Journal of Computational Physics*, 229:5755–5787, 2010.

[41] E. Godlewski and P. A. Raviart. *Numerical Approximation of Hyperbolic System of Conservation Laws.* Springer New York, 1996.

[42] J. P. Goedbloed, R. Keppens, and S. Poedt. *Advanced Magnetohydrodynamics: With Applications to Laboratory and Astrophysical Plasmas.* Cambridge University Press, 2010.

[43] J. P. Goedbloed and S. Poedt. *Principles of Magnetohydrodynamics: With Applications to Laboratory and Astrophysical Plasmas.* Cambridge University Press, 2004.

[44] V. Grandgirard, M. Brunetti, P. Bertrand, N. Besse, X. Garbet, P. Ghendrih, G. Manfredi, Y. Sarazin, O. Sauter, E. Sonnendrücker, J. Vaclavik, and L. Villard. A drift-kinetic Semi-Lagrangian 4D code for ion turbulence simulation. *Journal of Computational Physics*, 217:395–423, 2006.

[45] H. Guillard and R. Abgrall. *Modélisation Numérique des Fluides Compressibles.* Series in Applied Mathematics. North-Holland, 2001.

[46] A. Harten, P.D. Lax, and B. van Leer. On upstream differencing and Godunov-type schemes for hyperbolic conservation laws. *SIAM*, 25:35–, 1983.

[47] W.J. Hogan, E.I. Mosses, B.E. Warner, M.S. Soren, and J.M. Soures. The National Ignition Facility. *Nuclear Fusion*, 41(5):565–573, 2001.

[48] J.D. Huba. *NRL plasma formulary.* Naval Research Laboratory, 2013.

[49] S. Jin and Z.-P. Xin. The relaxation schemes for systems of conservation laws in arbitrary space dimensions. *Comm. Pure Appl. Math.*, 48:235–276, 1995.

[50] B. B. Kadomtsev. *Tokamak plasma, a complex physical system.* Institute of Physics Publishing, Bristol, 1993.

[51] A. G. Kulikovskii, N. V. Pogorelov, and A. Y. Semenov. *Mathematical Aspects of Numerical Solution of Hyperbolic Systems*. Chapmann and Hall/CRC, 2001.

[52] J. D. Lawson. Some Criteria for a Power Producing Thermonuclear Reactor. *Proceedings of the Physical Society. Section B*, 70(1):6, 1957.

[53] R.J. Leveque. *Finite-Volume Methods for Hyperbolic Problems*. Cambridge, 2004.

[54] C. D. Levermore. Moment Closure Hierarchies for Kinetic Theories. *Journal of Statistical Physics*, 83:1021–1065, 1996.

[55] C. D. Levermore and W. J. Morokoff. The Gaussian Moment Closure for Gas Dynamics. *SIAM Journal of Applied Mathematics*, 59:72–96, 1996.

[56] J. Lindl. *Inertial Confinement Fusion: The Quest for Ignition and Energy Gain Using Indrect Drive*. Springer and American Institute of Physics, New York, 1998.

[57] P.-H. Maire. A high-order cell-centered Lagrangian scheme for compressible fluid flows in two-dimensional cylindrical coordinates. *Journal of Computational Physics*, 228:6882–6915, 2009.

[58] P.-H. Maire, R. Abgrall, J. Breil, and J. Ovadia. A cell-centered Lagrangian scheme for two dimensional compressible frlow problems. *SIAM Journal on Scientific Computing*, 29:1781–1824, 2007.

[59] A. Mignone, P. Tzeferacos, and G. Bado. High-order conservative fonite difference GLM-MHD schemes for cell-centered MHD. *Journal of Computational Physics*, 229(17):5869–5920, 2010.

[60] K.W. Min and D.Y. Lee. Simulation of Kelvin-Helmholtz instabilities in resistive plasmas. *Geophysical research letters*, 23:3667–3670, 1996.

[61] T. Miyoshi and K. Kusano. A multi-state HLL approximate Riemann solver for ideal magneto-hydrodynamics. *Journal of Computational Physics*, 208(1):314–344, 2005.

[62] G. A. Mourou, P. J. Barry, and D. Perry. Ultrahigh-Intensity Lasers: Physics of the Extreme on a Tabletop. *Physics Today*, 51:22, 1998.

[63] C.-D. Munz, P. Omnes, R. Schneider, E. Sonnendrücker, and U. Voß. Divergence Correction Technique for Maxwell Solvers Based on a Hyperbolic Model. *Journal of Computational Physics*, 161:484–511, 2000.

[64] K. Nishikawa and M. Wakatani. *Plasma Physics, Basic Theory with Fusion Applications*. Springer Series on Atoms And Plasmas. Springer, third edition edition, 2000.

[65] S. Pfalzner. *An Introduction to Inertial Confinement Fusion*. Taylor and Francis Group, New York, London, 2006.

[66] K.G. Powell. An Approximate Riemann solver for magnetohydrodynamics (that works in more than one dimension). Technical Report NM-R9407, Centrum voor Wiskunde en Informatica (CWI). Amsterdam (NL), 1994.

[67] K.G. Powell, P.L. Roe, T.J. Linde, T.I. Gombosi, and D.L. De Zeew. A Solution-Adaptive Upwind Scheme for Ideal Magnetohydrodynamics. *Journal of Computational Physics*, 154:284–309, 1999.

[68] P. Savioni. M2 Plasmas : de l'Espace au Laboratoire : Introduction à la physique des plasmas, 2011-2012.

[69] R. Sentis. *Mathematical Models and Methods for Plasma Physics, Volume 1.* Birkhäuser, 2014.

[70] G. A. Sod. A Survey of Several Finite Difference Methods for Systems of Nonlinear Hyperbolic Conservation Laws. *Journal of Computational Physics*, 27:1–31, 1978.

[71] D. P. Stern. Euler Potentials. *American Journal of Physics*, 38(4):494–501, 1970.

[72] M. Tabak, J. Hammer, M.E. Glinsky, W. L. Kruer, S. C. Wilks, J. Woodworth, E. M. Campbell, M. D. Perry, and R. J. Mason. Ignition and high gain with ultrapowerful lasers. *Physics of Plasmas*, 1:1626, 1994.

[73] E.F. Toro. *Riemann Solvers and Numerical Methods for Fluids Dynamics, A Practical Introduction.* Springer, 1999.

[74] E.F. Toro, M. Spruce, and W. Speares. Restoration of the contact surface in HLL-Riemann Solver. *Shock waves*, 4:25–34, 1994.

[75] G. Tóth. The $\nabla \cdot \mathbf{B} = 0$ constraint in shock-capturing magnetohydrodynamics codes. *Journal of Computational Physics*, 161:605–652, 2000.

[76] B. van Leer. Toward the ultimate conservative difference scheme. V. A second order sequel to Godunov's method. *Journal of Computational Physics*, 32:101–, 1979.

[77] J. Vides Higueros. *Godunov-type schemes for hydrodynamic and magnetohydrodynamic modeling.* PhD thesis, Ecole Doctorale en Sciences Fondamentales et Appliquées, Université Nice-Sophia Antipolis, France, 2014.

[78] C. Viozat, C. Held, K. Mer, and A. Dervieux. On vertex-centered unstructured finite volume methods for stretched anisotropic triangulations. *Computer Methods in Applied Mechanics and Engineering*, 190:4733–4766, 2001.

[79] J. Wesson. *Tokamaks.* International Series of Monographs on Physics. Oxford Sciences Publications, 3rd edition, 2004.

[80] H. Zohm, C. Angioni, E. Fable, G. Federici, G. Gantenbein, T. Hartmann, K. Lackner, E. Poli, L. Prote, and O. Sauter. On the physics guidelines for a tokamak DEMO. *Nuclear Fusion*, 53(7):073019, 2013.

Modélisation MHD et Simulation Numérique par des Méthodes Volumes Finis. Application aux Plasmas de Fusion

Ce travail traite de la modélisation des plasmas de fusion qui est ici abordée à l'aide d'un modèle Euler bi-températures et du modèle de la magnétohydrodynamique (MHD) idéale et résistive. Ces modèles sont tout d'abord établis à partir des équations de la MHD bi-fluide et nous montrons qu'ils correspondent à des régimes asymptotiques différents pour des plasmas faiblement ou fortement magnétisés. Nous décrivons ensuite les méthodes de volumes finis pour des maillages structurés et non-structurés qui ont été utilisées pour approcher les solutions de ces modèles. Pour les trois modèles mathématiques étudiés dans cette thèse, les méthodes numériques reposent sur des schémas de relaxation.
Afin d'appliquer ces méthodes aux problèmes de fusion par confinement magnétique, nous décrivons comment modifier les méthodes de volumes finis pour les appliquer à des problèmes formulés en coordonnées cylindriques tout en gardant une formulation conservative forte des équations. Enfin nous étudions une stratégie pour maintenir la contrainte de divergence nulle du champ magnétique qui apparait dans les modèles MHD. Une série de cas tests numériques pour les trois modèles est présentée pour différentes géométries afin de valider les méthodes numériques proposées.

Mots-clés : Magnétohydrodynamique, Équations d'Euler bi-températures, Méthodes volumes finis, Schéma de relaxation, Contrainte de divergence nulle.

MHD Modeling and Numerical Simulation with Finite Volume-type Methods. Application to Fusion Plasma

This work deals with the modeling of fusion plasma which is discussed by using a bi-temperature Euler model and the ideal and resistive magnetohydrodynamic (MHD) ones. First, these models are established from the bi-fluid MHD equations and we show that they correspond to different asymptotic regimes for lowly or highly magnetized plasma. Next, we describe the finite volume methods for structured and non-structured meshes which have been used to approximate the solution of these models. For the three mathematical models studied in this thesis, the numerical methods are based on relaxation schemes.
In order to apply those methods to magnetic confinement fusion problems, we explain how to modify the finite volume methods to apply it to problem given in cylindrical coordinates while keeping a strong conservative formulation. Finally, a strategy dealing with the divergence-free constraint of the magnetic filed is studied. A set of numerical tests fir the three models is presented for different geometries to validate the proposed numerical methods.

Keywords: Magnetohydrodynamics, Bi-temperature Euler equations, Finite Volume method, Relaxation scheme, Divergence-free constraint.